Strain Control of Ferromagnetic Thin Films and Devices

Duncan Parkes, MSci.

School of Physics and Astronomy

University of Nottingham

Thesis submitted to the
University of Nottingham
for the degree of

Doctor of Philosophy

December 2015

Acknowledgements

I would like to thank my supervisor Dr. Andrew Rushforth for his advice and guidance during this PhD. I would also like to thank particularly Dr. Stuart Cavill without whose efforts many of the experiments discussed in this thesis would not have been possible.

I would like also to thank the collaborators I have had the pleasure to work with during my PhD, Dr Alexander Alekseev, Dr. Thomas Hayward and James Wheelwright, Dr. Jan Zemen, and Dr. Andrew Irvine.

Thank you to all those who gave me help and advice in the clean room, especially Dave Taylor, Jasbinder Chauhan, Chris Mellor, Mark Patton, Richard Cousins, and Simon Svatek.

I would like to thank all the other members of the spintronics group during my time here: Professor Bryan Gallagher, Dr. Kevin Edmonds, James Haigh, Arianna Casiraghi, Peter Wadley, Robin Marshall, Lucy Hurley (née Goff), Mu Wang, Stuart Bowe, Vicky Hills, Mo Khah, Fintan McGee, Carl Andrews, Debi Pattnaik, Aidan Hindmarch, Bryn Howells, Ryan Beardsley.

Thank you also to my family.

Abstract

Magnetic memory and logic technologies promise greater energy efficiency and speed than conventional, semiconductor-based electronics. To date, electrical current has been used to operate such devices, although voltage-control may be a more efficient way to control magnetisation. One route to achieving voltage control of magnetisation is to use a hybrid piezoelectric/ferromagnetic device in which a voltage applied to the piezoelectric induces a strain in the ferromagnetic layer, which in turn induces a magnetic anisotropy. In this thesis such hybrid devices are used to investigate the control of magnetisation by inducing uniaxial anisotropy in the ferromagnetic layer.

One material that shows promise for use as the ferromagnetic layer is $Fe_{81}Ga_{19}$. This material is attractive since it contains no rare earth elements, and in bulk crystals has been shown to be highly magnetically responsive to strain. This thesis investigates the magnetic properties of epitaxial $Fe_{81}Ga_{19}$ thin films grown by molecular beam epitaxy and it is demonstrated that these thin films retain the attractive magnetostrictive properties previously observed in bulk crystals. The presence of strong cubic magnetocrystalline anisotropy in the layers is exploited to demonstrate the non-volatile switching of magnetisation using strain-induced anisotropy in the absence of an applied magnetic field.

This thesis shows also the manipulation of magnetic anisotropies and control of the configuration of magnetic domains and domain walls in $Fe_{81}Ga_{19}$ at a range of different lateral dimensions, from 50 µm to 1 µm. It is shown that as the lateral dimensions of the

device structures studied are reduced the domain configuration appears more regular, and that strain-induced anisotropy is more able to control these domains. In wires around 1 µm in width it is shown that growth strain relaxation by lithographic patterning induces sufficient anisotropy to cause a change in the domain configuration of the wire studied.

Finally, this thesis begins to investigate how inverse magnetostriction can be used to tune the behaviour of domain walls in wires 1 µm wide and narrower. Experimental control of the field required to depin a vortex domain wall from a notch in a 1 µm wide Co wire is demonstrated. Using micromagnetic simulations it is shown that a large degree of control over the depinning of domain walls from notches in wires 1 µm wide and narrower is possible. The influence of in plane uniaxial magnetic anisotropy on the domain wall velocity in wires supporting in plane transverse domain walls driven by an external magnetic field is also investigated. Work previously done on the effect of uniaxial anisotropy on domain wall velocities close to Walker breakdown is extended in this thesis and in investigating the velocity and structure at driving magnetic fields far above walker Breakdown a second peak in domain wall velocity is observed, a phenomenon previously observed in wide wires, and wires under the influence of a transverse magnetic field.

Publications

R. Beardsley, **Parkes, D. E.**, J. Zemen, S. Bowe, K. W. Edmonds, C. Reardon, I. Isakov, P. A. Warburton, R. P. Campion, B. L. Gallagher, S. A. Cavill, and A. W. Rushforth. Effect of lithographically-induced strain relaxation on the magnetic domain configuration in microfabricated epitaxially grown $Fe_{81}Ga_{19}$. *Manuscript in preparation*, 2015.

S. A. Cavill, **Parkes, D. E.**, J. Miguel, S. S. Dhesi, K. W. Edmonds, R. P. Campion, and A. W. Rushforth. Electrical control of magnetic reversal processes in magnetostrictive structures. *Applied Physics Letters*, 102(3):032405, 2013.

D.E. Parkes and P. Wadley and M. Wang and A.T. Hindmarch and R.P. Campion and K.W. Edmonds and A.W. Rushforth and L.R. Shelford and Van Der Laan, G. and S.A. Cavill and V. Holý. Magnetostrictive thin films for microwave spintronics. *Scientific Reports*, 3, 2013. 87, 134

A. T. Hindmarch, **Parkes, D. E.**, and A. W. Rushforth. Fabrication of metallic magnetic nanostructures by argon ion milling using a reversed-polarity planar magnetron ion source. *Vacuum*, 86(10):1600 – 1604, 2012. 53

Parkes, D. E., R. Beardsley, S. Bowe, I. Isakov, P. A. Warburton, K. W. Edmonds, R. P. Campion, B. L. Gallagher, A. W. Rushforth, and S. A. Cavill. Voltage controlled modification of flux closure domains in planar magnetic structures for microwave applications. *Applied Physics Letters*, 105(6):062405, 2014. 133, 135

Parkes, D. E., S. A. Cavill, A. T. Hindmarch, P. Wadley, F. McGee, C. R. Staddon, K. W. Edmonds, R. P. Campion, B. L. Gallagher, and A. W. Rushforth. Non-volatile voltage control of magnetization and magnetic domain walls in magnetostrictive epitaxial thin films. *Applied Physics Letters*, 101(7):072402, 2012.

Contents

Chapter 1

Introduction and Background Theory

1.1 Introduction

Spintronics is a field of physics which seeks to investigate and exploit both the spin and charge of electrons. The beginnings of this field were set down as early as 1856 when William Thomson (later Lord Kelvin) observed [1] that the resistance of a ferromagnetic material was dependent on the direction of the magnetisation within the material with respect to the current direction, a phenomenon that came to be known as anisotropic magnetoresistance, or AMR. A schematic of AMR is shown in figure 1.1 (a). Sensor concepts using the effect were developed as early as 1971 [2], but it was not until 1990 that AMR sensors were used in the read heads of commerically available hard disk drives in the IBM 9345. Development of AMR-based read heads continued throughout the 1990s [3] although the relatively small magnetoresistance of a few per cent limited areal data densities to around 5 Gb/in^2 [4]. As demands on hard drive capacities increased, so too did the required sensitivity in read heads. It became apparent that simple AMR devices were no longer sufficient. AMR is discussed in greater detail in section 1.2.6.

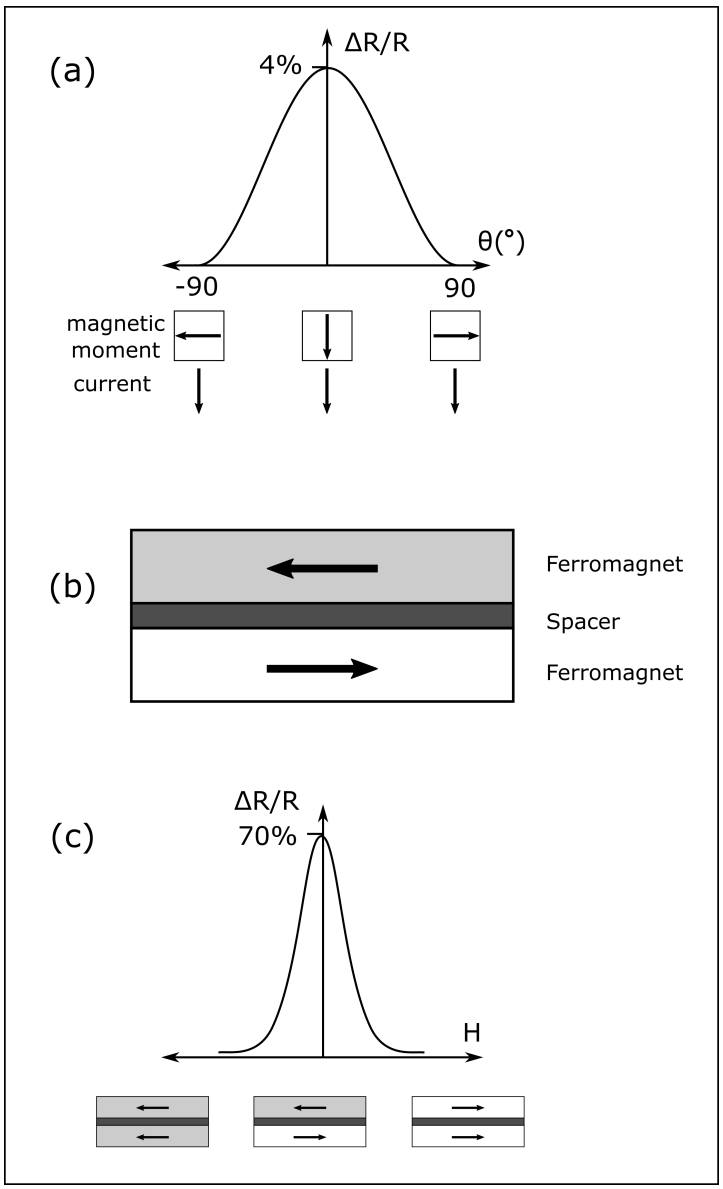

Figure 1.1: (a) Schematic representation of AMR. The maximum change in resistance typically is achieved when the magnetisation is rotated from parallel to perpendicular to the current direction and vice versa. (b) A GMR stack. A non-magnetic spacer layer separates two ferromagnetic layers. One of the ferromagnetic layers is often pinned to create a spin valve. (c) The greatest change in resistance in a GMR device is achieved when the magnetic moments in each ferromagnetic layer are oriented antiparallel to each other.

The solution to the problem of hard drive data densities came in the form of a new spintronic phenomenon: Giant Magnetoresistance (GMR). The initial discovery in Fe/Cr multilayers and [5] Fe/Cr/Fe sandwiches [6] showed a magnetoresistance of around 13 % at room temperature. This was soon greatly surpassed in Co/Cu layers with a GMR of 65 % [7]. GMR can be understood in terms of the Mott two current model of conductivity of ferromagnets [8]. Current in ferromagnets is carried independently by spin-up and spin-down electrons. These two current channels have different scattering rates as the d electrons provide a spin-dependent reservoir of states into which the current-carrying s-p electrons can be scattered. The difference in density of states at the Fermi energy of the spin-up and spin-down electrons results in the spin-dependent scattering rate. In a magnetic multilayer system, shown schematically in figure 1.1 (b), the resistance depends on the angle between the directions of the magnetic moments of each layer, and the system will typically have a lower resistance when the magnetic moments of each layer are parallel then when anti-parallel (figure 1.1 (c)). For hard-drive sensor applications the concept of the spin-valve was introduced [9] in which one of the layers is fixed or pinned, relative to the other, free, layer. This pinning is typically achieved by altering the coercivity of the pinned layer, or exhange coupling it to an antiferromagnet [10]. The first GMR-based hard drives were brought to market in 1997 (IBM DTTA-351680 HDD). GMR-based hard drives are now capable of reading disks with areal densities of around 100 Gb/in^2 [8].

The GMR sensor itself was also superceded by sensors based on tunnelling magnetoresistance (TMR). TMR was first observed at low temperature in 1975 [11] in ferromagnetic thin films separated by an insulating tunnel barrier. A schematic of a simple TMR structure is shown in figure 1.2 (a). Electrons may only tunnel through a barrier if there are sufficient unfilled states to which they may go. In a TMR device, if the magnetic moments of the ferromagnetic layers either side of the tunnel barrier are aligned parallel to each other, the majority (minority) spins in the first layer may tunnel into the unfilled states of the majority (minority) spins in the second layer. If the magnetic moments of the two ferromagnetic layers are however aligned anti-parallel the majority

(minority) spins in one layer may only tunnel into the minority (majority) spin states of the second layer. This shown schematically in figure 1.2 (b). The dependence of conductivity on the product of the density of states at the Fermi level of the two ferromagnetic layers then results in the TMR effect. In terms of spin polarisation $P = [D^{\uparrow}(E_F) - D^{\downarrow}(E_F)]/[D^{\uparrow}(E_F) + D^{\downarrow}(E_F)]$, where D is the density of states, the TMR ratio can be written as Julliere's formula:

$$R_{TMR} = \frac{2P_1P_2}{1 - P_1P_2} \tag{1.1}$$

where P_1 and P_2 are the spin polarisations for the first and second ferromagnetic layers respectively [11, 12]. Interest in TMR was re-ignited after the discovery of GMR and the realisation that the effect could be of technological and commercial interest. Initial room temperature observations of TMR in 1995 [13, 14] using an alumina tunnel barrier showed an effect only comparable to existing GMR-based devices. It was not until MgO-based tunnel barriers, which allowed coherent tunnelling, were developed that magnetoresistance ratios of 200 % were reported [15]. TMR has since been incorporated into spin-valve-type devices known as magnetic tunnel junctions (MTJs) [16]. Hard drives using TMR-MTJ technology have achieved areal densities of up to 300 Gb/in^2 in 2006 [17].

Despite the successes of hard drives, their limitations are becoming apparent in terms of access times, energy consumption, and mechanical reliability [18]. Spintronics may yet however have an important role to play in the future of computer memory and storage. One of the most promising spintronic contributions is magnetoresistive random access memory (MRAM)[19, 20, 21, 22, 23], which utilises the TMR-MTJ spin-valve technology originally developed for hard drives. Rather than having one read-head that searches a magnetic platter, MRAM has thousands or millions of spin-valves which can each be individually accessed and turned on, binary '1', or off, '0'. MRAM was first made commercially available in 2006 (Everspin MR2A16A) [24]. This first generation of MRAM used magnetic fields due to current carrying lines close to the MTJs to switch the magnetisation in the MTJ. A schematic of this

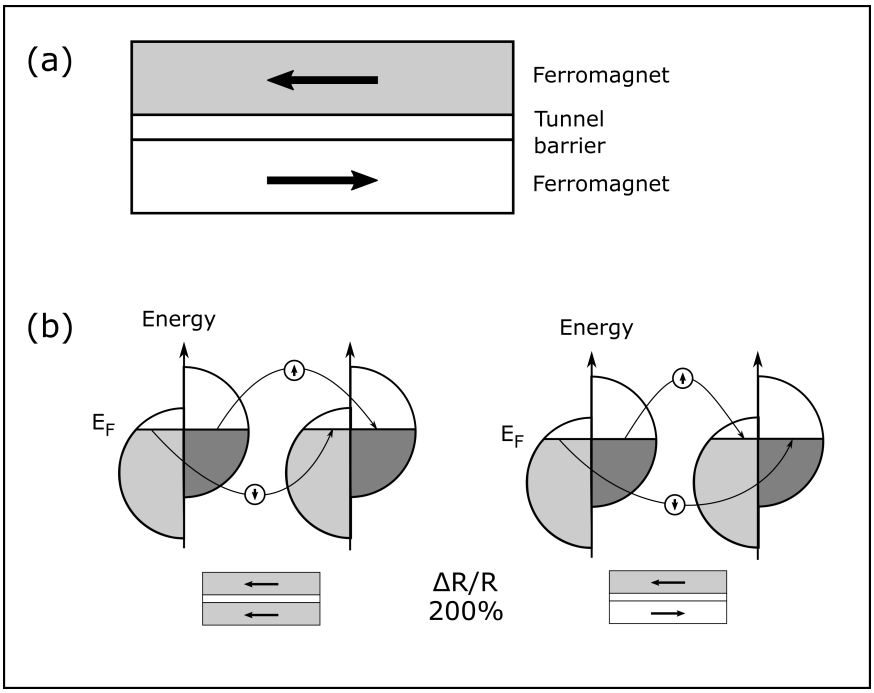

Figure 1.2: (a) Schematic representation of a simple TMR stack. Two ferromagnetic layers are separated by an ultrathin tunnel barrier. (b) A change in resistance of around 200 % may be achieved due the dependence of conductivity on the density of states of the two ferromagnetic layers. If the magnetic moments of the ferromagnetic layers either side of the tunnel barrier are aligned parallel to each other, the majority spins in the first layer may tunnel into the unfilled states of the majority spins in the second layer. If the magnetic moments of the two ferromagnetic layers are however aligned anti-parallel the majority spins in one layer may only tunnel into the minority spin states of the second layer.

arrangement is shown in figure 1.3 (a). In an array of such MTJ bits currents I_1 and I_2 are pulsed in such a way that only the target bit at the cross point of the two lines is switched. The resistance of the MTJ is read via a separate current path.

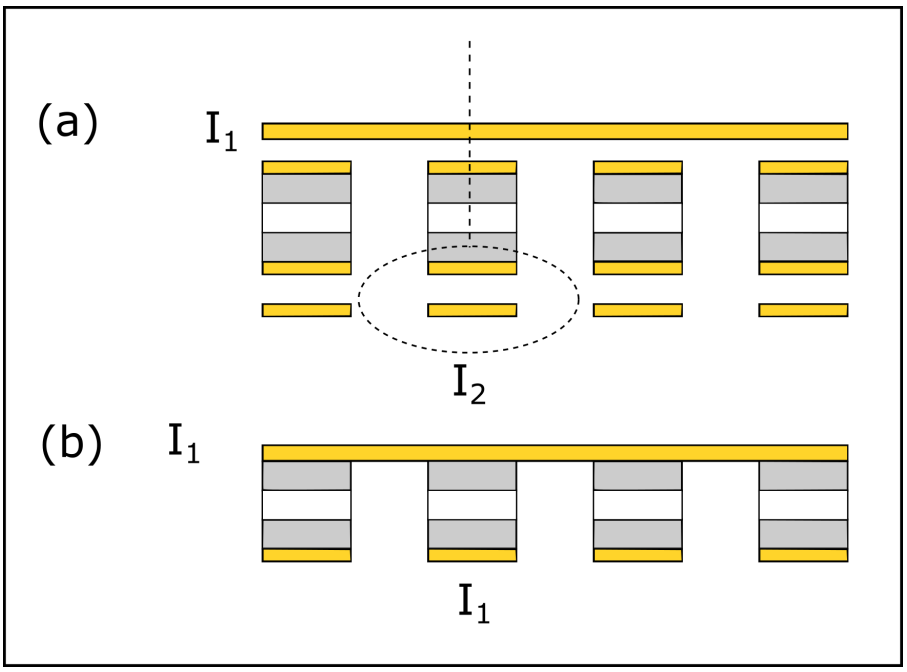

Figure 1.3: (a) Field-switching MRAM uses the stray fields due to two current carrying lines (I1 and I2). The dashed lines represent the stray field due to the current in the two lines. The bit at the cross-point of those two lines is switched. The bit is read by a separate current path. (b) STT-MRAM uses spin-transfer-torque to switch bits using current I1. A bit can be read using a lower current along the same current path.

Later implementations of MRAM have used the spin-torque effect to switch the magnetisation in MTJ bits. The spin-torque effect, or spin-transfer torque (STT) was initially predicted in 1996 [25] and later demonstrated experimentally in Co/Cu/Co multilayers and pillars[26, 27]. When a spin-polarised current passes through a ferromagnetic conductor there is a torque on the conductor due to the transfer of angular momentum from the polarised current. At sufficiently high current densities (typically around $1 \times 10^{10}\,\mathrm{A/m^2}$ [28]) the torque is able to flip the magnetic moment of an individual domain.

In the context of an MRAM MTJ [29], the current is passed through the fixed or pinned layer of the MTJ, and the resulting spin-polarised current is capabale of switching the magnetic moment of the free layer. Using the spin-torque effect to switch a magnetic bit has the immediate advantage of removing the need for an inherently de-localised magnetic field to write individual bits in the memory scheme. A schematic of a simple STT-MRAM scheme is shown in figure 1.3 (b). In this situation each bit is connected to a bit and a word line, which are capable or carrying a low current for read operations, and a high current for write operations.

The main appeal of MRAM technology over conventional RAM is that it is non-volatile, meaning that it does not require a constant supply of power to retain information. MRAM has the added appeal that as long as write voltage as are kept sufficiently low (roughly 400 mV [30]) to prevent dielectric breakdown of the MgO tunnel barrier, there is no apparent wear-out mechanism, leading to an unlimited read/write endurance. In addition to non-volatility the use of magnetisation rather than electrical charge to store data means that magnetic technologies such as MRAM have enhanced radiation hardness when compared to purely electrical system [31]. The key weakness in MRAM radiation hardness is the MgO tunnel barrier [20] which can be affected by charges induced by heavy-ion bombardment. A comparison of different magnetic and non-magnetic memory technologies is shown in table 1.1. Despite the apparent success of MRAM, a major challenge for the future may be the development of an MTJ memory cell that is compatible with the minimum sized transistors required for sufficiently high-density memory [32]. At smaller device sizes heat dissipation can also become more of a problem [33] as the high currents and small volumes involved, along with the fact that thermal conductivity and rate of radiation both scale with area, can increase temperatures to the point that reading and writing operations are disturbed.

One solution to the possible problems of the future of MRAM is the Racetrack memory concept proposed and developed by the team of Stuart Parkin at IBM [34, 35]. The simplest racetrack memory concept involves the STT-driven movement [36] of domain walls along nanowires of in-plane magnetised

material which can then be read using an MTJ sensor. A schematic of this simple racetrack arrangement is shown in figure 1.4 (a). Subsequent developments included the use of perpendicularly magnetised ultrathin layers of Co deposited on a Pt layer to enhance domain wall velocities [32] while the most recent iteration of the concept 'Racetrack Memory 4.0' also incorporates a synthetic antiferromagnet (SAF) in which two perpendicularly magnetised sub-racetracks are antiferromagnetically coupled via an ultrathin Ru layer [37]. This is shown schematically in figure 1.4 (b). The layers in this SAF can be tuned to reduce the net magnetic moment of the racetrack to almost zero, and produce domain wall velocities of close to 1000 m/s. That the domain walls in these SAF racetracks have no net magnetic field means that they can be packed more closely together than in a ferromagnetic racetrack. This combination of properties means that this Racetrack Memory 4.0 may offer a highly efficient, high-speed storage and memory solution. To achieve data density and cost comparable to magnetic disk drives a SAF racetrack must store approximately 100 domain walls. Storing multiple bits per cell in this way would also allow racetrack memory to reach a density around 100 times that of MRAM. A key promise of racetrack memory has been its suitability for 3D operation since a racetrack should in principle work whether it lies parallel or perpendicular to the plane. Although this may be achieveable by deposition of material on the side walls of deep trenches [32], this aspect of the racetrack concept has yet to be fully demonstrated.

The Racetrack memory concept encodes information as regions of magnetisation, separated by domain walls. It is however also possible to encode information in the domain walls themselves [38] such as the chirality of the vortex domain walls formed in wider and thicker wires [39, 40] which can be set by the wall nucleation method [41]. These two chiralities could represent the 0 and 1 in a binary system.

Throughout the development of magnetic memory and storage technologies, an electrical current has been used to manipulate the magnetisation. In hard drives[44] and early MRAM devices[45] control of magnetisation was achieved through the stray magnetic field due to a current carrying wire. Use of STT

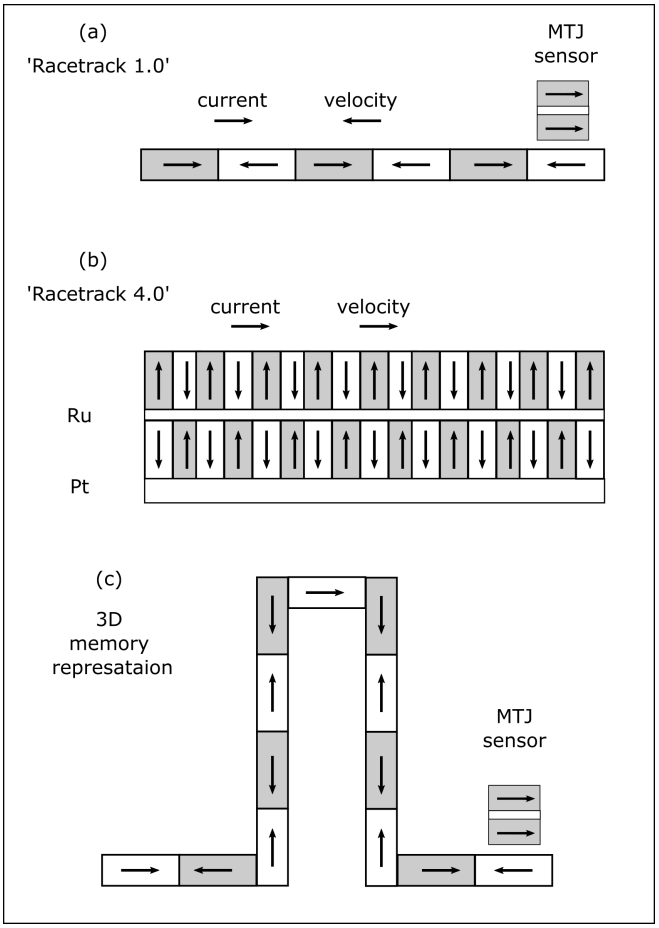

Figure 1.4: (a) Racetrack 1.0 used in-plane magnetised material combined with MTJ readout. (b) The most recent Racetrack 4.0 incorporating out-of-plane magnetisation, a Pt seed layer and Ru spacer layer to achieve higher densities and higher domain wall velocities. (c) Represenation of 3D Racetrack 1.0. One of the main appeals of racetrack memory is the possibility for 3D storage.

Table 1.1: Comparison of magnetic and non-magnetic memory technologies. STT-MRAM compares favourably with SRAM and DRAM. Data from [42], except racetrack from [43]

	SRAM	DRAM	Flash	STT - MRAM	Racetrack
Endurance	Unlimited	Unlimited	10^5	Unlimited	Unlimited
Read/write time (ns)	1	30	$100/10^6$	2-30	10
Density	Low	Medium	High	Medium	High
Write power	Medium	Medium	High	Medium	Medium
Standby power	High	Medium	Low	Low	Low

to control magnetisation has reduced the negative impact of stray fields as current-carrying lines can be magnetically shielded although the current densities required for STT switching of magnetisation are comparable to those which result in significant heating of the MTJ [46]. This heating can cause problems due to erroneous switching of magnetisation, particularly as device sizes are reduced to achieve higher areal densities[47]. The current-heating also represents wasted energy, which must be reduced to achieve higher efficiency memory systems. To minimise these current-heating effects, electric fields rather than electric currents are being targeted as possible technological solutions. Electric field-based magnetisation control solutions may reduce the energy dissipation in a device by a factor of 100 over that of STT-based devices [48].

Other possible variants of MRAM that build on STT-MRAM exist. One example is a STT-based, 3-terminal device [49, 50] which uses an additional terminal to reduce the voltage that needs to be applied across the dielectric in the MTJ. 3-terminal devices have also been proposed that incorporate the motion of a domain wall as the switching mechanism [51] (see figure 1.5). Novel MRAM schemes have also been proposed which use the spin-Hall effect [52], or spin-orbit torques [53] as the magnetisation switching mechanism [54], although current densities required in these schemes are relatively high, being

around 5×10^{11} A m^2[53].

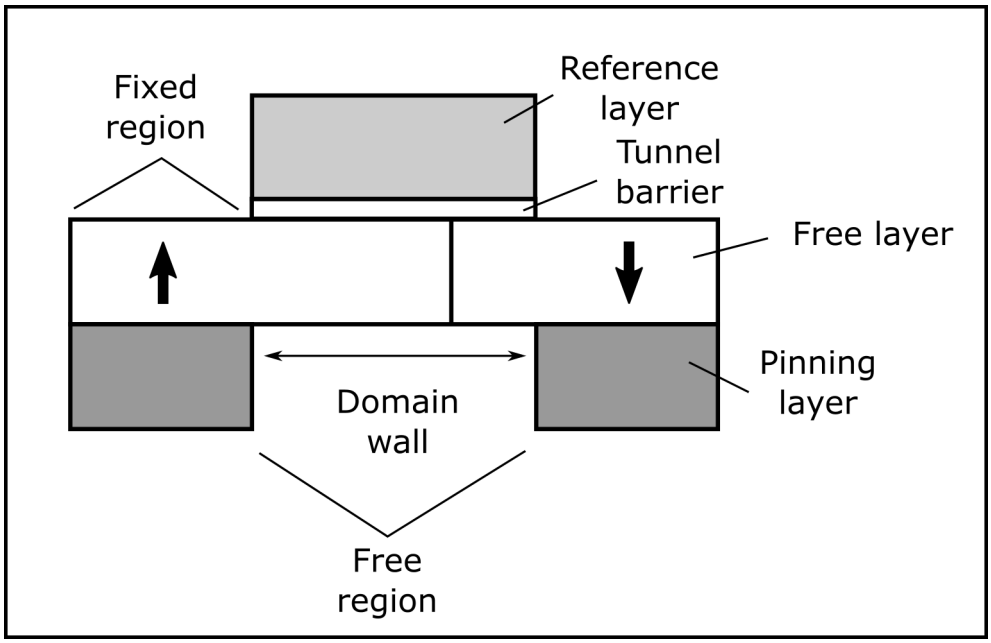

Figure 1.5: 3-terminal domain wall MRAM. Two ends of the free layer are fixed by a pinning layer, and a domain wall is moved within the free region between the two fixed regions. The free region forms a moveable free layer in an MTJ stack.

1.1.1 Electric Field Control of Magnetisation

Means of electric field control of magnetisation fall into two broad areas: direct and indirect [48]. Direct methods of magnetisation control include the modulation of carrier concentrations in magnetic semiconductors, the use of interface effects in ultrathin metallic films, and magnetoelectric coupling in multiferroic materials. Indirect methods of magnetisation control typically involve using magnetoelastic coupling to control magnetic properties through the application of an electric field to a piezoelectric actuator.

In ferromagnetic metals electrical field control of magnetisation in bulk materials is prevented by electric field screening by the high carrier concentration in these metals. The carrier concentration in semiconductors is typically several

orders of magnitude lower than that found in metals, which allows for electric field control of those carriers. In some semiconductors the charge carriers also determine the magnetic properties of the material which allowed the demonstration in 2000 of the manipulation of the magnetic phase transition in a thin film of the ferromagnetic semiconductor (In,Mn)As [55]. Similar electrical control of the Curie temperature and saturation moment was later demonstrated in (Ga,Mn)As [56]. Investigations into ferromagnetic semiconductors have since expanded beyond III-V semiconductors to include group II-VI [57] and group IV [58] materials. An important functionality was demonstrated in the electric-field-modulation of magnetic anisotropy to achieve magnetisation manipulation [59] and field-assisted switching of magnetisation [60]. A key limitation in ferromagnetic semiconductor development has been the Curie temperature, the highest of which is only around 170 K [61].

The progress made in electrical gating of ferromagnetic semiconductors encouraged studies of electrical control of metals which tend not to be limited by low Curie temperatures. As has been noted, screening in bulk ferromagnetic metals inhibits electric field control of magnetic properties. In thin films of FePt and FePd, however, it was demonstrated in 2007 that electric fields could modulate coercivity at room temperature [62]. Following this result studies of spin-dependent screening in metallic ferromagnets led to further demonstrations of electric field-induced control of magnetic anisotropy, which was attributed to the modulation of interface magnetic anisotropy[63, 64]. A significant demonstration using $BiFeO_3$ was the electric-field-induced magnetisation reversal in a ferromaget-multiferroic heterostructure in which the $BiFeO_3$ was coupled to the ferromagnetic metal Co_9Fe_1 [65, 66]. Modulation of interface charge carrrier density has also been shown to modify the surface magnetic anisotropy of ferromagnetic metals via spin orbit coupling due to the change in relative electron occupancy of the 3d orbitals [67]. This effect has been demonstrated recently in a number of systems[68] including Fe [63], Ni [69], and $Fe_{40}Co_{40}B_{20}/MgO/Fe_{40}Co_{40}B_{20}$ tunnel junctions [70, 71].

A voltage across a multiferroic in a ferromagnetic/multiferroic heterostructure may cause an alteration in the exchange interaction between the two

components of the structure. In this case the exchange coupling between the spins of the ferromagnet and the uncompensated spins of an antiferromagnetic multiferroic gives rise to an exchange bias, characteristic of such a ferromagnetic/antiferromagnetic interface. An electric field can then be used to control the antiferromagnetic spin orientation. Control of the exchange bias in this way has been demonstrated in multiferroic heterostructures using $BiFeO_3$[72], $YMnO_3$ [73] and $LaMnO_3$ [74]. Room temperature control has been achieved in multiferroic heterostructures incorporating the magnetoelectric ferromagnet Cr_2O_3. That room temperature effects have been observed suggests that there may a possibility for functional devices based on these effects in the future.

Electric-field-control using interface anisotropy has also been demonstrated in MTJs through the use of an electric field pulse to temporarily re-align the magnetic easy axis, causing precession of the magnetisation in the free layer of the MTJ. The use of this mechanism in field and STT induced switching MTJs increases the switching probability in those devices. Electric fields have also been used to show control of domain walls in perpendicularly magnetised ultrathin Co and CoB wires under an external magnetic field [75, 76]. The order of magnitude alteration of domain wall velocities observed in these systems is probably due to modification of the magnetic anisotropy by the electric field. Local electrical gating of ferromagnetic GdOx wires has also been used to demonstrate voltage control of domain wall pinning sites [77].

The third strand of direct electric field control of magnetisation is in the use of multiferroic materials in which two or more ferroic orders coexist, for example ferroelectricity and ferromagnetism[78, 79, 80]. Magnetoelectric coupling between the electric polarisation, P, and magnetisation, M, in such a material allows the control of M by applying electric field, E, and controlling P by applying magnetic field, H. One important multiferroic material is $BiFeO_3$ which, at room temperature, has a large spontaneous polarisation ($\approx 60\,\mu C/cm^2$) [81] and in thin films a weak ferromagnetic component of around $0.1\mu_B$ per Fe atom[82]. A comprehensive review of $BiFeO_3$ is given in [83]. Another important multiferroic material is$YMnO_3$, which grows epitaxially on several

subtrates including Pt(111) [84, 85], GaN[86], and ZnO[87]. The naturally occuring multiferroic FeO_4 is both ferrimagnetic and ferroelectric [88, 89, 90], and as a ferrite, could be of technological interest in microwave applications. Outside of $BiFeO_3$ however the typically low critical temperatures of multiferroics combined with the complexity of their crystal structures makes the adoption of intrinsic multiferroics in practical applications a difficult prospect [68].

1.1.2 Strain-Control of Magnetisation

It is also possible to indirectly achieve electric field control of magnetisation by utilising the piezoelectric properties of ferroelectrics, an approach which offers dramatic improvements in efficiency over competing current- or field-driven magnetic techniques, with no loss of performance [91]. The strain manipulation of magnetic properties is the main topic of my thesis. The strain experienced by the ferromagnetic layer in a multiferroic heterostructure will alter its magnetic properties through magnetoelastic coupling [80, 92, 93, 94]. Several approaches to coupling ferromagnetic and piezoelectric materials including sintering of particulate composites[80, 92, 95] and the use of lithographicaly defined magnetic material on ferroelectric substrates. A schematic of a ferromagnet/piezoelectric heterostructure is shown in figure 1.6.

In this way Weiler et al. [96] showed reversible 70° adjustment of the magnetisation direction in a polycrystalline Ni thin film. More recently Hockel et al. [97] demonstrated the strain-induced rotation of magnetisation involving the motion of individual domain walls in a patterned Ni ring deposited directly onto the metal contact of a piezoelectric substrate. Progess has also been made in the growth of epitaxial films deposited directly onto ferroelectric substrates including CoPd/PZT [98, 99], $Fe_3O_4/BaTiO_3(100)$ [100], $Fe_{50}Co_{50}/BaTiO_3$, $Ni/BaTiO_3$ [101, 102], $Co_{60}Fe_{20}B_{20}$/PMN-PT [103], and Fe_3O_4/PMN-PT [104]. It is not possible to epitaxially grow all materials directly on ferroelectric substrates. Rushforth et al. [105] demonstrated in 2008 the ability to control magnetocrystalline anisotropy in the ferromagnetic

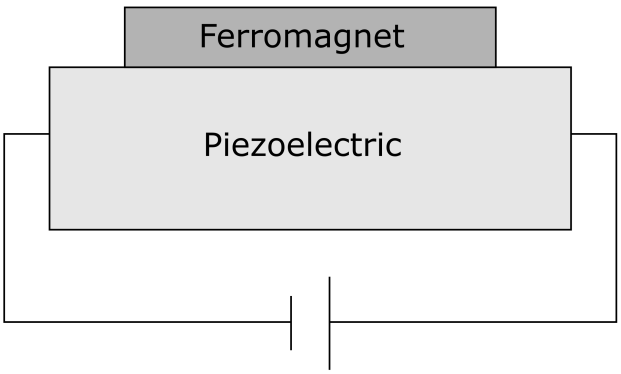

Figure 1.6: Ferromagnetic/piezoelectric heterostructure consisting of a ferromagnet deposited or bonded to a piezoelectric material. A voltage across the piezoelectric component induces a strain in the piezoelectric which in turn induces a change in the magnetic properties of the ferromagnet.

semiconductor GaMnAs where a GaAs substrate was bonded to a piezoelectric transducer. The same technique was used by Overby et al. [106] to demonstrate the principle of a memory device. These GaMnAs-based devices required that the ferromagnetic layer be grown on a separate GaAs substrate, and later bonded to a piezoelectric transducer.

In ferromagnetic devices with sufficiently small dimensions flux-closing Landau patterns and vortex domain configurations may form. These domain patterns have been shown to be a possible option for a 4-state memory device [107] and similar systems are also of interest for their possible use in resonators [108] and spin-torque vortex oscillators (STVOs) [108, 109]. In smaller structures the influence of other anisotropy sources may also become important when the material has a large magnetostriction. If there is a mismatch between the lattice constant of an epitaxially grown layer and the substrate, a strain can be built into the layer. When the layer is etched during fabrication, this strain is released at the edges of the structure. The effect of this strain-relaxation on magnetic anisotropy was studied extensively in the dilute magnetic semiconductor GaMnAs [110, 111, 112, 113] where the dilute magnetic moment allowed for the data to be understood in terms of a single

domain model.

To incorporate strain control into domain-wall-based memory concepts it is essential that there is a good understanding of how strain-induced anisotropy will affect the behaviour of domain walls. Two key areas of interest are the velocity of domain walls as they travel through wires, and the behaviour of domain walls pinned at notches or imperfections along the length of the wire. Notches may be present due to imperfections in fabrication, or introduced as part of a domain wall computing scheme [38] or to help facilitate the formation of only one chirality [114]. Since these notches may be considered a hindrance to the motion of domain walls along wires, or as features to help control the flow and structure of domain walls, it is important that the behaviour of these domain walls is understood. The depinning behaviour of a domain wall at a notch is highly dependent on the geometry of both the domain wall and the notch [115, 116]. Domain walls and domain wall behaviour, including pinning are discussed in greater detail in section 1.2.5. One important recent development is the memory device concept of Lei et al. [117] in which both piezoelectric and ferromagnetic layers were deposited onto a $SrTiO_3$ substrate to show a doubling of domain wall propagation fields under locally applied strain. The effect of strain-induced uniaxial anisotropy on domain walls in metallic nanowires has been studied in detail, including the deformation of the walls under strain [118], and the effect on domain wall mobility [119]. There have also been some early studies of the possibility of strain-induced motion of magnetic domain walls [120] which would not require any electric currents at all.

A hybrid multiferroic device requires two key elements: a piezo-electric material in which a strain is induced on the application of an electric field, and a magnetic material with sufficiently strong magnetostrictive behaviour to respond appropriately to the induced strain. Materials with a large magnetostriction coefficient typically contain rare earth metals, an example being Terfenol-D [121], which contains Dy, and is used in actuators, motor drives, transducers and sensors. This reliance on rare-earth elements is particularly problematic due to the large economic, social, and environmental costs asso-

ciated with the extraction and processing of the material [122]. One promising material which does not contain any rare-earth elements is 'Galfenol', $Fe_{81}Ga_{19}$, which has been shown to have the highest magnetostriction coefficient of any material not containing rare earths, over an order of magnitude larger than that for pure iron [123]. Previous studies on the magnetostrictive properties Galfenol have tended to focus on quench-cooled bulk crystals [123, 124], from which there has been success in terms of optimising the stoichiometry, and exploring the origin of the enhanced magnetostriction. For the material to be of use for future memory technologies, the same functionality must be demonstrated in thin films, as well as the bulk. $Fe_{(1-x)}Ga_x$ thin films have previously been grown by MBE, [125, 126] but clamping of the film to the substrate has prevented a study of the magnetostrictive properties. Futher information on Galfenol and other magnetostrictive materials is provided in section 1.3.

The motivation of this thesis is to continue this work into the strain-induced control of magnetisation in hybrid piezoelectric/ferromagnetic systems. The thesis presents investigations into the magnetic properties of $Fe_{81}Ga_{19}$, a possible new material for use in the ferromagnetic component of the devices, and examine how strain-induced uniaxial anisotropy affects the the behaviour of magnetisation and magnetic domain walls in devices with lateral length scales ranging from 45 µm to less than 100 nm. This thesis is laid out as follows: This chapter goes on to describe the theoretical ideas and background to the concepts covered in the thesis including magnetic anisotropies, magnetostrictive materials and micromagnetism. Chapter 2 describes the measurement systems and simulation techniques used to obtain the results in this thesis. Chapter 3 presents work investigating the magnetic, electrical and structural properties of epitaxial $Fe_{81}Ga_{19}$ thin films. A 45 µm device is used to investigate the highly magnetostrictive properties of our $Fe_{81}Ga_{19}$ film. The ability to reversibly switch the magnetisation direction between the two bi-axial easy axes in our layer is demonstrated, along with observation of the magnetic domain configuration involved in the reversal. In Chapter 4 the investigation is extended into microfabricated $Fe_{81}Ga_{19}$ devices in which a more regular

domain pattern is observed. The reversal mechanisms in 15 µm devices are explored and the control of flux-closing magnetic domain states using voltage induced strain is demonstrated. Length scales are reduced another order of magnitude in Chapter 5 which presents the results of a study of domain wall velocities and depinning fields in wires 1 µm wide and narrower. Concluding remarks and suggested areas for further investigation are in Chapter 6.

1.2 Magnetic Phenomena

1.2.1 Spin-orbit coupling

Spin orbit coupling (SOC) is the relativistic effect which couples the spin and orbital angular momenta of an electron. Spin orbit coupling is responsible for many magnetic and magneto-transport phenomena including [127] magnetocrystalline anisotropy and anisotropic magnetoresistance which are described in the following sections. The effect comes about as in the rest frame of a moving electron, the electron is influenced by the effective magnetic field resulting from the movement of the positively charged nucleus. This effective magnetic field due to the nucleus interacts with the spin of the electron, hence coupling the spin and orbital angular momenta. For an effective magnetic field experienced by the electron $\mathbf{B_{eff}} = \frac{1}{2m_e c^2}(\mathbf{p} \times \nabla V)$ the spin orbit coupling modifies the energy of the electron according to the Hamiltonian [128]:

$$\begin{aligned} H_{SO} &= \frac{e\hbar}{2m_e c^2}\mathbf{S} \cdot (\mathbf{p} \times \nabla V) \\ &= -\frac{e\hbar^2}{2m_e^2 c^2}\frac{1}{r}\frac{dV(r)}{dr}\mathbf{S} \cdot \mathbf{L} \\ &= \zeta(r)\mathbf{S} \cdot \mathbf{L} \end{aligned} \tag{1.2}$$

where $\mathbf{S}$ is the spin angular momentum of the electron, $\mathbf{L}$ the orbital angular momentum, m_e is the electron mass V is the electric potential at the position

of the electron and **p** is the electron's momentum. The expectation value of $\zeta(r)$, $\langle\zeta(r)\rangle$ gives the spin-orbit coupling constant, ζ. Coupling constant values for a selection of materials are shown in table 1.2.

Table 1.2: Spin-orbit coupling strengths (ζ) of a number of magnetic, and non-magnetic materials. Materials of particular relevance to this thesis are highlighted in bold. Values taken from [129]

Element	Symbol	Atomic Number	Atomic Mass (u)	ζ(1/cm)
Aluminium	Al	13	26.981538	62
Cobalt	**Co**	**27**	**58.9332**	**550**
Copper	Cu	29	63.546	857
Dysprosium	Dy	66	162.5	2074
Gallium	**Ga**	**31**	**69.723**	**464**
Gold	Au	79	196.96655	5104
Hydrogen	H	1	1.00794	0.24
Iron	**Fe**	**26**	**55.845**	**431**
Nickel	Ni	28	58.6934	691
Platinum	Pt	78	195.078	4481
Ruthenium	Ru	44	101.07	1042

1.2.2 Exchange Energy

In a ferromagnetic the exchange interaction favours parallel alignment of the magnetic moments. From the Heisenberg Hamiltonian[130] it is known that the exchange energy between two neighbouring spins $\mathbf{S}_1$ and $\mathbf{S}_2$, separated by angle ϕ, is

$$E_{exch} = -J\mathbf{S}_1 \cdot \mathbf{S}_2 = -2JS^2 \cos\phi \tag{1.3}$$

where J is the exchange integral. In a ferromagnet the exchange energy is minimised when the spins are aligned parallel to each other.

The exchange energy is very large over short distances, so the angle between the two spins is small. In this case the equation can be approximated as:

$$E_{exch} = JS^2\phi^2 + \text{const}$$

The exchange constant, A, can also be used to characterise the strength of this exchange coupling:

$$A = \frac{n}{a} JS^2 \tag{1.4}$$

where n is the number of atoms per unit cell ($n = 1$ for a simple cubic lattice) and a is the lattice parameter.

1.2.3 Magnetic Anisotropy

Magnetic anisotropy refers to the preference for the magnetisation of a sample to lie along a particular direction[131] and is defined as the energy required to rotate the magnetisation from an easy to a hard direction [128]. In the absence of an applied magnetic field, the magnetisation prefers to lie along one of the easy axes defined by the anisotropy of the system. Possible origins of anisotropy in a material include the crystal symmetry, sample shape, and stress. The strength of an anisotropy is typically characterised by anisotropy coefficients, K, an energy density with units J/m^3. Anisotropy can also be represented as an effective field, H_K, called the anisotropy field. If $\mathbf{M}$ deviates from an easy axis, this anisotropy field induces a precession about the easy axis that tends to force the magnetisation back along the easy axis. The value of the anisotropy field along a particular direction can be read from a hysteresis loop as the magnetic field required to just saturate a magnetic sample along that direction. A schematic of the anisotropy field in a hysteresis loop is shown in figure 1.7 for field along a uniaxial hard axis. This use of anisotropy fields to determine magnetic anisotropy is discussed in greater detail in chapter 2.

1.2.3.1 Magnetocrystalline Anisotropy

The origin of magnetocrystalline anisotropy is the spin-orbit interaction, which results in certain orientations of molecular orbitals or bonding charge distributions being more energetically favourable than others[131]. The magnetic elements Fe, Ni and Co each have different magnetocrystalline anisotropies. bcc Fe has cubic anisotropy in which the $\langle 100 \rangle$ directions are easy axes, with

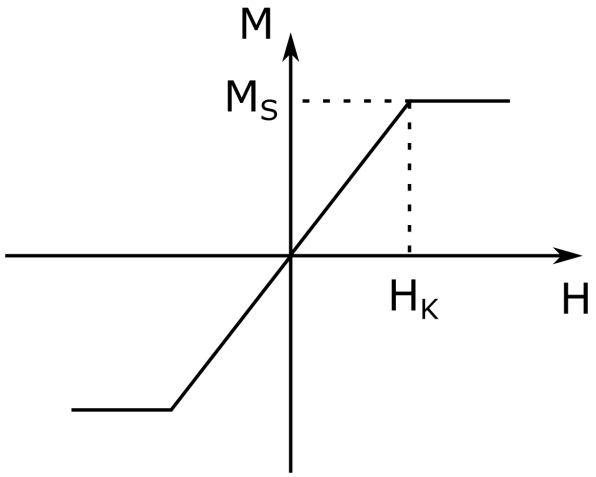

Figure 1.7: Hard axis hysteresis loop showing saturation magnetisation, M_S and anisotropy field H_K. The value of the anisotropy field along a particular direction can be read from a hysteresis loop as the magnetic field required to just saturate a magnetic sample along that direction.

$\langle 111 \rangle$ being magnetically hard. In fcc Ni there is also cubic anisotropy, but $\langle 111 \rangle$ directions are easy directions, whereas $\langle 100 \rangle$ are hard axes. hcp Co has uniaxial anisotropy with the [0001] c axis being much easier than the $\langle 1000 \rangle$ basal plane. The structures and anisotropy directions of these elements are shown schematically in figure 1.8.

To first order, the uniaxial anisotropy energy density can be expressed as

$$E_U = K_U \sin^2(\theta) \tag{1.5}$$

where K_U is the uniaxial anisotropy coefficient and θ is the angle between the magnetisation and easy axis. hcp Co has a uniaxial $K_1 = 7.0 \times 10^5\,\mathrm{J/m^3}$ at room temperature [131].

An expression for the cubic anisotropy energy density can be arrived at by an expansion of the free energy in terms of direction cosines of magnetisation

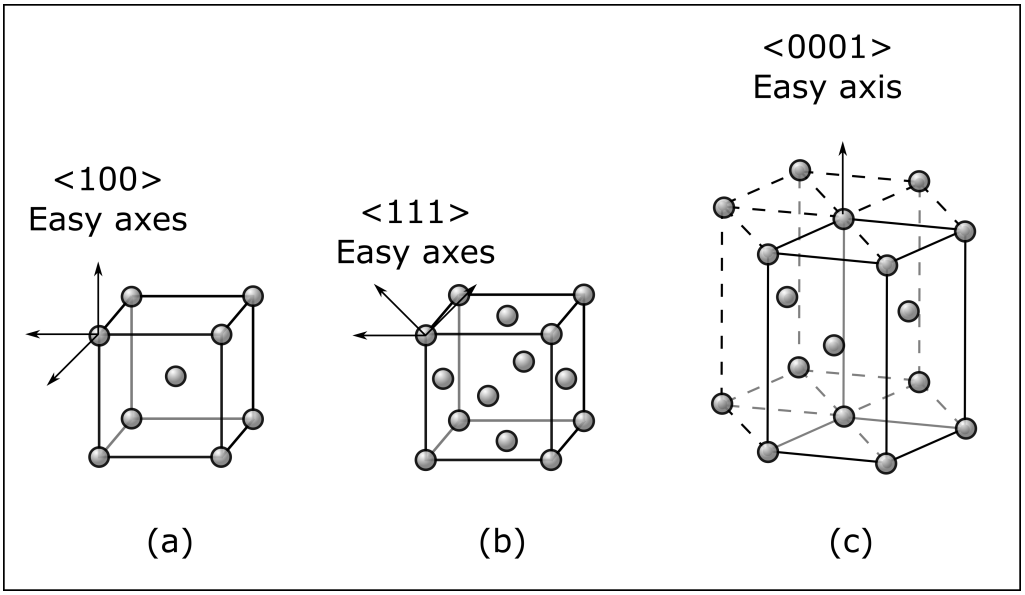

Figure 1.8: Crystal structure and magnetic easy axis directions for (a) bcc iron, (b) fcc Ni, (c) hcp Co.

with respect to the principal crystal axes, α [131]:

$$E_C = K_0 + K_1(\alpha_1^2\alpha_2^2 + \alpha_2^2\alpha_3^2 + \alpha_3^2\alpha_1^2) + K_2(\alpha_1^2\alpha_2^2\alpha_3^2) \tag{1.6}$$

In spherical coordinates ($\theta,\ \phi$) the coefficient of K_1 can then be written:

$$\sin^4\theta\cos^2\phi\sin^2\phi + \cos^2\theta\sin^2\theta = \frac{\sin^4\theta\sin^2 2\phi + \sin^2 2\theta}{4} \tag{1.7}$$

Typical room temperature values of K_1 for cubic Ni and Fe are $5.2 \times 10^4\,\mathrm{J/m^3}$ and $-12 \times 10^4\,\mathrm{J/m^3}$ respectively [131].

The samples in this thesis with magnetocrystalline anisotropy have both cubic and uniaxial anisotropy, with the magnetisation confined to the plane of the film, in which case we can write the magnetocrystalline anisotropy energy density for an in-plane magnetic material as (to first order):

$$E_{anis} = -\frac{K_C}{4}\sin^2(2\theta) + K_U\sin^2(\theta) \tag{1.8}$$

where K_C and K_U are the lowest order biaxial (cubic) and uniaxial anisotropy constants (see [132]) and θ is the angle between the magnetisation and a crystal axis.

Magnetoelastic Anisotropy

If the crystal lattice of a magnetic material is distorted, its magnetic properties may also be altered due to the spin-orbit coupling. This is called magneto-elastic anisotropy. Magnetoelastic anisotropy is related to the phenomenon of magnetostriction, by which the dimensions of a magnetic specimen will change when it is exposed to a magnetic field [127]. The magnetostriction, λ, is simply the fractional change in length (strain) experienced by the magnetic specimen as it is subjected to the magnetic field. The magnetostriction under a saturating magnetic field is denoted λ_S. In crystalline materials the magnetostriction depends on the direction of the applied field relative to the crystal axes. In cubic materials the relevant coefficients are λ_{100} and λ_{111} which correspond to magnetostriction along the $\langle 100 \rangle$ and $\langle 111 \rangle$ crystallographic directions respectively. For example [131] iron has $\lambda_{100} = 20.5 \times 10^{-6}$ and $\lambda_{111} = -21.5 \times 10^{-6}$, while nickel has $\lambda_{100} = -40.6 \times 10^{-6}$ and $\lambda_{111} = -25 \times 10^{-6}$. The sign of these values denotes the fact that magnetising iron along $\langle 100 \rangle$ will cause an expansion along that direction and a contraction along $\langle 111 \rangle$, whereas nickel will contract along the direction of magnetisation for any crystal orientation. In addtion to λ_s, which refers to the strains produced at magnetic saturation, magnetostrictive effects can also be described in terms of the magnetoelastic coupling constant, B, corresponding to the magnetic stress that causes λ_s.

The magnetoelastic effect, sometimes referred to as the inverse magnetostriction effect, or the Villari effect [131], is also important as it allows the manipulation of magnetic properties using strain. If λ_s is positive it is easier to magnetise a sample along the tensile stress direction, and harder along the compressive stress direction. The reverse is true for λ_s negative. The inverse magnetostriction effect is shown schematically in figure 1.9.

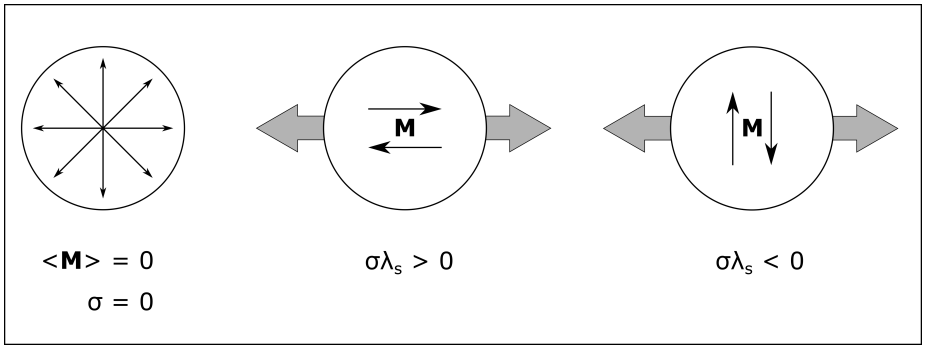

Figure 1.9: Inverse magnetostriction, magnetoelastic, or Villari, effect. Tensile stress (σ) acting on a material with positive λ_s favours magnetisation to lie along that direction. The reverse is true for materials with negative λ_s.

The method used to induce a strain in a magnetic layer bonded to a piezoelectric transducer is given in chapter 2. The magneto-elastic contribution to the magnetic free energy density in this siutation is given by [133]

$$E_{ME} = B_1[\varepsilon_{xx}(\alpha_1^2 - \frac{1}{3}) + \varepsilon_{yy}(\alpha_2^2 - \frac{1}{3}) + \varepsilon_{zz}(\alpha_3^2 - \frac{1}{3})] + B_2[\varepsilon_{xy}\alpha_1\alpha_2 + \varepsilon_{yz}\alpha_2\alpha_3 + \varepsilon_{xz}\alpha_1\alpha_3] \tag{1.9}$$

where B_1 and B_2 are magnetoelastic constants, α_1, α_2 and α_3 represent the direction cosines of the magnetisation along the x, y and z directions respectively, and ε_{xx}, ε_{yy}, etc. are the components of the strain tensor. Assuming only magnetisation in the plane of the film ($\alpha_3 = 0$), and the strain terms ε_{xy}, ε_{yz} and ε_{xz} are negligible compared to ε_{xx}, ε_{yy}, ε_{zz} assuming no shear strain:

$$E_{ME} = B_1[\varepsilon_{xx}(\alpha_1^2 - \frac{1}{3}) + \varepsilon_{yy}(\alpha_2^2 - \frac{1}{3})] \tag{1.10}$$

The assumption of no shear strain is reasonable as in this thesis the ferromagnetic crystal is elongated along a cubic axis. The known Poisson ratio of the piezoelectric transducer ν_{piezo} is used, using the assumption that the strain is transmitted to the ferromagnetic layer in such a way that the in-plane deformation of the sample coincides with that of the piezoelectric transducer. This is a reasonable assumption in this thesis as the ferromagnetic samples

used are orders of magnitude thinner than the piezoelectric transducers (see chapter 2). The relation between ε_{xx} and ε_{yy} is given by the Poisson ratio, $\varepsilon_{xx} = -\nu_{\text{piezo}}\varepsilon_{yy}$. In this thesis ν_{piezo} is taken to be 0.5 [134]. To determine the change in volume associated with the strain it is necessary to also find the fractional change in thickness ε_{zz} for which the formulation described by Brandlmaier et al.[135] and Sander[136] is used. The elastic energy of a cubic crystal with elastic moduli c_{ij} is given by:

$$E_{el} = \frac{1}{2}c_{11}(\varepsilon_{xx}^2 + \varepsilon_{yy}^2 + \varepsilon_{zz}^2) + c_{12}(\varepsilon_{xx}\varepsilon_{yy} + \varepsilon_{yy}\varepsilon_{zz} + \varepsilon_{xx}\varepsilon_{zz}) \tag{1.11}$$

again, assuming no shear strain. Since no stress is applied perpendicular to the film plane $\dfrac{\partial E_{el}}{\partial \varepsilon_{zz}} = 0$. So equation (1.11) gives

$$\varepsilon_{zz} = -\frac{c_{12}}{c_{11}}(\varepsilon_{xx} + \varepsilon_{yy}) \tag{1.12}$$

Taking $v_{piezo} = 0.5$ it follows that for the out-of-plane deformation of the sample

$$\varepsilon_{zz} = -0.5\frac{c_{12}}{c_{11}}\varepsilon_{xx} = -0.5\frac{\nu_{\text{film}}}{1-\nu_{\text{film}}}\varepsilon_{xx} \tag{1.13}$$

so, with $\nu_{\text{film}} = 0.5$, $\varepsilon_{zz} = -0.5\varepsilon_{xx}$. The elastic constants for bulk $Fe_{81}Ga_{19}$ were found by Clark et al. [123] to be $c_{11} = 195\,\text{GPa}$ and $c_{12} = 155\,\text{GPa}$, which corresponds to $\nu_{\text{film}} = 0.44$. Since the exact value of ν_{film} for the layers used in this thesis is not known, using 0.5 is a reasonable approximation.

The magnetoelastic constant B_1 is given by [133].

$$B_1 = \frac{3}{2}\lambda_{100}(c_{12} - c_{11}) \tag{1.14}$$

where λ_{100} is the relevant magnetostriction constant and c_{12} and c_{11} are the elastic constants.

Therefore, the change in magneto-elastic energy for a rotation of the magnetisation by an angle ψ from the [010] direction (with [010] defined as the x

axis) is:

$$\Delta E_{ME} = \frac{3}{2}\lambda_{100}(c_{12} - c_{11})(\varepsilon_{xx} - \varepsilon_{yy})\cos^2\psi \tag{1.15}$$

Shape Anisotropy

In addition to the anisotropies originating from spin-orbit-coupling previously described, there can also be a significant anisotropy which depends on the shape of the magnetic sample, and originates from the magnetostatic interaction of the magnetisation with the magnetic field it itself induces. Magnetostatic energy is also key to the formation of domains and domain walls, which are discussed in greater detail in section 1.2.5.

Starting from the basic relationship $\mathbf{B} = \mu_0(\mathbf{H} + \mathbf{M})$, taking the divergence, and rearranging, the divergence of magnetisation, $\mathbf{M}$ is found to be:

$$\nabla \cdot \mathbf{M} = \frac{\nabla \cdot \mathbf{B}}{\mu_0} - \nabla \cdot \mathbf{H} \tag{1.16}$$

From Maxwell's equations it is known that $\nabla \cdot \mathbf{B} = 0$ which gives

$$\nabla \cdot \mathbf{H} = -\nabla \cdot \mathbf{M} \tag{1.17}$$

The physical meaning of equation 1.17 is that for any divergence in $\mathbf{M}$ there is a corresponding field $\mathbf{H}$ which acts to maintain the condition that there is no divergence in $\mathbf{B}$. The field acts in opposition to the magnetisation of the ferromagnet, so is often referred to as the demagnetising field. The demagnetising or shape anisotropy energy density can then be written in terms of the magnetisation of the sample $\mathbf{M}$ and the demagnetising field $\mathbf{H_{demag}}$:

$$E_{\text{demag}} = -\frac{1}{2}\mu_0 \int_{sample} \mathbf{H_{demag}} \cdot \mathbf{M} dV \tag{1.18}$$

where the factor of a half avoids double counting of magnetic moments within the sample.

The shape anisotropy energy density can also be written in terms of a de-

magnetising factor, N. This factor takes into account the effect of the shape of a magnetic specimen through the magnetic charges resulting from the termination of lines of $\mathbf{M}$ at the specimen surface [137]. Demagnetising factors have been derived analytically for rectangular prisms of arbitrary dimensions [138], and ellipsoids [139]. For an ellipsoidal ferromagnet $E_{demag} = 2\pi N M_s^2$. Each orthogonal direction may have a different demagnetising factor, which must obey $N_x^2 + N_y^2 + N_z^2 = 1$, so as not to go beyond the total possible energy. In 1 dimension the demagnetising factor tends to $N = 1$, as the other dimensions approach zero. In thin films, the shape anisotropy is typically only important in the out of plane direction for which $N_z \approx 1$, with $N_x \approx N_y \approx 0$. To minimise shape anisotropy energy a magnetic material can form domains, the configuration of which will tend to reduce or minimise the demagnetising field, and hence the demagnetising, or shape, anisotropy energy. Domain formation will continue until the total magnetic free energy is minimised.

1.2.4 Magnetic Free Energy Density

A total magnetic free energy density can be written to account for the exchange energy, magnetic anisotropies, and any external sources of energy such as the Zeeman energy term resulting from an externally applied magnetic field. The total magnetic energy density can be written as:

$$E_{total} = E_{exch} + E_{anis} + E_{demag} + E_{Zeeman} + E_{ME} \tag{1.19}$$

where E_{exch} is the exchange energy between spins, E_{anis} refers to anisotropy energy associated with the crystal lattice, E_{demag} is the demagnetising energy associated with dipole-dipole magnetostatic interactions, and E_{Zeeman} is the energy associated with interaction of spins with an applied magnetic field. E_{ME} is the magnetoelastic energy induced by strain present in the material. The balance of these different energies is important for understanding the formation and control of magnetic domains and domain walls.

1.2.5 Magnetic Domains and Domain Walls

The magnetostatic energy, given in equation (1.18), is minimised by minimising the demagnetising field. The number of lines of **M**, or flux, which terminate on the surface (giving a stray field via equation (1.17)) can be reduced by forming flux-closed magnetic domains. An example of a flux-closing domain configuration is shown in figure 1.10.

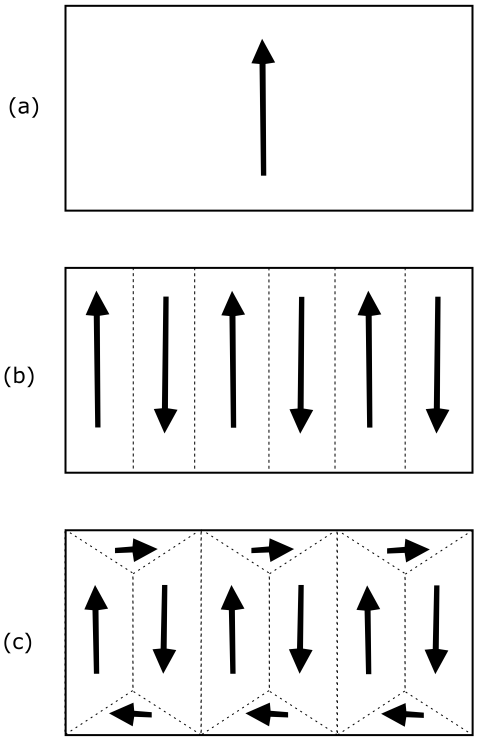

Figure 1.10: Schematic of domains in a magnetic thin film. The domain pattern becomes increasingly flux-closed from (a) to (c). The resulting domain pattern is similar to that which might be observed in a material with cubic anisotropy, with a uniaxial anisotropy along the short-axis of the rectangle.

Domains are separated by domain walls. The presence of a domain wall incurs an energy cost since it involves the local magnetisation pointing along a direction not favoured by the various contributions to the magnetic free energy (equation (1.19)). Some basic ideas about domain walls can be understood by considering a domain wall separating two domains with antiparallel mag-

netisation in a material with uniaxial anisotropy (K_U)[131]. In the absence of exchange energy, the domain wall would be one atomic layer thick and there would be an abrupt switch from one magnetisation orientation to the other. In reality, however, this configuration would involve a large exchange energy cost as exchange energy increases with increasing angle between adjacent spins, see equation (1.3). The exchange energy is minimised by minimising the angle of rotation between adjacent spins, which requires a large number of interatomic spacings, N, in the domain wall. In this case the angle between adjacent spins is approximately π/N, and the exchange energy is $\approx JS^2(\frac{\pi}{N})^2$. The energy per unit area of a wall N spacings with area a^2, in a material with lattice parameter a is then given by:

$$\sigma_{exch} = JS^2\frac{\pi^2}{Na^2} \tag{1.20}$$

which is clearly minimised by maximising N, and making the wall as wide as possible.

The magnetisation in the two domains is oriented to lie along an easy axis direction, which means that the spins in the domain wall necessarily lie along non-easy directions. This situation has an energy cost associated with it that can be represented approximately by:

$$\sigma_{anis} \approx K_U Na \tag{1.21}$$

which is minimised by reducing the wall width. The equilibrium wall width is then that which minimises the sum of these two energy terms:

$$\sigma_{anis} + \sigma_{exch} = JS^2\frac{\pi^2}{Na^2} + K_U Na \tag{1.22}$$

which is minimised for $N = \sqrt{(\frac{JS^2\pi^2}{K_U a^3})}$. This number of spacings corresponds

to a wall thickness δ of approximately:

$$\delta = Na = \pi\sqrt{\frac{A}{K_U}} \tag{1.23}$$

where A is the exchange stiffness parameter (equation (1.4)). In soft magnetic materials with low anisotropy, such as Fe, this domain wall width is around 100 nm to 200 nm, whereas in materials with high anisotropy the width may be as small as 10 nm. The energy density of the domain wall is found by inserting this width into equation (1.22). Typical values are around 0.1 mJ/m^3

To minimise this energy cost a magnetic system tends to form as few domains as necessary, and those that are produced will be of a type which has the smallest energy cost associated with it. In a bulk magnetic material the preferred rotation is within the plane of the wall. In which case the domain wall is called a Bloch wall (see figure 1.11 (a)). In in-plane magnetised thin films, a Bloch wall will incur an additional demagnetising energy cost as the magnetisation rotates out of the plane of the film. Therefore, it becomes favourable for the magnetisation to rotate perpendicular to the plane of the wall, in the plane of the film. These are called Néel walls (see figure 1.11 (b)).

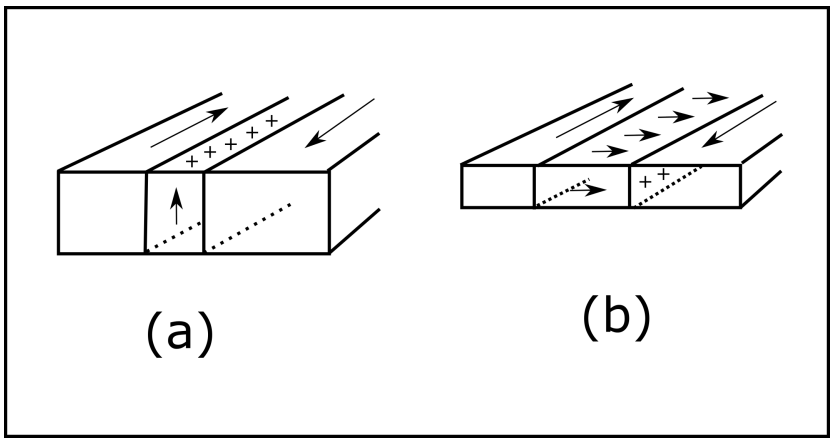

Figure 1.11: Schematic examples of a Bloch (a) and Néel (b) domain wall. The magnetisation in the Bloch wall rotates in the wall plane, whereas in the Néel wall the magnetisation rotates perpendicular to it. '+' symbols represent the magnetic charges formed by the wall.

In patterned magnetic structures such as strips, ribbons, or wires, the role of geometry and shape anistropy becomes more significant and more novel domain wall types may be present [140]. This is particularly true in soft magnetic materials with low magnetocrystalline anisotropy. The result of the relatively enhanced shape anisotropy means that in structures such as wires, the magnetisation tends to point along the length of the wire. In a two-domain situation a 180° domain wall must exist. In 1997 McMichael and Donahue [40] predicted two possible domain wall types for such a system. Firstly the transverse wall (figure 1.12 (a)) in which the spins rotate in the plane of the film. The wall is asymmetric along the y-axis to further reduce the shape anisotropy. Secondly the vortex wall (figure 1.12 (b)) in which spins rotate in the plane of the film about a central core, with magnetisation pointing in the positive or negative z direction. By analysis of the energies of the transverse and vortex wall McMichael and Donahue were able to produce a phase diagram of domain wall types as a function of film thickness and wire width. A schematic of the domain wall phase diagram is shown in figure 1.13. The key conclusion from it is that vortex domains tend to be favoured in wider, thicker wires. This phase diagram was later refined by Nakatani and Thiaville [39] to include additional asymmetric domain walls (figure 1.12 (c)) which are energetically favourable in a small range of geometries. The full phase diagram [141, 142], including the asymmetric domain walls [143], has since been observed experimentally.

Domains and domain walls can be controlled by manipulating the magnetic energy landscape. If the energies are adjusted such that one direction of magnetisation becomes more favourable relative to another, then the domains with magnetisation pointing along that direction will grow at the expense of others. The motion of domain walls under the influence of a magnetic field was described in one dimension by Schryer and Walker [144]. This model describes the exact solution for the motion of 180° domain walls, and predicts three regimes of motion [145], with velocities typically up to a few hundred m/s [146, 147]. Up to a critical field, the Walker breakdown field, the domain wall velocity increases steadily and is characterised by uniform motion. Beyond

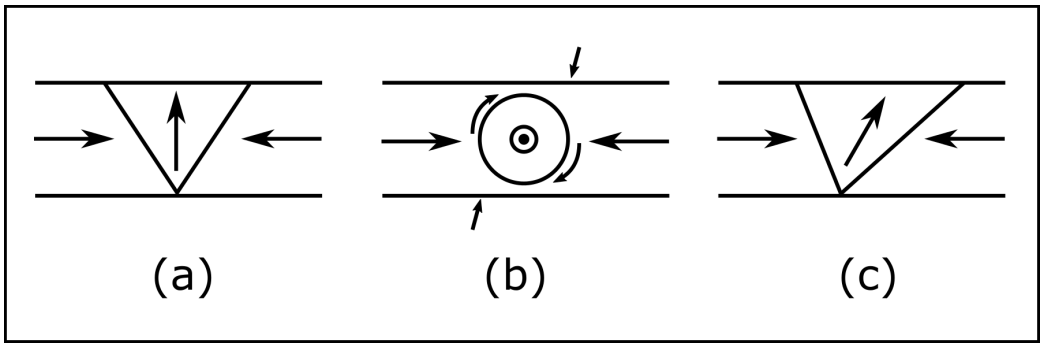

Figure 1.12: Schematic examples of domain wall types found within thin-film wires. (a) Symmetric transverse wall (b) Vortex Wall. Smaller arrows denote regions where stray field enters the vortex wall. (c) Antisymmetric transverse wall.

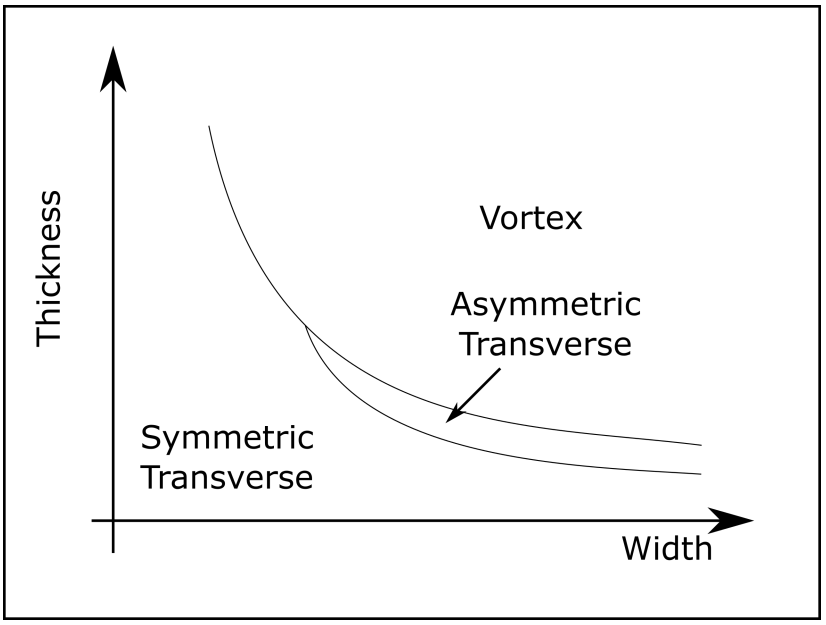

Figure 1.13: Phase diagram of domain wall types in magnetic wires as a function of width and thickness. Vortex domain walls tend to be favoured in wider, thicker wires. A boundary region of asymmetric transverse walls exists between vortex and symmetric domain walls for some wire dimensions.

the critical field, no steady state solution is possible and there lies a region where the average velocity of the wall decreases with increasing applied field. In these solutions the magnetisation of the wall oscillates between Bloch and Néel wall configurations, while the wall itself oscillates back and forth. The breakdown of the wall is characterised by vortex-like structure of the wall. At still higher fields the domain wall velocity increases with turbulent motion that is difficult to analyse in detail [145]. A summary of the three domain wall motion regimes is shown in figure 1.14. This 1D model for a single domain wall in an infinite magnetic material captures the essential features of the behaviour of Néel and Bloch domain walls in nanowires [148], but tends to over estimate the breakdown field and the maximum velocity [149]. There is also another regime of motion, not studied in this thesis, in which domain walls creep along by thermally activated jumps [150]. The disorder in such systems washes out the Walker breakdown and suppresses the peak in velocitiy associated with it. The motion of domain walls in nanowires is discussed further in chapter 5.

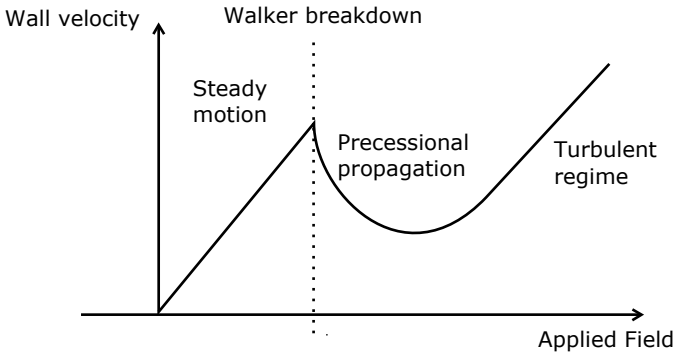

Figure 1.14: Sketch of domain wall velocity as a function of applied field. There are three regimes of motion: steady motion at low fields below Walker breakdown, precessional motion immediately after Walker breakdown, and turbulent motion at magnetic fields far above Walker breakdown. Domain wall velocities are typically up to a few hundred m/s, although Walker breakdown is typically less than 100 m/s [146, 147]

1.2.5.1 Domain Wall Pinning

The energy of a domain wall depends on its size so it could be expected then that smaller domain walls in narrower constrictions are more readily pinned at a constriction, which acts as an attractive potential well. The magnetic field required to depin the domain wall from that narrower constriction is greater than a wider one. Although instructive, this simple picture of domain wall pinning and depinning does not fully account for the nuanced elements of the behaviour of domain walls, in particular in neglecting the differences in spin structure between the vortex and transverse domain walls found in wires [140].

Transverse domain walls do largely follow the simple picture above, vortex domain walls behave radically differently. It has been shown experimentally that vortex walls are in fact repelled from the constriction itself, being pinned instead next to the constriction [141, 151, 152]. The potential landscape experienced by transverse (a) and vortex domains (b) is shown in figure 1.15. Note that there is a small energy barrier between the the potential well and flat potential surrounding it. This was observed by measurements of the magnetic fields required to move a domain wall into the notch, rather than depin from it [153]. Domain walls at constrictions have been observed as occupying the locations indicated by these energy landscapes [140]. On which side of the constriction a vortex wall is pinned is determined by the slight geometrical asymmetries of the notches observed. A vortex domain wall has two areas where a stray field occurs [140] (shown schematically in figure 1.12 (b)) and one of these areas becomes pinned at the constriction, with the centre of the wall itelf being pinned directly adjacent to the constriction.

A domain-wall-pinning potential well can be characterised with three key parameters: depth, width and curvature. The depth of the potential well corresponds to the pinning strength and can be probed by measuring the externally applied field required to depin the domain wall from the well, as a function of constriction width. The depth of pinning potential wells has been well studied [115, 140, 151, 153]. The spatial extent or width of a domain

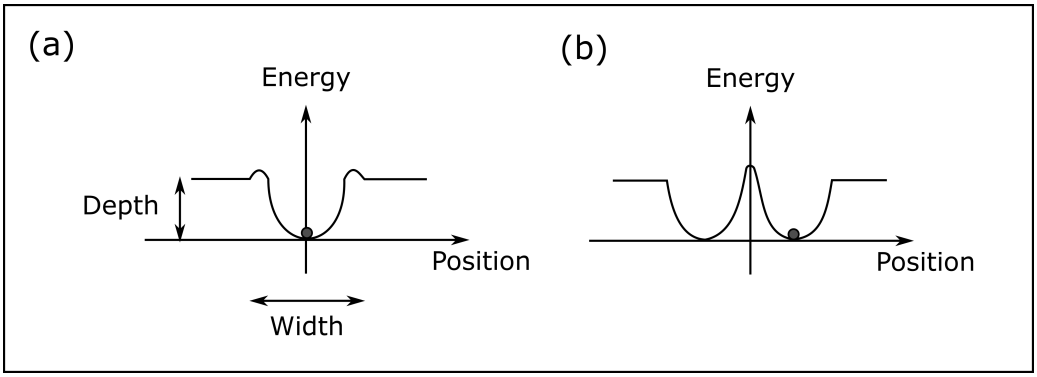

Figure 1.15: Pinning potentials due to a constriction experience by (a) a transverse wall and (b) a vortex wall. The transverse wall is attracted to the constriction. The vortex wall is repelled from the constriction itself, but is pinned adjacent to the wall. (After [140].)

wall pinning potential has also been well studied by varying the shape of the constriction [115, 152]. Finally, the profile or curvature is also needed to fully characterise a domain wall pinning potential. In static measurements the exact nature of the curvature is not crucial, but in dynamic oscillatory measurements the pinned domain wall can oscillate within its potential well [140]. This has been observed in permalloy ring structures [140, 154]. Notches in magnetic wires are a common means of introducing a pinning constriction, but other pinning schemes have been used, including protusions from the wire [153], sharp bends [155, 156, 157], and the pinning potential at the join between an injection pad and the wire [141, 158]. Combinations of notch constrictions have been used as a means of selecting domain wall types [159].

1.2.6 Anisotropic Magnetoresistance

In 1856 William Thomson (Lord Kelvin) observed that the resistance of a magnetic material depends on the direction of an applied magnetic field with respect to the direction of the current flowing through the sample [1]. Since these initial observations AMR has been further investigated in a range of 3d transition metals and alloys [160, 161, 162, 163].

The origin of this anisotropic magnetoresistance (AMR) is attributed to the spin-orbit coupling [163] which causes the density of states, the shape of the Fermi surface and scattering probabilities to become a function of the magnetisation direction. The origin of AMR can be further understood in terms of the model developed by Campbell, Fert and Jaoul (CFJ) [162], and described by Malozemoff[164]. This CFJ model builds on the two-current interpretation of conduction in ferromagnets introduced in section 1. In this model current proceeds through a ferromagnet in two parallel channels with resistivity $\rho_\uparrow$ for spin-up electrons, and $\rho_\downarrow$ for spin-down electrons. In the absence of spin-orbit coupling, each channel has contributions to the resistivity of ρ_{ss} from scattering between like-spin s states, and ρ_{sd} from scattering between like-spin s and d states. Spin orbit coupling introduces scattering between spin-up and spin-down states. Crucially, the proportionality factor of this coupling, γ, is anisotropic. From the CFJ model, for low temperatures, it can then be written that:

$$\begin{aligned} \rho_{\parallel\uparrow} &= \rho_{\perp\uparrow} + \gamma\rho_{\perp\downarrow} \\ \rho_{\parallel\downarrow} &= \rho_{\perp\downarrow} - \gamma\rho_{\perp\downarrow} \end{aligned} \tag{1.24}$$

where $\rho_\parallel$ and $\rho_\perp$ are the resistivities for current parallel and perpendicular to the field, respectively. This result relies on two key assumptions. Firstly that $\rho_\downarrow$ is predominantly due to s-d scattering, such that $\rho_\downarrow = \rho_{sd\downarrow} + \rho_{ss\downarrow} \approx \rho_{sd\downarrow}$, and secondly that $\rho_{\perp\uparrow}$ is due entirely to s-s scattering as in strongly ferromagnetic materials all of the spin-up d states are pushed below the Fermi surface. From equations 1.24, Campbell, Fert and Jaoul [162] derived their formula for AMR:

$$\frac{\Delta\rho}{\rho} = \frac{\rho_\parallel - \rho_\perp}{\rho} = \gamma[(\rho_\downarrow/\rho_\uparrow) - 1] \tag{1.25}$$

In bulk alloys at low temperature, the AMR can be as large as around 20 % such as in NiFe at 20 K. At higher temperatures phonon scattering reduces the AMR magnitude down to around 5 % [165]. Typical AMR values in thin films are further reduced to just a few per cent due to surface scattering and

structural defects.

There are two aspects to the anisotropic magnetoresistance, a longitudinal AMR parallel to the current direction (ρ_{xx}), and a transverse term perpendicular to the current flow (ρ_{xy}). By convention 'positive AMR' refers to the situation when ρ_{xx} is larger when the magnetisation is parallel to the current than when perpendicular to it. 'Negative AMR' then refers to the opposite case. These conventional terms are strictly appropriate only when the AMR is predominantly a function of the angle between the magnetisation and the current direction. There are materials in which the ordered crystalline structure results in a significant component of the AMR which is dependent on the angle between the magnetisation and the crystal axes. In these material systems the positive and negative AMR terminology is less meaningful.

In 1938 Döring [166] established experimentally that bulk Ni single crystals had a more complicated magnetoresistance than that observed in polycrystals and found that it was necessary to consider both the angle between the current and the crystallographic axes and the magnetisation. Magnetoresistance measurements of epitaxial Fe thin films [165] have shown that a more complicated relationship than the simple isotropic case is required there too. In this case the AMR can be written as

$$\frac{\rho - \rho_{av}}{\rho_{av}} - \delta = C_1 \cos^2\psi + C_2 \cos^4\psi + C_3 \cos\psi \sin\psi + C_4 \cos\psi \cos^3\psi \quad (1.26)$$

where ψ is the angle between the magnetisation and the current direction.

van Gorkom et al. [165] conclude that in general the coefficients, C, can vary significantly through the 4.2 K to 230 K range studied.

Phenomenologically[163], the functional forms can be found by considering the projection of the electric field onto directions parallel and perpendicular to the current flow. This gives expressions for the AMR which are suitable for isotropic, polycrystalline samples, or materials with small crystalline con-

Table 1.3: Table of AMR at 300 K and 77 K for different magnetic materials. The value $\Delta\rho/\rho_{av}$ is the AMR.

Alloy	Temp K	$\Delta\rho/\rho_{av}$ %	ρ_{av} $\mu\Omega\,cm$	$\Delta\rho$ $\mu\Omega\,cm$	Ref
Fe	300	0.2	9.8	0.02	[167]
	77	0.3	0.64	0.002	[168]
Co	300	1.9	13	0.25	[163]
Ni	300	2.02	7.8	0.16	[169]
	77	3.25	0.69	0.023	[167]

tributions to the AMR:

$$\rho_{xx} = \rho_{av} + \Delta\rho \cos 2\theta \tag{1.27}$$

and

$$\rho_{xy} = \rho_{av} + \Delta\rho \sin 2\theta \tag{1.28}$$

where θ is the angle between the current and the direction of magnetisation, $\Delta\rho = \rho - \rho_{ave}$, and ρ_{ave} is ρ averaged over 360°.

1.2.7 Magneto-Optical Kerr Effect

Faraday first observed in 1846 [170] the rotation of polarisation of light transmitted through a magnetised material. The change in polarisation due to light reflected from a magnetised material was later observed by Kerr in 1877 [171]. This reflection effect is now called the magneto-optical Kerr effect (MOKE). The use of MOKE in experiments in this thesis is discussed in chapter 2.

Maxwell in 1873 [172] established the phenomenological explanation of magneto-optical effects as being the result of the different propagating velocities of the two circular modes making up linearly polarised light. It is possible to rigorously derive the magneto-optic effects [173, 174], but the important conclusions can be understood by considering the Lorentz force acting on light-agitated electrons[145]. Magneto-optic effects allow the dielectric field for

displacement, $\mathbf{D}$, to be written as

$$\mathbf{D} = \varepsilon(\mathbf{E} + iQ_v\mathbf{M} \times \mathbf{E}) \tag{1.29}$$

where $\mathbf{E}$ is the electric field associated with the electromagnetic wave, $\mathbf{M}$ the magnetisation, ε the permittivity and Q_v the Voigt constant which determines the strength of the magneto-optic effect. A linearly polarised light beam will induce motion of electrons parallel to the plane of polarisation, that is the plane of the electric field, $\mathbf{E}$, of the light. For light conventionally reflected (i.e. no magneto-optic effects) the reflected plane of polarisation is the same as that of the incident light. This conventional reflected component is denoted $\mathbf{R}_N$. In addition to this conventional interaction there will also be a small Lorentz interaction as the electrons move within the magnetic field of the material. This component is perpendicular to both the magnetisation, $\mathbf{M}$, and the electric field $\mathbf{E}$. The velocity of this secondary motion is proportional to

$$v_{Lor} = -\mathbf{M} \times \mathbf{E} \tag{1.30}$$

The origin of the form of this Lorentz velocity can be found by going back to the expression for the Lorentz force, $\mathbf{F} = q(\mathbf{E} + \mathbf{v} \times \mathbf{B})$. Taking $\mathbf{B}$ to be proportional only to $\mathbf{M}$ and that for an electron drift velocity, μ, $\mathbf{v} = \mu\mathbf{E}$, reversing the order of the cross product gives the desired result in equation (1.30). From this motion and Huygens' principle (reflection and transmission at an interface) the Faraday amplitude, $\mathbf{R}_F$, for transmission and the Kerr amplitude $\mathbf{R}_K$ for reflection are found. The reflected light will then be a superposition of $\mathbf{R}_N$, and $\mathbf{R}_K$. By convention the angle of rotation of the polarisation plane θ_K is positive if the plane of polarisation turns clockwise when the observer faces the source.

Magneto-optical effects in ferromagnetic materials were initially understood in terms of an effective field [174]. Although this interpretation produced the right order of magnitude of the effects, it was incompatible with the Heisenberg's exchange interaction model of ferromagnetism since the exhange

interaction does not directly couple an electron's spin to its orbital motion. This problem was solved by Hulme in 1932 [175] who noted that the spin-orbit interaction allowed magneto-optic effects within the Heisenberg model. The spin-orbit origin of magneto-optical effects was fully derived using perturbation theory in 1955 [176].

This longitudinal MOKE interaction is shown schematically in figure 1.16.

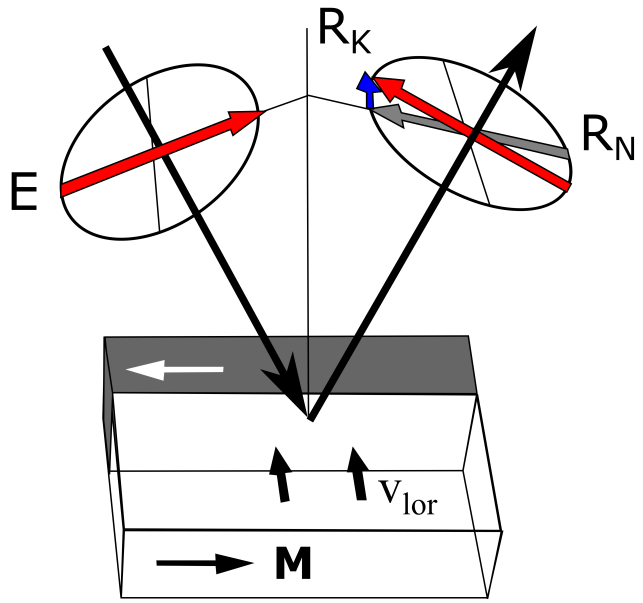

Figure 1.16: Longitudinal MOKE. For ordinary (R_N) and Kerr (R_K) reflected electric field amplitudes. E is the direction of polarisation of the light. $v_{\mathbf{lor}}$ is the Lorentz motion. Adapted from [145].

In this thesis the longitudinal Kerr effect is used in which the magnetisation is in the plane of the sample and pointing along the plane of incidence of the beam. For normally incident light there is zero magneto-optical contribution as $\mathbf{M}$ points along the direction of $\mathbf{E}$ and $\sin 0 = 0$. By rotating the incident beam away from normal incidence the angle between $\mathbf{E}$ and $\mathbf{M}$ is opened up and the magneto-optical contribution increases.

1.2.8 X-Ray Magnetic Circular Dichroism

A technique for analysing magnetic materials is the X-ray magnetic circular dichroism (XMCD) in which x-rays incident on a sample excite electrons from core energy levels. Information is obtained by measuring the difference in x-ray absorption spectra (XAS) for positively and negatively circularly polarised light. The technique is element specific as the binding energy of an electron in a core level is unique to the absorbing element. Magnetic sensitivity comes from the polarisation of the x-rays. The x-ray absorption is typically measured by detection of secondary electrons escaping the sample surface [177]. The sample depth is determined by how far these electrons travel out of the sample and is typically around 2 nm to 10 nm. The XMCD mechanism can be understood as a two step process, shown schematically in figure 1.17. In the first step left- (LCP) or right- circularly polarised (RCP) photons transfer angular momentum to the excited photoelectrons. The photon angular momentum couples to the orbital angular momentum of the electron. If the core states are spin-orbit split, as in the case of $p_{1/2}$ and $p_{3/2}$ the photon angular momentum is transferred to both the spin and the orbital angular momenta. In X-ray spectroscopy the L edge refers to absorption from the 2p orbital, to the 3d orbital. L_2 refers to $2p_{1/2}$, while L_3 refers to $2p_{3/2}$. It can be shown from consideration of Fermi's Golden Rule [178] the L_3 RCP light excites more (62.5%) spin up than (37.5%) spin down electrons. The reverse holds for LCP light. For the L_2 edge RCP light preferentially couples to spin down electrons (25% spin down to 75% spin up). Again, the opposite is the case for LCP light. An example of an XMCD spectrum for RCP and LCP light is shown in figure 1.18, measured from a sample of $Fe_{81}Ga_{19}$ from wafer Mn746. Data from this wafer is presented in chapter 3.

In this first step the 'spin up' and 'spin down' are defined relative to the photon spin direction. The effects are therefore independent of the magnetisation of the material itself. The second component to XMCD is that electrons may only be excited if there are sufficient empty states for them to be excited to. This second step accounts for the magnetic properties of the sample since

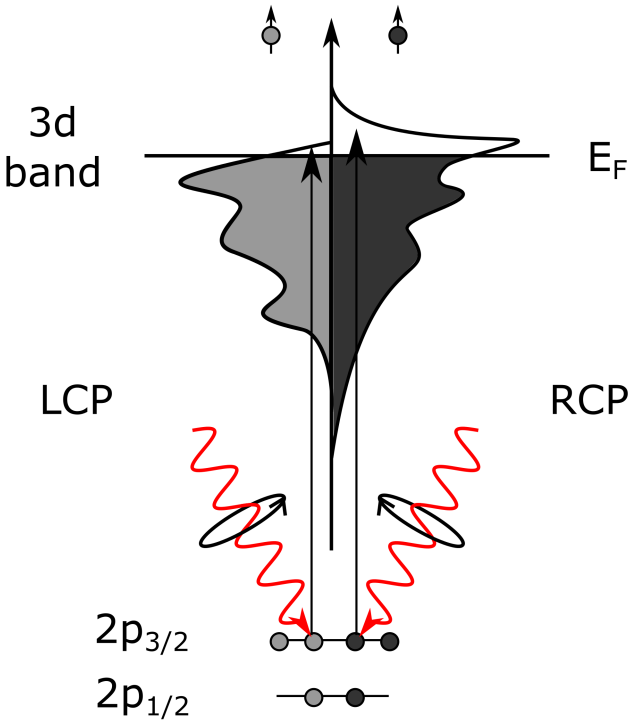

Figure 1.17: The XMCD effect illustrated for the L-edge absorption edge in Fe. Left- (LCP) or right- circularly polarised (RCP) photons transfer angular momentum to the excited photoelectrons. The photon angular momentum couples to the orbital angular momentum of the electron. Electrons may only be excited if there are sufficient empty states for them to be excited to. The transition intensity is proportional to the number of empty d states of a given spin.

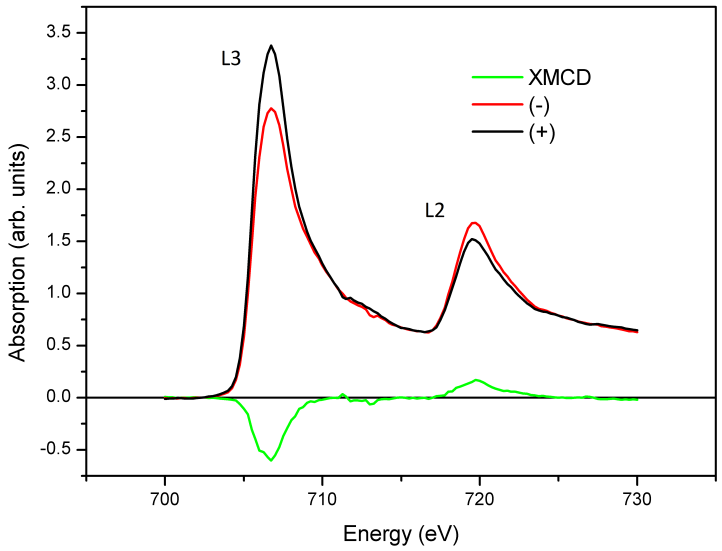

Figure 1.18: Typical x-ray energy scan of Fe (in $Fe_{81}Ga_{19}$), showing L2 and L3 edges for RCP (+) and LCP (-) light. The XMCD difference between the two scans is also shown.

the difference in the density of states above the Fermi level of a ferromagnet therefore acts as a spin-sensitive detector. The transition intensity is proportional to the number of empty d states of a given spin. Electrons emitted by these processes undergo further collisions before they exit the sample, causing the emission of secondary electrons. The method of implementing XMCD to obtain magnetic contrast images is described in chapter 2.

1.3 Magnetostrictive Materials

To successfully control magnetisation with strain it is necessary that the magnetic material responds strongly to a given strain. Increased interest in magnetostrictive materials for sonar applications during the 1940s continued into the 1960s during which time it was observed that the rare-earth elements terbium [179] and dysprosium [180] showed magnetostrictions as large as $10\,000 \times 10^{-6}$ at low temperatures. Room temperature magnetostriction was, however, severely limited by the low Curie temperature of these materials. Increases in Curie temperature were achieved by alloying with 3d transition metals such as iron in $TbFe_2$ and $DyFe_2$[179], although the high magnetocrystalline anisotropy (around $5 \times 10^7\,J/m^3$ [181]) of these materials still limited useability. Investigations into the proportions of Tb and Dy in the alloys led to the development of $Tb_{27}Dy_{73}Fe_{195}$ (commercially, terfenol-D), which has a magnetostriction of 2000×10^{-6} at room temperature with a much lower magnetic anisotropy ($K_1 = -6 \times 10^4\,J/m^3$ [182]) than $TbFe_2$ or $DyFe_2$. In addition to the drawbacks associated with containing rare-earth elements, Terfenol-D is also brittle [180], which limits its applicability in harsh operating environments.

In the last 10 years or so a potential alternative to Terfenol-D has been developed, called Galfenol. Galfenol, an FeGa alloy with magnetostrictive properties markedly enhanced over those of pure iron was developed by Clark et al. [183] as a quench-cooled bulk crystal [123, 124]. The magnetostrictive properties of FeGa are highly composition dependent, with the highest peak

in λ_{100} appearing at 19 %, with another peak at around 28 % Ga. A sketch of the magnetostrictive properties of Fe_xGa_{1-x} is shown in figure 1.19.

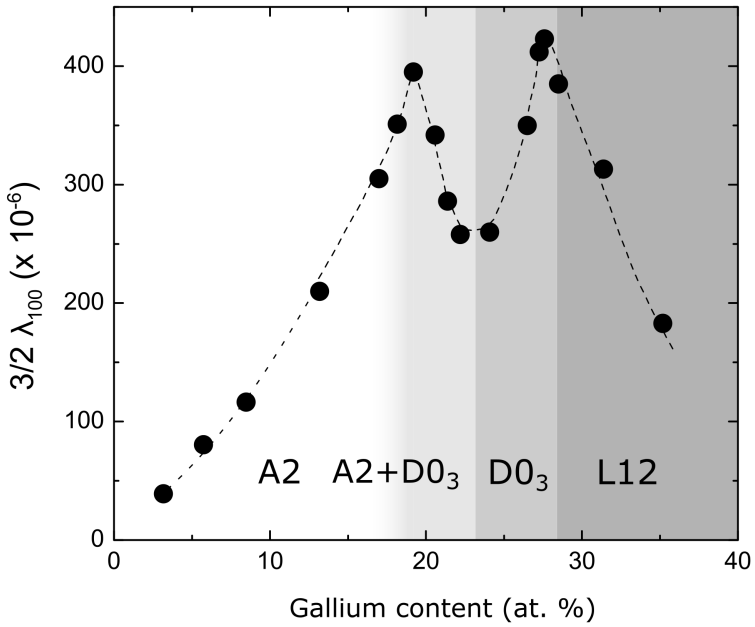

Figure 1.19: Sketch of the magnetostriction coefficient $\frac{3}{2}\lambda_{100}$ as a function of gallium concentration x in $Fe_{1-x}Ga_x$. The structure of the material changes to accomodate the greater Ga concentration. There are two peaks in λ_{100} 19 % and 28 % Ga.

The two peaks have two different origins [184, 185]. The first peak at 19 % Ga is thought to be due to local ordering of gallium atoms [186] which form pairs along the ⟨100⟩ directions, but not maintaining long-range order. The quench cooling used to form bulk samples was important for crystallising this partially ordered state. Schematics of the structuring within FeGa are shown in figure 1.20. The phase-diagram of Galfenol is discussed in greater detail in [187]. Ga atoms form nanoclusters within the bcc (A2) Fe lattice. These nano-precipitates have a D03 structure and are disorted to an intermediate tetragonal phase (such as D022) to make the structure closer to the fcc L12 equilibrium phase. There is evidence that these nanoclusters are the origin of the enhanced magnetostriction [188, 189] and that there is a local strain in the vicinity of the clusters [190]. The second peak is due to a drop in elastic

constant $C\prime = c_{11} - c_{12}$[191, 192].

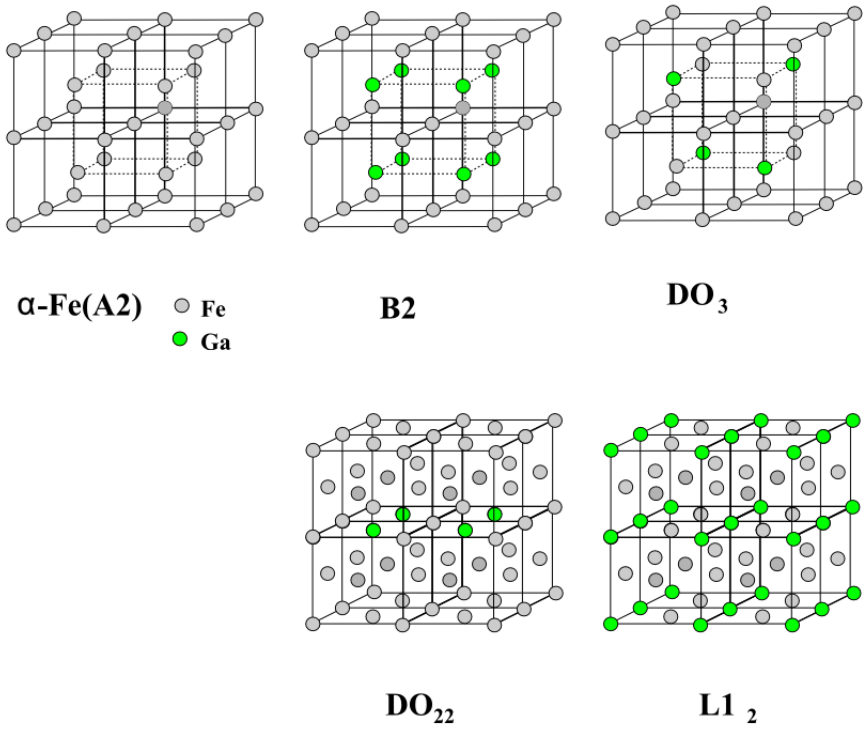

Figure 1.20: The suggested crystal structures of FeGa. $Fe_{81}Ga_{19}$ is thought to consist of D03 FeGa nanoprecipitates in an A2 Fe matrix. Ga atoms form nanoclusters within the bcc (A2) Fe lattice. These nano-precipitates have a D03 structure and are disorted to an intermediate tetragonal phase (such as D022) to make the structure closer to the fcc L12 equilibrium phase.

The magnetostriction constant λ is important, but other properties also contribute to the suitability of a material for magnetostrictive devices. Table 1.4 shows a summary of the magnetic properties of $Fe_{81}Ga_{19}$ compared to pure magnetic materials. For many practical applications the magnetoelastic coupling, B_1, (see equation (1.14)) is the important value since it determines the strength of the magnetoelastic contribution to the magnetic free energy. In laterally confined systems, however, the shape anisotropy may become important, in which case the ratio $|B_1|/M_S^2$ becomes the factor determining the ability to control magnetisation using strain. This table demonstrates how re-

markably high the value of magnetostriction in $Fe_{81}Ga_{19}$ is compared to pure Fe. The relatively small elastic modulus of $Fe_{81}Ga_{19}$ and large saturation magnetisation means that in confined systems, its behaviour may be comparable, or less sensitive than Ni. In this thesis we have investigated devices fabricated from both Co and $Fe_{81}Ga_{19}$.

Table 1.4: Summary of magnetostrictive properties for different materials. Saturation magnetisation (M_s), elastic constant ($c_{11} - c_{12}$), magnetostriction $3/2\lambda_{100}$, and magnetoelastic constant B_1. The ratio $|B_1|/M_s^2$ is a measure of how responsive to strain a device made from that material might be. Higher values are more responsive.

Material	M_S (MA/m)	$c_{11} - c_{12}$ (GPa)	$3/2\lambda_{100}$ (10^{-6})	B_1 MJ/m^3	$\lvert B_1\rvert/M_s^2$ µJm/A^2
$Fe_{81}Ga_{19}$	1.386	19.7[123]	395[123]	-7.78	4.0
Fe	1.712[193]	48[194]	30[123]	-1.44	0.5
Ni	0.49[193]	46.6[194]	-46[127]	2.15	9.0
Co	1.431[193]	71.1[194]	-75[195]	5.33	2.6

1.4 Micromagnetism

Micromagnetism is a formalism which allows macroscopic properties such as magnetic domains and stray magnetic fields to be simulated using approximations for the fundamental atomic behaviour of a material, such as the exchange interaction and other properties. At the heart of micromagnetic simulations is the Landau-Lifshitz-Gilbert (LLG) equation which describes the time-evolution of a magnetic dipole moment $\mathbf{M}$ in an effective magnetic field $\mathbf{H}_{\text{eff}}$.

$$\frac{\partial \mathbf{M}}{\partial t} = -\gamma \mathbf{M} \times \mathbf{H}_{\text{eff}} - \frac{\gamma\alpha}{|\mathbf{M}|}\mathbf{M} \times (\mathbf{M} \times \mathbf{H}_{\text{eff}}) \tag{1.31}$$

where γ is the gyromagnetic ratio and α is the damping parameter. To understand this equation we can can look at the two parts separately. The first term $-\gamma\mathbf{M} \times \mathbf{M}_{\text{eff}}$ describes the precession of magnetisation $\mathbf{M}$ about an effective field $\mathbf{H}_{\text{eff}}$. This expression comes from the torque felt by a magnetic

moment $\mathbf{M}$ in a magnetic field $\mathbf{H}$

$$\tau = \frac{d\mathbf{L}}{dt} = \mathbf{M} \times \mathbf{H} \tag{1.32}$$

where $\frac{d\mathbf{L}}{dt}$ is the time differential of the angular momentum. The magnetic moment of an electron is related to its angular momentum by $\mathbf{M} = -\gamma\mathbf{L}$. Taking the time derivative of this equation and substituting in the expression for torque in equation (1.32) gives us the first term in equation (1.31). $\mathbf{H}_{\text{eff}}$ contains information about the magnetic environment the magnetisation is in, not just the applied magnetic field. We can obtain the effective field by considering the free energy of the magnetisation. The effective field is defined as

$$\mathbf{H}_{\text{eff}} = -\frac{1}{\mu_0}\frac{\partial E}{\partial \mathbf{M}} \tag{1.33}$$

where E contains energy contributions from the different terms in the total magnetic free energy, in equation (1.19).

The second term, $-\frac{\gamma\alpha}{|\mathbf{M}|}\mathbf{M}\times(\mathbf{M}\times\mathbf{H}_{\text{eff}})$, is a damping term with a damping coefficient α that exists phenomenologically to bring the system to equilibrium. The exact physical meaning of α is still an active area of research [130, 196]. An important development has been the recent theoretical demonstration that the Gilbert damping term originates from spin-orbit coupling [197]. For accurate time-resolved, dynamical simulations, an accurate representation of the Gilbert damping parameter is required. Typical values are $\alpha = 0.002$ for Fe [198], and $\alpha = 0.043$ for Ni [199]. For quasi-static simulations, a larger damping parameter may be used to force the system to equilibrium faster.

Another important concept in micromagnetic calculations is that of the exchange length. The exchange length can be thought of as the region over which the exchange energy is constant, and is a characteristic length that determines the smallest resolvable feature in a simulation [200]. The exchange

length, l_{ex}, is given by the equation

$$l_{ex} = \sqrt{\frac{A}{K}} \tag{1.34}$$

where A is the exchange stiffness, and K is the anisotropy coefficient of the system. In thin films of magnetically soft materials where shape anisotropy dominates $K = K_d = \frac{\mu_0 M_S^2}{2}$. The exchanges length is typically less than 5 nm. The use of equation (1.31) in micromagnetic calculations will be described in more detail in chapter 2, along with the relevant micromagnetic parameters.

Chapter 2

Materials and Techniques

This chapter contains information about the materials and experimental techniques used in this thesis.

2.1 Materials Used

The different wafers and chips used to obtain the results presented in this thesis are summarised in table 2.1. The Mn-series of wafers are 2 inch wafers grown by molecular beam epitaxy (MBE). Mn635 was $Fe_{81}Ga_{19}$ grown on an un-doped, semi-insulating GaAs substrate, suitable for transport and optical measurements. Mn746 was $Fe_{81}Ga_{19}$ grown on an n-doped (Si, $1 \times 10^{24}/m^3$) GaAs substrate for XMCD-PEEM measurements, since doping prevents charging of the substrate by making it electrically conducting. Devices were made by lithography and etching, after which the substrates were thinned from 350 µm to 150 µm to increase the transmission of strain through the substrate before being mounted on piezoelectric transducers. Sample dp012 was sputtered as part of a lift-off fabrication process. Using a substrate thickness of 100 µm meant that the substrates did not have to be thinned before being mounted on piezoelectric transducers. Pt was used as a buffer, while Al was used as a capping layer.

Table 2.1: Summary of growths used in this thesis

ID number	Substrate	Material (nm)
Mn635	350 µm GaAs (001)	$Fe_{81}Ga_{19}$(21)/GaAs (3)
Mn746	350 µm n-doped GaAs (001)	$Fe_{81}Ga_{19}$(14)/GaAs (1.5)
dp012	100 µm Si (111)	Pt(5)/Co(10)/Al(2.5)

2.1.1 Growth

Samples in the 'Mn' series were grown using MBE by Dr. Richard Campion. The MBE samples were grown by co-evaporation from Fe and Ga Knudsen cells at a base pressure of 2×10^{-10} Torr. The GaAs(001) substrate was prepared by a high temperature (550 °C) bake in vacuum followed by deposition at high temperature of a GaAs buffer layer. The $Fe_{81}Ga_{19}$ itself was grown at room temperature. The growth rates (calibrated by x-ray reflectivity) of $Fe_{81}Ga_{19}$ in Mn635 and Mn746 were 6.5 nm/h and 6.9 nm/h respectively. The $Fe_{81}Ga_{19}$ layer was capped by an amorphous GaAs capping layer to protect the metal from oxidation. A simple schematic of the MBE system used is shown in figure 2.1 (a).

The crystal structure of the layers was investigated by high-resolution x-ray diffraction by Dr. Peter Wadley. The determination of the crystal structure using x-rays is discussed in greater detail in section 2.3.7. Stoichiometric ratios were set by pre-calibrated growth rates and confirmed by SQUID magnetometry carried out by Dr. Andrew Rushforth prior to the start of my PhD. SQUID magnetometry is discussed in greater detail in section 2.3.6.

Sample dp012 was sputtered using a magnetron sputter system from high purity (99.999 %) Co, Al, and Pt targets, with growth rates (calibrated by x-ray reflectivity) of 0.018, 0.045, and 0.046 nm/s respectively. The substrates were Si(111) which had windows defined by electron beam lithography in PMMA for nanowires. Sputtering was carried out at room temperature with a base pressure of 6.8×10^{-8} Torr. During growth, with 30 sccm Ar flow, the pressure was 1.7×10^{-3} Torr. The sample was rotated at 20 rpm to ensure a

uniform growth profile.

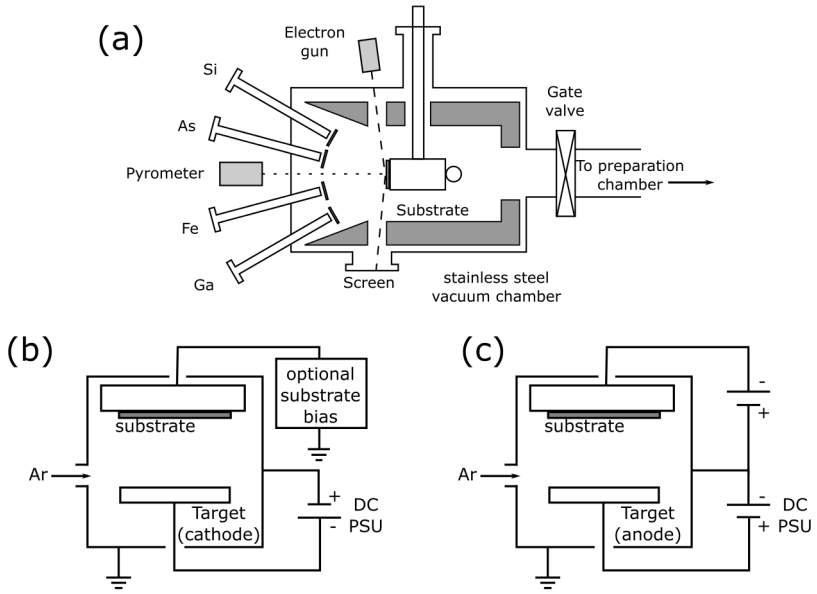

Figure 2.1: (a) Schematic Diagram of MBE growth chamber. The electron gun and screen are for *in-situ* RHEED (Reflection High Energy Electron Diffraction). The pyrometer monitors the substrate temperature. (b) Schematic of sputter chamber configuration. Also shown is the ion-milling setup made by reverse biasing one of the sputter targets, and applying a negative bias to the substrate manipulator (c).

2.2 Fabrication

2.2.1 Lithography

Standard photo- and electron-beam-lithographic techniques were used to make the samples in this thesis. Unless otherwise stated processing and fabrication was carried out in the nanofabrication and clean room facilities at Nottingham. The processing steps for the 'Mn' series of samples is summarised in table 2.2.

Table 2.2: Summary of the processing steps used to make the samples in this thesis. A combination of photo- and electron-beam-lithography techniques were used.

Step	BPRS 150 (UV)	PMMA 495k (E-beam)	AR-N (E-beam)
Spin resist	4 krpm	5 krpm	4 krpm
Edge bead	yes	no	no
Hotplate	90 °C, 2 min	180 °C,2.5 min	90 °C, 2 min
Expose	75 J/cm^2	300 µC/cm^2	150 µC/cm^2
Develop	AZ400K	15 H_2O:35 IPA	AZ706 MIF
Etch	Wet etch	Ion milling	Ion milling
Strip resist	Warm acetone	Warm acetone, resist stripper	Warm acetone, resist stripper

The electron beam lithography stages for sample dp012 were done by Dr Andrew Irvine, University of Cambridge using a EBL system capable of producing narrower wires with better edge definition than the Nottingham system. For these samples rather than etching, material was deposited through windows in the resist in Nottingham.

2.2.2 Ion milling

Ion milling is a ballistic process involving Ar^+ ions being fired at the sample to be etched. Ion milling of samples for MOKE measurements in chapter 3 and 4 was done using a reversed-polarity planar magnetron sputter source, as described in [201], using a 630 V bias and a pressure of 1.6×10^{-3} Torr during milling, from a base pressure of 1.4×10^{-8} Torr. The sample was rotated at 20 rpm to promote an even etch profile, with a target-substrate distance of 200 mm. A schematic of the ion-milling system used is shown in figure 2.1 (c). For the XMCD-PEEM measurements described in chapter 4 the samples were milled by a dedicated milling system at University College London.

2.2.3 Substrate Thinning

To achieve better transmission of the strain from the transducers to the magnetic films the GaAs substrates were thinned following the other fabrication steps. A standard fast GaAs etch[202] of $5\,H_2SO_4 + 40\,H_2O_2 + 5\,H_2O$ was used to thin the GaAs substrates from 350 µm to 150 µm. This solution had a nominal etch rate of 10 µm/min, although testing showed that this rate decreased over the etch time. A graph of etch depth as a function of etch time for a range of test samples is shown in figure 2.2. Also shown in this graph is a fit to a curve of the form $y = y_0 + A\exp(R_0 t)$ where y the etch depth, and t the etch time. Fitting coefficients were $y_0 = 210(50)$ µm, $A = -200(50)$ µm/min and $R_0 = -0.1(4)$/min.

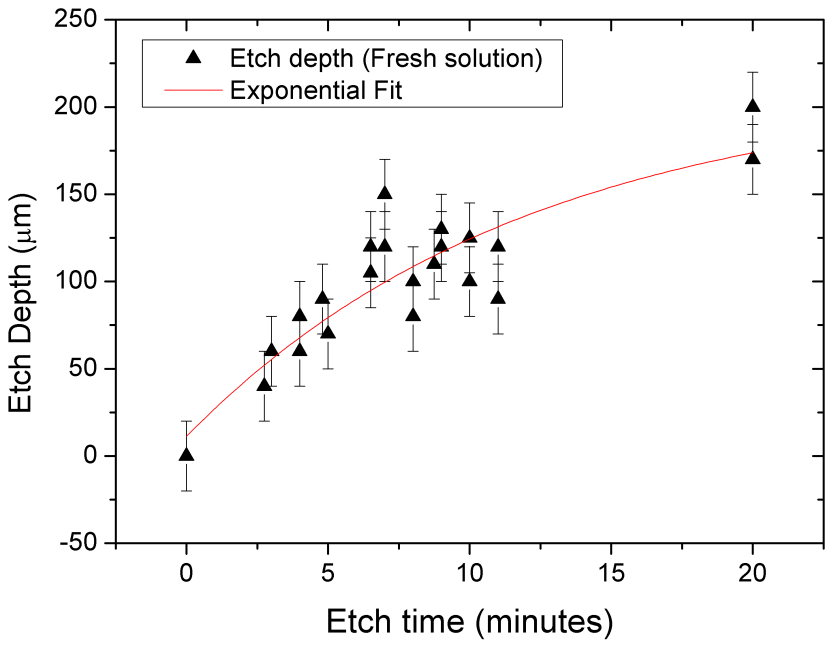

Figure 2.2: Etch depth of GaAs substrates as a function of etch time, with exponential fit. Error bars are from the z-scale on the optical microscope used to determine etch depth.

This wet etching was done after the other fabrication stages, so it was im-

portant to protect the grown-on side by mounting the samples face-down on a glass slide using BPRS photoresist. Etching was done by immersing the samples mounted on the slide into the etch solution. The solution was stirred and the slide turned every minute or so to reduce the risk of a wedge-shaped etch profile. The etch was stopped in ultra-pure water after which the samples were removed from the slide using acetone followed by IPA and dried with nitrogen gas. The etch depth was then measured by observing the focal point in an optical microscope with z-axis calibration for the top and bottom sides of the sample.

2.2.4 Piezoelectric transducers

The piezoelectric transducers used to induce strain in this thesis were Piezomechanik GmbH Parts: Pst 150/5x5/7, Pst 150/3x3/7, which have a safe operating voltage range of $-30\,\mathrm{V}$ to $150\,\mathrm{V}$ at room temperature, which corresponds to a range of applied strain of around 1×10^{-3}. The piezoelectric transducers were prepared in the following way. First the polymer coating on the transducer was removed using glass paper. The piezoelectric transducer was then cleaned with IPA. Epo-Tek H70E two part epoxy was used to bond the samples to the piezo. This epoxy was selected as it does not outgas in ultra high vacuum systems. The recommended cure of $80\,^{\circ}\mathrm{C}$ for $2\,\mathrm{h}$ was used unless otherwise stated. This curing procedure has the effect of building in a strain to the samples as there is a non-isotropic expansion coefficient of the piezoelectric material. A photograph of samples mounted and bonded to a piezoelectric transducer for transport measurements is shown in figure 2.3.

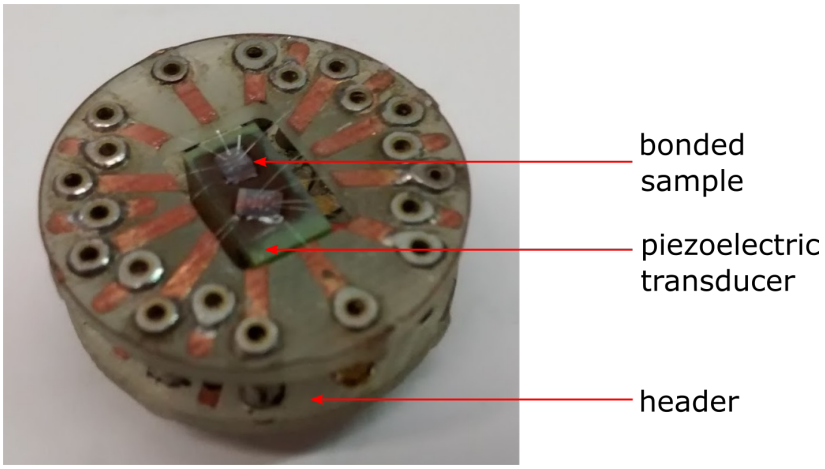

Figure 2.3: Photograph of samples mounted to a piezoelectric transducer and bonded to a header suitable for transport measurements.

2.3 Measuring Instruments and Procedures

2.3.1 Magnetotransport

System Description

The transport measurements described in this thesis were principally carried out in a helium-cooled cryostat capable of temperatures in the range 4.2 K to 400 K. A schematic of the cryostat used is shown in figure 2.4. The cryostat system was principally used to maintain a measurement temperature of 300.00(1) K. The sample was situated between the poles of a rotatable electromagnet capable of applying a field of up to 0.5 T with a resolution of 5×10^{-4} T. In chapter 3 measurements were also done in the absence of any external magnetic field. In this case the sample probe was removed from the cryostat and mounted in such a way that external magnetic fields were shielded by mu-metal to reduce the effect of any external fields.

Four-terminal measurements of transverse and longitudinal voltages were carried out with a Keithley 2400 sourcemeter and Keithley voltmeters in constant current mode, with a current of 2 mA. Current-voltage measurements

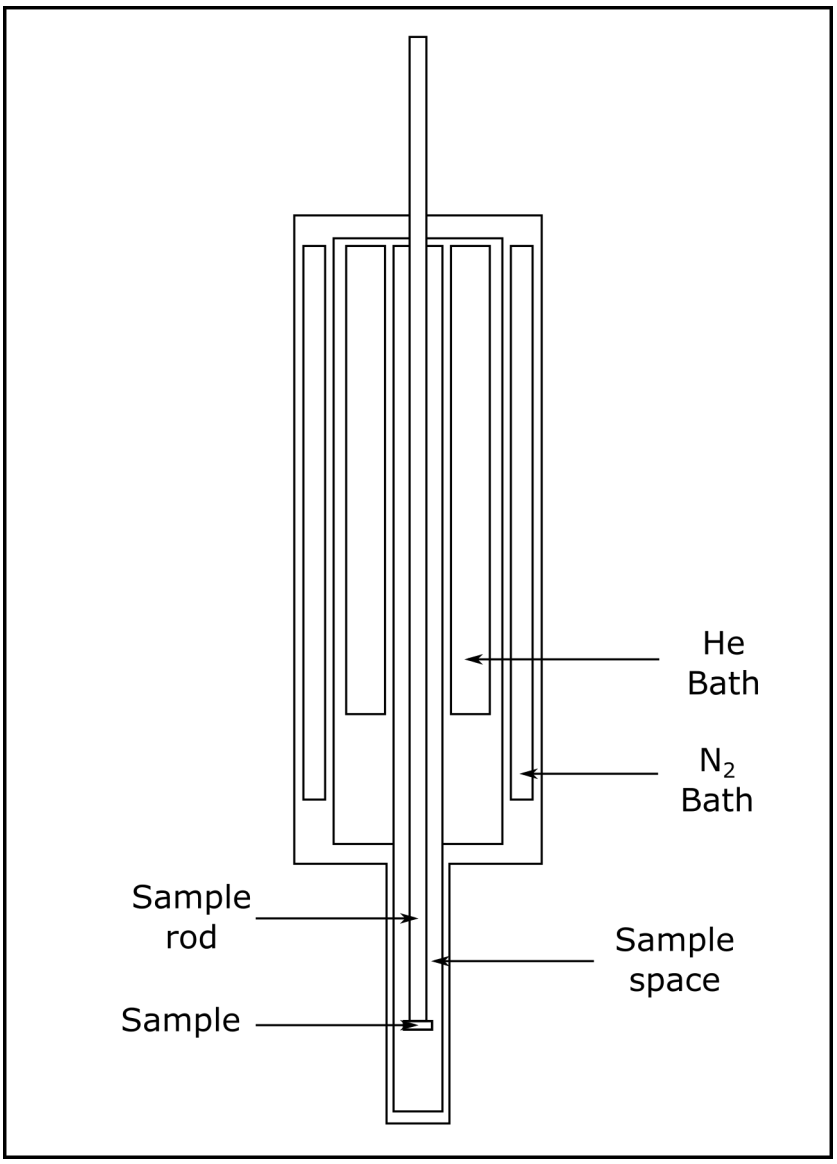

Figure 2.4: Schematic of cryostat used for magnetotransport measurements. The sample was situated between the poles of a rotatable electromagnet capable of applying a field of up to 0.5 T.

confirmed that the sample was Ohmic up to this current, indicating that no significant Joule heating was present. Where necessary piezoelectric transducers were controlled by a separate Keithley 2400 sourcemeter. The maximum leakage current of the piezoelectric transducer was below 800 nA. The experiments were controlled and data collected via LabView programs.

Measurement Description

The magnetotransport measurements described in this thesis were carried out on Hall bars with dimensions shown schematically in 2.5. This figure also shows the notation and polarity conventions used.

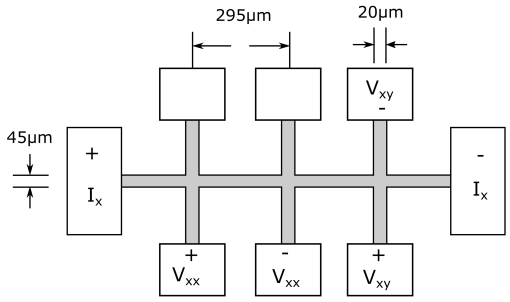

Figure 2.5: Schematic of Hall bar device including notation and polarity conventions. I is the current which flows through the device, V_{xx} and V_{xy} are the longitudinal and transverse voltages, respectively.

For in-plane anisotropic magnetoresistance measurements the sample was mounted on an appropriate sample probe and placed in a saturating field capable of rotation through 200° in the plane of the film. Magnetic field sweeps were also carried out along different directions.

2.3.2 Sample Preparation

It was known [105] that the recommended curing procedure for the piezoelectric transducers introduced a 'built-in' strain due to the anisotropic thermal

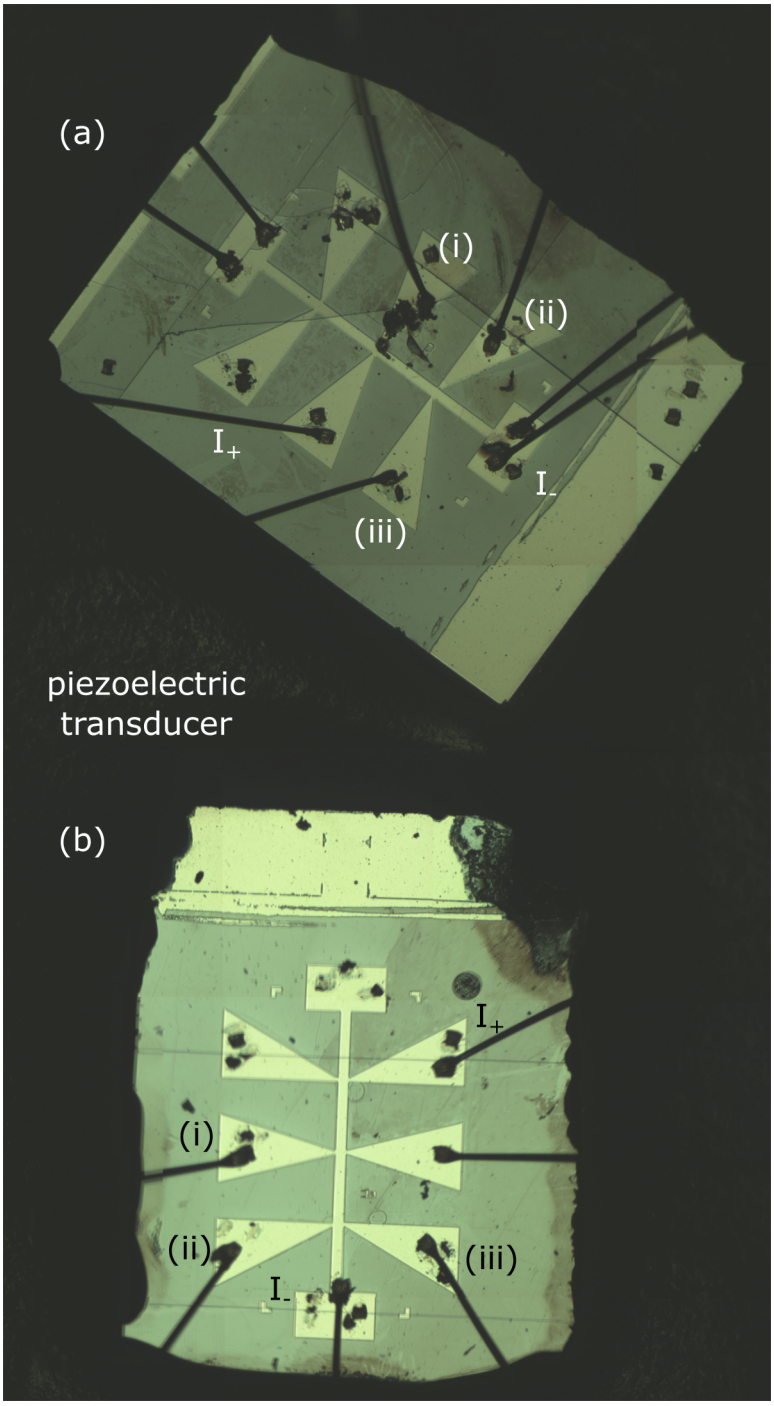

Figure 2.6: Microscope image of $Fe_{81}Ga_{19}$ Hall bars on which magnetotransport measurements were made. The piezoelectric transducer extends beyond the image bounds. The extent of the transducer can be seen more clearly in figure 2.3.(a) Hall bar oriented with long-axis at 45° to long-axis of piezeoelectric transducer (b) Hall bar oriented with long axis parallel to long-axis of piezoelectric transducer. Labelled are the current source I_+ and drain I_-, and probes for R_{xx} (i-ii) and R_{xy} (ii - iii) measurement.

expansion coefficient of the piezoelectric material. The transducer expands non-isotropically, the glue cures, and then as the sample cools this strain is introduced. This built-in strain limited the extent to which both tensile and compressive strain could be applied along both the [100] and [010] axes of the $Fe_{81}Ga_{19}$. To get around that situation, rather than use the recommended curing process, the sample was bonded to the transducer and during the curing process, and the sample heated above the ferroelectric Curie temperature (around 150 °C), causing the PZT to expand isotropically. An electric field was applied to the transducer as it was cooled down through the Curie temperature to repolarise the PZT. A schematic of the transducer-mounted Hall bar is shown in figure 2.7. It is important that the $Fe_{81}Ga_{19}$ was mounted in such a way that the strain induced will be parallel to the [100]/[010] directions, since it is only the λ_{100} magnetostriction constant which is enhanced relative to Fe.

2.3.3 Strain Calibration

Calibration of the strain is very important. It was known that the transducers used are capable of applying a strain of 10^{-3}. However, due to the elastic properties of the glue used to bond the sample to the transducer, and the GaAs substrate, the actual strain experienced by the sample will be reduced. The treatment of the PZT during the glue-curing process may also have affected the maximum possible strain. To determine the exact strain we are able to apply two different techniques were used.

Firstly the sample itself was used as a strain gauge. By applying a saturating field any anisotropic magnetotransport effects were removed, since the magnetisation direction was prevented from moving away from the direction of the applied field. Secondly, to confirm this first measurement of the strain a $Ni_{80}Cr_{20}$ resistance bridge was also fabricated on a GaAs substrate thinned in the same way as the $Fe_{81}Ga_{19}$ Hall bar. This resistance bridge strain gauge was bonded to a piezoelectric transducer in the same manner as the $Fe_{81}Ga_{19}$ Hall bar. Resistance measurements of the two strain gauges are shown in

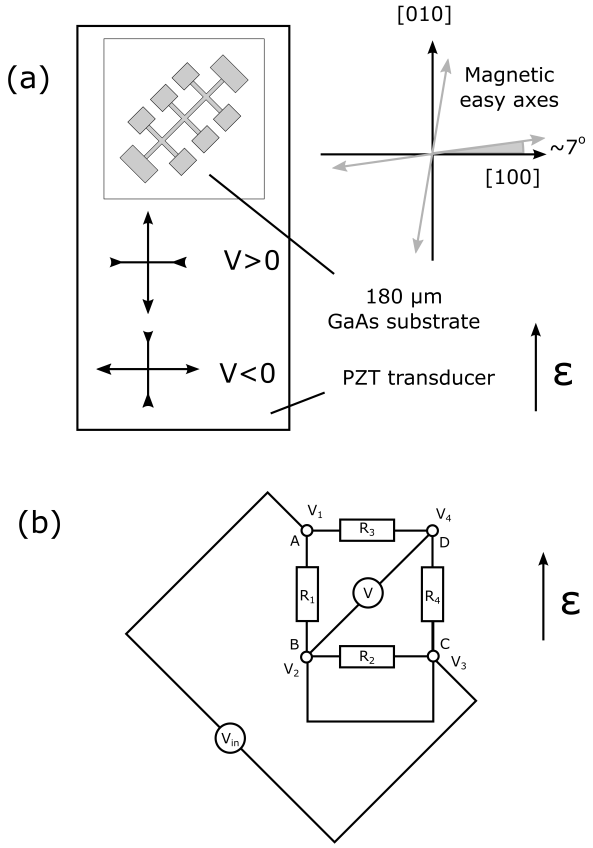

Figure 2.7: (a) Schematic of Hall bar mounted on piezoelectric transducer, along with the crystallographic and magnetic easy axes of FeGa. (b) Resistance bridge used for strain calibration.

figure 2.8.

In general resistance varies with strain with a dependency on both the geometrical changes, and changes of the resistivity with strain [203, 204, 205]. The change in resistivity originates from the distortion of the Fermi surface in the metal induced by the distortion of the lattice. The combination of geometrical and resistivity changes is often combined into a single term, the gauge factor, which determines how strain will scale with a change in resistance. The gauge factor itself can be thickness dependent. For the thickness of $Ni_{80}Cr_{20}$ strain gauge used, a gauge factor of around 2 is expected [206]. $Fe_{81}Ga_{19}$ is less well studied as a strain-gauge material, with little literature about the strain dependence of resistivity of either Ga, Fe, or $Fe_{81}Ga_{19}$ itself. In the sections below it is shown that geometrical considerations produce a gauge factor for the $Ni_{80}Cr_{20}$ in the range expected. A geometrical consideration of the gauge factor is also made for the $Fe_{81}Ga_{19}$ Hall bar measured as a strain gauge. The close agreement of the resistance bridge and Hall bar curves indicates that using the saturated Hall bar as a strain gauge provides an acceptable measure of the strain.

$\mathbf{Ni_{80}Cr_{20}}$ Strain Gauge

The strain measured by the $Ni_{80}Cr_{20}$ resistance bridge strain gauge can be deduced as follows. Looking at the schematic of the resistance bridge in figure 2.7 there are some relationships between the voltages and resistances that can be observed:

$$(V_2 - V_1) + (V_3 - V_2) = V_{in}$$
$$(V_4 - V_1) + (V_3 - V_4) = V_{in}$$

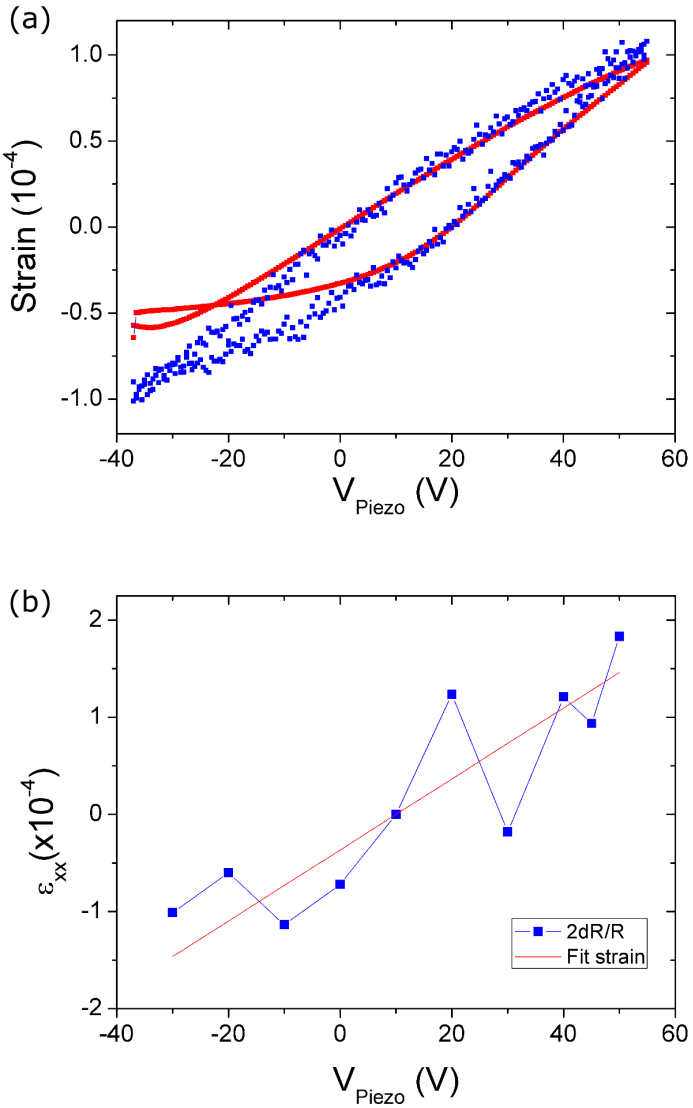

Figure 2.8: a) The uniaxial strain along the direction of the transducer to which the samples were bonded as a function of the voltage applied. The strain was determined at T=300 K using a $Ni_{80}Cr_{20}$ resistance bridge (red symbols) and using the change in the longitudinal resistance of the $Fe_{81}Ga_{19}$ Hall bar in a saturating magnetic field of 0.5 T applied along the direction of the current (blue symbols). b) Strain measurements later extracted from field sweep measurements. Additional noise is present since the measurements were not made during a continuous voltage sweep as in a). The linear fit (red line) has an intercept of $-2(2) \times 10^{-5}$ and gradient of $3.3(7) \times 10^{-6}$/V

and since $IR_1 + IR_2 = IR_3 + IR_4$,

$$V_2 = V_{in}\frac{R_2}{R_1 + R_2}$$
$$V_4 = V_{in}\frac{R_4}{R_3 + R_4}$$

Using the assumption that $R_1 + R_2 = R_3 + R_4$, then this becomes

$$V_2 - V_4 = V_{out} = V_{in}\frac{R_2 - R_4}{R_1 + R_2}$$

For a volume of material in the resistance bridge of width w, thickness t and length l, when the long axis of the transducer is along l it can be said that [134] that $\frac{\partial w}{w} = \frac{\partial t}{t} = -\frac{1}{2}\frac{\partial l}{l}$, in order to conserve volume. The corresponding change in resistance of the volume of material will then be $\partial R = \frac{\partial R}{dl}\partial l + \frac{\partial R}{\partial w}\partial w + \frac{\partial R}{\partial t}\partial t$. Substituting in the correct expressions for the partial differentials of R from the equation $R = \frac{\rho l}{wt}$ yields

$$\partial R = \frac{\rho}{wt}\partial l - \frac{\rho l}{w^2 t}\partial w - \frac{\rho l}{wt^2}\partial t.$$

dividing both sides of this equation by $R = \frac{\rho l}{wt}$ leaves

$$\frac{\partial R}{R} = \frac{\partial l}{l} - \frac{\partial w}{w} - \frac{\partial t}{t}$$

which in terms of $\frac{\partial l}{l}$ is

$$\frac{\partial R}{R} = \frac{\partial l}{l} + \frac{1}{2}\frac{\partial l}{l} + \frac{1}{2}\frac{\partial l}{l}$$

so to determine the strain ε_{xx}, along l:

$$\frac{\partial R}{R} = 2\frac{\partial l}{l} = 2\varepsilon_{xx}$$

If the strain is along w then $\frac{\partial w}{w} = \varepsilon_{xx}$ and the expression for $\frac{\partial R}{R} = -2\varepsilon_{xx}$

Bringing the change in resistance together with the strain applied to the resistance bridge, with R_1 and R_4 being under tensile strain, and R_2 and R_3 being under compressive strain gives:

$$\begin{aligned} R_1 &\to (1 + 2\varepsilon_{xx})R_1 \\ R_4 &\to (1 + 2\varepsilon_{xx})R_4 \\ R_2 &\to (1 - 2\varepsilon_{xx})R_2 \\ R_3 &\to (1 - 2\varepsilon_{xx})R_3 \end{aligned}$$

Finally, the expressions for the voltages of the strained bridge are:

$$\begin{aligned} V_2 - V_4 &= V_{in}\frac{(1 - 2\varepsilon_{xx})R_2 - (1 + 2\varepsilon_{xx})R_4}{(1 + 2\varepsilon_{xx})R_1 + (1 - 2\varepsilon_{xx})R_2} \\ V_2 - V_4 &= V_{out} = -2V_{in}\varepsilon_{xx} \end{aligned}$$

Which have been simplified since the initial resistances $R_1 = R_2 = R_3 = R_4$. Measurements of the different resistances in the bridge show that they are equal within 2 % of each other, so the assumption is justified. See table 2.3. This leaves

$$\varepsilon_{xx} = \frac{-V_{out}}{2V_{in}}$$

.

Table 2.3: Differences in resistance bridge resistances, relative to resistance R_1.

Resistance label	Difference (%)
R_2	-1.6
R_3	-1.5
R_4	0.1

$Fe_{81}Ga_{19}$ Hall Bar Strain Gauge

In addition to the $Ni_{80}Cr_{20}$ resistance bridge the $Fe_{81}Ga_{19}$ Hall bar itself was also used to measure the strain. The use of an $Fe_{81}Ga_{19}$ hall bar was confirmed as a reasonable measurement of the strain by measuring a Hall bar for which the current was applied along the same direction of the strain. An image of this device is shown in figure 2.6 (a). In this case the strain $\varepsilon = \frac{\delta R_{xx}}{2R_{xx}}$. Figure 2.8 shows that there is good agreement between the $Fe_{81}Ga_{19}$ and $Ni_{80}Cr_{20}$ strain measurements for much of the voltage range studied. The deviation at large negative voltages may be due to different properties of the two transducers used. Having established that considering only geometrical factors to determine the gauge factor of FeGa gives a reasonable estimate of the strain, a method to determine the strain in a Hall bar rotated 45 degrees from the axis of the uniaxial strain is now considered. The strain was also measured using the transverse resistance of the Hall bar shown in figure 2.7, which was used to investigate the magnetostrictive properties of $Fe_{81}Ga_{19}$. In this case the Hall bar was oriented in such a way that the current direction was at 45° to the strain axis. An image of this Hall bar is shown in figure 2.6 (b). The case for a Hall bar with current along a direction 45° to the strain axis is shown in figure 2.9.

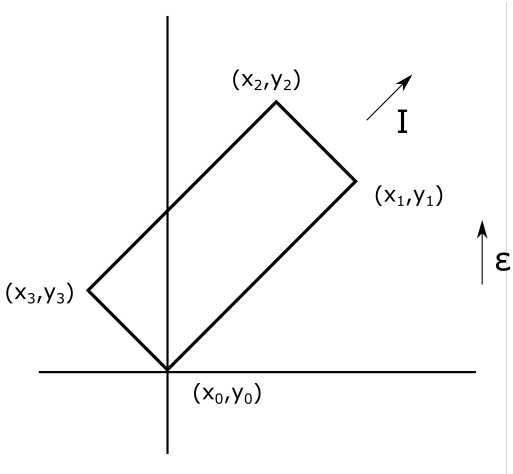

Figure 2.9: Schematic for determining the effect of a strain at 45°.

The strain along the x direction is defined as ε_{xx}, and strain along the y direction defined as $\varepsilon_{yy} = -\frac{\varepsilon_{xx}}{2}$, and along z, $\varepsilon_{zz} = \frac{-\varepsilon_{xx}}{2}$. Before any strain is induced in the system, the x and y coordinates can be written down in terms of the dimensions l and w.

$$
\begin{aligned}
x_1 &= l\cos 45^\circ & y_1 &= l\sin 45^\circ \\
x_2 &= l\cos 45^\circ w\cos 45^\circ & y_2 &= l\sin 45^\circ + w\sin 45^\circ \\
x_3 &= -w\cos 45^\circ & y_3 &= w\sin 45^\circ
\end{aligned}
$$

After the strain is applied, these coordinates become:

$$
\begin{aligned}
x_0' &= x_0 & y_0' &= y_0 \\
x_1' &= (1+\varepsilon_{xx})x_1 & y_1' &= (1-\frac{\varepsilon_{xx}}{2})y_1 \\
x_2' &= (1+\varepsilon_{xx})x_2 & y_2' &= (1-\frac{\varepsilon_{xx}}{2})y_2 \\
x_3' &= (1+\varepsilon_{xx})x_3 & y_3' &= (1-\frac{\varepsilon_{xx}}{2})y_3
\end{aligned}
$$

and

$$
\begin{aligned}
l' &= [(x_1'-x_0')^2 + (y_1'-y_0')^2]^{1/2} \\
&= [(x_1 - x_0 + \varepsilon_{xx}x_1)^2 + (y_1 - y_0 - \frac{\varepsilon_{xx}}{2}y_1)^2]^{1/2} \\
w' &= [x_3'^2 + y_3'^2]^{1/2} \\
t' &= (1-\frac{\varepsilon_{xx}}{2})t
\end{aligned}
$$

These changes in dimensions due to the strain can be equated with the changes

in resistance of the Hall bar.

$$R = \frac{\rho l}{wt} \qquad R' = \frac{\rho l'}{w't'}$$
$$\Delta R = \rho[\frac{l'}{w't'} - \frac{l}{wt}]$$
$$\frac{\Delta R}{R} = \frac{wt}{l}[\frac{l'}{w't'} - \frac{l}{wt}] = \frac{l'}{l}\frac{w}{w'}\frac{t}{t'} - 1$$

Solving these equations numerically yields

$$2\frac{\Delta R}{R} = \varepsilon_{xx} \tag{2.1}$$

The value of $\varepsilon_{xx} - \varepsilon_{yy}$ is often the quantity of interest, in which case it can be said that

$$\varepsilon_{xx} - \varepsilon_{yy} = \frac{3}{2}2\frac{\Delta R}{R} = 3\frac{\Delta R}{R} \tag{2.2}$$

2.3.4 Magneto-optical Kerr effect imaging equipment

System Description

In this thesis two types of MOKE measurement systems are used. Firstly a wide-field microscope capable of imaging with magnetic contrast along a particular axis (figure 2.10 (a)). Secondly a focussed laser MOKE system capable of resolving changes in direction of magnetisation in devices as narrow as 100 nm (figure 2.10 (b)).

The wide field microscope system used was that at beamline I06 at Diamond Light Source, and was based on a Zeiss Axio microscope. Strain-free lenses combined with a polariser and analyser allowed the magnetically sensitive imaging to be done, with a maximum spatial resolution of around 300 nm[207]. In-plane component of the magnetisation was of interest so it was necessary to have the light incident at an oblique angle. This was achieved by using an

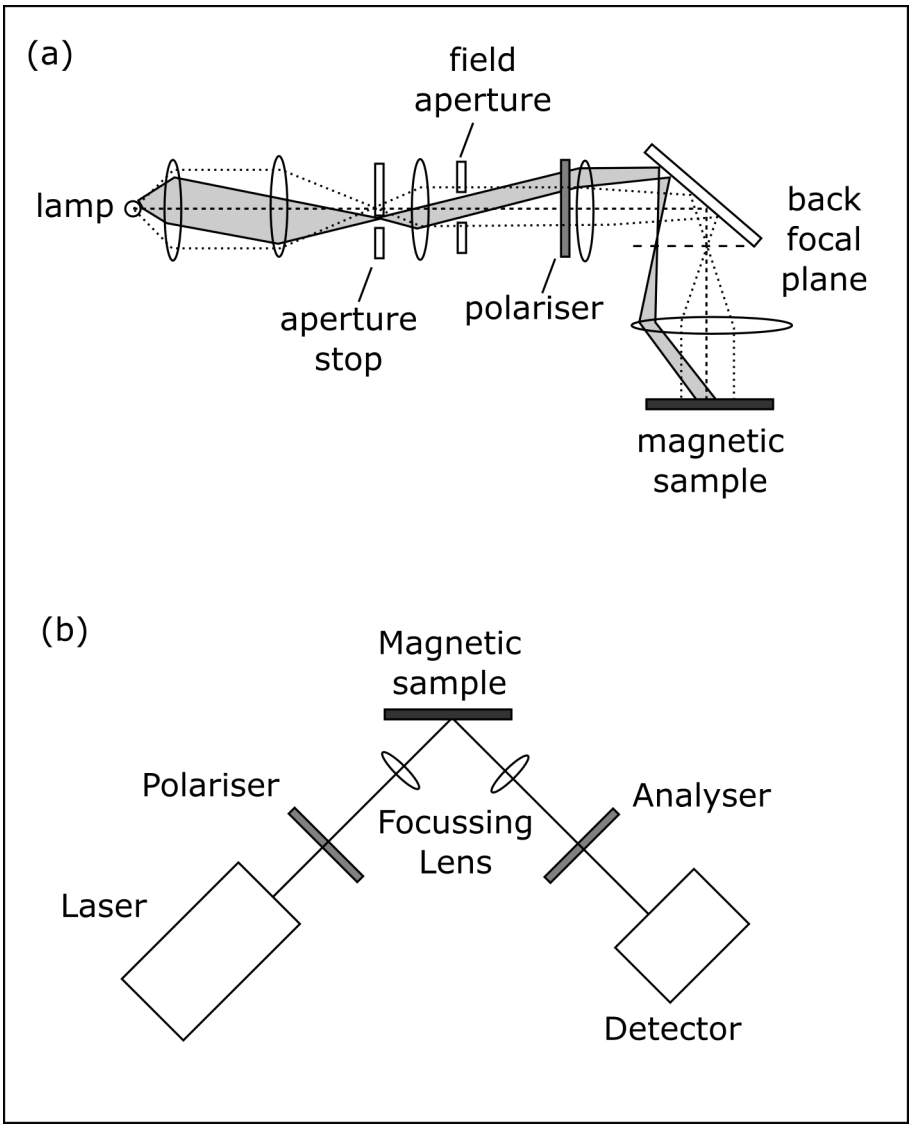

Figure 2.10: The types of MOKE measurement setup used in this thesis. (a) Wide field microscope configured for sensitivity to the in-plane component of magnetisation. The aperture stop is configured to block out the centre of the incident light beam to ensure that incident light arrives a the sample at an oblique angle. (b) Focussed laser MOKE system capable of focussing laser spot of size 4 µm onto the sample

aperture to block out the centre of the incident light beam, leaving only that at oblique angles.

The focussed MOKE equipment was used in the Department of Engineering at the University of Sheffield, under the guidance of Dr. Tom Hayward. In this system polarised laser light of wavelength 532 nm from a Coherent Verdi V-2 laser was focussed into a spot of around 4 µm onto the sample. Light reflected from the sample was passed through an analyser onto a detector. The analyser was set to close to extinction to allow only the Kerr signal through to the detector. In this set-up the intensity varies as the sin of the Kerr angle which maximises sensitivity. The sample was placed in the poles of a magnet capable of applying a field of approximately 100 mT, determined from a calibration table. The field can be driven at a frequency of up to 20 Hz. Either single shot measurements, sweeping the field from negative field to positive field and back again, or multiple averages were recorded via an Agilent Infinium 54832D oscilloscope.

Measurement Description

For the wide field microscope experiments in chapters 3 and 4 images were taken at voltages in the range −30 V to 50 V. The images taken were then processed using the ImageJ software package. A summary of the processing steps used in ImageJ is shown in figure 2.11. The whole stack of images from a field sweep was loaded into the software, in the order that they were taken. The first image in the sequence is that for a saturating field along a particular direction. This first, magnetically saturated, image was subtracted from all of the images in the stack to leave images representing the difference in magnetic contrast between each image and the saturated starting condition. Where information about the average magnetisation projection within a particular section of the magnetic material was required a region of interest (ROI) was defined in the software and applied to the whole stack. The average pixel intensity was then extracted and normalised. Since each image was associated with a particulary value of applied field, a M-H loop could be created for that

ROI.

For the focussed laser MOKE experiment in chapter 5, the laser spot was positioned at different points along a Co wire. The spot, approximately 4 µm in size, detected the magnetisation direction of the wire in this spot. By sweeping the magnetic field forwards and backwards with a frequency of 20 Hz up to 100 sweeps could be measured. The effect of induced uniaxial strain on the depinning behaviour of a domain wall in the wire was investigated.

2.3.5 X-Ray Magnetic Circular Dichroism Photo-emission electron Microscopy Equipment

System Description

XMCD-PEEM measurements were carried out at beamline I06 of the Diamond Light Source synchrotron. Electrons are generated in an electron gun then accelerated first by a linear accelerator, a booster synchrotron and finally the large storage ring. The storage ring is a many-sided polygon with straight sections joined by bending magnets which steer the electrons around the ring. As an electron passes through the bending magnet it emits radiation. On I06 X-ray photons are emitted from the storage ring to the beamlines using an insertion device called an undulator which forces the electron path to oscillate, producing x-rays. The undulator produces a narrow beam of bright light, the energy and polarisation of which is tunable by moving individual arrays of dipole magnets within the undulator. The I06 beamline at Diamond uses high intensity soft x-rays, with energies in the range 80 eV to 2 keV.

X-rays incident on the sample induce the emission of electrons in the manner described in chapter 1. Electrons leaving the sample are accelerated to 20 keV due to the potential difference between the sample and objective lens. The electrons pass through a set of transfer lenses and an energy analyser, which removes chromatic aberrations, before being imaged by a micro channel plate/CCD image intensifier. For greatest image intensity it is necessary

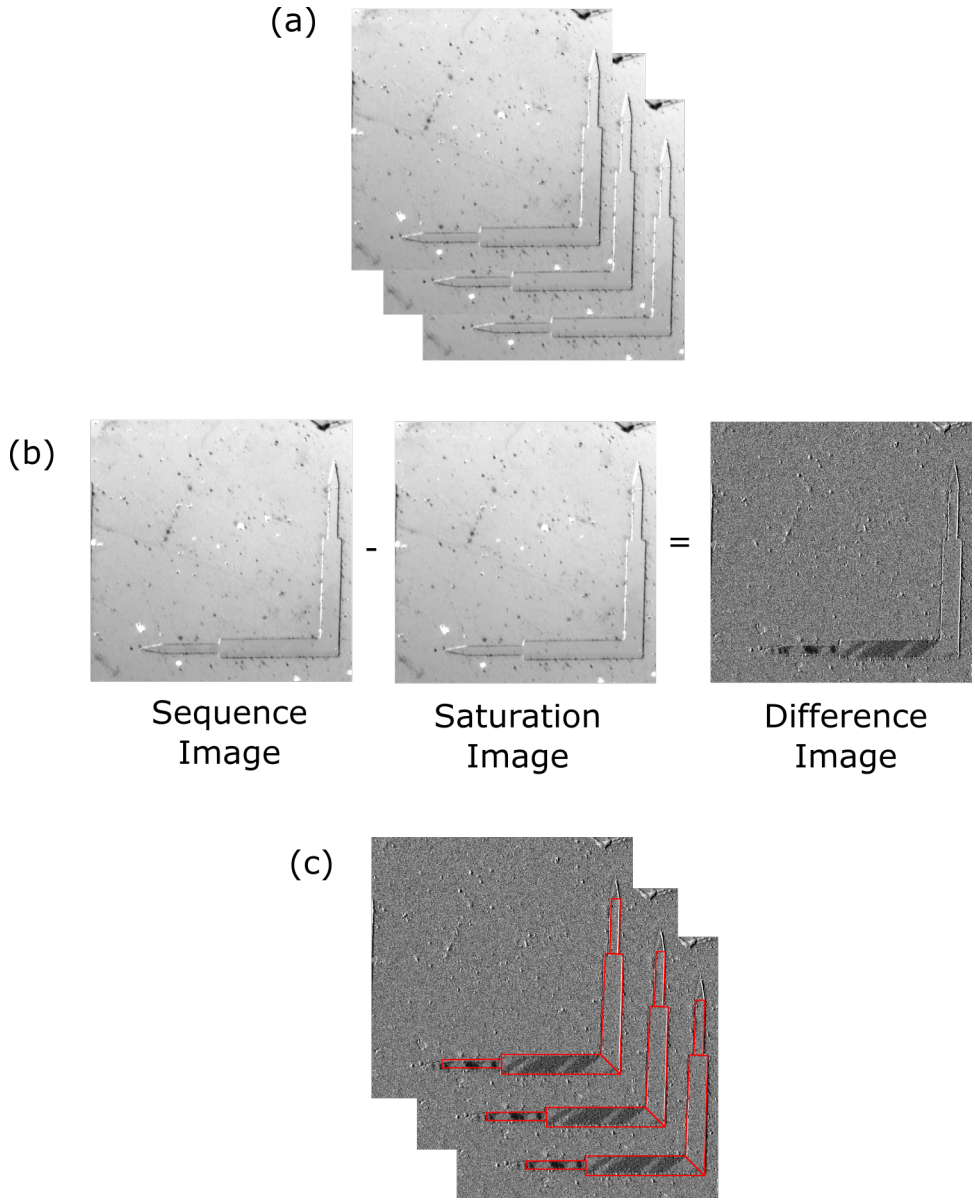

Figure 2.11: Steps used to process wide-field microscope MOKE images. (a) The whole stack of images from a field sweep was loaded into the software, in the order that they were taken. (b) The first image in the sequence is that for a saturating field along a particular direction. This first, magnetically saturated, image was subtracted from all of the images in the stack to leave images representing the difference in magnetic contrast between each image and the saturated starting condition. (c) Where information about the average magnetisation projection within a particular section of the magnetic material was required a region of interest (ROI) was defined in the software and applied to the whole stack. The average pixel intensity was then extracted and normalised. Since each image was associated with a particulary value of applied field, a M-H loop could be created for that ROI.

to maximise the peak in the secondary electrons by adjusting the accelerating voltage to ensure the peak in the secondary electrons is at 20 keV. The XMCD-PEEM system has a spatial resolution of 60 nm[208].

Measurement Description

To build up an image with magnetic contrast we then need to take images with both left- and right-circularly polarised light, taken with x-ray energies on the edge jump of the material in question. Since the background intensity could be different for different images it is also important to take images with x-ray energies off-edge, that is not on the L3 or L2 edge. It is possible to use either the L2 or the L3 edge to get contrast. In practice the edge which gives best contrast for a given material is used.

Intensities for the right circularly polarised (RCP) (+) and left circularly polarised LCP (-) x-rays of the L3 edge are given by

$$X_+ = \frac{I_{L3+}}{I_{\mathbf{pre-edge}}} \tag{2.3}$$

$$X_- = \frac{I_{L3-}}{I_{\mathbf{pre-edge}}} \tag{2.4}$$

where $I_{\mathbf{pre-edge}}$ is the off resonance energy.

The XMCD, D, and the related asymmetry, A, are given by

$$D = X_+ - X_- \tag{2.5}$$

$$A = \frac{X_+ - X_-}{X_+ + X_-} \tag{2.6}$$

.

In a measurement four images are taken: LCP on edge, off edge; RCP on edge off edge. Using Igor image processing software the image stacks are first drift corrected before the XMCD and asymmetry are found by performing equations 2.5, 2.6 on the images. The contrast in the XMCD image will be

proportional to the angle of incidence of the beam of electrons. From this contrast the greyscale images can be interpreted magnetisation directions.

2.3.6 SQUID

The magnetometry measurements described in this thesis were carried out with a commercially available Quantum Design MPMS-X super-conducting quantum interference device (SQUID) magnetometer. Using the reciprocating sample measurement option the system has a sensitivity of up to 1×10^{-12} A/m. A schematic of the SQUID system used is shown in figure 2.12 (a). The current passed through the weak link in the Josephson junction in a SQUID is proportional to the magnetic flux through a search coil connected to the junction[209] (see figure 2.12 (b)). When a sample is moved through the detection coils the magnetic moment causes a change in the magnetic flux through the pickup coil. The corresponding change in current can be seen as a series of interference fringes. It is possible to count these to measure the change in magnetic flux, or to use a feedback system to compensate for the external field and lock the system onto one of the fringes. The feedback voltage is then proportional to the magnetic flux. It is this second method that is used in the MPMS. Shielding from external magnetic fields is important to improve the sensitivity of the device. This field protection is achieved by placing the SQUID in a region of a small, constant magnetic field enclosed by a superconducting shield. The pickup coils are also arranged as a second-order gradiometer. These efforts combine to make the SQUID highly insensitive to magnetic noise. The MDMS system is routinely calibrated using a Pd reference sample provided by the manufacturer.

The super conducting quantum interference device (SQUID) magnetometry measurements described in this thesis were carried out by Dr. Andrew Rushforth. For measurements the sample is mounted in a drinking straw. A stepper motor moves this straw, connected to the end of a sample rod, along the axis of the gradiometer. The SQUID feedback voltage is measured as a function of the position of the sample within the gradiometer. Fitting to this spatial

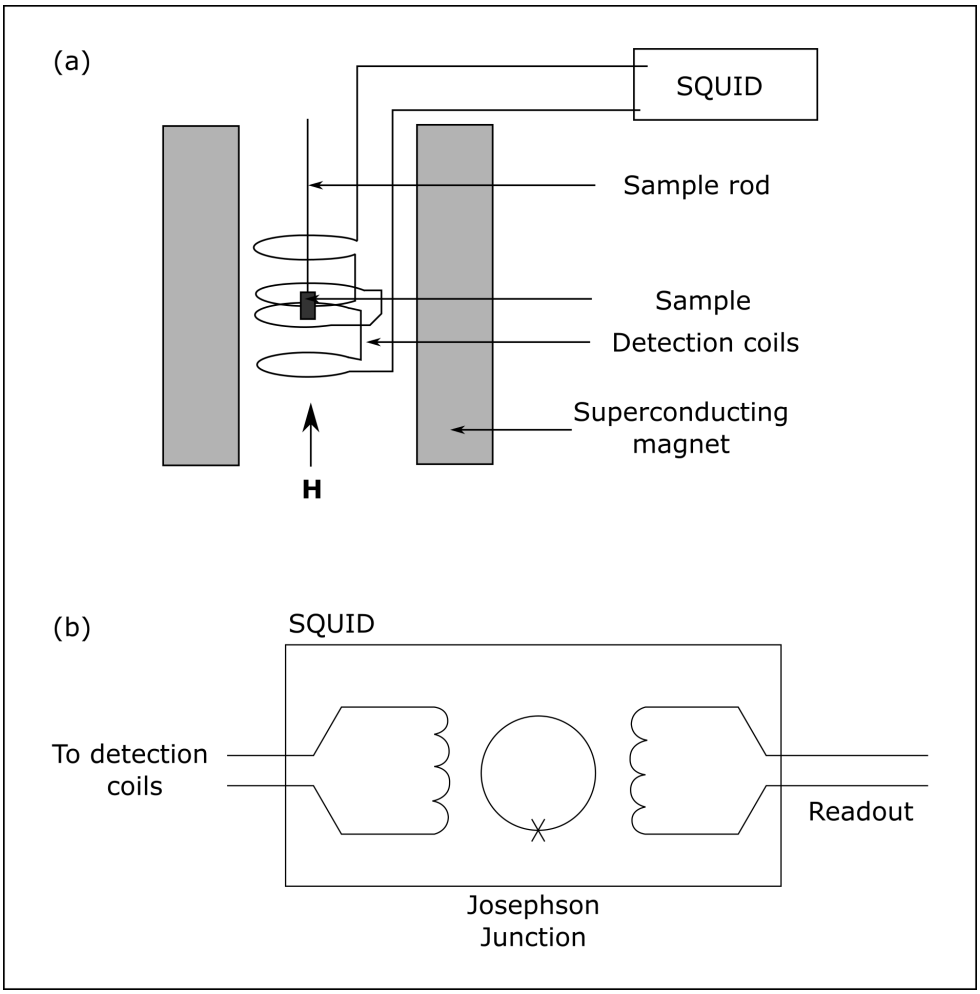

Figure 2.12: Schematic of (a) SQUID system and (b) SQUID. When a sample is moved through the detection coils the magnetic moment causes a change in the magnetic flux through the pickup coil. The corresponding change in current can be seen as a series of interference fringes. A feedback system is used to compensate for the external field and lock the system onto one of the fringes. The feedback voltage is then proportional to the magnetic flux.

dependence by the Quantum Design software gives the projection along the measurement direction of the magnetic moment of the sample.

M vs H loops were carried out using the SQUID at constant temperature. Sweeping the field from large positive, to large negative and back to large positive for a range of applied field directions gives a complete set of M vs H loops at a given temperature. An example of the hysteresis loops obtained from the SQUID is shown in figure 2.13 (a). M vs H loops measured in this way will generally have a diamagnetic background. This can be removed by fitting to the regions above the saturation magnetisation. Anisotropy constants were extracted from the magnetometry data using the method described in ref [210], which uses coefficients determined from the magnetic energy of an isolated in-plane magnetic domain. In the single domain approximation the energy density of the magnetic sample can be written as

$$E = -K_C \sin^2(2\theta)/4 + K_U \sin^2(\theta) - MH\cos(\phi - \theta) \tag{2.7}$$

where K_C and K_U are the lowest order biaxial and uniaxial anisotropy constants, H is the external magnetic field, M the magnetisation, and θ and ϕ are, respectively, the angle of M and H to the $[1\bar{1}0]$ direction. By looking at the case with zero applied field (i.e. $H = 0$) equation 2.7 it is possible to determine the remnant magnetisation direction. In this case the derivative of the energy density with respect to angle can be written

$$\frac{\partial E}{\partial \theta} = K_U \sin 2\theta - K_C \sin 2\theta \cos 2\theta \tag{2.8}$$

which when equated to zero, gives an expression for the remenant magnetisation direction:

$$\theta = \frac{1}{2}\arccos\left(\frac{-K_u}{K_c}\right) \tag{2.9}$$

The magnetic free energy density equation can also be used to determine the anisotropy fields from magnetic field sweeps along a particular direction. An example of hysteresis loops used to obtain anisotropy fields is shown in figure 2.13 (b). Starting with the case of $\phi = 90°$, the first and second derivatives

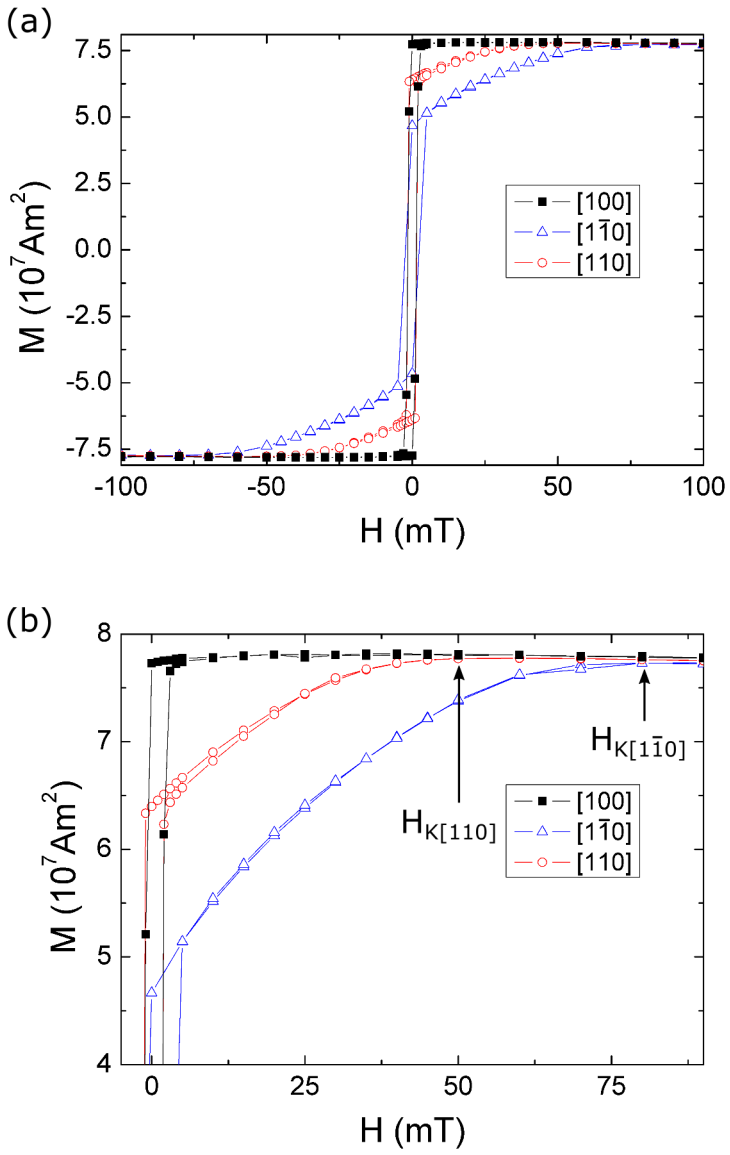

Figure 2.13: (a) Examples of M-H loops from SQUID data. (b) Zoomed in region of (a) showing anisotropy fields $H_{K,[110]}$ and $H_{K,[1\bar{1}0]}$ extracted from loops.

of equation (2.7) are:

$$\frac{\partial E}{\partial \theta} = K_U \sin 2\theta + K_C \sin 2\theta \cos 2\theta - M_s H \cos\theta \tag{2.10a}$$

$$\frac{\partial^2 E}{\partial \theta^2} = 2K_U \cos 2\theta + 2K_C \cos 4\theta + M_s H \sin\theta \tag{2.10b}$$

There is a minimum energy density when the first derivative is equal to zero, and the second derivative is greater than zero. The magnetisation along the [110] direction is then

$$M_{[110]} = M_s \ for \ H > |2K_C - 2K_U|/M_S \tag{2.11a}$$

$$M_{[110]} = M_s \sin\theta \ for \ H < |2K_C - 2K_U|/M_S \tag{2.11b}$$

So the anisotropy field along the [110] direction is:

$$H_{K,[110]} = \frac{2(K_U - K_C)}{M_s} \tag{2.12}$$

Treating the case for $\phi = 0°$ first and second derivatives to the magnetic free energy density of

$$\frac{\partial E}{\partial \theta} = K_U \sin 2\theta + K_C \sin 2\theta \cos 2\theta + M_s H \sin\theta \tag{2.13a}$$

$$\frac{\partial^2 E}{\partial \theta^2} = 2K_U \cos 2\theta + 2K_C \cos 4\theta + M_s H \cos\theta \tag{2.13b}$$

There is a minimum energy density when the first derivative is equal to zero, and the second derivative is greater than zero. The magnetisation along the $[1\bar{1}0]$ direction is then

$$M_{[1\bar{1}0]} = M_s \ for \ H > |2K_C + 2K_U|/M_S \tag{2.14a}$$

$$M_{[1\bar{1}0]} = M_s \cos\theta \ for \ H < |2K_C + 2K_U|/M_S \tag{2.14b}$$

So the anisotropy field along the $[1\bar{1}0]$ direction is:

$$H_{K,[1\bar{1}0]} = \frac{2(K_U + K_C)}{M_s} \tag{2.15}$$

2.3.7 X-ray Diffraction

System Description

X-ray diffraction (XRD) is a technique useful for non-destructively determining the structural properties of a crystal. X-ray diffraction relies on the Bragg condition for maximising the intensity of a diffracted beam at a particular angle [211]

$$n\lambda = 2d\sin\theta \tag{2.16}$$

where the integer n is the order of the diffraction, λ is the X-ray wavelength, d is the interplanar spacing, and θ is the angle of incidence of the x-rays. The diffraction of a plane wave off successive plane of a crystal structure is shown in figure 2.14.

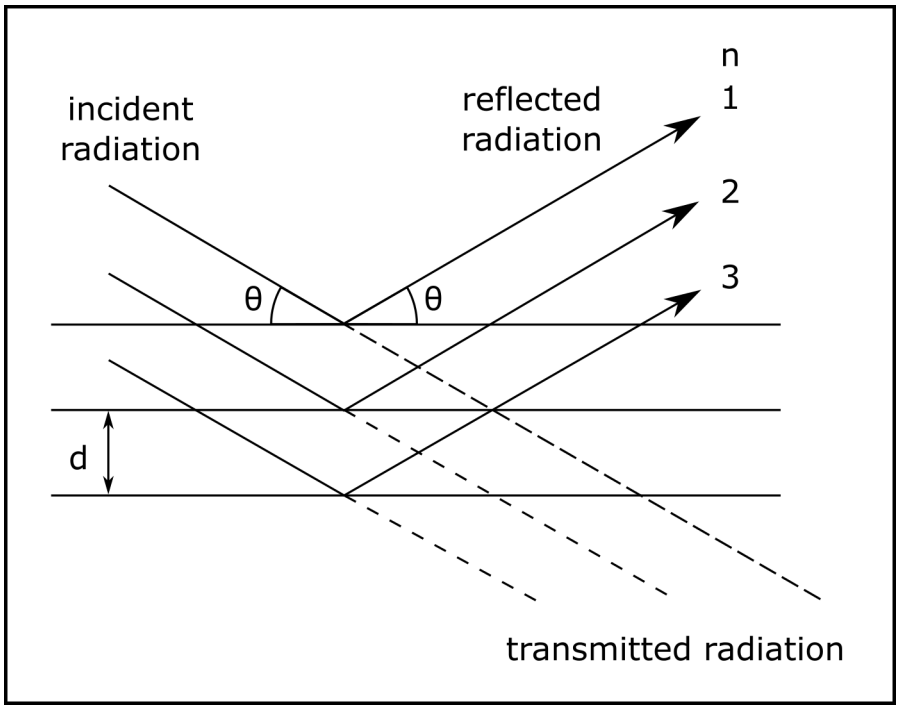

Figure 2.14: Bragg diffraction (of order n) of x-rays by the planes in a crystal. The x-rays are incident at angle θ onto planes separated by a length d.

X-ray diffraction measurements described in this thesis were made using a

Phillips Panalytical X'Pert Materials Research Diffractometer (MRD) by Dr Peter Wadley, using the CuK_α wavelength of 0.154 nm [211]. A schematic of the XRD setup is shown in figure 2.15. The x-ray beam is passed through a beam conditioner which act to collimate and monochromate the beam, as well as limit the spatial width of the beam. The sample is mounted on a stage capable of adjustment of x, y, z and ϕ (rotation about about an axis perpendicular to the plane of the sample), ψ (tilt - rotation about an axis lying in the plane of the sample). The X-ray source is at a fixed angle ω (the angle between the incident beam and the sample surface), and the detector at an angle 2θ between the incident beam and diffracted beam. The angular resolutions achievable in the X'Pert system are: 0.01° for tilt (ψ) and rotation (ϕ), and 0.0003° for ω and 2θ.

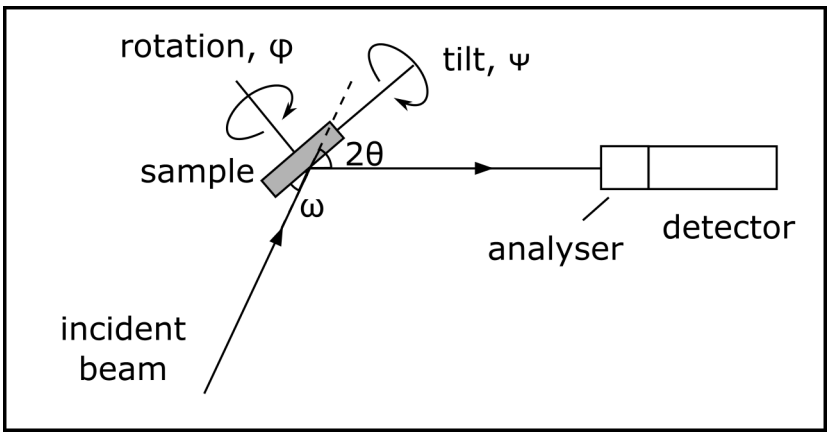

Figure 2.15: XRD measurement configuration. The x-ray beam is passed through a beam conditioner which acts to collimate and monochromate the beam, as well as limit the spatial width of the beam. The sample is mounted on a stage capable of adjustment of x, y, z and ϕ (rotation about about an axis perpendicular to the plane of the sample), ψ (tilt - rotation about an axis lying in the plane of the sample). The X-ray source is at an angle ω (the angle between the incident beam and the sample surface), and the detector at an angle 2θ between the incident beam and diffracted beam.

Measurement Description

In this thesis three scans were used to determine properties of thin films used: $2\theta - \omega$, ω or rocking scan, and ϕ scan. The $2\theta - \omega$ involves both the incident beam angle ω and the detector angle 2θ being coupled and simultaneously rotated, which gives information about the out of plane lattice parameter of the thin film and substrate. The out-of-plane lattice parameter is given by the Bragg relation, equation 2.16. From the full width at half maximum (FWHM) of the peak it is possible to determine the thickness of the film, using the Scherrer formula [211]

$$FWHM = \frac{0.9\lambda}{t \cos\theta_B} \tag{2.17}$$

where the FWHM is expressed in radians, λ is the x-ray wavelength, t is the layer thickness, and θ_B is the Bragg angle of the reflection. X-ray diffraction of films with a finite number of atomic planes may also show Laue oscillations on either side of the principal peak [212]. Laue oscillations can be seen on either side of the peak between 62° and 63° in figure 2.16, taken from XRD data presented in chapter 3. The separation of these oscillations is a measure of the number of coherently scattering atomic planes. Information can be manually extracted from the $2\theta - \omega$ scan, or done more accurately by fitting the diffraction curve using the Panalytical Epitaxy software. An ω scan, or rocking curve, gives information about defects or mosaicity in the sample as the diffraction planes of individual mosaic blocks will match the Bragg condition 2.16 at different angles. In an ω scan the incident beam rotated ("rocked") through the Bragg angle θ_B while the detector is held at a fixed angle 2θ. The width of such a rocking curve is then a direct measure of the range of orientations present in the crystal. Each subgrain of a mosaic crystal successively satisfies the Bragg condition. In a ϕ scan the detector 2θ and incident beam ω angles are fixed on a Bragg peak as ϕ is rotated. The measured intensity in such a scan is proportional to the number of grains in the film that have their normal to the crystal planes picked out by that Bragg peak. A random orientation of grains in a thin film will result in a featureless

ϕ scan, whereas a scan of an epitaxial thin film will be characterised by a small number of discrete peaks, four in the case of a cubic crystal.

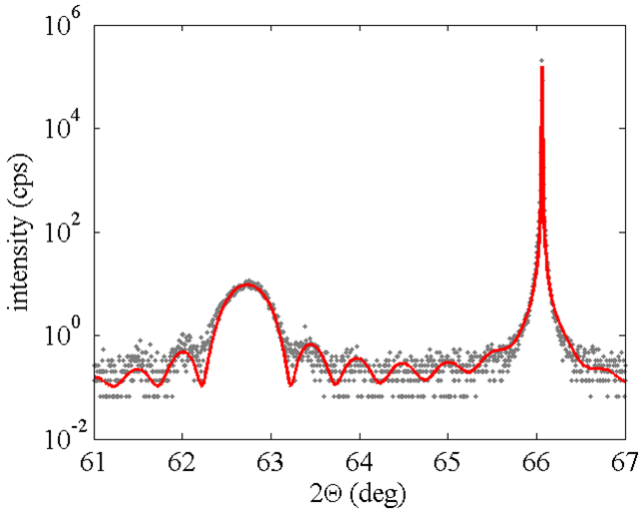

Figure 2.16: Example of Laue oscillations on either side of the peak in XRD 2ω scan between 62° and 63°

2.3.8 X-ray Reflectivity

Similar in concept to x-ray diffraction is x-ray reflectivity (XRR) in that it is a non-destructive, non-contact technique for determination of film properties [213]. XRR is relevant to this thesis as it was the technique used by others to calibrate the growth rates of the MBE and sputter systems described in section 2.1.1. XRR is capable of determining the thickness of films in the range 1 nm to 200 nm with a precision of around 0.1 nm to 0.3 nm [213].

In XRR the intensity of the reflected beam of x-rays incident on a sample is measured as a function of incident angle. A schematic of an XRR measurement are shown in figure 2.17. The sample is initially aligned such that it cuts the incident x-ray beam in half, with the sample surface and incident beam being essentially parallel. Total internal reflection occurs for incident angles ω below the critical angle ω_c. Typical incident angles are in the range 0.25° to 3°. When ω is above ω_c the reflections from the different interfaces

in the sample interfere and gives rise to interference fringes. The thickness of each layer determines the period of the interference fringes. Surface and interface roughness result in diffuse scattering which gives rise to a more rapidly reduced intensity with increasing reflected angle. An equation for the layer thickness is given in reference [214]:

$$m\lambda = 2D\sqrt{\sin^2\omega_i - \sin^2\omega_c} \tag{2.18}$$

where m is the order of the reflected fringe, ω_c is the critical angle, ω_i is the angle at which the fringe appears, and D is the layer thickness. In this thesis, however, the thickness was determined using the software XPert Reflectivity (Version 1.1) from PANalytical which allows different layers including the substrate, growth and capping layers to be simulated.

2.3.9 Micromagnetic Calculations

Software Description

Micromagnetic calculations allow the behaviour of device geometries for different materials under a range of conditions to be modelled. By solving the magnetic equation of motion, the Landau-Lifshitz-Gilbert (LLG) equation (equation (1.31)), for given initial anisotropy conditions we can determine the ground state configuration, or see how the system will evolve with time. More details of micromagnetism are given in chapter 1.

There are two key problems in the evaluation of magnetic behaviour using micromagnetism. The first is to accurately approximate the effective magnetic field, H_{eff} and the second is to evaluate the time evolution of the LLG equation (see equation (1.31)) [215]. The effective field can be found from the derivative of the free energy terms given in equation 1.19 [216]. The anisotropy, exchange and magnetostatic energy terms in this equation must be accounted for in a micromagnetic calculation, and form the basis of the micromagnetic equations.

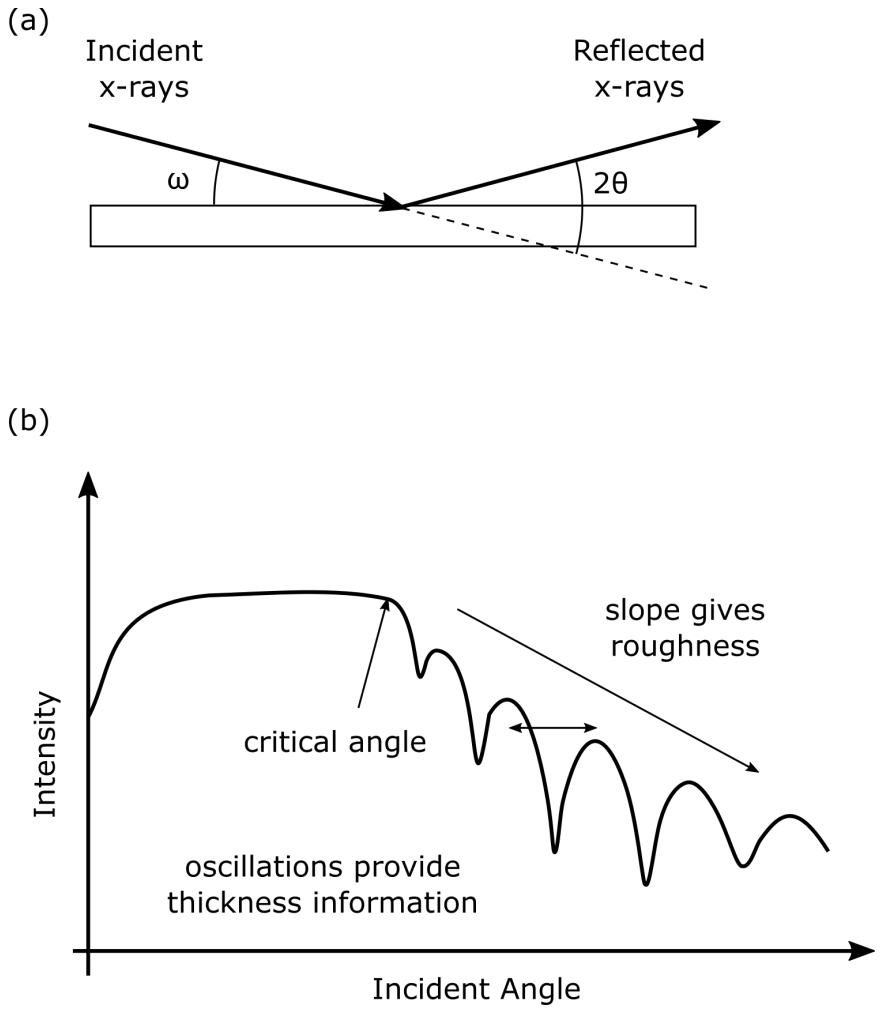

Figure 2.17: (a) X-ray reflectivity scan orientation (b) Sketch of x-ray reflectivity trace. Total internal reflection occurs for incident angles ω below the critical angle. The thickness of each layer in a sample determines the period of the interference fringes. Surface and interface roughness result in diffuse scattering which gives rise to a more rapidly reduced intensity with increasing reflected angle.

To calculate the effective field and solve the LLG equation (equation (1.31)) the continuum interpretation of time and space must be discretised [215]. A common approach to the discretisation of the problem is the finite difference (FD) method in which the continuum is replaced by a set of discrete regions. A comprehensive review of finite difference methods in micromagnetism is given in reference [217].

In the FD model the partial derivatives of a function $u(\mathbf{r}, t)$ are approximated by finite differences Δx, Δy, Δz, and Δt such that

$$u(x + \Delta x, y, z, t) = u(x, y, z, t) + \Delta x \frac{\partial u}{\partial x}(x, y, z, t) \\ \frac{(\Delta x)^2}{2} \frac{\partial^2 u}{\partial x^2}(x, y, z, t) + \ldots \tag{2.19}$$

The partial derivatives in the LLG equation (equation (1.31)) replaced by the appropriate FD approximations which can then be solved using an iterative numerical process to obtain an approximate solution. In micromagnetic FD solutions, the calculation region is divided into equally sized cubes or cuboids of volume $V_i = \Delta x \times \Delta y \times \Delta z$, with magnetic moment $M_i = M_s V_i$. The time evolution of $\mathbf{M}$ is found by integrating equation (1.31) for each computational cell.

In this thesis the Object Oriented Micromagnetic Framework (OOMMF) is used which discretises the calculation region and iteratively solves the LLG equation. The anisotropy energy and Zeeman energy terms can both be evaluated relatively easily as they are both local in nature, and can be calculated individually for each cell. The exchange and magnetostatic energies are more difficult to determine [215, 216, 217]. In OOMMF, the exchange energy is approximated using a 6 nearest neighbour interaction [218, 219]:

$$E_i = \sum_{j \in N_i} A \frac{\mathbf{m}_i \cdot (\mathbf{m}_i - \mathbf{m}_j)}{\Delta_{ij}^2} \tag{2.20}$$

where N_i is the set of the six cells nearest to cell i, A is the exchange stiffness and Δ is the descretisation step size between cells i and j. The magnetostatic

energy in OOMMF is computed using the methods described in [220, 221] and a fast fourier transform convolution [218].

Calculation Description

OOMMF uses 'evolvers' to coordinate the solving of the LLG equation and update the magnetisation configuration from one discretised time step to the next. It is into the evolver functions that the Gilbert damping parameter, α is set, along with the timestep to be used along with other parameters. OOMMF offers evolvers using a first order Euler method, or a Runge-Kutta method [218]. The overall coordination of the micromagnetic simulation carried out by OOMMF is done by 'drivers'. It is into the driver function that parameters such as mesh size, initial magnetisation configuration and stopping criteria are entered. The stopping criteria specifies the point at which a stage in the simulation should be considered complete. Possible options for stopping criteria include 'stopping_dm_dt' which specifies a threshold in the maximum $|d\mathbf{m}/dt|$, the 'stopping_time' which simply sets a maximum time limit for the simulation, or 'stage_iteration_limit', which sets the maximum number of iterations for a particular stage. It is the 'stopping_dm_dt' stopping parameter that is used in OOMMF simulations in this thesis. For quasistatic simulations a stopping_dm_dt in the range $0.01\,^{\circ}$/ns to $1.0\,^{\circ}$/ns is reasonable[222]. Other evolver and driver parameters used in the OOMMF calculations presented in this thesis are specified in the relevant chapters. A summary of micromagnetic parameters for some materials, including those used in this thesis are shown in table 2.4.

Calculations were initialised using an image to set the initial magnetisation conditions. Simulation parameters were input via the OOMMF problem file which included values for the cubic and uniaxial magnetocrystalline anisotropies, saturation magnetisation and exchange constant. For some calculations further automation was done using a python script to pass the output (.omf) file of one simulation into the input of a following one. Calculations requiring long simulation times were carried out using the Nottingham

Table 2.4: Summary of some micromagnetic parameters. Gilbert damping (α), Exchange stiffness (A), saturation magnetisation, and exchange length ($l_{ex} = \sqrt{2A/\mu_0 M_S^2}$).

Material	α	A (1×10^{-11} J/m)	M_S (MA/m)	l_{ex} (nm)
$Fe_{81}Ga_{19}$	0.017[223]	1.3[224]	1.386	3.3
Fe	0.002[198]	2.1[222]	1.712[193]	3.5
Ni	0.043[199]	0.9[222]	0.49[193]	7.7
Co	0.008[225]	1.9[226]	1.431[193]	3.8

High Performance Computer cluster (HPC). OOMMF outputs both scalar and vector data which can be further processed and analysed. Vector maps of magnetisation and stray field as well as other quantities can be made. Scalar data output includes energy densities of the different contributions to the total energy as well as the aggregate magnetisation in the simulated region.

Chapter 3

The Magnetic, Electrical and Structural Properties of Epitaxial $Fe_{81}Ga_{19}$ Thin Films.

3.1 Introduction

This chapter describes the investigations of the structural, electrical and magnetic properties of epitaxial MBE-grown $Fe_{81}Ga_{19}$ films. The investigations demonstrate how a high quality, MBE-grown thin film of $Fe_{81}Ga_{19}$ has magnetostrictive properties comparable to the best so far reported for bulk material. It is also shown that this highly magnetostrictive behaviour, combined with biaxial magnetocrystalline anisotropy, can be utilised to demonstrate reversible, non-volatile switching of magnetisation using only induced strain, in the absence of an externally applied magnetic field.

The study begins by characterising the crystal and magnetic properties of the layer. The AMR is measured at the measurement temperature to be used as a tool for determining the magnetisation direction. Using a PZT piezoelectric transducer uniaxial strain is induced in the $Fe_{81}Ga_{19}$ layer to demonstrate control of the magnetic easy axis in the absence of an external field.

Magnetotransport measurements reveal that the high-quality, MBE-grown sample has magnetostrictive properties comparable with the best observed in bulk $Fe_{(1-x)}Ga_x$. The samples used in this chapter are from wafer Mn635, a 21.0(2) nm layer of $Fe_{81}Ga_{19}$ grown by MBE onto a GaAs(001) substrate. Devices were patterned into Hall bars 45 µm across, as described in chapter 2.

3.2 Characterisation of Mn635

3.2.1 X-ray Diffraction

The first stage of characterisation of wafer Mn635 was X-ray diffraction to determine the out-of-plane lattice parameter of the crystal. X-ray measurements were carried out by Dr. Pete Wadley. The $2\theta - \omega$ scan in figure 3.1 clearly shows two peaks: a strong, narrow one for the GaAs substrate and a weaker broader peak for the $Fe_{81}Ga_{19}$ layer. The presence of a single peak indicates that the film is crystalline with a single lattice parameter in the growth direction. The $2\theta - \omega$ scan was fitted by standard XRD software using a model of a single crystal layer on a semi-infinite substrate, which indicated a lattice parameter along the growth direction of $a_\perp = 0.296\,07(3)$ nm, and a layer thickness of $t = 21.0(2)$ nm. The lattice parameter corresponds to a lattice mismatch of $\frac{a_\perp - a_0}{a_0} = 4.6\,\%$, where $a_0 = 0.283$ nm corresponds to half of the GaAs substrate lattice parameter. Also important in this thesis is the relaxed, bulk, $Fe_{81}Ga_{19}$ lattice parameter, a reference value [227] for which is $a_{Bulk} = 0.287$ nm. With Poisson ratio ν it can be written that:

$$\frac{a_{bulk} - a_0}{a_{bulk}} = \nu \frac{a_\perp - a_{bulk}}{a_{bulk}} \tag{3.1}$$

which means that the expected out-of-plane lattice parameter of the $Fe_{81}Ga_{19}$ would be:

$$a_\perp = a_{bulk} + \frac{1}{\nu}(a_{bulk} - a_0) = 0.296(2)\,\text{nm} \tag{3.2}$$

where the value $\nu = 0.45(5)$ for $Fe_{81}Ga_{19}$ was taken from reference [228]. This reference value of $a_\perp$ is within the uncertainty of that measured for the $Fe_{81}Ga_{19}$ layer used in this study, so one can be confident that the measured value is reasonable.

The four-fold symmetry shown in the ϕ scan shown in the inset of figure 3.1 confirms the epitaxial relationship between the $Fe_{81}Ga_{19}$ film and the substrate [229]. In addition to reflection high-energy electron diffraction (RHEED) measurements observed during growth, the single-crystal nature of the mean crystal structure was confirmed by the sharp majority component in the ω scan, also shown as an inset in figure 3.1.

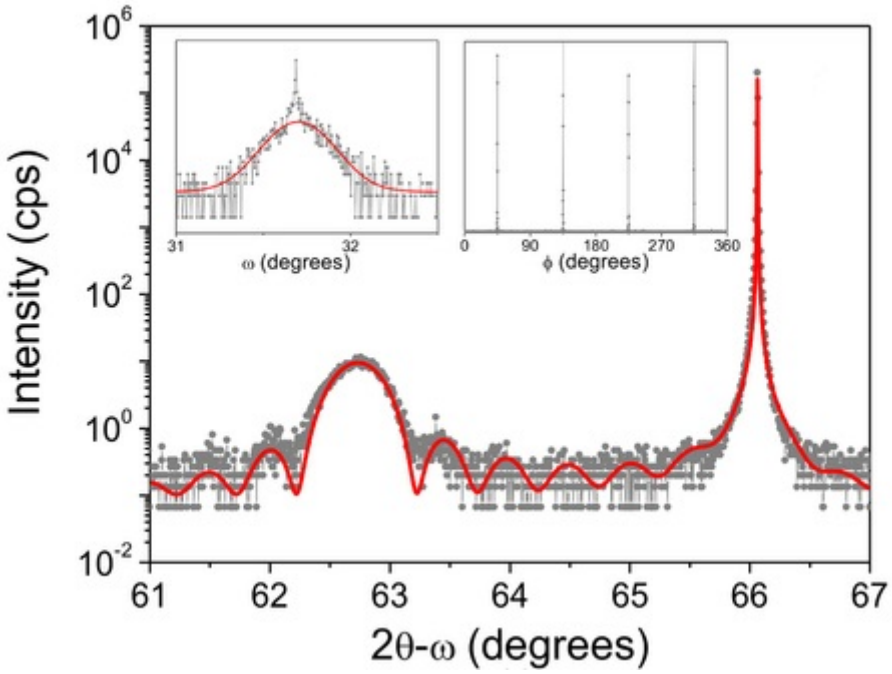

Figure 3.1: XRD scans along with fitted curves (red). The main figure shows X-ray diffraction $2\theta-\omega$ scan of the $Fe_{81}Ga_{19}$ film on a GaAs substrate showing the sharp reflection from the GaAs substrate at around 66° and the $Fe_{81}Ga_{19}$ layer peak at around 62.75°. The central sharp peak of the inset ω scan is indicative of a film with few defects and little mosaicity. The four vertical lines of the inset ϕ scan confirm the epitaxial relationship between the $Fe_{81}Ga_{19}$ film and the substrate. Measured by Dr Pete Wadley.

3.2.2 SQUID Magnetometry

The magnetic anisotropy was characterised using SQUID magnetometry carried out by Dr. Andrew Rushforth at 300 K. Figure 3.2 shows SQUID magnetometry field sweeps along an easy axis [100] and two hard axes [110] and $[1\bar{1}0]$. Using the method described in section 2.3.6 the magnetic anisotropies were found to be $K_c = 32.7\,\mathrm{kJ/m}$ favouring the [100]/[010] direction, and $K_u = 8.6\,\mathrm{kJ/m}$ favouring the [110] direction. Using equation (2.9) the easy axes were found to be rotated from [100]/[010] by 7°. This was confirmed to be in agreement with the SQUID data by considering the remenant magnetisation projection along the [110] and $[1\bar{1}0]$ directions, which were $6.40(5) \times 10^{-4}\,\mathrm{A\,m^2}$ and $4.7(50) \times 10^{-4}\,\mathrm{A\,m^2}$ respectively and give an offset angle from the [100] direction of $\theta = 9(3)°$. SQUID magnetometry in combination with thickness measurements from x-ray diffraction, was also used to determine the saturation magnetisation of the film, which was found to be $1.4(1)\,\mathrm{MA/m}$, from the sample volume of $5.57(2) \times 10^{-13}\,\mathrm{m^3}$. This confirmed the composition to be $x = 0.188(4)$.

3.2.3 Measurement of AMR in $Fe_{81}Ga_{19}$

In this study the AMR is used to determine the magnetisation direction from magnetotransport measurements. A full systematic study of the AMR in $Fe_{81}Ga_{19}$, whilst potentially an interesting topic of research, was not the intention, and is beyond the scope of the current study.

The Hall bar sample (described in section 2.3.1) was placed in a magnetic field, such that the magnetic field was in the plane of the sample. A saturating magnetic field of 0.5 T was rotated in the plane of the sample through a range of 200° whilst the transverse and longitudinal voltages were measured. The results of these measurements are shown in figure 3.3, along with statistical fits to the curves, and the associated residuals are shown in figure.

The experimental data was fitted to both second and fourth order equations

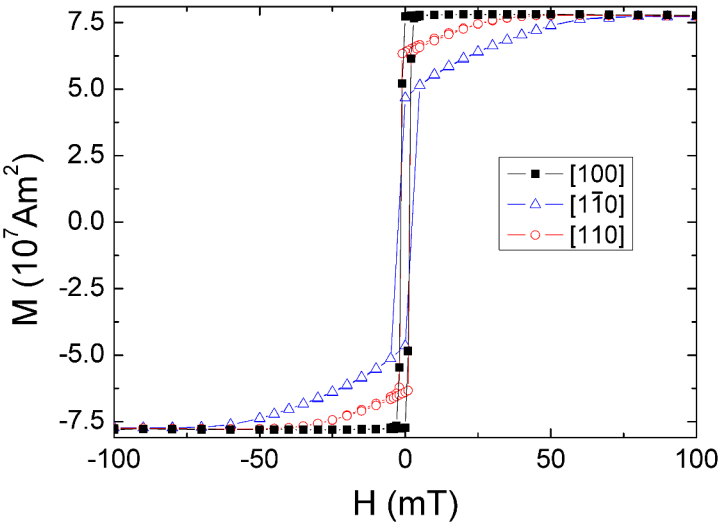

Figure 3.2: SQUID magnetometry magnetic hysteresis loops of the unprocessed $Fe_{81}Ga_{19}$ sample measured at 300 K for field applied along [100] (black), [1$\bar{1}$0] (blue), and [110] (red) directions. Measured by Dr. Andrew Rushforth.

for ρ_{xx}:

$$\rho_{xx} = \rho_{xx,0} + A\sin 2\theta \tag{3.3a}$$

$$\rho_{xx} = \rho_{xx,0} + A\sin 2\theta + B\sin 4\theta \tag{3.3b}$$

and ρ_{xy}:

$$\rho_{xy} = \rho_{xy,0} + C\cos 2\theta \tag{3.4a}$$

$$\rho_{xy} = \rho_{xy,0} + C\cos 2\theta + D\cos 4\theta \tag{3.4b}$$

where θ is the magnetisation direction with respect to current direction. A summary of the fitting parameters used is given in table 3.1.

The inclusion of a fourth order term does improve the fit to the data although examination of the coefficients and residuals (figure 3.3) reveal that this term is small relative to the second order term (0.8 % and 7.5 % for ρ_{xx} and ρ_{xy} respectively)and the value of the coefficient of the second order term changes

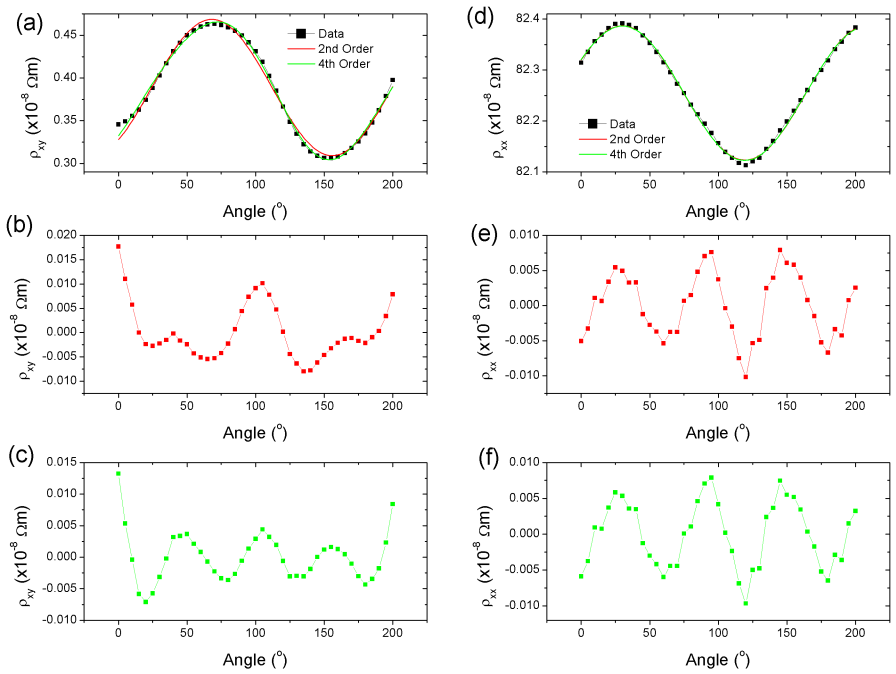

Figure 3.3: Transverse (a) and longitudinal (d) resistivity measured as a function of angle for a magnetic field of 0.5 T applied in the plane of the $Fe_{81}Ga_{19}$ film, along with statistical fits to second and fourth order phenomenological expressions for the change in resistivity. Also shown are the residuals from the second order fit for ρ_{xy} (b) and ρ_{xx} (e), and the residuals for the fourth order fit for ρ_{xy} (c) and ρ_{xx} (f).

Table 3.1: Summary of fitting parameters used to fit experimental ρ_{xx} and ρ_{xy} data to equations (3.4) and (3.3) respectively. Also shown is the R^2 value indicating the closeness of the sum-of-squares fitting in each case.

ρ	Fit Order	(μΩ cm)	(μΩ cm)	(μΩ cm)	R^2
		$\rho_{xx,0}$	A	B	
xx	2	82.2550(8)	0.1329(1)	-	0.9974
	4	82.2551(9)	−0.132(1)	$1(1) \times 10^{-3}$	0.9973
		$\rho_{xx,0}$	C	D	
xy	2	0.389(1)	−0.079(1)	-	0.988
	4	0.3881(6)	−0.080(1)	0.0060(9)	0.994

by less that 1 % when the 4th order term is included in the fit. Therefore, as an approximation, this thesis considers only the lowest order terms. Knowledge of the coefficients for the AMR equations then allows the direction of M to be determined from magnetotransport measurements in the subsequent sections. Inspection of the residuals of the fourth-order fit indicates that the largest residual contribution is approximately 13 % of the fitting parameter C for ρ_{xy} and 6 % of the fitting parameter A for ρ_{xx}. It is noted that the value of $\rho_{xx,0} = 82.2550(8)\,\mu\Omega\,\mathrm{cm}$ is in agreement with that previously measured in Galfenol, $85(5)\,\mu\Omega\,\mathrm{cm}$ [230].

3.3 Control of Magnetic Anisotropies by Strain

3.3.1 Control of Magnetic Easy Axis Using Strain

The magnetisation direction of a sample will tend to prefer to lie along the direction of the easy magnetic axis or axes. This easy axis is the direction of magnetisation which will minimise the magnetic free energy of the system. An equation for which is shown in equation (1.19). In this section this easy axis is controlled by introducing a strain-induced anisotropy energy term to the magnetic free energy, by applying a strain via a PZT piezoelectric transducer. For a given strain induced in the magnetic layer, the effect on the magnetisation will depend on its magnetostrictive properties. The AMR characterised in section 3.2.3 is used here to track the rotation of the magnetisation direction and the induced strain used to favour either the [010] or [100] cubic easy axes of the layer.

At zero applied field, the magnetisation will lie along an easy axis direction. In the case of the unstrained $Fe_{81}Ga_{19}$ layer this will be along either [100] or [010]. With the application of a magnetic field along either of these easy axis directions one would not expect to see a measurable change in AMR signal, since the magnetisation would simply flip from parallel to the field to anti-parallel to the applied field. As the magnetisation changes direction, there

will be a intermediate state which could be detected as a change in resistance. The time and field resolution of the measurements here were not sufficient to detect this intermediate state. If however a magnetic field were applied along a hard axis direction, a change in the AMR signal would be expected as the magnetisation is pulled away from the zero-field position along the easy axis, towards the direction of the applied field.

Figure 3.4 shows magnetic field sweeps along [010] and [100] axes. These axes are aligned to the transducer such that a positive voltage applied to the transducer induces a tensile strain in the transducer along the [010] direction, with a corresponding compression along [100]. The reverse is true for a negative voltage applied to the piezoelectric transducer. The maximum change in the transverse resistivity is consistent with the amplitude of the AMR measured in section 3.2.3. The plots in figure 3.4 demonstrate how it is possible, by inducing a particular strain in the piezoelectric transducer, to select either [100] or [010] as the magnetic easy axis of the $Fe_{81}Ga_{19}$ layer. In figure 3.4 (a) a large positive voltage (50 V) was applied to the transducer, which induced a tensile strain along the [010] direction ($\varepsilon = 8.6(2) \times 10^{-5}$), with magnetisation along this direction. Sweeping the field along the [010] easy axis showed no significant change in resistance, indicating no change in magnetisation direction with respect to current. Sweeping the field along the [100] hard axis however showed two switching events. First as the field is reduced to zero from a negative saturating field, and the magnetisation direction returns to its preferred easy axis direction, and then again as the magnetisation is pulled away from the easy axis to along the [100] axis by a saturating positive field. Two switching events then also occurred as the field was swept from a saturating positive field, through 0 T to a saturating negative field. Figure 3.4 (b) shows similar field sweeps with a large negative voltage applied to the transducer $V_P = -30$ V, which corresponds to a compressive strain along the [010] ($\varepsilon = -8.0(2) \times 10^{-5}$), causing the magnetisation to favour the [100] direction at zero magnetic field. The easy axis field sweep shows no significant change in magnetisation direction. The hard axis sweep however shows the same two steps of the magnetisation direction as it returns to the easy axis at low field,

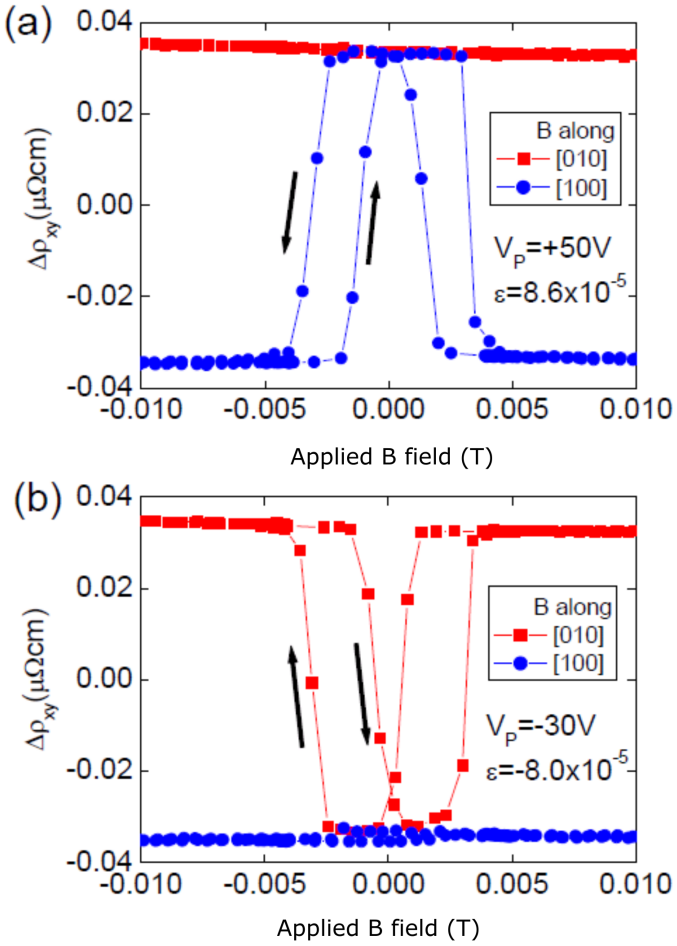

Figure 3.4: Change in transverse resistivity, $\Delta\rho_{xy}$, as a function of applied magnetic field for (a) large tensile strain and (b) large compressive strain along [010]. The magnetic easy axis changes from along the [010] direction in (a), for tensile strain along this direction, to being along the [100] direction in (b), for compressive strain along [010].

and is then pulled back away from the easy axis as the field is increased.

3.4 Determination of Magneto-elastic Properties of $Fe_{81}Ga_{19}$

The hysteresis loops found from the magneto-transport data were also used to extract information about the magnetostrictive properties of the $Fe_{81}Ga_{19}$ layer. It was not possible from the measurements undertaken to determine separately the magnetostriction and elastic constants due to the clamping of the $Fe_{81}Ga_{19}$ film to the substrate. The magneto-elastic constant, B_1, could however be extracted. It is B_1 which determines the strength of the magneto-elastic energy contribution to the magnetic free energy, as discussed in chapter 1, equation (1.15). B_1 can be found by knowing how much magnetoelastic energy is put into the system for a given strain, $(\varepsilon_{xx} - \varepsilon_{yy})$. A fit to the field sweep data using a model based on the magnetic free energy density, including a magneto-elastic energy density term, was used to find B_1,

$$E(\psi) = \frac{K_C}{4}\sin^2(2\psi) + K_U \sin^2(\psi - \frac{\pi}{4}) - MHcos(\delta - \psi) + E_{ME} \qquad (3.5)$$

where ψ is the angle between the magnetisation and the [010] crystal direction. The first term represents the cubic magnetocrystalline anisotropy density, favouring easy axes along the [100] and [010] direction. The second term is a uniaxial magnetocrystalline anisotropy energy density, typically found in Fe films deposited on GaAs (001) substrates, of order 5×10^4 J/m^3 [231], which favours the [110] direction for our films. The third and fourth terms represent, respectively, the Zeeman energy of the magnetisation M interacting with the external field, H applied at an angle δ to the [010] direction, and the magnetoelastic energy induced by the applied strain. The fitting program also included a parameter representing a domain wall de-pinning energy density, E_{Depin}, which allowed magnetisation switching events between local energy minima if the energy saved in doing so was greater than this domain wall de-pinning energy density. This term was not included in the magnetic free

energy, rather it was used to set the condition for when switching occurred. A schematic of this process is shown in figure 3.5. The shaded region represents the the magnetic anisotropy contribution to the energy density of the domain wall associated with the misalignment of the spins relative to the anisotropy direction (see chapter 1). An alternative interpretation of E_{Depin} is that it in fact represents a nucleation energy density. The MOKE images presented section 3.5.1 are evidence in favour of it being a depinning energy density as they indicate that the pinning and depinning of domain walls is key to the magnetisation reversal process in this sample.

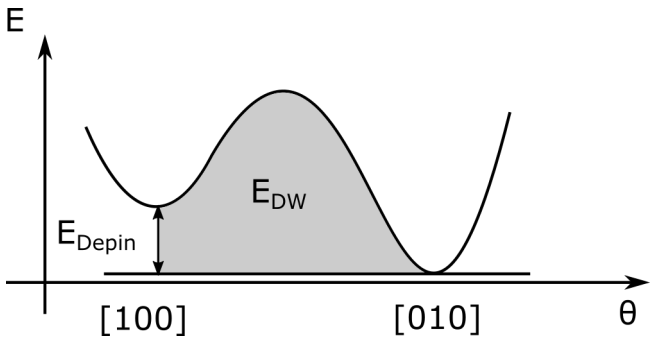

Figure 3.5: Schematic of the magnetic free energy density as a function of angle θ. The shaded area (E_{DW}) represents the magnetic anisotropy contribution to the domain wall energy corresponding to the misalignment of the magnetisation with the easy anisotropy direction as it transitions from [100] to [010]. E_{Depin} is the value used as a fitting parameter for determining magnetoelastic properties. The magnetisation is free to switch energy density minimum if the energy saved in doing so is greater than the set value of E_{Depin}.

The transport data was first converted into a representation of the magnetisation rotation using the AMR equations. By rearranging the equation for ρ_{xy} (1.28) an expression for the magnetisation direction with respect to the current was found. It is possible to determine the angle of the magnetisation direction with respect to current θ with

$$\theta = \frac{1}{2}\arcsin\left(\frac{\rho_{xy} - \rho_{av}}{\Delta\rho}\right) \tag{3.6}$$

An example of ρ_{xy} for 40 V across the piezoelectric transducer is shown in

figure 3.6(a). The magnetisation direction rotates between ±45° from the current direction, which in this case is at an angle 45° to the applied field axis, along [100]. This angle θ, while mathematically correct, is valid in multiple quadrants of the magnetisation rotation. A judgement was therefore made as to which region a particular measurement belonged based upon the known field direction in the measurement, with the biaxial easy axes having determined the sense of the magnetisation rotation. The result of this interpretation is shown as θ_M in figure 3.6(b). The colours correspond to the regions indicated in the schematic of the magnetisation reversal process shown in figure 3.7. As the magnetic field is reduced from a large negative value the magnetisation rotates away from $[\bar{1}00]$ into region 1, towards the biaxial easy axis direction, not favoured by the strain induced easy axis anisotropy (non-bold dashed line) before switching abruptly towards the bold dashed line at low field magnitude. At zero field the magnetic easy axis lies in region 2. As the field is increased along the [100] direction the magnetisation rotates through region 3, towards the axis of the applied field, until it lies along the [100] direction. The reverse process then happens as the magnetic field is reduced and the magnetisation rotates again towards the non-favoured biaxial easy axis direction and through region 4. At zero field the magnetisation is in region 5, lying along a direction close to [010] and the zero-strain biaxial easy axis. Finally as the applied magnetic field is increased the magnetisation rotates to lie along the $[\bar{1}00]$ direction. In practical terms this meant that regions 3, 4 and 5 were interpreted as rotations relative to [100], where as regions 1, 2 and 6 were interpreted as rotations relative to [010].

Having established the angle of the magnetisation, θ_M the projection M of the saturation magnetisation M_s along the field direction could be found with

$$M = M_S \sin(\theta_M). \tag{3.7}$$

An example of the magnetisation direction found in this way is shown in figure 3.6 (c). The non-zero value of M/M_s at zero magnetic field corresponds to the rotation away from the $\langle 100 \rangle$ direction of the easy axis caused by the intrinsic uniaxial anisotropy term K_U(see section 2.3.6). The uncertainty in

the magnetisation projection was estimated, rather than determined statistically, from the uncertainty in the angle corresponding to the uncertainty in the resistance measurement.

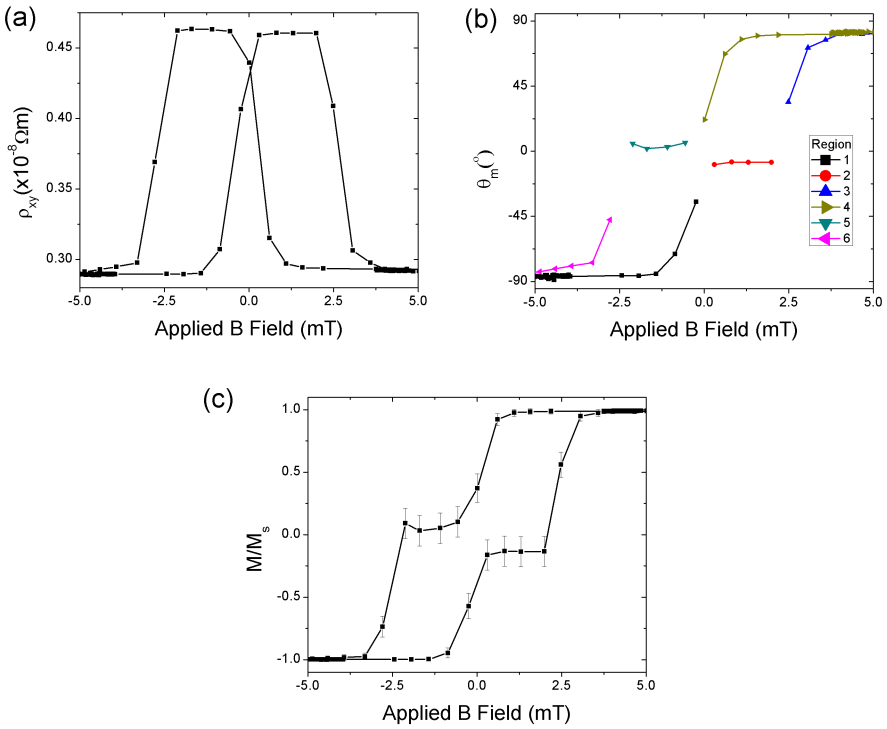

Figure 3.6: Steps used to determine magnetisation direction from magneto-transport data showing case for $V_P = 40\,\mathrm{V}$, with field applied along the [100] direction. (a) Initial ρ_{xy} transverse resistivity measurement. (b) Angle of magnetisation interpreted as rotation away from [100] and [$\bar{1}$00]]. The colours correspond to the regions indicated in the schematic of the magnetisation reversal process shown in figure 3.7. (c) M/M_S for the projection of magnetisation along the field direction. The error bars shown are an estimate based on the uncertainty in the angle calculated from ρ_{xy}.

A fit to the field-sweep data is shown in figure 3.8 which also shows the corresponding resistivity vs field graph. Fitting was done by adjusting the magneto-elastic energy density and domain wall de-pinning energy density to minimise the absolute differences between the experimental switching fields and those produced by the simulation. Two switching events H_{c1} and H_{c2}

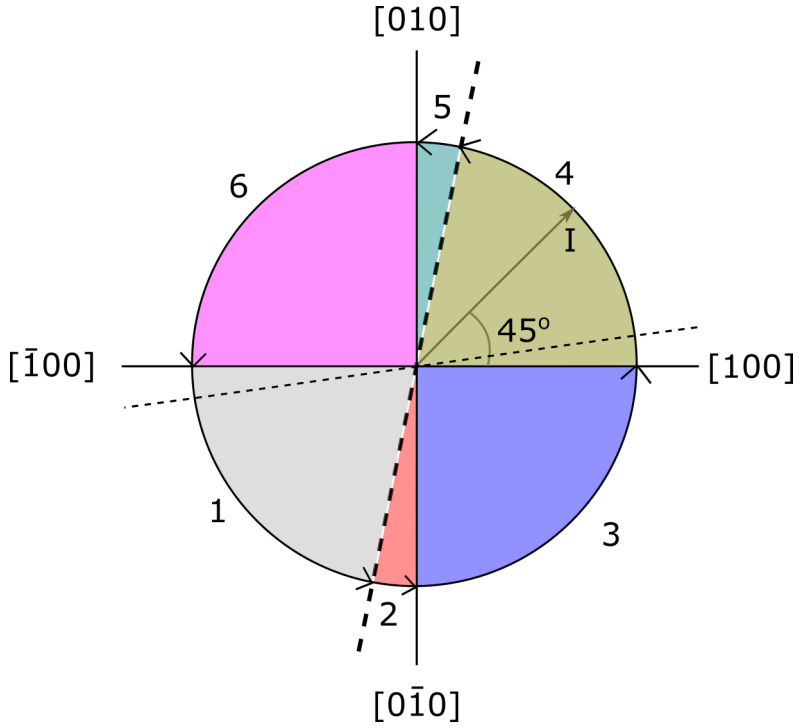

Figure 3.7: Different magnetisation direction regions used for interpreting magnetisation direction from magnetotransport data (see 3.6). The current direction at 45° to the [100] direction is also labelled. The bold dashed line represents the biaxial easy axis favoured by the strain-induced uniaxial anisotropy. As the magnetic field is reduced from a large negative value the magnetisation rotates away from [$\bar{1}$00] into region 1, towards the biaxial easy axis direction, not favoured by the strain induced easy axis anisotropy (non-bold dashed line) before switching abruptly towards the bold dashed line at low field magnitude. At zero field the magnetic easy axis lies in region 2. As the field is increased along the [100] direction the magnetisation rotates through region 3 towards the axis of the applied field. The reverse process happens as the magnetic field is reduced and the magnetisation rotates again towards the non-favoured biaxial easy axis direction and through region 4. At zero field the magnetisation is in region 5, lying along a direction close to both [010] and the zero-strain biaxial easy axis. Finally as the applied magnetic field is increased the magnetisation rotates to lie along the [$\bar{1}$00] direction.

were defined as the magnetisation first switched from the hard axis to the easy axis, and then from the easy axis to the hard axis again. Shown in figure 3.8 is the data for a voltage of 40 V, which induces a tensile strain favouring the [010] direction. The magnetisation switches first from the [100] axis, to the [010] axis, and finally back to lie along the [100] axis.

The two free parameters in the model, the magnetoelastic and domain wall energies, were adjusted to fit to these switching fields. The magnetoelastic energy term shifts the average position of H_{c1} and H_{c2}, such that higher magnetoelastic energies result in higher average switching fields. Increasing the domain wall depinning energy density term increases the separation between the two fields. Estimates of the error bounds of these fitting parameters were obtained by adjusting the parameters to achieve a fit with the maximum and minimum values of magnetic field within the switching region. The full set of hysteresis loops used for fitting the data are shown in figure 3.10. At strains close to zero, the magnetisation tends to switch from parallel to anti-parallel to the hard axis, without lying along an intermediate direction at low field. This indicates that the two axes are equally energetically favourable, which is to be expected if the magnetoelastic energy has effectively been removed from equation 3.5. As the absolute value of the strain is increased, however, it becomes increasingly energetically favourable for the magnetisation to lie at low field along the axis preferred by the strain. As the strain is increased, the magnetisation is able to switch away from the hard axis sooner. A higher field is also required to switch the magnetisation away from its easy axis. This behaviour is consistent with increasing the magnetoelastic energy term in equation 3.5.

The dependence of the extracted magneto-elastic energy on strain is shown in figure 3.11 (a). Also shown is a line representing the values that would be obtained for quench-cooled bulk $Fe_{81}Ga_{19}$, using $\frac{3}{2}\lambda = 3.95 \times 10^{-4}$ and $(c_{12} - c_{11}) = 39.4\,\text{GPa}$, from [123]. This corresponds to $B_1 = 1.56 \times 10^7\,\text{J/m}^3$. A linear fit of the experimental data, shown as a red line on the graph, reveals that the $Fe_{81}Ga_{19}$ thin film studied has $B_1 = 1.39(7) \times 10^7\,\text{J/m}^3$ indicating that the MBE-grown film studied here has comparable magnetoelastic prop-

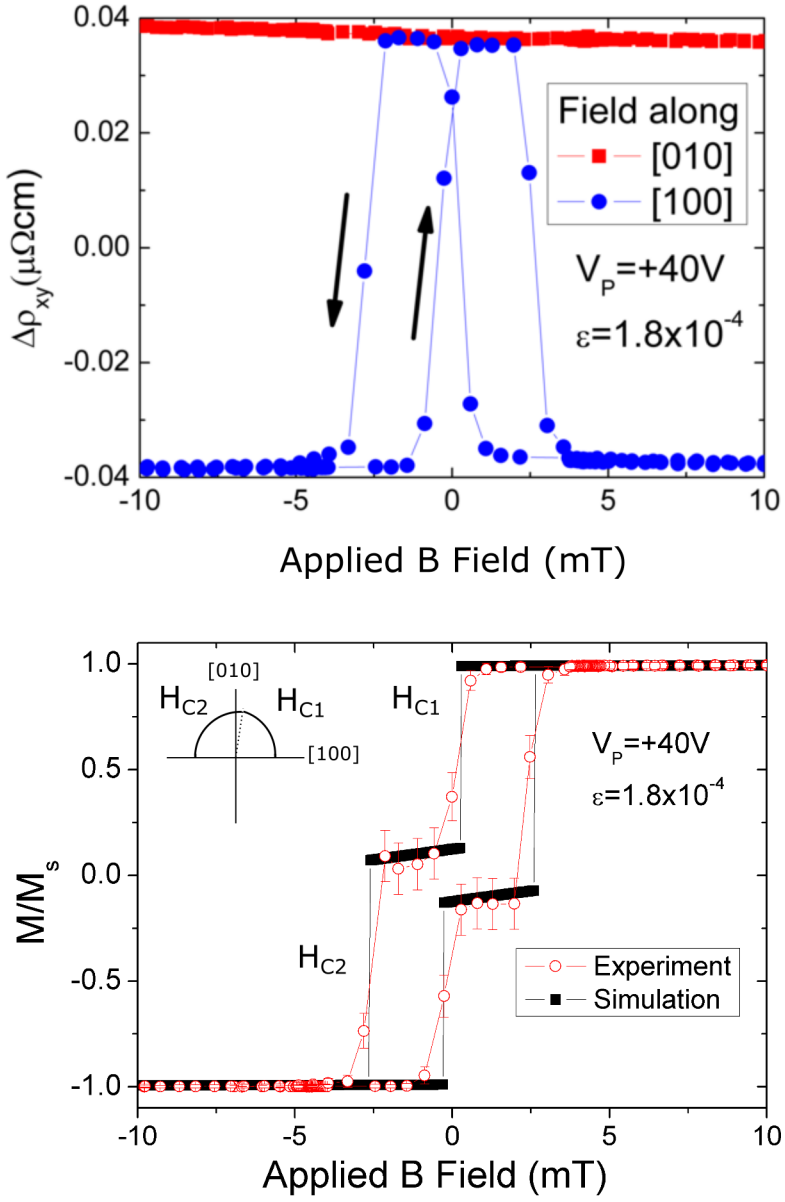

Figure 3.8: Fitting to transport hysteresis loops. a) The initial transport data. b) M vs H loop derived from transport data showing switching fields H_{c1} and H_{c2}, as well as an example of the simulated fit produced by the model used. Estimates of the error bounds of these fitting parameters were obtained by adjusting the parameters to achieve a fit with the maximum and minimum values of magnetic field within the switching region.

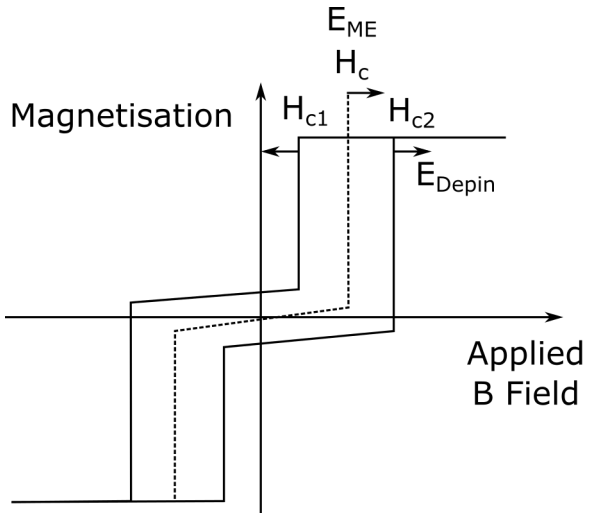

Figure 3.9: The effect of the two fitting parameters E_{Depin} and E_{ME} on the simulated hysteresis loop. Increasing the domain wall depinning energy density E_{Depin} term increases the separation between the two fields. The magnetoelastic energy E_{ME} term shifts H_{c1} towards zero field and H_{c2} away from zero field.

erties to the previously studied bulk material.

The domain wall de-pinning energy density, shown in figure 3.11(b) was not found to have a significant dependence on the induced strain. The average domain wall depinning energy density was found to be $1950(50)\,\mathrm{J/m^3}$. Although the domain wall energy density itself would be affected by the change in anisotropy affected by the strain, the additional energy density introduced in the fitting procedure represents a domain wall depinning energy density. The evidence presented here suggests that this domain wall depinning energy density is independent of strain. Why this should be the case is not immediately obvious.

One possible explanation for the strain-dependence of E_{Depin} is as follows. Pinning of domain walls in the sample results from spatial variations in the magnetic anisotropy energy density. If E_{DW} is the magnetic anisotropy contribution to the domain wall energy density, then the spatial variation of this value might look the solid line ($E_{ME,1}$) in figure 3.12. The domain wall would be pinned at minima in this curve until the application of an external mag-

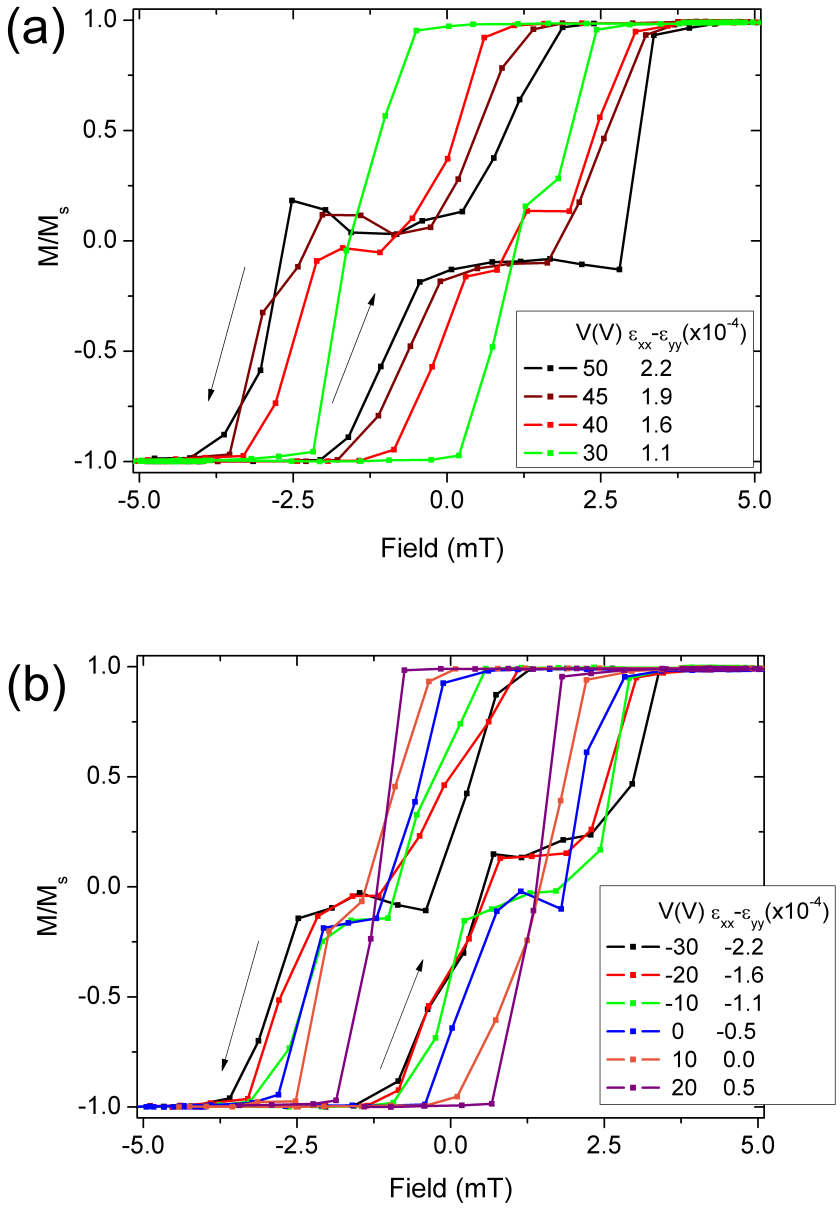

Figure 3.10: Hysteresis loops derived from magnetotransport measurements. (a) Strain favours [010] axis, field is applied along [100] axis. (b) Strain favours [100], field is applied along [010]. For clarity error bars have been omitted.

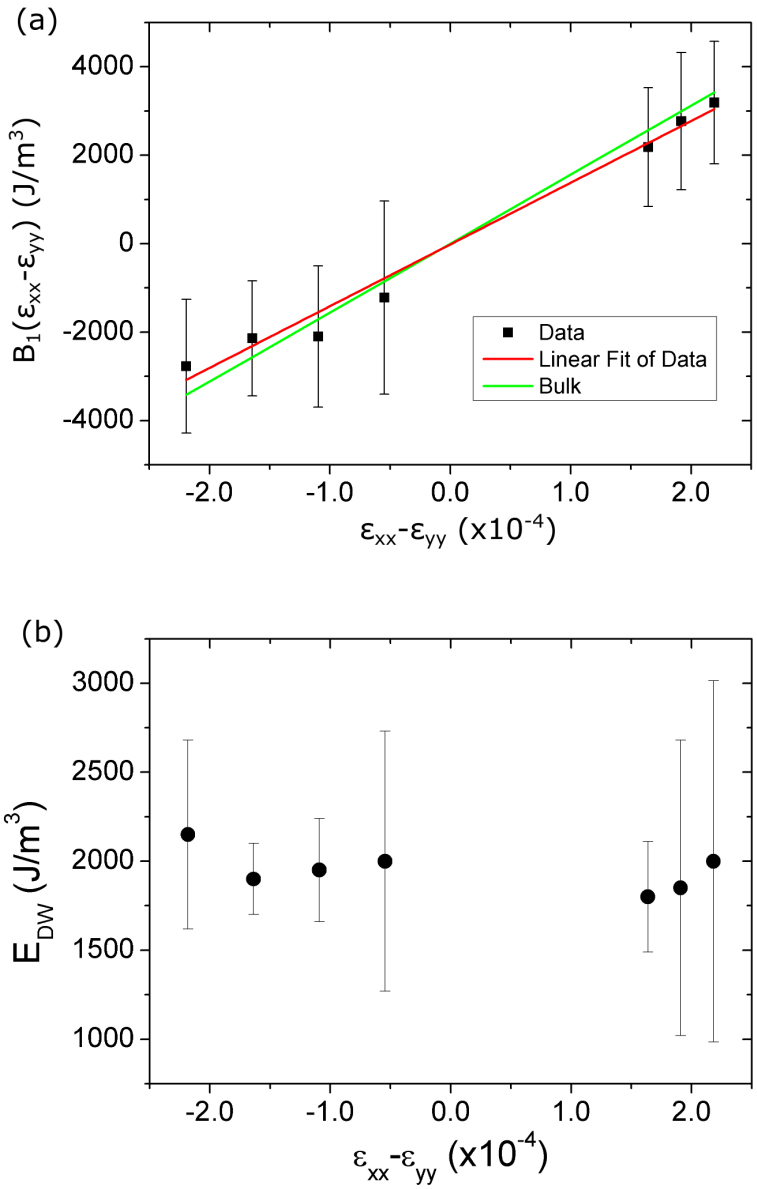

Figure 3.11: (a) Magnetoelastic constant, B_1 as a function of strain. Also shown on this graph (green line) is $B_1 = 1.56 \times 10^7$ J/m^3 as a function of strain for bulk $Fe_{81}Ga_{19}$, using parameters from [123], and a linear fit to the experimental data for thin-film $Fe_{81}Ga_{19}$ corresponding to $B_1 = 1.39(7) \times 10^7$ J/m^3 (red line). (b) Domain wall depinning energy density term, E_{Depin} as a function of strain. Estimates of the error bounds of individual $B_1(\varepsilon_{xx} - \varepsilon_{xy})$ and E_{Depin} were obtained by adjusting the parameters to achieve a fit with the maximum and minimum values of magnetic field within the switching region.

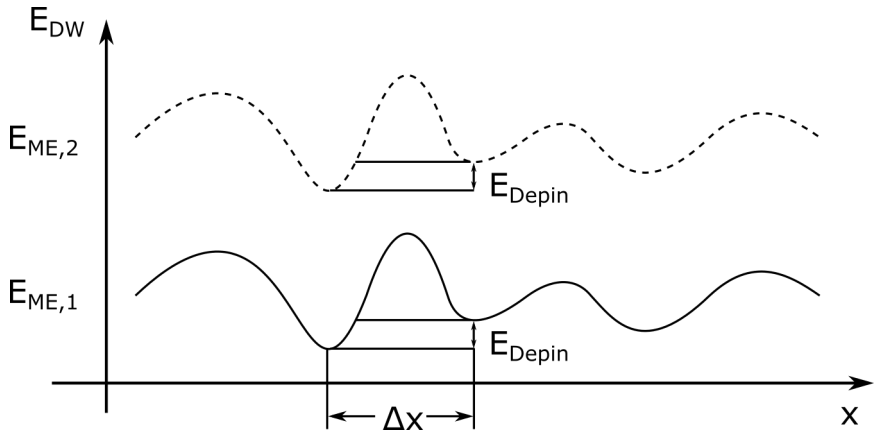

Figure 3.12: Pinning of domain walls in the sample results from spatial variations in the magnetic anisotropy, such as that shown in the solid line ($E_{ME,1}$). A uniform strain-induced anisotropy would affect the domain wall energy density (E_{DW} in figure 3.5) equally across the spatial extent of the sample, resulting in an overall shift in the spatial variations of the domain wall energy, depicted as the dashed curve ($E_{ME,2}$). As the magnetisation rotates through angle θ, the domain wall moves through a distance Δx (in one dimension). In the fitting simulations E_{Depin} is associated with a single, global move in the angle θ of the magnetisation direction. In this figure E_{Depin} instead represents a local depinning energy density.

netic field provides sufficient energy to move the domain wall to the next minimum. A uniform strain-induced anisotropy would affect the domain wall energy density equally across the sample, resulting in an overall vertical shift in the spatial variations of the domain wall energy without changing the overall shape of the curve, depicted as the dashed curve ($E_{ME,2}$) in figure 3.12. A domain wall will move through a distance Δx (in one dimension) if the increase in domain wall energy (E_{Depin}) is offset by the reduction of the magnetic free energy in the region spanned by Δx as the magnetisation angle in that region rotates. Since the increase of domain wall energy (E_{Depin}) is not affected by a uniform induced strain then one would not expect to measure a strain dependence of the term E_{Depin} in the experiment. In the fitting simulations in this study, E_{Depin} was treated as a single, global depinning event. In reality there may be multiple pinning sites as depicted in energy landscape in figure 3.12. Section 3.5 introduces evidence that supports the idea that domain wall depinning happens across large areas of the device studied. Within the limited resolution of the transport measurements it may be that E_{Depin} represents an average depinning energy.

3.5 Non-volatile switching of magnetisation using strain

Section 3.4 showed that by inducing strain in a $Fe_{81}Ga_{19}$ layer it is possible to select either [010] or [100] as the preferred easy axis direction. In this section it is demonstrated that it is possible to switch between those two directions using only induced strain, in the absence of an externally applied magnetic field. For this experiment magnetisation was saturated along [010] and the sample removed from the magnetic field and placed in μ metal shielding. This starting magnetisation direction along the [010] direction corresponds a tensile strain along this direction. The voltage applied to the transducer and hence the strain was then swept from 50 V ($\varepsilon = 8.6 \times 10^{-5}$) to -30 V ($\varepsilon = -8.0 \times 10^{-5}$).

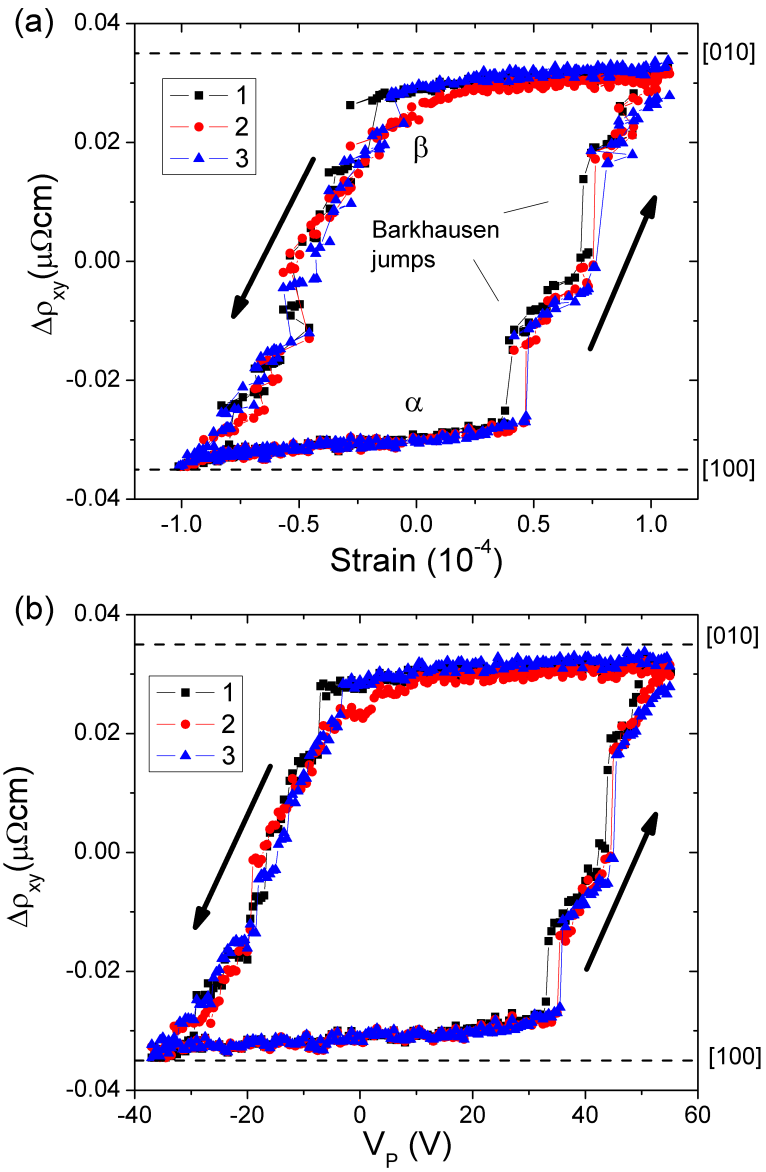

Figure 3.13: The change in transverse resistivity with respect to both strain (a) and voltage applied to the transducer (b). Non-volatile switching of magnetisation is demonstrated as the magnetisation is set to state α or β depending on the strain history of the device. Barkhausen-like jumps in the loop suggest that the switching proceeds via the motion and depinning of domain walls. Values for $\Delta\rho_{xy}$ corresponding to the [010] and [100] directions are marked on these graphs.

Figure 3.13 shows several sweeps of the strain induced (a), and the corresponding applied voltage (b). The significant feature to highlight in this figure is the non-volatility in both voltage and strain. In this study the magnetisation was set into two different states (labelled α and β in figure 3.13 (a)) at both zero voltage and zero strain. With the application of smaller maximum voltage amplitudes to the piezoelectric transducer a family of minor hysteresis loops could also have been produced, with a corresponding range of remenant magnetisation states. This was not, however, possible because a crack developed in the device after the third sweep of the voltage on the piezoelectric transducer making further measurements impossible. The graphs of ρ_{xy} vs V and ρ_{xy} vs strain show evidence of Barkhausen effect events commonly seen in M vs H loops as the jumps in resistivity indicate that domain walls undergo many pinning and depinning events as the voltage and strain are swept. There are many small jumps in resistivity, indicating a large number of pinning sites, in addition to a few large jumps which are evidence for some domain walls moving over relatively large distances. These observations are supported by the MOKE microscopy images discussed in section 3.5.1. The magnetisation does not point along the [010]/[100] directions at $V_P = 0\,\mathrm{V}$ which is attributed to the small uniaxial component of the anisotropy favouring the [110] direction and causing the easy axes to be offset by 7° when the strain is zero.

The measured value of ρ_{xy} included an offset, ρ_{offset}, which is independent of magnetic field. The original data, without offset removed are plotted in figure 3.14 as a function of strain (a) and voltage (b). This offset may have arisen from imperfect alignment of the transverse voltage probes (shown schematically in figure 3.15), which tends to mix the ρ_{xx} signal into the ρ_{xy} measurement. From the data presented in table 3.1, $\rho_{xx} \approx 82 \times 10^{-8}\,\Omega\,\mathrm{m}$, which will also be the resistivity of one square of the Hall bar. Taking the offset resistivity to be $0.17 \times 10^{-8}\,\Omega\,\mathrm{m}$, this corresponds to 2.1×10^{-3} squares of material. The length of one square is 45 µm, so the voltage probe misalignment of the transverse voltage probes would need to be around 95 nm to fully explain the measured offset. This degree of misalignment is not unreasonable given the

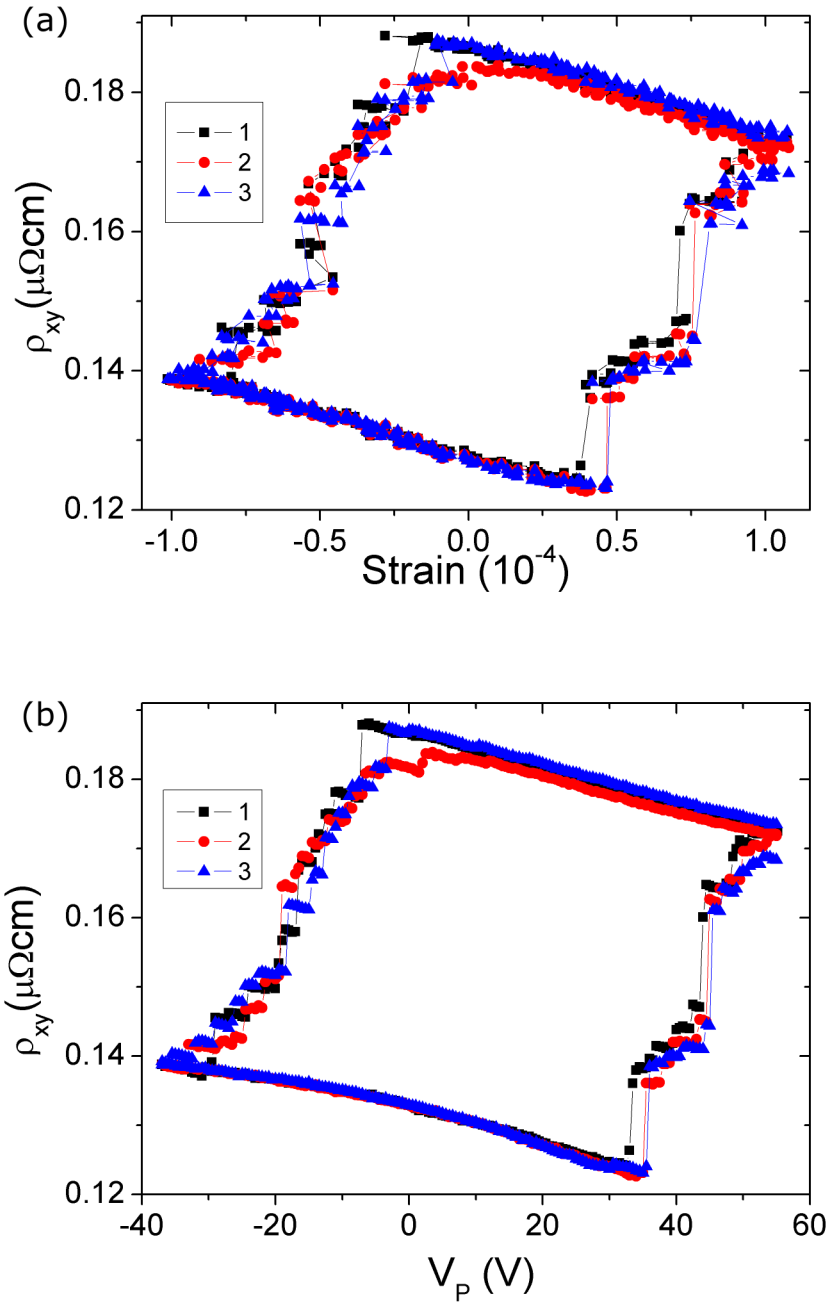

Figure 3.14: The change in transverse resistivity ρ_{xy} with respect to both strain (a) and voltage applied to the transducer (b). In this figure the offset due to misalignment of the voltage probes of the Hall bar has not been removed.

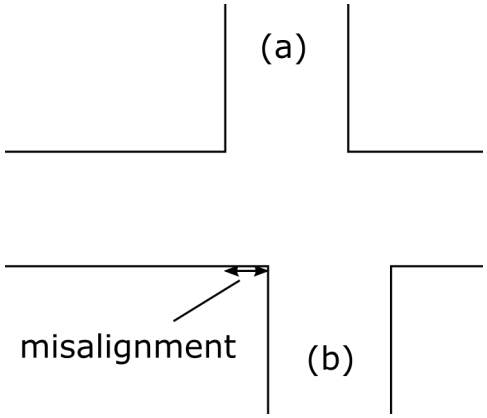

Figure 3.15: Schematic of the spatial offset of transverse voltage probes which may give rise to the offset in ρ_{xy} measured. A probe offset in the transverse probes (a) and (b) means that a contribution from ρ_{xx} is mixed into the ρ_{xy} signal.

size of the Hall bar and tolerances of the lithography, which suggests that it is a reasonable explanation for the offset in measured resistivity.

In this study an inhomogeneity in the strain will contribute to this offset which can therefore be strain dependent. ρ_{offset} is approximately 1 part in 1×10^4 of the longitudinal resistance and has a weak dependence on strain. To determine the strain dependence ρ_{xy} was measured as a function of strain with a saturating magnetic field along the [100] and [010] directions. This is shown in figure 3.16. The dependence of the offset on strain is approximately linear and the slope of each line $\frac{d\rho_{xy}}{d\varepsilon} = 156.8\,\mu\Omega\,\text{cm}$ for both the forward and reverse direction of magnetic field. ρ_{offset} was defined as the average of the curves along the [100] and [010] directions. This has been subtracted from the measured data in figure 3.13 to show $\Delta\rho_{xy} = \rho_{xy} - \rho_{\text{offset}}$. After subtraction of this offset the variations in ρ_{xy} are due only to variations in the direction of the magnetisation.

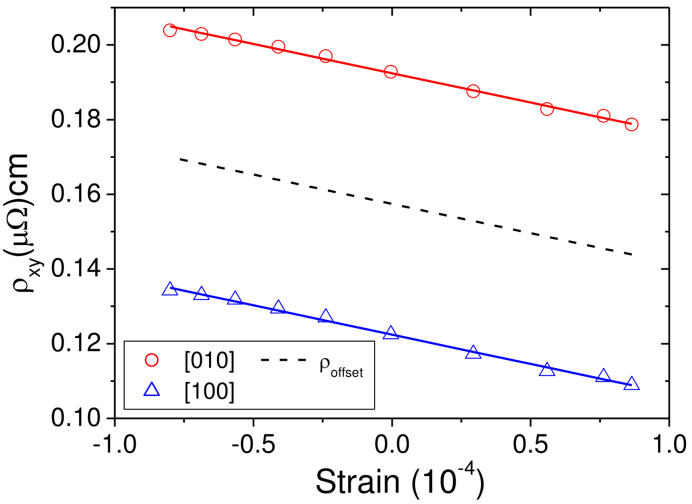

Figure 3.16: Graph showing the offset in ρ_{xy} as a function of strain. The offset is likely due to imperfect alignment of the voltage probes of the Hall bar.

3.5.1 MOKE Microscopy of Magnetisation Switching

MOKE microscopy was also used to study the mechanism of the switching of magnetisation between the two strain states. The microscopy images shown in figure 3.17 are of the same section of the Hall bar as was used for transport measurements. These images were taken by Dr. Stuart Cavill. 3.17(a) shows a similar sequence of sweeping the strain as shown for magnetotransport measurements in figure 3.13. The ρ_{xy} magnetotransport measurements were taken across the voltage probes visible in these images. The changes in the contrast of the majority of the region between the contacts in figure 3.17 (a) (ii) and (iii) reflect the changes in magnetisation detected in the magnetotransport measurements.

Further evidence of the switching mechanism of the magnetisation within the contact region is found in figure 3.17(b) which shows a sequence of images as an increasingly tensile strain is applied from image (i) to image (iv). These sequences show that the magnetisation reversal occurs by the motion of magnetic domain walls. The changes in the domains appear disordered with the

domain walls overcoming multiple pinning sites, which is consistent with the evidence of Barkhausen-like jumps observed in figure 3.13. The domain walls themselves are not straight lines and appear to have no definite preferred orientation, although there is a general tendency to lie roughly across the bar. The MOKE microscope images also reveal that the Hall bar is not fully reversed by the strain: some vestigial domains remain at the edges. These vestigial domains may result from domain wall pinning due to anisotropy variations, imperfections in growth and lithography or local variations in the strain, which result in local inhomogeneities in the magnetic anisotropy.

The images shown in figure 3.17 clearly show that the pinning and depinning of domain walls is key to the magnetisation reversal process in this sample. This supports the interpretation in section 3.4 of E_{Depin} as being a depinning energy density, rather than being related to domain wall nucleation. Furthermore, there are multiple pinning sites within the transport measurement region, which also supports the possibility that E_{Depin} represents an average depinning energy.

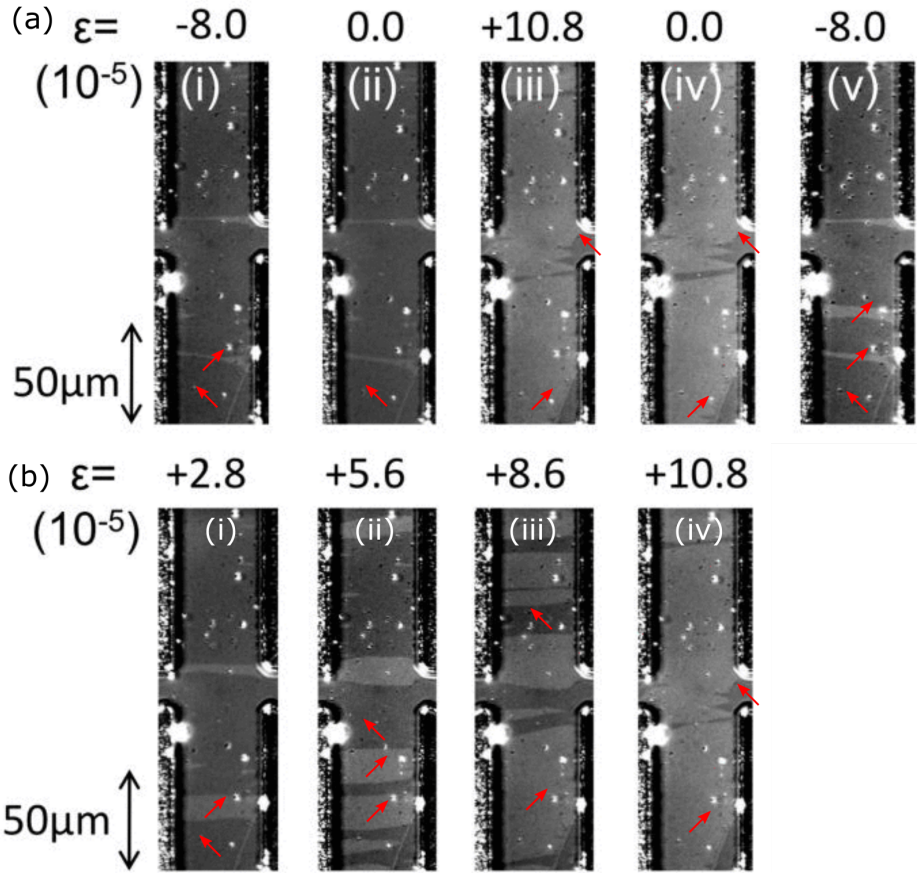

Figure 3.17: MOKE microscopy images of the voltage probe region of the Hall bar studied. The red arrows indicate the direction of magnetisation projection in different domains in the Hall bar. (a) The importance of strain history in setting the domain configuration. (i-ii) magnetisation direction within the voltage probe region set by large compressive strain. (iii-iv) large tensile strain changes the majority magnetisation direction within the voltage probe region. (v) The original majority magnetisation component is reset by a large compressive strain. (b) the mechanism of switching involving the motion of several domain walls over 10s of microns as increasingly tensile strain is induced in the layer (i - iv). MOKE images taken by Dr Stuart Cavill.

3.6 Conclusions

This chapter began by presenting the characterisation of the basic structural and magnetic properties of the MBE-grown layer of $Fe_{81}Ga_{19}$ studied. XRD

was used to find the out-of-plane lattice parameter in the compressed epitaxial layer, from which the fully relaxed lattice parameter was calculated. The XRD results presented also showed the good epitaxial and single-crystal growth of the $Fe_{81}Ga_{19}$ layer. SQUID magnetometry was used to determine the magnetocrystalline anisotropy constants of the $Fe_{81}Ga_{19}$ layer. The layer was found to have cubic magnetic anisotropy favouring the [100]/[010] directions and a weaker uniaxial component favouring the [110] direction. This results in a biaxial anisotropy with easy axes offset by 7° from the [100]/[010] directions. The AMR of $Fe_{81}Ga_{19}$ was studied at room temperature to provide a tool for determining the direction of magnetisation using magnetotransport.

Magnetotransport was further used to demonstrate the setting of two distinct magnetic easy axes using strain induced via a piezoelectric transducer. Simulations of magnetisation reversal based on the expression for the magnetic free energy were used to fit to the magnetotransport data in order to extract the magnetoelastic coupling constant. The value of $B_1 = 1.39(7) \times 10^7\,\mathrm{J/m^3}$ for this MBE-grown layer was comparable to that for single-crystal bulk material of $B_1 = 1.56 \times 10^7\,\mathrm{J/m^3}$. This chapter has shown that measuring the magnetotransport properties of hybrid ferromagnetic/piezoelectric devices provides a reliable method of determining the magnetostrictive properties of thin films clamped to substrates.

The highly magnetostrictive properties of the MBE-grown layer were exploited to demonstrate switching of the magnetisation in the Hall bar between two easy axes in the absence of an externally applied magnetic field. Evidence from magnetotransport and MOKE microscopy data indicates that domain pinning processes are an important mechanism in the switching of magnetisation in the device studied. The fitting to magnetotransport-derived hystersis loops does however seem to suggest that the domain wall depinning energy density is not strain-dependent within the resolution of this measurement. The demonstration in this chapter of voltage-controlled non-volatile switching of near-90° magnetisation direction is important for its potential applicability to technology. A device based on this could be used to create a memory that can be written with only an electric field. For the device to be of technolog-

ical interest, however, the same, or similar effects must also be observed at more technologically relevant scales: certainly below 1 µm, and ideally below 100 nm. On these length scales the magnetisation reversal may occur by the motion of single domain walls, or an alternative single domain model may become relevant.

Chapter 4

Strain Control of Magnetic Domains in Micro-fabricated $Fe_{81}Ga_{19}$

4.1 Introduction

Device applications will require devices with dimensions much smaller than the 45 µm bars investigated in chapter 3 [232]. As device size is reduced the relative influence of shape anisotropy is increased, favouring the formation of domains. In the Hall bar devices discussed in chapter 3 the magnetisation reversal mechanism involved the motion of domain walls with no well defined shape and between random pinning sites determined by imperfections in the material structure or fabrication which caused an irregular pattern of domains. If domain walls are to be used as elements in future memory [34, 35] and logic [233] technologies they will need to be formed in a regular pattern and be able to move between well defined positions so that information can be reliably stored and accessed.

This chapter builds on the work presented in chapter 3 to show how the balance of magnetocrystalline, magnetostatic and strain-induced anisotropies

can be tuned in micron-sized devices fabricated from a single crystal $Fe_{81}Ga_{19}$ film. Both growth-induced strain and a strain induced by a piezoelectric transducer are used to induce and control the formation of ordered domains.

The magnetic reversal characteristics as a function of voltage applied to a piezoelectric transducer are investigated in an L-shaped bar with 8 µm and 15 µm wide sections. It is also demonstrated in this device that the uniaxial anisotropy induced in the $Fe_{81}Ga_{19}$ layer can be used to control the ordered flux-closing magnetic domain state found in the device in the absence of an externally applied magnetic field. The control of an ordered domain configuration using strain-induced uniaxial anisotropy is further demonstrated in micron-sized disks where XMCD-PEEM and micromagnetic calculations are used to observe the control of the flux-closing domain configuration.

Finally the importance of the relaxation of growth strain in the magnetic domain configuration of 1 µm wide $Fe_{81}Ga_{19}$ wires is investigated. It is found that a distorted flux-closing domain pattern is supported in the wire by the presence of the growth-relaxation-induced uniaxial anisotropy, transverse to the long axis of the wire, an observation which may be of use or a hindrance in the development magnetisation- and domain-wall-based technologies using $Fe_{81}Ga_{19}$.

4.2 Control of Anisotropies and Domains in 15 µm wide $Fe_{81}Ga_{19}$ device

In this section a piezoelectric transducer is used to induce strain in a 15 µm wide bar fabricated from the same $Fe_{81}Ga_{19}$ thin film (wafer Mn635) used in chapter 3. By manipulating the strain-induced anisotropy energy the magnetic reversal characteristics of the device are tuned. The control of the configuration of an ordered domain pattern using voltage-induced strain in the absence of a magnetic field is also demonstrated.

4.2.1 Sample

The sample studied was an L-shaped structure fabricated from wafer Mn635, as used in chapter 3, by electron beam lithography and Ar ion milling, using the reverse-biased sputter system described in chapter 2. The arms of the structure were 125 µm long each with two sections, one of width 15 µm and one of width 8 µm. The two widths of the structure allowed the effect of varying shape anisotropy to be studied. The ends of the arms were tapered. The arms were oriented so as to lie along the [010]/[100] axes of the $Fe_{81}Ga_{19}$ layer. An image of the device obtained by wide-field microscopy is shown in figure 4.1 (d). The GaAs (001) substrate was thinned to 150 µm before being bonded to a piezoelectric transducer. The bonding process was the one described chapter 2 and did not attempt to compensate for any built-in strain resulting from the glue curing process. In this experiment there was no means of directly characterising the strain induced by the piezoelectric transducer. The strain induced in the magnetic layer was instead inferred from the measurements in chapter 3 and evidence from this experiment.

From SQUID magnetometry carried out on this layer (Mn635) and presented in chapter 3 it was known that the cubic anisotropy was parallel and perpendicular to the arms of the L-bar, with $K_c = 32.7\,\mathrm{kJ/m}$ along the [100] and [010] directions. The uniaxial anisotropy arising from the GaAs interface was along the [110] direction with $K_u = 8.6\,\mathrm{kJ/m}$.

4.2.2 Controlling Interplay of Anisotropies

The balance of anisotropies in the sample determines the magnetic domain configuration and the magnetisation reversal behaviour. In addition to the cubic and uniaxial magnetocrystalline anisotropies, there was also present a shape-induced anisotropy favouring magnetisation pointing along the long axis of each arm. Strain-induced uniaxial anisotropy energy favoured magnetisation along the the vertical arm of the structure for positive strain.

Spatially resolved MOKE images, with a pixel size of 0.4 µm, taken at different

points along magnetic field sweeps for different voltages applied to the piezoelectric transducer reveal the effect on the domain configuration of changing the strain-induced uniaxial anisotropy. Images were taken using the Kerr imaging microscope at Diamond Light Source with Dr. Stuart Cavill, now at the School of Physics, University of York. The images presented here are background-subtracted images, using the method described in chapter 2.

The different reversal mechanisms for three voltages, V_P, applied to the piezoelectric transducer are discussed in the following sections. The different reversal mechanisms observed at the different voltages mean that it is not meaningful to compare the coercivities across the voltage range.

50V

The behaviour of the average projection of magnetisation in each arm is different due to the different balance of anisotropies in each section. For the case where +50 V is applied to the piezoelectric transducer shown in figure 4.1 (a) the magnetization component along the field direction (parallel to the vertical arm of the L-shape) is shown normalised to the saturation magnetization. It is known from section 2.3.3 that this corresponds to a large tensile strain of approximately 2×10^{-4} along the axis of the vertical arm of the L-bar (labelled 3 and 4 in figure 4.1 (d)). In this case the strain induced anisotropy dominates the magnetic free energy density and the vertical and horizontal sections have similar reversal characteristics resulting in square hysteresis loops in each section. There is a significant reduction, of around 5 mT, in the coercivity of section 1 compared to the coercivities the other three sections which are all equal within the measurement accuracy. This difference in coercivity comes from the additional shape anisotropy in section 1 compared to section 2. The shape-induced anisotropy acts in greater opposition to the strain-induced anisotropy to make the magnetisation reversal relatively easy in this section. This reduces the energy barrier for 180° switching in this section, compared to sections 2, 3 and 4.

The individual MOKE images in figure 4.2 reveal that the magnetisation

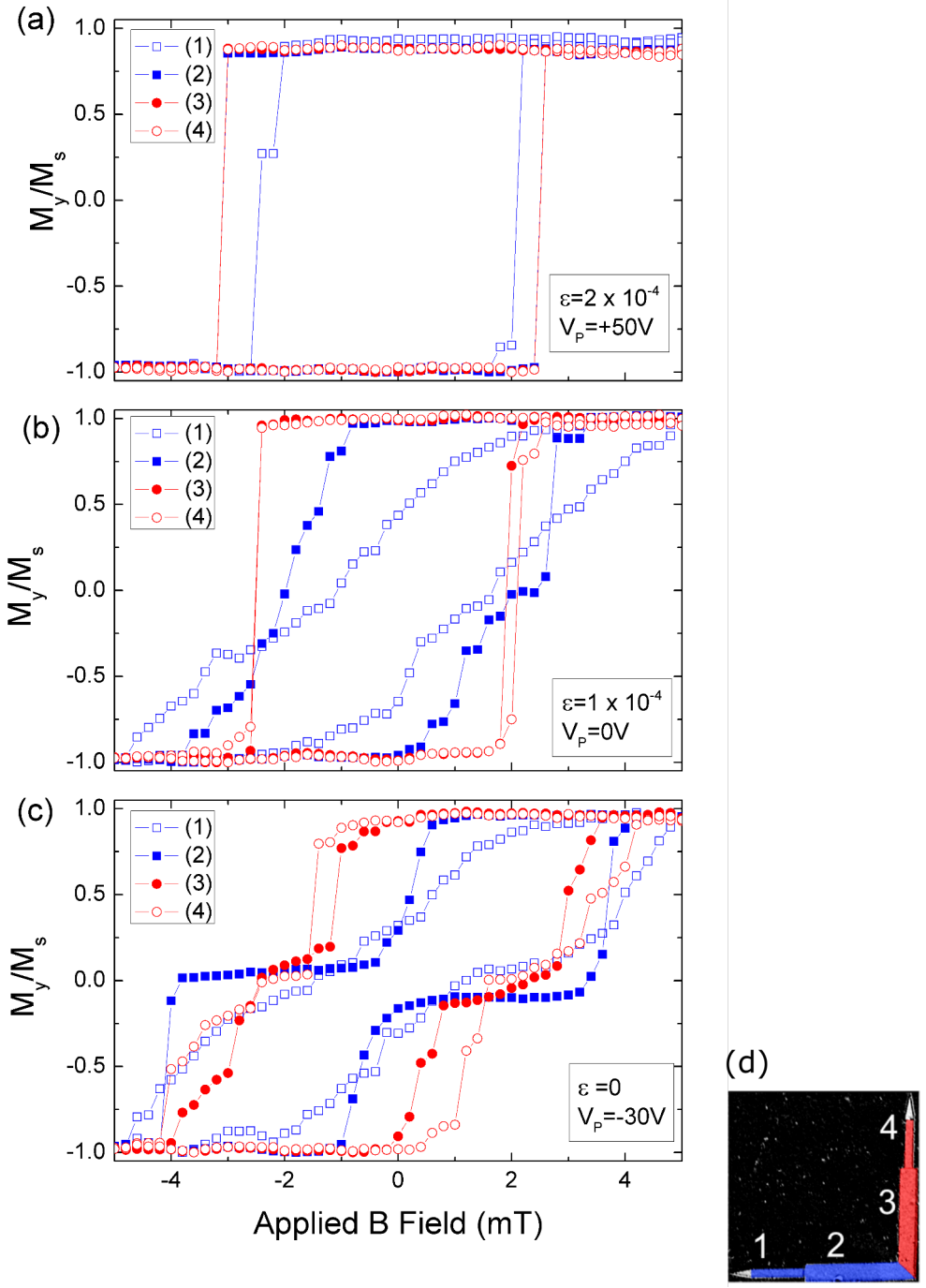

Figure 4.1: Hysteresis curves for the vertical (y) component of magnetisation obtained by MOKE microscopy images for different voltages applied to the piezoelectric transducer: 50 V (a), 0 V (b), −30 V (c). Also shown are the approximate strain values associated with these voltages. Plots are shown for the different regions of the L-shaped bar studied (d).

reversal takes place via nucleation of a 180° domain wall in the narrow, horizontal section of the wire (section 1). The domain wall then sweeps through the whole structure. Domain wall nucleation takes place in this narrow section because this is where the shape-induced anisotropy acts most strongly against the strain-induced anisotropy, allowing magnetisation to reverse at a lower field in this section than else where.

0V

M vs H loops for the case where $V_P = 0\,\mathrm{V}$, are shown in figure 4.1 (b). It is estimated that this voltage corresponds to a tensile strain of 1×10^{-4}. This estimation comes from magnetotransport measurements on a device similar to that presented in chapter 3, but without the electric field cooling. In this device $-30\,\mathrm{V}$ was required to compensate the built-in strain. From the strain calibration in section 2.3.3, $-30\,\mathrm{V}$ corresponds to a strain of around 1×10^{-4}. In the vertical arm (sections 3 and 4 in figure 4.1) the strain-induced anisotropy acts along the same direction as the shape-induced anisotropy, strengthening the easy axis along this arm. This results in a square magnetic hysteresis loop for both wide (3) and narrow (4) sections of the vertical arm similar to that observed in figure 4.1(a). Reversal is too rapid to be captured by the time resolution of the measurements and proceeds via motion of one or more domains walls along the arm. In the horizontal arm (labelled 1 and 2 in figure 4.1) the strain-induced anisotropy acts in the direction perpendicular to the bar and therefore perpendicular to the axis preferred by the shape-induced anisotropy. From figure 4.2 (c) and (d) it is seen that the magnetisation reversal proceeds gradually via the formation of a domain state consisting of regions where magnetisation points either along or transverse to the bar. This flux-closing domain pattern shown in figure 4.2 forms to minimise the stray magnetic field in that section and arises when a magnetic anisotropy component is induced in a direction perpendicular to the axis preferred by the shape-induced anisotropy. As in the case for $V_P = 50\,\mathrm{V}$ there is an approximately 1 mT reduction of the coercivity in section 1, the narrower of the horizontal sections, in which relatively larger shape anisotropy acts in

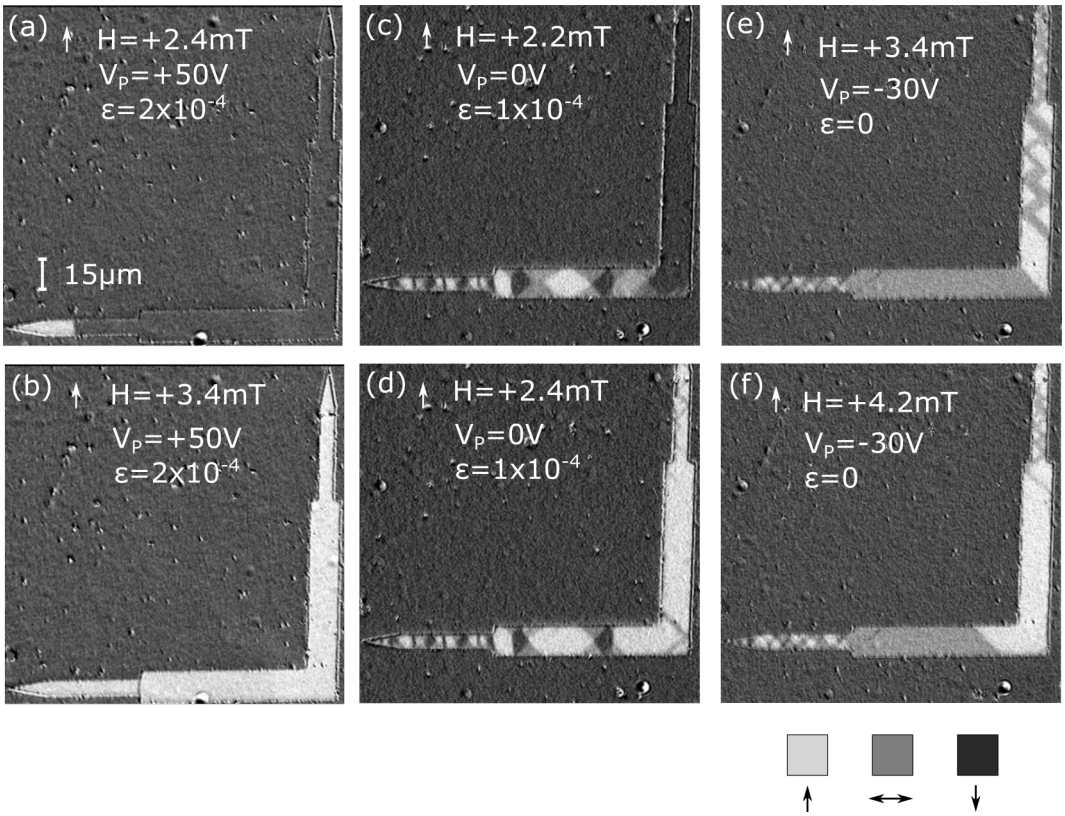

Figure 4.2: MOKE microscopy images showing examples of the reversal process. The magnetic field H is applied in the vertical direction, indicated by arrows. The field value is shown in each panel along with the applied voltage, V_P, and approximate strain, ε. Contrast is indicated by the colour boxes. (a, b) 50 V: Magnetisation reversal takes place via nucleation of a 180° domain wall in the narrow, horizontal section of the wire (section 1). The domain wall then sweeps through the whole structure. (c, d) 0 V: The magnetisation reversal proceeds gradually via the formation of a domain state consisting of regions where magnetisation points either along or transverse to the bar. (e, f) −30 V: Transition from magnetisation along the horizontal direction to the vertical proceeds via formation of a multi-domain zig-zag structure in the vertical arm with domains pointing along and perpendicular to the arm. By contrast, in the horizontal arm the transition takes place via motion of a 90° domain wall that sweeps along the arm.

greater opposition to the strain-induced anisotropy.

-30V

The strain at $-30\,\mathrm{V}$ applied to the piezoelectric transducer appears to approximately compensate the strain built in during fabrication. Similar strain-compensation behaviour has been previously observed in studies of (Ga,Mn)As [105] and evidence for this behaviour in this device is in the characteristic hysteresis loops for a material with biaxial anisotropy (figure 4.1 (c)). In this case the [100]/[010] axes are approximately equivalent easy axes of the device. The shape anisotropy remains in each of the arms, making the arm direction the easy axis for that arm. Sweeping from negative field the first step in the hysteresis loop represents rotation of the magnetisation from negative vertical to horizontal. The second step shows switching from horizontal to positive vertical. The effect of the shape-induced anisotropy is to shift the first step to a more negative field value and the second step to a more positive field in the horizontal arm (sections 2 and 3).

In the vertical arm (sections 3 and 4) the opposite trend is true. Here shape anisotropy makes it more favourable for the magnetisation to lie along the vertical direction at zero field. Transition from magnetisation along the horizontal direction to the vertical proceeds via formation of a multi-domain zig-zag structure in the vertical arm, shown in figure 4.2 (e) and (f), with domains pointing along and perpendicular to the arm. By contrast, in the horizontal arm the transition takes place via motion of a 90° domain wall that sweeps along the arm. 90° domain walls are common in epitaxial iron films [145], and one forms in this case because of the biaxial magnetocrystalline anisotropy in the film, in that the [100] and [010] are approximately equivalent easy directions at this voltage, as the in-built strain induced during the glue-curing process has been compensated by the voltage-induced strain. There remains the presence of the shape-anisotropy of the two wide sections (2 and 3), either side of the corner, although their equivalent shape means that the shape anisotropy energy of each will also be equivalent. The rela-

tively larger shape-induced anisotropy energy in the narrower section (section 1) still favours flux-closure domains, hence the sloping hysteresis loop.

4.2.3 Control of Ordered Domain Structure

Unlike in the 45 µm Hall bar device studied in chapter 3, the domain structures in this 15 µm device are ordered, as a result of the relatively large shape-induced anisotropy. In this section it is demonstrated how voltage-induced strain can be used to control this ordered domain pattern. The wide horizontal section of the wire (section 2) was first initialised in a flux-closure state. The magnetic field was then set to zero before the voltage applied to the piezoelectric transducer (V_P) was swept.

The evolution of the magnetic domain pattern in region 2 as the voltage applied to the transducer is varied is shown in figure 4.3. At $V_P = 0$ (figure 4.3 (a))there are clear triangular regions of longitudinally magnetised domains. These surround central regions where magnetisation points transverse to the bar. With $V_P = 30\,\mathrm{V}$ (figure 4.3 (b)) the longitudinal triangles diminish in size as the transverse directions become increasingly an easier axis than along the bar length. Only at the edges of the bar is it favourable for the magnetisation to point along the bar due to competition between magnetocrystalline anisotropy, strain-induced and magnetostatic anisotropy energies present in the system. By $V_P = 60\,\mathrm{V}$ (figure 4.3 (c)) the strain-induced anisotropy has almost completely extinguished the longitudinal domains. On returning to $V_P = 0\,\mathrm{V}$ (figure 4.3 (d)) the domain pattern shows little change from the domain configuration at higher voltage, indicating hysteresis in the system. This hysteresis could be due to local inhomogeneities in the composition or crystal structure of the $Fe_{81}Ga_{19}$ film causing pinning of domain walls, or could be the result of hysteresis in the transducer as observed in section 2.3.3. The triangular longitudinal domains are recovered by $V_P = -30\,\mathrm{V}$ (figure 4.3 (e)).

Micromagnetic calculations were carried out to confirm the understanding of the competition between different anisotropies. The wide horizontal (section

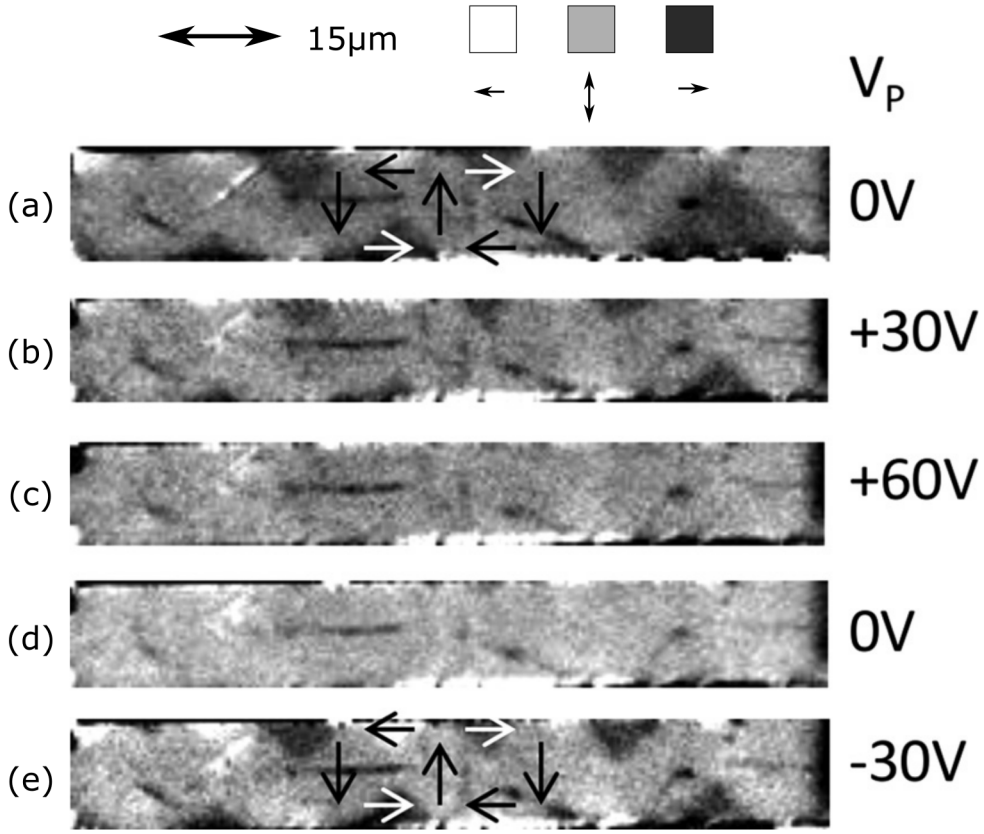

Figure 4.3: MOKE microscope images showing the evolution of the domain pattern in section 2 of the horizontal bar in the absence of a magnetic field for different voltages, V_P applied to the piezoelectric transducer. Contrast is indicated by arrows and the colour boxes. (a) At $V_P = 0$ there are clear triangular regions of longitudinally magnetised domains. These surround central regions where magnetisation points transverse to the bar. (b) With $V_P = 30\,\mathrm{V}$ the longitudinal triangles diminish in size as the transverse directions become increasingly an easier axis than along the bar length. Only at the edges of the bar is it favourable for the magnetisation to point along the bar due to competition between magnetocrystalline anisotropy, strain-induced and magnetostatic anisotropy energies present in the system. (c) By $V_P = 60\,\mathrm{V}$ the strain-induced anisotropy has almost completely extinguished the longitudinal domain. (d) On returning to $V_P = 0\,\mathrm{V}$ the domain pattern shows little change from the domain configuration at higher voltage, indicating hysteresis in the system. (e) The triangular longitudinal domains are recovered by $V_P = -30\,\mathrm{V}$

2) was simulated using a mesh size of 25 nm × 25 nm × 20 nm. In most situations this mesh size is far too large, and would result in unreliable simulation output. A more reasonable mesh size would be smaller than the exchange length in $Fe_{81}Ga_{19}$, around 4 nm. The very large size of the simulation region however prohibits the use of a more conventionally sized mesh. This mesh element size was acceptable here because of the relatively low energy density contribution of the exchange energy. The magnetocrystalline anisotropies used were those determined for wafer Mn635 by SQUID magnetometry. Also included was an extra uniaxial anisotropy energy, K_S, which represents the strain-induced anisotropy from the piezoelectric transducer, favouring magnetisation pointing transverse to the bar studied for $K_S > 0$. Only the ground state configuration was required (that is not time-resolved dynamics) so the calculations were run with a high damping factor of $\alpha = 0.5$. The result of each calculation at a given value of K_S was used as the starting configuration for the next K_S value. The range of K_S studied was based on the measurements of the magnetoelastic coupling constant $B_1 = 1.39 \times 10^7\,\mathrm{J/m^3}$, and the strain range determined in section 2.3.3 of around $\varepsilon_{xx} - \varepsilon_{yy} = 2 \times 10^{-4}$ for the voltage range used in this experiment. This corresponds to an anisotropy range required for modelling of around $4\,\mathrm{kJ/m^3}$. The stopping parameter used was 'stopping_dm_dt = 1.0'.

The results of these simulations are shown in figure 4.4. Within the range of anisotropies studied the simulations qualitatively agree with those observed in the MOKE images. The energies involved in the simulation (figure 4.4 (b)) reveal how the strain induced anisotropy energy increases sub-linearly as it is compensated by domain rearrangement, at the expense of the demagnetisation energy, as domains in the favoured direction grow. The uniaxial magnetocrystalline energy remains high because magnetisation is everywhere predominantly pointing 45° to the uniaxial easy direction [110].

To further confirm the qualitative agreement between the experimental image and the micromagnetic calculation the Matlab implementation of the Otsu method of threshold selection [234, 235] was used to bin the magnetisation data of both the MOKE microscope images and the micromagnetic simula-

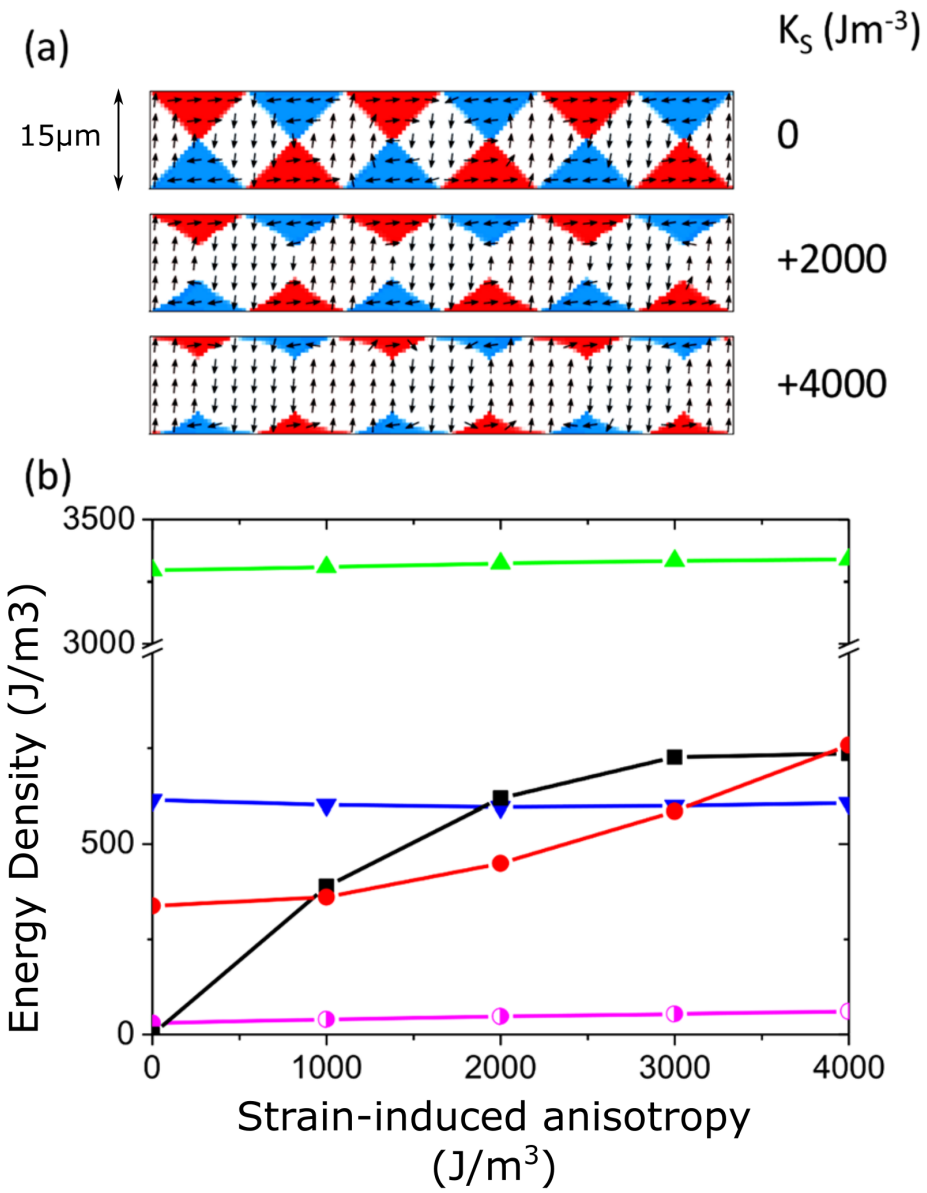

Figure 4.4: (a) The remnant magnetic domain configuration of section 2 of the horizontal arm calculated by micromagnetic simulations for different values of the strain-induced anisotropy energy coefficient (K_s). (b) The contributions of the strain-induced (black squares), demagnetisation (red full circles), cubic magnetocrystalline (blue down triangles), and uniaxial magnetocrystalline anisotropy (green up triangles) anisotropy energy terms to the total magnetic free energy in the remnant domain configuration as a function of K_S. The small contribution of the exchange energy is represented by half-filled circles.

tion output into perpendicular and parallel components. The Otsu binning method works by calculating the optimum threshold between binning levels to minimise the variance of pixels in each bin. The steps of this binning are shown in figure 4.5. To combine pixel values corresponding to parallel and anti-parallel magnetisations, the absolute pixel values, I_{abs}, were found using

$$I_{abs} = |I - I_{mean}| + I_{mean} \tag{4.1}$$

where I corresponds to the image pixel values and I_{mean} is the mean pixel value of the image. This means that pixels that were initially black become white pixels, and that sections where magnetisation is perpendicular to the bar are grey initially, so will give a low value of I_{abs}, whereas sections magnetised along the bar would be black or white initially and would give larger values of I_{abs}. The results of the binning are shown graphically in figure 4.6. The increase in uniaxial anisotropy in 4.6(a) clearly tends to favour magnetisation perpendicular to the bar axis, at the expense of those domains with magnetisation lying parallel to the bar axis. There is broadly the same trend in the MOKE microscope images 4.6(b) which shows that magnetisation perpendicular to the bar axis is favoured as the voltage across the piezoelectric transducer is increased. That the magnetisation components are not of equal proportion at $-30\,\mathrm{V}$ may be because the built-in strain is in fact not completely compensated at this voltage.

These micromagnetic simulations, with zero free parameters, have shown good agreement with experimentally obtained results. The simulations have also shown that the range of K_S required to manipulate domains in these devices is relatively small compared to K_U and K_C in this system, but is consistent with the range used to switch the magnetic easy axis direction in chapter 3.

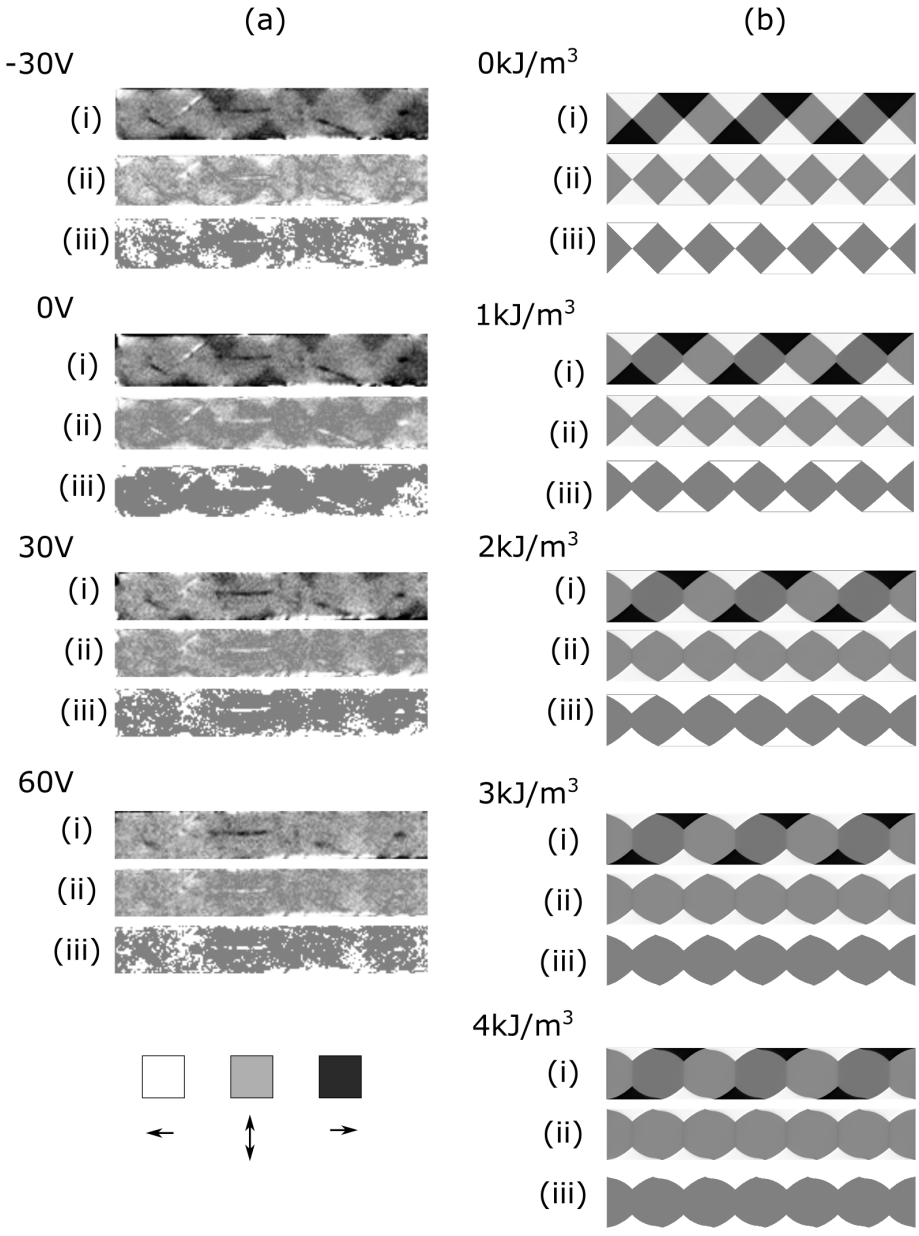

Figure 4.5: Analysis of images to determine proportion of bar section with magnetisation lying parallel and perpendicular to the bar axis for (a) MOKE microscopy images and (b) micromagnetic simulations. In each case (i) corresponds to the raw image, and (ii) to the absolute pixel values of the raw image. (iii) shows bins corresponding to magnetisation parallel (white) and perpendicular (grey) to the bar axis.

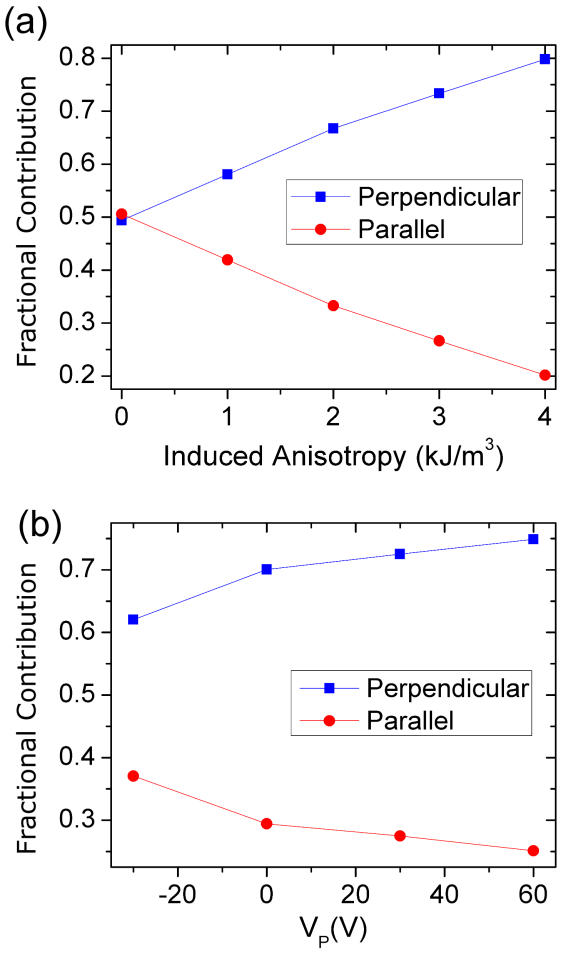

Figure 4.6: Parallel and perpendicular magnetisation components in (a) micromagnetic simulation output images (b) MOKE microscope images. Increasing the voltage (V_P) across the piezoelectric transducer has the effect of increasing the uniaxial anisotropy perpendicular to the bar. The steps in obtaining these values are shown in figure 4.5. The increase in uniaxial anisotropy in (a) clearly tends to favour magnetisation perpendicular to the bar axis, at the expense of those domains with magnetisation lying parallel to the bar axis. There is broadly the same trend in the MOKE microscope images (b) which shows that magnetisation perpendicular to the bar axis is favoured as the voltage across the piezoelectric transducer is increased. That the magnetisation components are not of equal fractional contribution at $-30\,\mathrm{V}$ may be because the built-in strain is in fact not completely compensated at this voltage.

4.3 Modification of Flux Closure Domains In Micron-Sized Discs

This section provides an additional example of how an ordered domain configuration can be manipulated using strain-induced anisotropy, by controlling the flux-closing domain configuration of a 2.2 µm $Fe_{81}Ga_{19}$ disc. Disc structures are of interest because they tend to form vortex or flux-closing domain configurations which may be used in memory devices and spin-torque oscillators [236].

4.3.1 Sample

Samples in this study were produced from wafer Mn746, a 14 nm thick sample of $Fe_{81}Ga_{19}$ on an n-doped GaAs (100) substrate, with a 1.4 nm thick amorphous GaAs capping layer to prevent oxidisation. It was necessary to use an n-doped conducting substrate to prevent charging during the XMCD-PEEM imaging process. From previous X-ray studies on $Fe_{81}Ga_{19}$ (see chapter 3) it was known that this material grows epitaxially on GaAs (001). SQUID magnetometry showed the anisotropies to be $K_c = 18.9\,\mathrm{kJ/m^3}$, favouring the [100]/[010] direction, and $K_u = 12.4\,\mathrm{kJ/m^3}$, favouring the [110] direction.

4.3.2 XMCD-PEEM measurements

XMCD-measurements were made on the disc sample to investigate the domain configuration as a function of voltage applied to the piezoelectric transducer. Strain was induced in the magnetic layer along the [010] direction via a voltage applied to a piezoelectric transducer. Figure 4.7 reveals how the magnetisation has formed a flux-closing domain pattern to minimise the stray field. By adjusting the voltage applied to the piezoelectric transducer the strain-induced anisotropy in the $Fe_{81}Ga_{19}$ layer was manipulated (figure 4.7) (a – d). This changed the balance of energies which caused the domains

to reconfigure. The strain-induced anisotropy axis is along the [010] direction. Domains parallel to this direction grow at the expense of those perpendicular to it. The asymmetry in the black and white triangular regions is caused by the intrinsic uniaxial anisotropy present in the $Fe_{81}Ga_{19}$ layer, which favours magnetisation along the [110] direction.

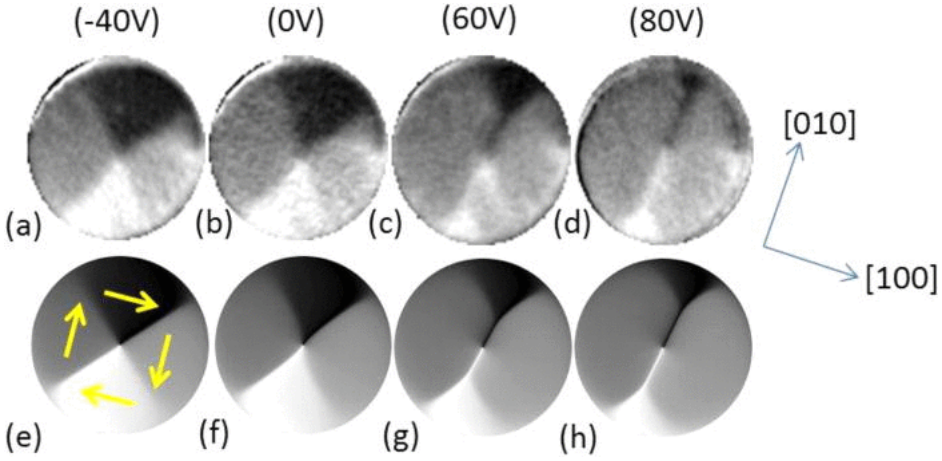

Figure 4.7: Evolution of magnetic domain pattern in a 2.2 µm circular FeGa/PZT structure for different voltages applied to the PZT transducer (top, a-d). Micromagnetic simulation of the 2.2 µm FeGa/PZT device (bottom) with K_S equal to (e) 0, (f) 3.5, (g) 8.4, and (h) 10 kJ/m^3. The yellow arrows indicate the direction of magnetisation in each domain.

Micromagnetic calculations confirmed that the domain configuration can be controlled by uniaxial anisotropy. Micromagnetic calculations were carried out using the Object Oriented Micromagnetic Framework (OOMMF). The cell size used 2 nm × 2 nm × 10 nm to create a 2-dimensional array of 3-dimensional spins. The stopping parameter used was stopping_dm_dt = 1.0. Figure 4.7 (e–f) shows the domain configuration calculated for a range of uniaxial anisotropies. The energy of constant uniaxial strain-induced anisotropy, K_S, is comparable to the range expected for the strain induced by this piezoelectric transducer at this temperature and voltage range [223]. The need to apply a large negative bias to the piezoelectric transducer to produce the state expected for zero induced strain is consistent with the observation of near-cubic biaxial anisotropy in the hysteresis loop in figure 4.1(c). Dynamic

micromagnetic calculations carried out by Stuart Cavill revealed that the voltage-induced strain can cause a marked change in spin oscillations, and the frequency and orbital motion of the central core of the flux-closing domain state [236]. These observations will be of interest for the study of tuneable spin-torque oscillators, but a study of the dynamics is beyond the scope of this present work and will be carried out separately.

4.4 Effect of Growth Strain on Magnetic Domain Configuration

This section presents investigations into an additional contribution to the anisotropy energy which can result from the relaxation of growth strain at the edges of lithographically patterned bars when the width is reduced to the order of 1 µm. This strain-relaxation originates from a lattice mismatch between the epitaxially grown magnetic layer and the substrate.

4.4.1 Sample

The sample was fabricated from wafer Mn746, described in chapter 2 and section 4.3. From this 14.3 nm layer of $Fe_{81}Ga_{19}$ a bar of width 1.2 µm was fabricated using electron beam lithography carried out by Dr. Ryan Beardsley and Ar ion milling by Paul Warburton and Ivan Isakov from the London Centre of Nanotechnology, University College London. The milled depth was greater than the film thickness which resulted in a 100 nm GaAs mesa with the $Fe_{81}Ga_{19}$ and capping layers on top, as shown in figure 4.8 (a). This investigation focusses on the behaviour in one 6 µm-long arm of an L-shaped structure.

4.4.2 XMCD and micromagnetic calculations

The sample was imaged using the X-ray Photoemission electron microscope as described in chapters 1 and 2. Figure 4.12 (a) shows an image of the domain configuration in the 1.2 µm by 6 µm bar. The flux-closure domain configuration observed is different to that seen in previous studies of wires with width 45 µm and 15 µm presented in figures 3.17 and 4.3 respectively, in that the regions with magnetisation perpendicular to the length of the bar are broadened at the edges of the bar. This is attributed to the relatively larger effect of strain relaxation at the bar edges in this smaller device, as will be explained in the following section.

Finite element structural calculations were carried out by Dr. Jan Zemen using the COMSOL software package to gain insight into the structural behaviour of a strain-relaxed bar. A bar was simulated as having infinite length and the same cross sectional dimensions as the experimental device. A fixed structural constraint was set at the substrate boundaries and an initial in-plane compressive strain of $(a_{Bulk} - a_0)/a_{Bulk} = 1.4\,\%$ was included in the $Fe_{81}Ga_{19}$ layer, where $a_{Bulk} = 0.287\,\text{nm}$ is the bulk lattice parameter of $Fe_{81}Ga_{19}$, and a_0 is half the lattice parameter of GaAs. The over-etch into the GaAs substrate was included in the calculation. Figure 4.8(a) shows the simulated layer profile and the relaxed strain as a function of position in the bar cross section. From these calculations it was possible to extract the strain profile shown in figure 4.9, which reveals that there is strongly localised strain at the edges of the bar. There is a non-zero strain relaxation in the centre of the cross section, which increases in amplitude away from the bar centre. A similar, edge-localised effect was also seen in the previous studies on GaMnAs-based device. An interesting feature of this profile is the abrupt decrease in amplitude in the regions near to the edges of the bar. This discontinuity seems to arise from the GaAs capping layer, which tends to suppress the relaxation of the in-built strain by partially clamping the top surface as shown in 4.8 (b). The GaAs cap was included in the calculation as a single 1.4 nm thick layer, which assumed bulk-like amorphous GaAs properties, with no oxidation.

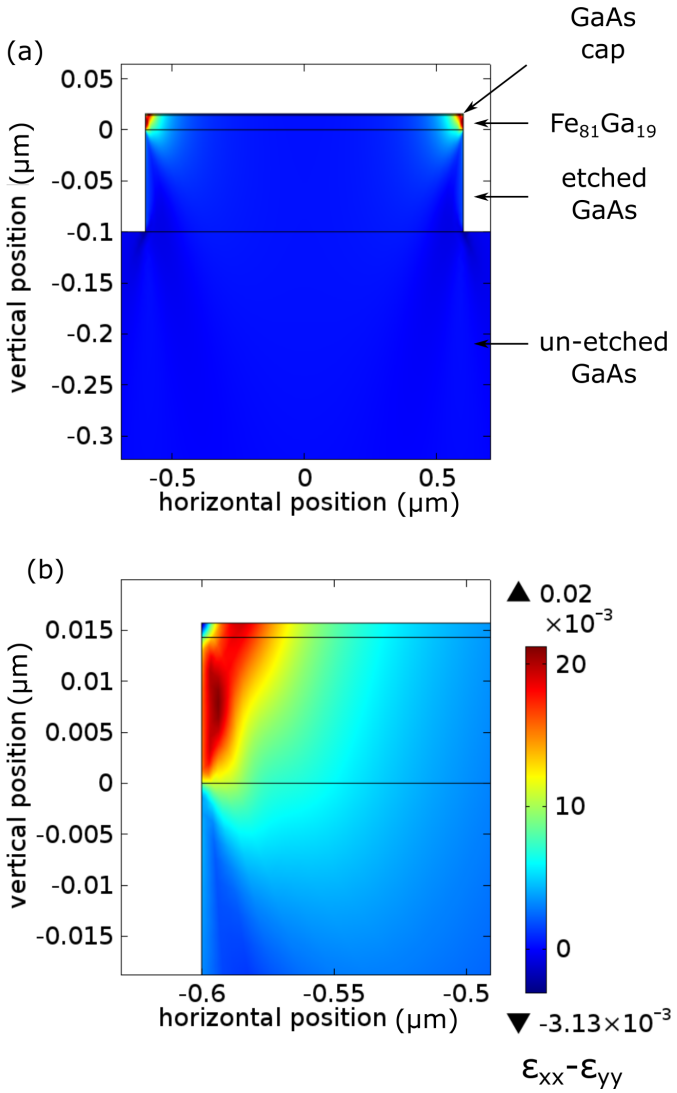

Figure 4.8: (a) The layer structure of the experimental device and color scale map showing the relaxation of the growth strain as a function of position in the bar. (c) A zoomed section of (a) showing the relaxation of the growth strain as a function of position in the edge region of the bar

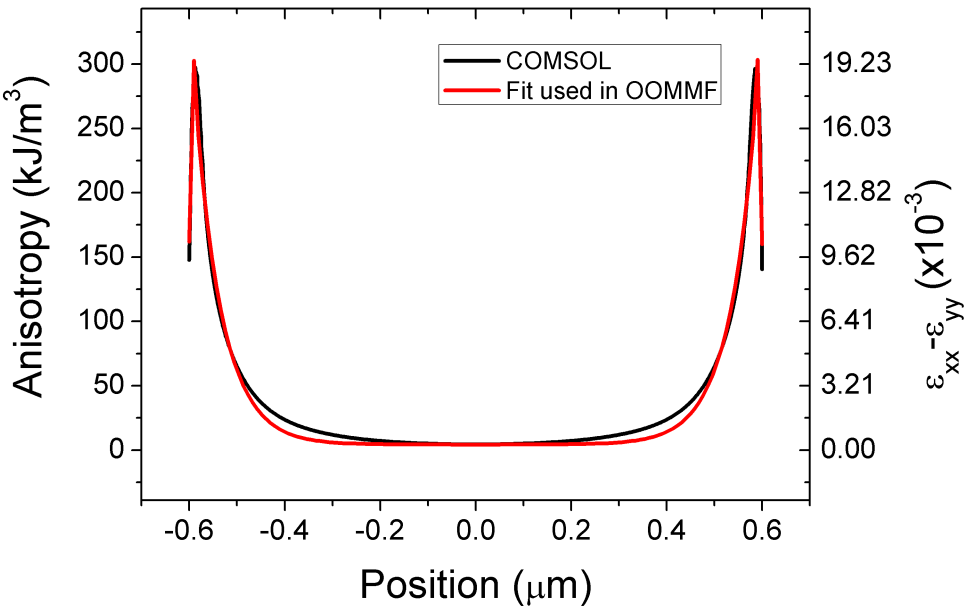

Figure 4.9: The simulated strain and anisotropy energy profile across the $Fe_{81}Ga_{19}$ bar at the FeGa/Cap interface. The COMSOL simulation is shown (black) along with the fit (red) used to input into the OOMMF micromagnetic simulation.

To understand the experimentally observed domain configuration micromagnetic calculations were performed using OOMMF. The simulation used magnetocrystalline anisotropy coefficients taken from the SQUID magnetometry, a cell size of 2 nm × 2 nm × 10 nm, $\alpha = 0.5$ and stopping_dm_dt = 0.01. A 10 nm z dimension of cell size was based on the nominal $Fe_{81}Ga_{19}$ layer thickness. The OOMMF simulation was initialised in a flux-closing state, with flux-closing units (see figure 4.10) having an aspect ratio of 1:1.3, which is the average aspect ratio present in the experimental image. A 6 µm-long bar and an infinitely-long bar (that is, periodic boundary conditions) were simulated. The approximate equivalence of the shape anisotropy in each of these situations was confirmed by simulating devices initially saturated along the negative x-direction, as a function of magnetic field applied along the y-direction. The results of these simulations are shown in figure 4.11.

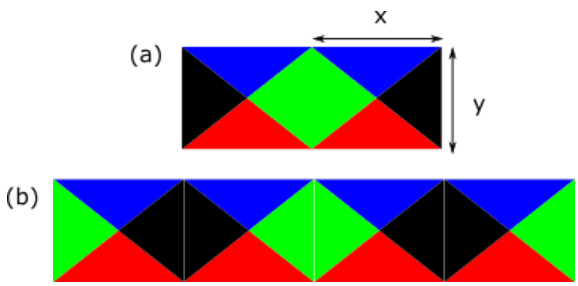

Figure 4.10: Bitmap initialisation for (a) periodic, and (b) 6 µm long wire section. $y = 1.2$ µm. The ratio $x/y = 1.3$ was the average ratio present in the experimental image.

The change in energy density corresponding to the simulated strain was found using the relation between strain and magneto-elastic energy, $\Delta E = 3/2\lambda_{100}(c_{12} - c_{11})\varepsilon$, with the value of $3/2\lambda_{100}(c_{12} - c_{11}) = 1.56 \times 10^7$ J/m^3, taken from the study of the magnetostrictive properties of MBE-grown $Fe_{81}Ga_{19}$ presented in chapter 3. To include this term in the micromagnetic calculations the simulated energy density profile was approximated using an exponential rise and a linear fall for each edge of the region studied, as shown in figure 4.9. This strain-induced anisotropy energy was then included in the OOMMF calculation as an additional uniaxial magnetocrystalline anisotropy term, K_S, with the anisotropy axis perpendicular to the

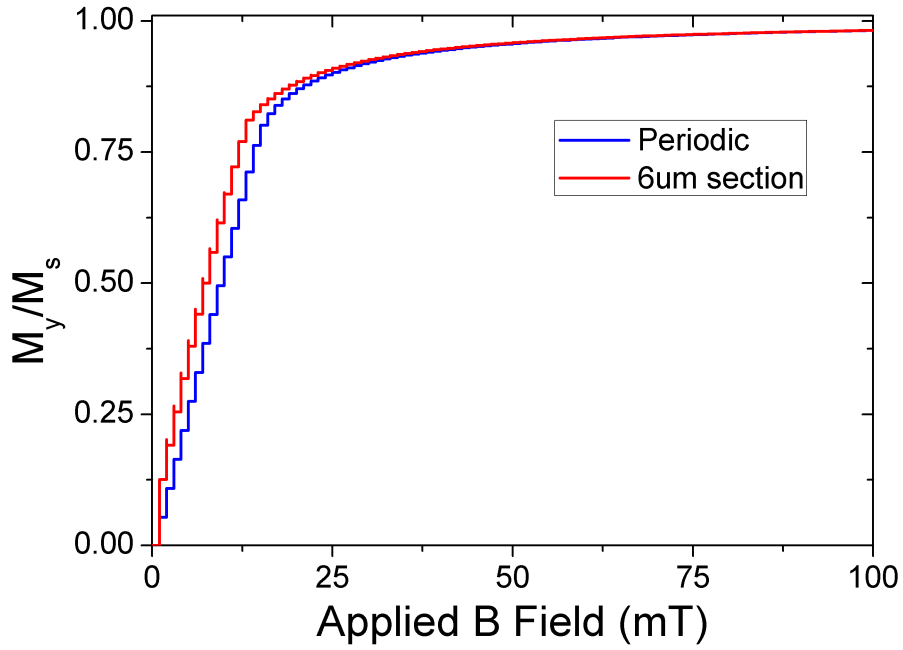

Figure 4.11: Normalised y-component of magnetisation as a function of applied B field for finite (blue line) and periodic (red line) simulations. The magnetocrystalline and strain-induced anisotropies were turned off in these simulations, so these curves show the approximate equivalence of the shape anisotropy in each of the simulations.

length of the bar. The linear sections were represented (in units of J/m^3) by $K_S = \pm -4.56 \times 10^{13} y + 5.52 \times 10^5$, where y was the transverse position along wire. The exponential fitted to the COMSOL curve was, again with units of J/m^3, $K_S = y_0 + A \exp((w - y)/R)$ where $y_0 = 13 \times 10^3\,J/m^3$, $A = 10 \times 10^6\,J/m^3$ and $R = -5.72\,m$, again with y the transverse position along the wire. $w = 0\,nm$ for the right-hand exponential and $w = 1200\,nm$ for the left hand exponential.

The results of micromagnetic calculations based on the approximated anisotropy profile are shown in figure 4.12(b). Similar to the experimental data, the ground state is a flux-closure pattern with the regions magnetised perpendicular to the length of the bar. To observe the broadening of the domain boundaries at the edges and centre of the bar the magnitude of the strain-induced anisotropy was increased by a factor of two in the simulations shown in figure 4.12(c). Many approximations were used to model the strain induced in the $Fe_{81}Ga_{19}$ sample including modelling it as a homogeneous, infinitely-long, strip with zero edge roughness. That the essential qualitative features of the experiment can be recovered by altering the simulation by only a factor of two are an indication the model is reasonable.

Figure 4.12(d) shows a calculation without the additional strain-induced anisotropy, which reveals that the bar will not support the regular flux closure domain configuration in the absence of the strain-induced anisotropy due to the dominant role of the shape-induced anisotropy. Calculations on bars with the same 1.2 µm width, but using periodic boundary conditions to simulate infinite length, shown in figure 4.12(e), revealed that a very similar flux closure pattern exists when the strain induced anisotropy is included. This final simulation confirms that the domain configuration in the simulations of the finite-length bar were not the result of the end-effects present in the simulation.

In $Fe_{81}Ga_{19}$ the cubic magnetocrystalline anisotropy supports magnetic easy axes along the [100] and [010] directions. The magneto-elastic effects are largest in the direction of strain relaxation due to the magnetostriction con-

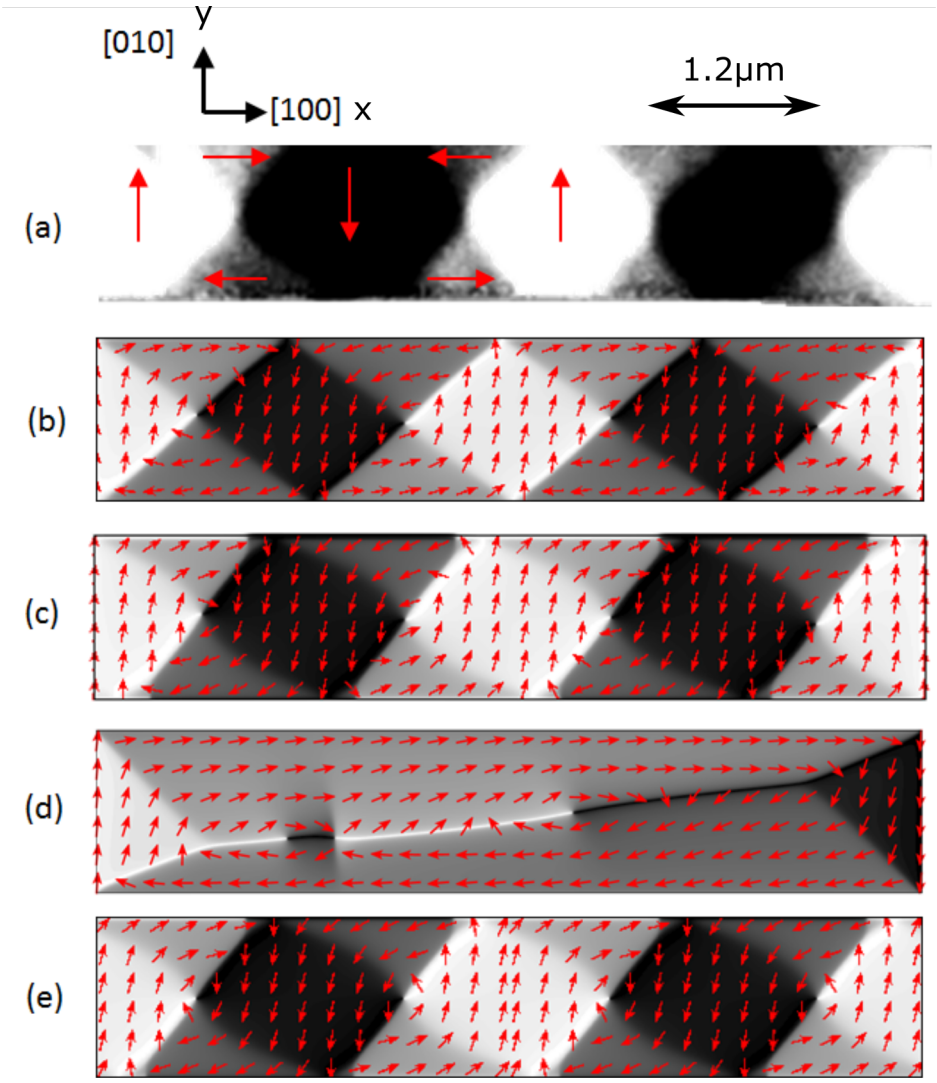

Figure 4.12: (a) Experimental PEEM image with arrows indicating the magnetization direction. (b) OOMMF simulation for the 1.2 µm × 6 µm bar with an anisotropy profile that includes the calculated strain relaxation profile. (c) To observe the broadening of the domain boundaries at the edges and centre of the bar the magnitude of the strain anisotropy term was increased by a factor of two in the simulations. (d) Calculation without the additional strain-induced anisotropy which reveals that the bar will not support the regular flux closure domain configuration in the absence of the strain-induced anisotropy. (e) Calculation on bars with the same 1.2 µm width, but using periodic boundary conditions to simulate infinite length. Here two identical images of the periodic unit cell have been stitched together.

stant in $Fe_{81}Ga_{19}$ being an order of magnitude larger along the [010]/[100] directions than the [110] direction [123]. To further confirm the qualitative agreement between the experimental image and the micromagnetic calculation the Matlab implementation of the Otsu method of threshold selection [234, 235] was used to bin the magnetisation data into perpendicular and parallel components. The results of this analysis for both the simulated and experimentally obtained images are shown in figure 4.13. The experiment (figure 4.12(a)) and simulation (figure 4.12 (b)) are in excellent agreement with 80 % and 74 % of the magnetization perpendicular to the bar respectively. The control simulation, with no strain relaxation (figure 4.12(d)), is dominated by the shape anisotropy and shows only 18 % of the magnetisation perpendicular to the bar.

This investigation has revealed that relaxation of growth strain may be an important consideration in the study and design of micron sized devices based on $Fe_{81}Ga_{19}$. In the 1.2 µm wide bars investigated, the strain-induced anisotropy stabilises the formation of a regular flux-closure domain configuration and distorts the features near the edges of the bar. Growth strain is an additional degree of freedom to be controlled or manipulated in the design of nanoscale magnetic devices and experiments. The strain relaxation is largest in the region around 50-100 nm from the edges of the structure, therefore, the effects observed may well be more prominent in narrower wires, which offers potential for further investigation and tuning of the strain-relaxation-induced anisotropy. These observed effects could become very important as devices from MBE-grown $Fe_{81}Ga_{19}$ layers are scaled down to sub-micron sizes.

This has been a limited study, examining just a single device experimentally and there are a number of things that could be done to develop it further. From an experimental stand point it would be interesting to observe more devices over a range of widths, which would alter the relative effect of any strain-relaxation present. It would also be interesting to study a range of orientations of the bar with respect to the $Fe_{81}Ga_{19}$ axes which would effectively vary the magnetoelastic effect of any strain relaxation. Orienting the bar axis along the [110] direction would be of particular interest as the magnetostric-

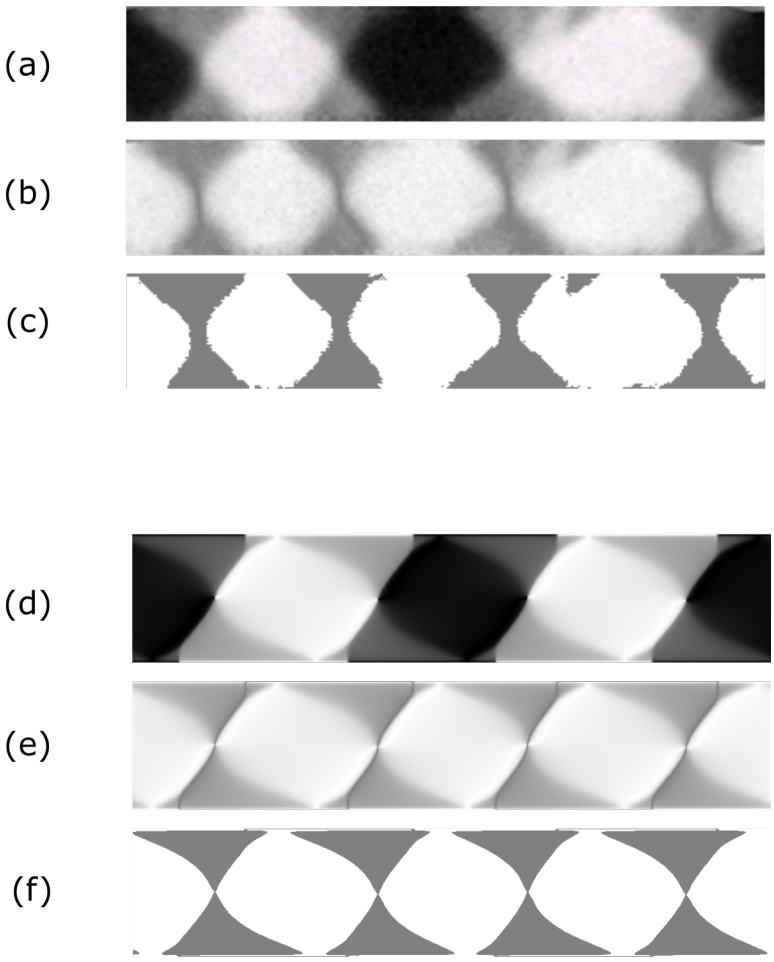

Figure 4.13: Grey-level binning analysis for PEEM (a–c) and micromagnetic simulation (d–f) images. (a, d), the original image. (b, e) The absolute pixel values. (c, f) Bins corresponding to components parallel and anti-parallel (grey) and perpendicular (white) to the bar axis.

tion in $Fe_{81}Ga_{19}$ is not enhanced along this direction, so the effect on the magnetisation of any strain-relaxation would be much reduced. The results presented here also seem to indicate that the capping layer is important, and future studies could include an investigation of different capping thicknesses and materials to determine exactly the role it plays, and also optimise the strain-relaxation if it is to be used in future technologies.

The simulations could also be developed further to better reflect the physical system. It would be particularly interesting to more directly combine the micromagnetic and microstructural calculations, possibly be using a finite element micromagnetic package to take an of the strain profile directly from the finite element microstructural calculation. The microstructural calculation could also include more realistic variations in material parameters, such as oxidation of the capping layer or the $Fe_{81}Ga_{19}$.

These possible future experimental and simulated studies would have scientific interest as they may better determine the existence, origin and significance of the strain-relaxation. A better understanding of the strain relaxation in $Fe_{81}Ga_{19}$ would also be of interest for the optimisation and development of possible technological applications.

4.5 Conclusion

This chapter explored the control of anisotropies and magnetic domains in microfabricated $Fe_{81}Ga_{19}$ devices with sizes of order 10 µm and smaller. The work presented in this chapter highlights the importance of size and scaling on the future of devices based on magnetostrictive principles. As different anisotropies are introduced the behaviour of domains and our ability to control them is altered.

Firstly in an L-shaped bar with 8 µm and 15 µm wide sections, the magnetic reversal characteristics as a function of voltage applied to a piezoelectric transducer were investigated. Also in this bar it was demonstrated that the uniaxial anisotropy induced in the $Fe_{81}Ga_{19}$ layer could be used, in the absence of an

externally applied magnetic field, to control the ordered flux-closing magnetic domain state found in the device. Another example of the control of an ordered domain configuration was investigated in micron-sized disks. XMCD-PEEM and micromagnetic calculations demonstrated the 'pinching' of the flux-closing domain configuration using strain-induced uniaxial anisotropy. The voltage-control of magnetisation in disks may have technological applications in microwave electronics, and this initial demonstration has laid the foundations for future work in this area.

The importance of the relaxation of growth strain in the magnetic domain configuration of 1 µm wide $Fe_{81}Ga_{19}$ wires was investigated. It was found that a distorted flux-closing domain pattern could be supported in the wire by the presence of the growth-relaxation-induced uniaxial anisotropy, transverse to the long axis of the wire. This observation could be of use or a hindrance in the development magnetisation- and domain-wall-based technologies using $Fe_{81}Ga_{19}$.

Chapter 5

Control of Domain walls in Nanowires

5.1 Introduction

This chapter examines the effect of uniaxial strain-induced anisotropy on domain wall motion and depinning from a notch in micron and sub-micron sized wires. The chapter begins by looking at the depinning behaviour of domain walls in micron-wide wires of Co bonded to a piezoelectric transducer. Focussed MOKE supported by micromagnetic calculations is used to investigate the pinning behaviour of vortex domain walls and how the strain dependence of the depinning field depends on the chirality of the domain wall. Clockwise vortex domain walls are much more sensitive than anticlockwise vortex domain walls to uniaxial anisotropy and variations in the notch depth. Modulation of the depinning field of two chiralities of vortex domain walls in 1 µm wide wires is achieved, with the depinning field of anti-clockwise vortex walls having a negative dependence on uniaxial anisotropy along the wire axis, while clockwise vortex domain walls generally have a positive, but smaller dependence. The simulations and measurements for vortex walls show reasonable agreement in terms of the fields required to depin the domain wall from the notch studied. Analysis of the micromagnetic simulation outputs for a range

of simulated notch depths indicates that there are two depinning regimes for the clockwise domain wall, which results in a wide variation in the sensitivity of the domain walls of this chirality to depinning. There were significant differences in the dependence of depinning field on uniaxial anisotropy of the two wires studied which may have been due to slight differences in the lithography or deposition of the two wires. Such variation in the effects observed between devices is likely to be problematic for device applications, so future studied must address the sensitivity of the anisotropy-dependence of depinning behaviour to such issues.

The chapter goes on to simulate the behaviour of domain walls in 100 nm and 48 nm nanowires which support transverse walls rather than vortex walls. The changes in domain wall mobility observed in the simulations are broadly in keeping with the changes associated with a change in domain wall width resulting from the additional uniaxial anisotropy energy. The agreement with the expected theoretical values is not as good in wider wires, which, it is speculated, is due to the increased deviation from the narrow wire regime. An important result of this chapter is that it is found that in nanowires 100 nm wide there is a second peak in average domain wall velocity at high driving fields above the Walker breakdown regime when the wire is under the influence of a uniaxial anisotropy. This observation builds on previous studies where similar effects have been observed both experimentally and in simulations of relatively wide wires [237], wires under the influence of transverse magnetic fields [238] and perpendicularly magnetised ferromagnetic semiconductors [239].

Finally, this chapter also begins to investigate how strain-induced uniaxial anisotropy affects the depinning of transverse walls from notches in wires of width 48 nm and 100 nm. It is observed that in the 48 nm wires studied there is a linear dependence of depinning field on strain, with a negative gradient. In the 100 nm wires studied, however, the relationship is non-linear, with a positive average gradient. This large difference in behaviour across the range of anisotropy energy densities and wire widths studies marks out a large area of parameter space to explore in the future.

5.2 Focussed MOKE measurements of microwires

5.2.1 Sample

The sample used for this study was labelled dp012c, consisting of a stack of Pt(5 nm)/Co(10 nm)/Al(2.5 nm) sputtered onto a 100 µm Si (111) substrate. This sample featured 1 µm wide wires with a 675 nm deep triangular notch defined using electron beam lithography by Dr Andrew Irvine at the University of Cambridge. Further details of the growth and fabrication of this sample are given in chapter 2.

A schematic of the device layout is shown in figure 5.1. One end of the wire has a large pad to facilitate domain wall nucleation where it joins the wire. The other end has a tapered section to suppress domain formation there [240]. Two devices were measured on this chip: dp012c-1, and dp012c-2. dp012c-2 was fabricated in an identical way to dp012c-1, but was rotated by 90°. In device dp012c-1 a positive voltage applied to the transducer induced a tensile strain perpendicular to the length of the bar. In device dp012c-2 a positive voltage induced a tensile strain parallel to the length of the bar.

5.2.2 Depinning Fields in Co

The sample was mounted in an electromagnet, capable of applying up to 30 mT along the length of the wire at a frequency of 20 Hz. For the experiment a 4 µm diameter laser spot was focussed onto the sample, in the position marked in figure 5.1. Domain wall processes are stochastic in nature, so 100 measurements of hysteresis loops were made to build up a picture of the aggregate domain wall behaviour.

Device dp012c-1 was measured first. The hysteresis loop from a single field sweep shown in figure 5.2 shows clearly the rapid change in magnetisation direction that is associated with a domain wall moving along a wire past the laser spot. A domain wall is nucleated in the injection pad on the left hand

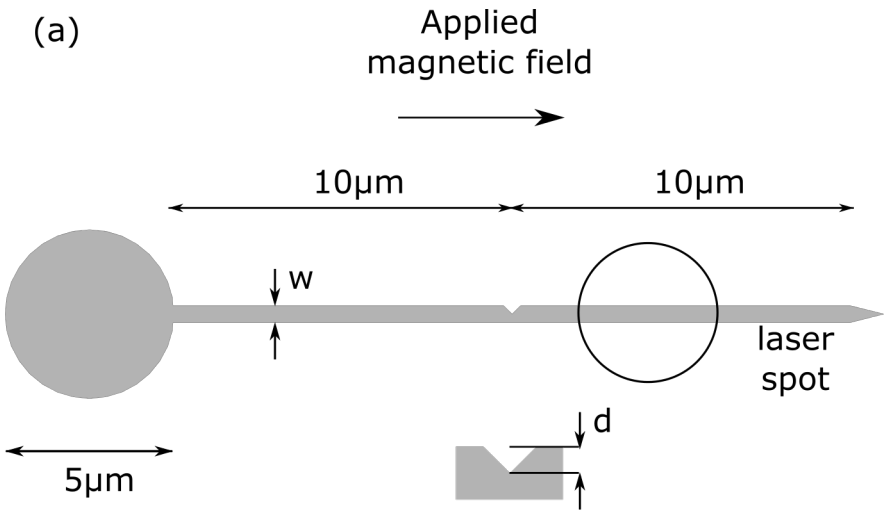

Figure 5.1: (a)Schematic of the device measured by MOKE in Sheffield. Two devices of this geometry were measured: dp012c-1 and dp012c-2. dp012c-2 was oriented orthogonally to dp012c-1 on the piezoelectric transducer. Also shown is the approximate size and location of the laser spot used. w = 1 µm, d = 675 nm. (b) AFM image of notch.

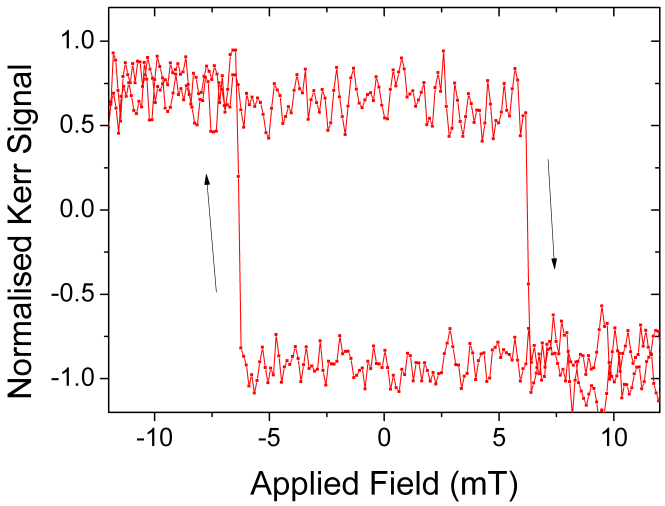

Figure 5.2: Single-shot MOKE hysteresis loop. The magnetisation signal rapidly switches as a domain wall depins from the notch and sweeps through the wire. This MOKE hysteresis loop was measured on a device similar to the dp012c device studied in this chapter, with zero bias applied across the transducer.

side of the device (shown in figure 5.1). The laser spot is sensitive to the local change in magnetisation associated with the movement of domains away from the nucleation pad from left to right. The main focus of this study was the behaviour of domain walls moving from left to right under the influence of a positive magnetic field.

The depinning field of a vortex domain wall at an asymmetric notch depends on its chirality [115, 241] so one would expect to see evidence of two depinning fields, corresponding to clockwise and anti-clockwise vortex walls. An example of this double step is shown in figure 5.3 where there are steps at around 7.5 mT and 11 mT. This figure shows an averaged hysteresis loop built up from 100 individual field loops. The figure also shows that there is evidence of a third, smaller step at 4.0 to 4.5 mT. This is likely due to an optical interference fringe from the Airy disk of the laser spot picking up a small part of the section of wire between the nucleation pad and the notch, which has a lower reversal field, consistent with the field at which this smaller step occurs

(see figure 5.4).

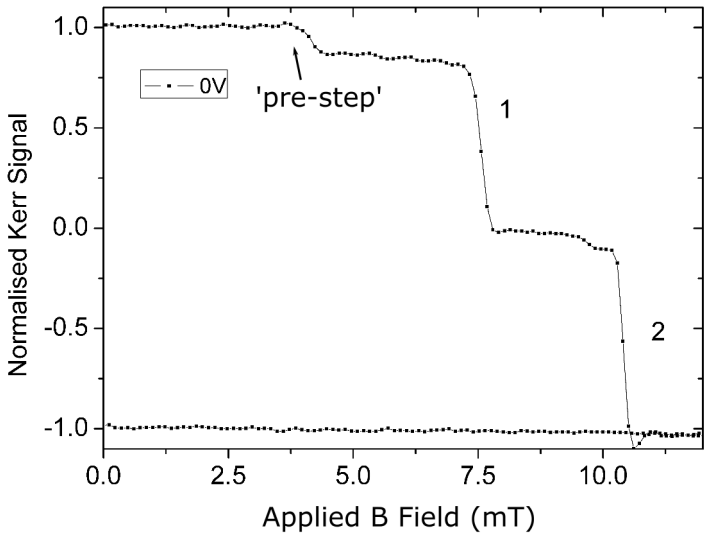

Figure 5.3: Example of the expected double step in averaged MOKE hysteresis loops from the presence of clockwise and anticlockwise vortex domain walls. A smaller 'pre-step' at around 4.5 mT may originate from a reflection of the laser from the nucleation pad. This example was taken from device dp012c-1, with zero bias across the transducer.

The reversal fields with the laser spot positioned on the region of wire after the nucleation pad and before the notch are shown in figure 5.4(a). These switching fields are interpreted as the fields required to nucleate domain walls. This graph itself shows evidence of a dependence on the voltage applied to the transducer. The switching fields for positive 5.4(b) and negative 5.4(c) fields are also shown which indicate that there is a significant variation over the voltage range studied. At higher positive voltages there is variation between the two repeated measurements at the same voltage indicating that there is a stochastic element to the domain wall nucleation which may be due to hysteresis or drift within the piezoelectric transducer.

Measurements with the laser spot focusing in a region to the right hand side of the notch, as shown in figure 5.1, were carried out for a range of voltages applied to the piezoelectric transducer in the range 48 V to −30 V. The hys-

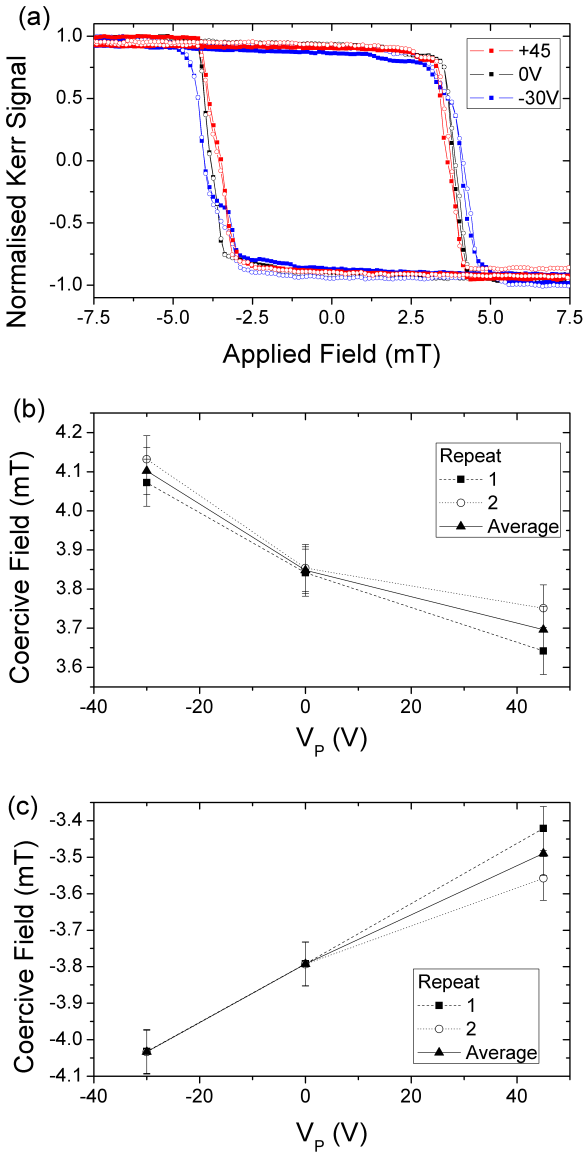

Figure 5.4: (a) Averaged MOKE hysteresis loops of the reversal field of Co wire in the region between the nucleation pad and the notch. This represents the magnetic field required to inject a domain wall from the injection pad into the wire. The coercive field in these loops was measured as the field required to reduce the (averaged) normalised Kerr signal to zero. The variation in this coercivity as a function of voltage is shown for positive (b) and negative (c) applied magnetic field. There are significant differences in the coercive field as a function of voltage, although the differences between measurement runs are within the uncertainty of the measurements, as determined from the the minimum B field step size.

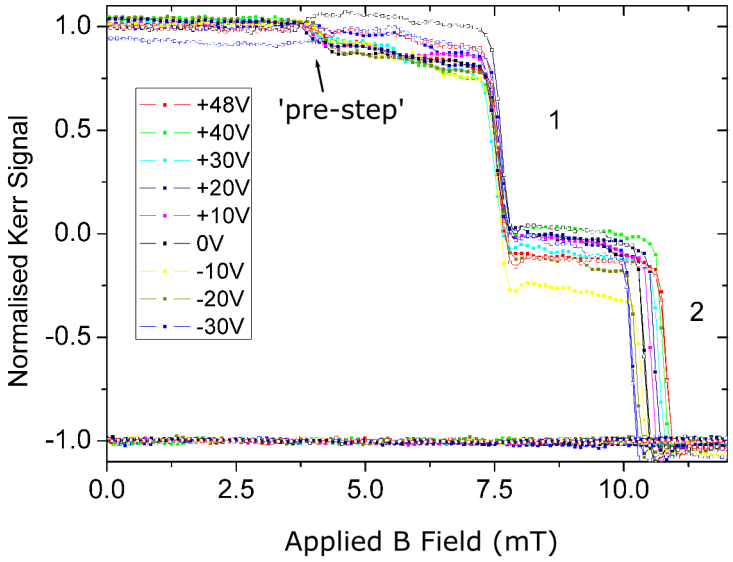

Figure 5.5: Averaged MOKE hysteresis loops of device dp012c-1 for different voltages applied to the piezoelectric transducer. There are three clear steps. The 'pre-step' is at the same switching field as in figure 5.4 so corresponds to the nucleation of the domain wall in the wire. The first depinning event, labelled '1', at approximately 7.5 mT is much less sensitive to changes in voltage than the second, labelled '2', at around 10 mT.

teresis loops collected at each transducer voltage are shown in figure 5.5. The two main depinning events are present in the loops and it is clear that the second depinning field is much more strongly dependent on the strain induced by the piezoelectric transducer. The two depinning fields as a function of voltage applied to the transducer are shown in figure 5.6(a). The fitting parameters of a linear fit to each of the plots are given in table 5.1. This graph and the linear fits to the data confirm the trends observed in the hysteresis loops for the second depinning event to be much more sensitive, since the gradient parameter, H_E is up to around 20 times larger for the second chirality than the first.

Table 5.1: Fitting parameters for linear fits to depinning field as a function of voltage (see figure 5.6), H_0 is the offset, and H_E the slope. The superscript H denotes depinning fields derived from fits to the single-shot measurement histograms in figure 5.8.

Device	Chirality	H_0 mT	H_E mT/V	R^2
dp012c-1	1	7.556(9)	−0.0005(3)	0.1276
	2	10.403(6)	0.0087(2)	0.9928
dp012c-2	1	3.75(2)	0.0042(5)	0.8861
	2	6.72(2)	−0.0121(4)	0.9867
dp012c-2^{H}	1	3.68(3)	0.0017(7)	0.2951
	2	6.69(1)	−0.0126(3)	0.9926

Following on from the measurements on device dp012c-1, the depinning behaviour in device dp012c-2 was investigated by James Wheelwright at the University of Sheffield which confirmed the chirality dependent response to the strain induced by the transducer. Figure 5.7 shows the characteristic double step behaviour associated with averaging over two switching events. A plot of the depinning fields for device dp012c-2 as a function of voltage applied to the transducer is shown in figure 5.6(b). The fitting parameters for a linear fit to each chirality are shown in table 5.1. The trends observed in this device are broadly consistent with those observed in device dp012c-1 in as much as the second chirality (higher depinning field) is more sensitive to strain. An important distinction to make however is that the second device

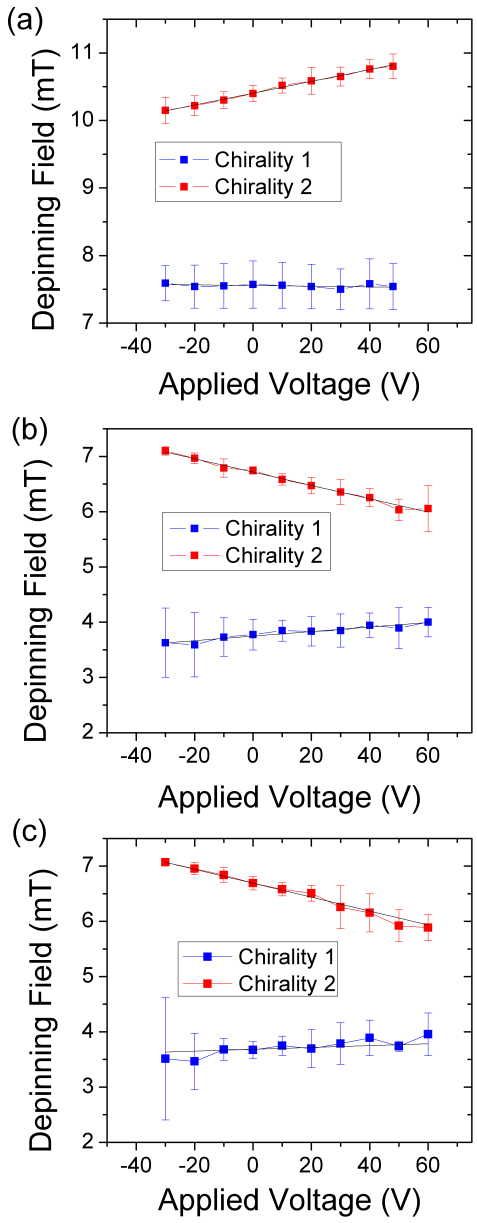

Figure 5.6: Depinning fields as a function of voltage applied to the piezoelectric transducer for (a) device dp012c-1,(b) device dp012c-2, and (c)dp012c-2^{H} determined from histograms of single-shot measurements. The difference in sign of the slopes between (a) and (b-c) is due to the orthogonal orientation of the wires in each device, which changes the sign of the magnetoelastic energy induced by the strain. In (a) and (b) the error bars were determined from beginning and end of the switching events in the averaged MOKE loops (figure 5.5 and 5.7 respectively). The error bars in (c) come from the Gaussian fits to the histograms in figure 5.8.

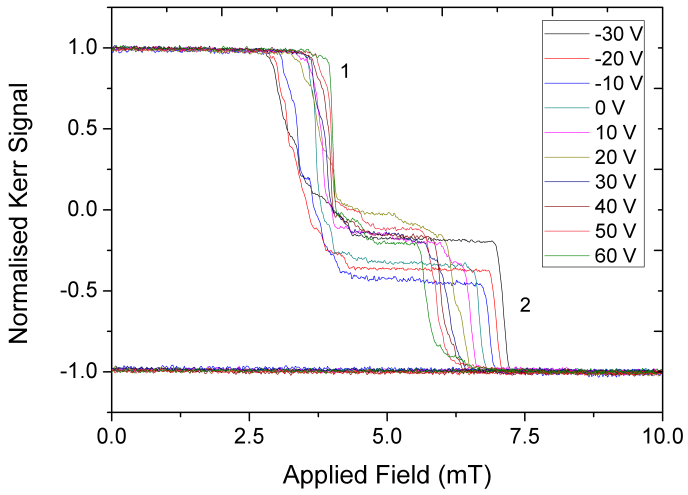

Figure 5.7: Averaged MOKE hysteresis loops as a function of voltage applied to the piezelectric transducer for device dp012c-2, as measured by James Wheelwright at the University of Sheffield. The first switching event is much more sensitive to strain induced by the piezoelectric transducer than the second.

was oriented at 90° to the first so that positive voltage applied to the transducer induced tensile strain parallel to the wire axis rather than perpendicular to it. This explains why in device dp012c-1 the depinning fields tend to converge at high positive voltage, while in device dp012c-2 the depinning fields diverge at high positive voltage. The depinning fields are markedly lower for device dp012c-2 compared to dp012c-1, and the depinning field associated with the first chirality appears to be much more responsive to strain than was observed in dp012c-1. These variations may be due to slight variations in lithography or local anisotropy. As this figure shows the average of 100 field sweeps, the broadening of the step in the hysteresis loop at the first switching event indicates that the domain wall depinning took place over an appreciable range of fields.

Histograms of single shot measurements shown in figure 5.8 reveal more information about the distributions of depinning events. It is immediately clear that the depinning event at higher field is more susceptible to the strain in-

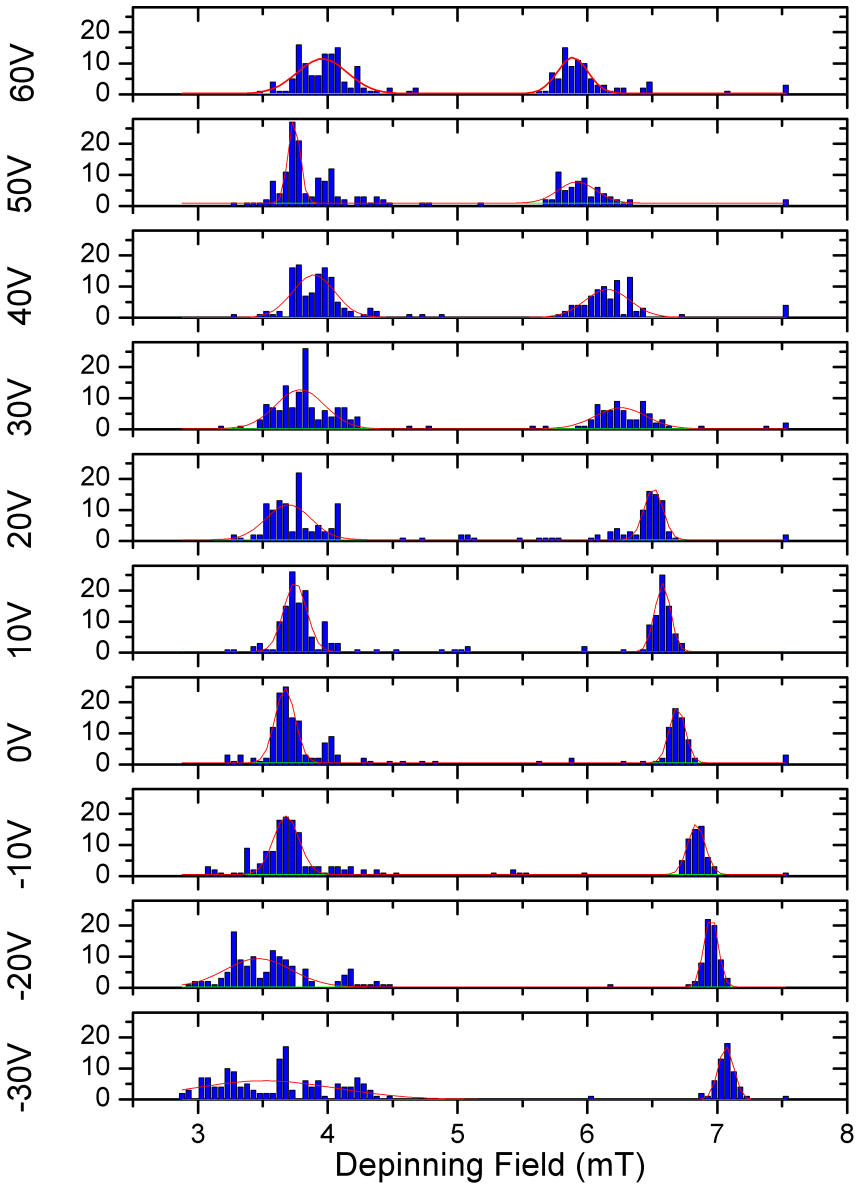

Figure 5.8: Histograms of depinning fields for different voltages applied to the piezoelectric transducer for device dp012c-2. Red lines are Gaussian fits to the data. Data collected by James Wheelwright at the University of Sheffield.

duced by the piezoelectric transducer than the depinning at lower field. The variation in depinning fields for larger positive voltages applied to the transducer is greater than at large negative voltages for the second chirality. The first chirality, which switches at a lower field, shows a generally larger degree of variation in switching field across the whole range of voltages studied. To quantify the degree of variation observed a Gaussian was fitted to the two histogram peaks originating from the two depinning field regimes observed. From figure 5.8 it can be seen that the second chirality, at higher field, is closer to Gaussian behaviour. The depinning event at lower field is generally not so well approximated as a Gaussian where there appear to be multiple peaks, close to the average depinning field. The Gaussian fits to the histograms were used to create the graph of depinning field as a function of voltage shown in figure 5.6(c). The fitting parameters for each plot are given in table 5.1. The trends in depinning field as a function of voltage applied to the transducer observed in the hysteresis loops are also seen in the histograms, in addition to confirmation of the broad range of depinning fields for the first depinning event. Explanation for the additional broadening of depinning fields of the first depinning event was provided by micromagnetic simulations, discussed in the following paragraphs.

Further insight into the depinning behaviour of these wires was gained from micromagnetic calculations. A 1 µm wide wire with notch depths of of 675 nm, 650 nm and 500 nm were simulated for clockwise (CW DW) and anticlockwise (ACW DW) vortex walls passing the notch. The micromagnetic parameters used were $M = 1400\,\mathrm{kA/m}$, $A = 3 \times 10^{-11}\,\mathrm{J/m}$, and a damping of $\alpha = 0.2$. This relatively large damping parameter was used to suppress oscillation of the domain wall before it reached the notch. Oscillations would introduce a stochastic element because the domain wall would be at a different phase of the oscillation cycle for each single shot measurement due to thermal fluctuations and variations in the nucleation field.

To make a direct comparison between the experiment and micromagnetic simulations a relationship between the piezoelectric transducer voltage and strain was required. Since the strain was not directly measured on these devices the

same linear relationship between voltage and strain-induced anisotropy described in section 2.3.3 for the GaAs-mounted devices was assumed, with the equation $\varepsilon_{xx} - \varepsilon_{xy} = -3(3) \times 10^{-5} + 5(1) \times 10^{-6}/\mathrm{V}$. The corresponding magnetoelastic energy was then calculated multiplying $\varepsilon_{xx} - \varepsilon_{yy}$ by the value of $B_1 = 5.33\,\mathrm{MJ/m^3}$ of Co from chapter 2. The sign of the energy density was changed for device dp012c-1 to account for its 90° rotation relative to device dp012c-2 and the micromagnetic simulations, so that positive anisotropy energy density corresponds to an easy axis perpendicular to the bar axis for both devices. The depinning fields for devices dp012c-1, dp012c-2, the histogram-derived values for dp012c-2, and simulated depinning fields are shown in figure 5.9.

Table 5.2: Fitting parameters for the linear fits to data in figure 5.9 where H_0 is the offset, and H_E the slope. The superscript H denotes depinning fields derived from fits single-shot measurement histograms.

Device	Chirality	H_0 mT	H_E $\times 10^{-4}\mathrm{mT}/(\mathrm{J/m^3})$	R^2
dp012c-1	1	7.553(9)	0.2(1)	0.1276
	2	10.456(6)	−3.3(1)	0.9928
dp012c-2	1	3.80(1)	1.4(2)	0.8861
	2	6.54(1)	−4.7(1)	0.9867
dp012c-2$^{\mathrm{H}}$	1	3.69(3)	0.63(3)	0.2951
	2	6.61(1)	−4.7(1)	0.9926
Simulation 675 nm	CW	3.72(4)	2.4(1)	0.9897
	ACW	6.00(4)	−2.0(1)	0.9895
Simulation 625 nm	CW	4.42(4)	0.3(1)	0.6275
	ACW	6.00(2)	−2.0(6)	0.9895
Simulation 500 nm	CW	3.97(9)	0.8(2)	0.8462
	ACW	5.93(2)	−1.70(6)	0.9895

A summary of the fitting parameters for linear fits to each of the data is given in table 5.2. Although there are differences in the exact values of these parameters, it is important to note that there is agreement in the signs of the gradients of the fits for the simulated and experimentally determined values, as well as two distinct depinning fields at zero uniaxial anisotropy. This agreement of the general trends observed in the simulations and experiment

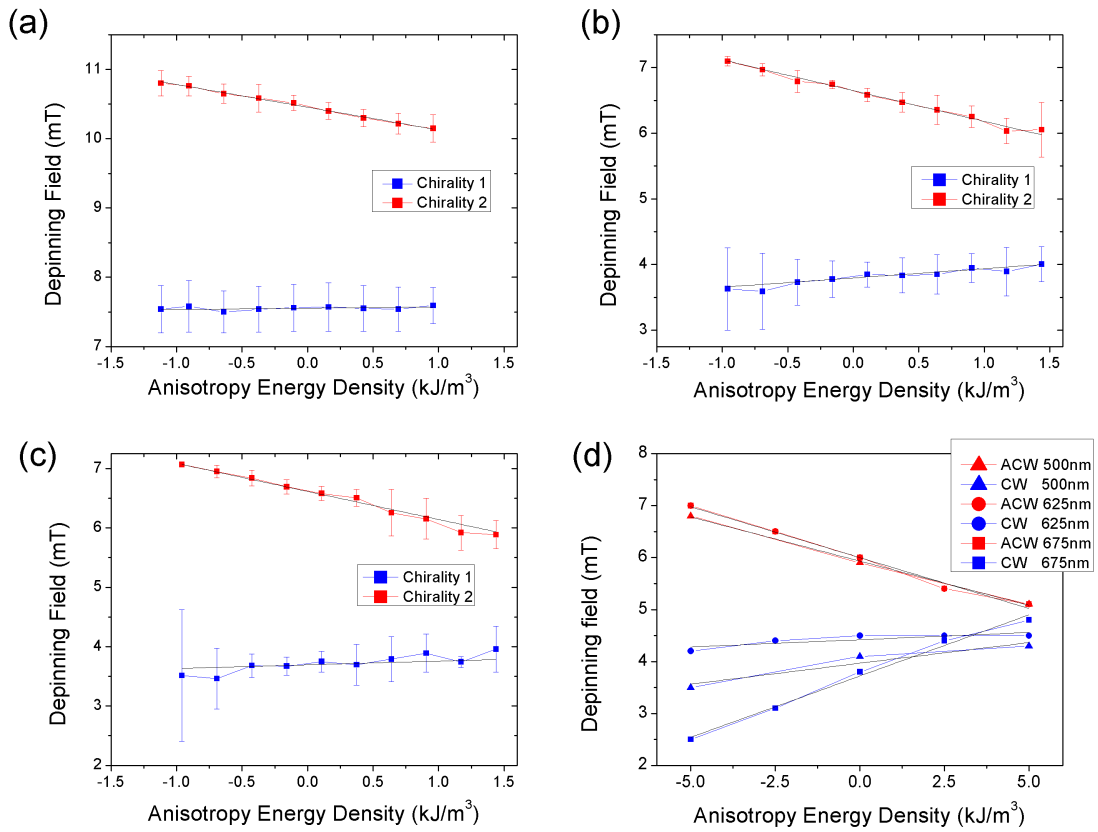

Figure 5.9: Depinning fields as a function of (approximate) anisotropy energy density, along with linear fits to the data (black lines). Positive anisotropy energy density corresponds to an easy axis perpendicular to the bar axis. Averaged MOKE measurements were made on two devices (a) dp012c-1 (b) dp012c-2. Gaussian fits to histograms of single shot measurements of dp012c-2 were also used to extract depinning fields (c). (d) Micromagnetic simulations for 500 nm, 625 nm and 675 nm.

is an indication that the simulation is at least capturing the essential physics of the experimental system. Also immediately clear is that in the 675 nm simulation the clockwise vortex domain wall simulation is much more strongly dependent on anisotropy than that of the anti-clockwise wall. This is not the case in the other simulations, or the experiments. Each of the devices and simulation measurements is addressed in more detail in the following paragraphs.

The fitting parameters of device dp012c-1 are in best agreement with the 625 nm notch depth simulation. The gradients of the first switching event, associated with the clockwise domain wall, are in agreement within the error of the two statistical fits. The anti-clockwise domain wall, corresponding to the switching event at higher field has gradients that are not in such agreement, although they are still within 50 % for the simulated and experimental data, and like the experiment the depinning fields of the anti-clockwise wall is more sensitive to the induced anisotropy.. The intercepts of the experimental data for this device are around twice as large as the simulated values.

For both the averaged-MOKE and single-shot histograms, the fitting parameters of device dp012c-2 are in closer agreement with the 500 nm simulation. Here the gradients of the first switching event (clockwise domain wall) agree to within three times the uncertainty of each value. The gradient of the depinning fields associated with the anti-clockwise domain wall has the same sign in the simulation, although the value is nearly three times smaller in the simulation than the experiment. The intercept of the linear fit to the experimental data for device dp012c-2 is generally in closer agreement with the simulations than device dp012c-1. Although still not within the uncertainty of the values, the worst agreement of the intercept is around 15 %.

It is also interesting to note the variation in the fitting parameters of the range of simulations. These are presented graphically in figure 5.10 showing the gradient (a) and intercept (b). In both cases, as seen in figure 5.9(d), the clockwise domain wall is much more sensitive to changes in notch depth than the anticlockwise wall. For the clockwise domain wall there is a marked rise

in the gradient parameter, corresponding to a greater dependence of depinning field on uniaxial anisotropy, at 675 nm. 625 nm represents a minimum in the gradient, although there is a much smaller increase for 500 nm than 675 nm. For the intercept, 625 nm corresponds to a maximum. Why there might be this large change in behaviour for 675 nm can be better understood by examining the output images of the micromagnetic simulations.

Examination of the output images of the micromagnetic simulations at zero uniaxial anisotropy energy density for 675 nm (figure 5.13), 625 nm (figure 5.12), and 500 nm (figure 5.11) reveal that these notch depths span two different types of behaviour in the clockwise vortex domain wall, while the behaviour of the anti-clockwise domain wall is consistent across the three notch depths. For all three depths the ACW DW (d – f) remains pinned before the notch, and requires a larger field to reverse the magnetisation in the region after the notch. After depinning, the propagating domain wall resembles a transverse wall (f). From these simulations it was also possible to extract depinning fields as a function of uniaxial anisotropy, representing the strain induced anisotropy induced by the piezoelectric transducer.

In both the 625 nm (figure 5.12)and 500 nm (figure 5.11) deep notches the clockwise vortex core is temporarily pinned at the notch (b). As the field is increased it passes the notch, still recognisable as a vortex core (c), although there is also the addition of a large transverse-like-wall component that is nucleated at the notch as the field is increased.

For 675 nm (figure 5.13) the behaviour of the clockwise vortex domain wall is different than in the other two widths studied. The CW DW (a – c) passes through the notch with the vortex core being pinned at the notch. The domain wall that emerges from the notch is purely transverse, without the remaining vortex core component observed in the 625 nm and 500 nm notches.

The micromagnetic simulations of different notch depths may well then be able to explain the experimental observations. Firstly the anti-clockwise domain wall is relatively unaffected by variations in the notch depth as the vortex core is pinned adjacent to the notch, and the depinning may in fact be

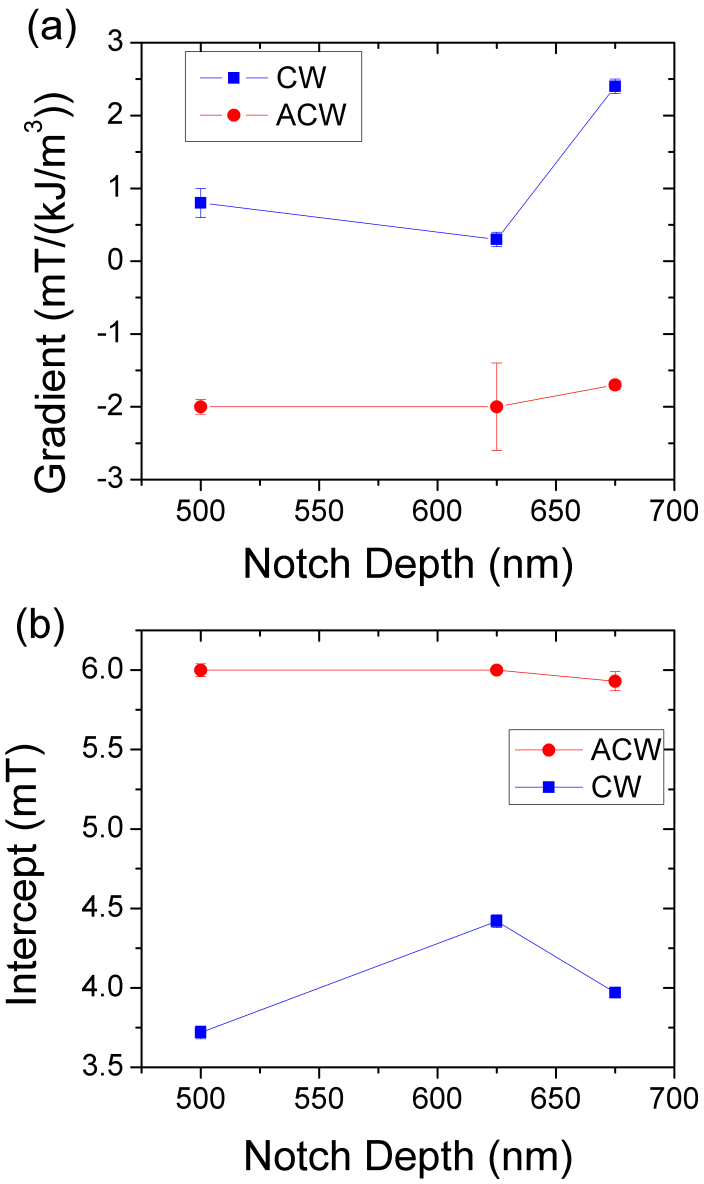

Figure 5.10: (a) Dependence of depinning field on uniaxial anisotropy (gradients of figure 5.9(d)). The depinning of the anti-clockwise where domain wall is much less dependent on the depth of the notch than the clockwise vortex domain wall, where is a marked rise in gradient for the 675 nm deep notch. (b) Depinning field at zero uniaxial anisotropy (intercepts of 5.9(d)). In both plots the error bars are the errors in the linear fits to the plots in figure 5.9(d).

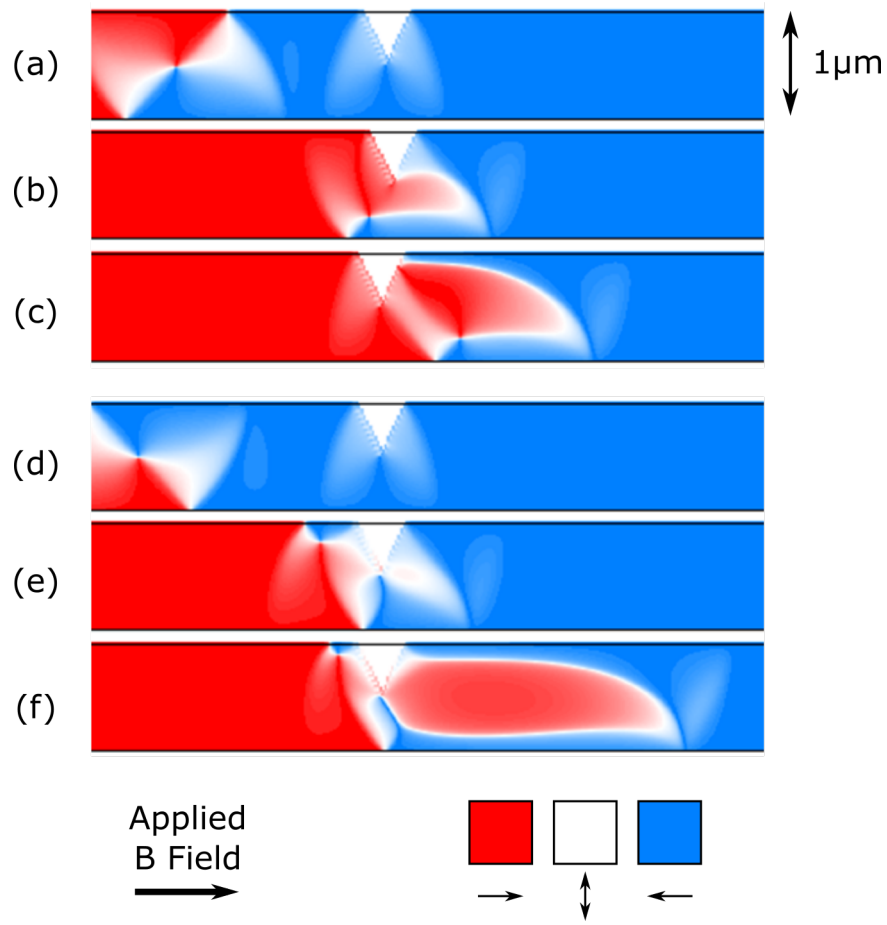

Figure 5.11: Micromagnetic simulations at zero uniaxial anisotropy energy density for 500 nm notch depth of a clockwise (a–c), and anticlockwise (d–f) vortex domain wall as it approaches and passes through a notch. The clockwise vortex core (a – c) is temporarily pinned at the notch (b). As the field is increased it passes the notch, still recognisable as a vortex core (c), although there is also the addition of a large transverse-like-wall component that is nucleated at the notch as the field is increased. The ACW DW (d – f) remains pinned before the notch, and requires a larger field to reverse the magnetisation in the region after the notch. After depinning, the propagating domain wall resembles a transverse wall (f).

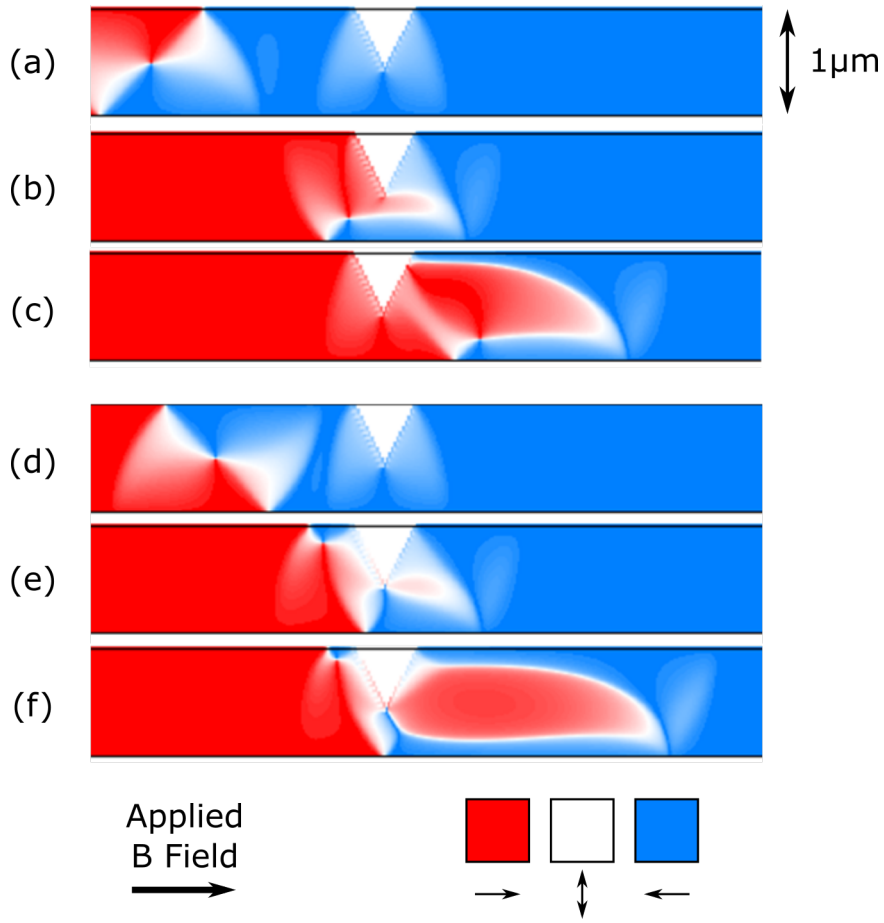

Figure 5.12: Micromagnetic simulations at zero uniaxial anisotropy energy density for 625 nm notch depth of a clockwise (a–c), and anticlockwise (d–f) vortex domain wall as it approaches and passes through a notch. The clockwise vortex core (a – c) is temporarily pinned at the notch (b). As the field is increased it passes the notch, still recognisable as a vortex core (c), although there is also the addition of a large transverse-like-wall component that is nucleated at the notch as the field is increased. The ACW DW (d – f) remains pinned before the notch, and requires a larger field to reverse the magnetisation in the region after the notch. After depinning, the propagating domain wall resembles a transverse wall (f).

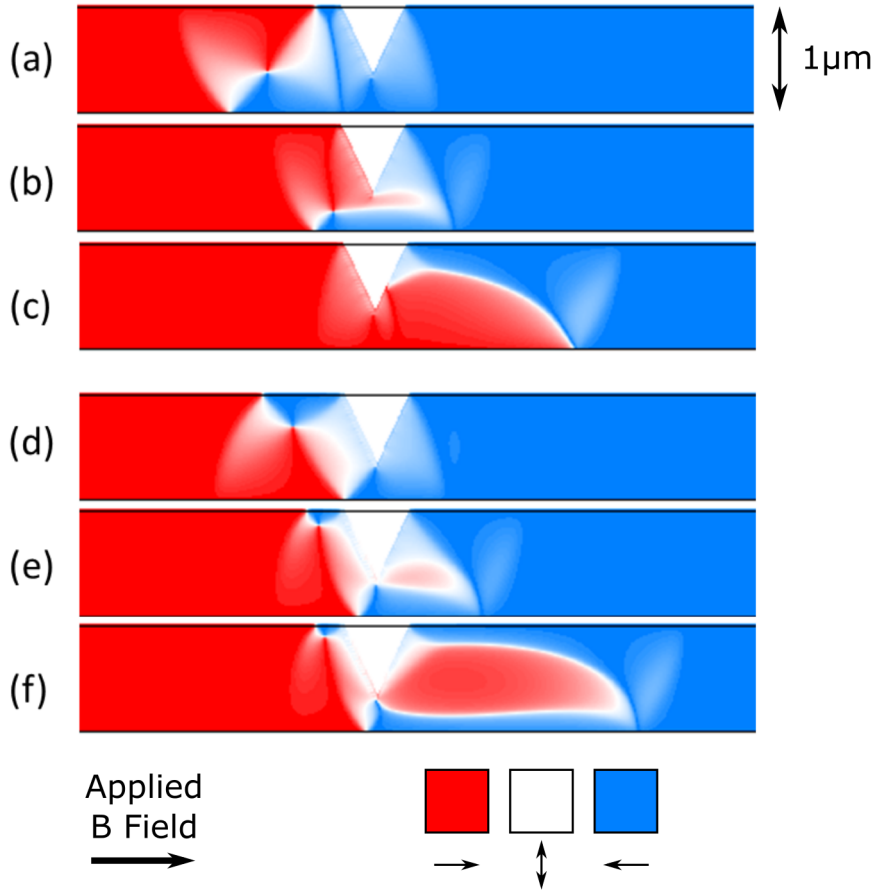

Figure 5.13: Micromagnetic simulations at zero uniaxial anisotropy energy density for 675 nm notch depth of a clockwise (a–c), and anticlockwise (d–f) vortex domain wall as it approaches and passes through a notch. The vortex core of the clockwise wall is pinned (b) and then annihilated (c) at the notch. The vortex core of the anticlockwise wall (d) remains pinned before the notch, while the rest of the domain wall is pinned at the peak of the notch (e). The propagating wall resembles a transverse wall (g).

a nucleation of a transverse-like domain wall on the other side of the notch. The average depinning field of this chirality, however, does change significantly between devices in the experiment, which is not in agreement with the simulations. The clockwise domain wall is much more sensitive to the character of the notch, and is much more accurately simulated by a notch depth of 500 nm. The micromagnetic simulations also reveal that there is a large dependence of the depinning field on uniaxial anisotropy when the vortex core remains pinned at the notch. This is the case for the anticlockwise wall in all of the notch depths studied, and the clockwise domain wall for the 675 nm deep notch. One explanation for this could be that the nucleation of the transverse-like wall from the notch is more sensitive to the uniaxial anisotropy than the depinning of the vortex core. Although the notch itself was constant during the experiment, it could be that slight variations in the spatial extent of vortex, or the vortex core location of the clockwise domain walls nucleated resulted in some being pinned, and passing through, while the vortex core of some of the domain walls was annihilated at the notch. This might explain the large spread of depinning fields reflected in the uncertainties of the data in figure 5.9, and the range of possible dependencies on uniaxial anisotropy. A key deficiency in the simulations is the unrealistically high damping parameter, which suppresses movement of the vortex core of the domain walls. In the physical devices the vortex core is more free to move as the wall proceeds along the wire, and the exact position of the core as it reaches the notch could be an important factor in determining the pinning and depinning behaviour.

To build on these measurements it would first be interesting to measure more, perhaps 1000 rather than the 100 used here, single-shot hysteresis loops to better determine if there are indeed multiple peaks in the first depinning field. To fully investigate this deviation between the micromagnetic calculations and measurements it would be informative to image the formation and depinning of each domain wall such that the depinning field could be matched to a particular domain wall configuration, or position of the vortex core as it arrived at the notch. The physical system could be better simulated by using a lower,

more realistic damping parameter and including edge roughness, which acts as a series of smaller pinning sites along the wire length [242]

The evidence presented here suggests that there is sufficient voltage or strain control of the device to manipulate the depinning field in at least one of the vortex domain wall chiralities. However, since even the two devices studied here have shown variability in the depinning field offset, it would also be interesting to see the results of a more in-depth study which perhaps looked at the variability of behaviour across perhaps tens or even hundreds of devices. This is certainly an important question to ask when thinking about the applicability of such a system to viable memory technologies or devices.

5.3 Micromagnetic Calculations of Sub-micron Wires

For technological applications wires of width 100 nm or less may be more favourable than wider wires. In these narrower wires transverse domain walls tend to be favoured[39], which have already been shown to be sensitive to and configurable by the uniaxial anisotropy induced by strain. Bryan et al. showed how in-plane uniaxial anisotropy affects both the domain wall width and the phase boundary between transverse and vortex walls [120]. In this section micromagnetic calculations are used to investigate the effect of uniaxial anisotropy on domain wall velocities and the fields required to depin transverse domain walls from a notch in the wire. Chapter 2 described the three velocity regimes: steady motion before Walker breakdown, precessional propagation immediately after Walker breakdown, and a turbulent regime at driving fields much higher than the Walker breakdown field.

The average domain wall velocity in the steady regime, before Walker breakdown, can be approximated [147, 238, 243] as

$$v = \frac{\gamma_0 \Delta}{\alpha} H_x \tag{5.1}$$

where α is the Gilbert damping, γ_0 is the gyromagnetic ratio, Δ is the wall width, and H_x is the driving field. Above Walker breakdown the time averaged velocity $\bar{v}$ becomes

$$\bar{v} = \frac{\alpha\gamma_0\bar{\Delta}}{1+\alpha^2}H_x \tag{5.2}$$

where $\bar{\Delta}$ is the time-average domain wall width.

Bryan et al. [120] investigated magnetic field driven domain wall motion in planar nanowires in which the domain wall was subjected to a magnetic field transverse to the wire axis. They found dramatic changes to the average domain wall velocity when the transverse field was applied, both before and after Walker breakdown. Although there was some change to the domain wall width with the transverse magnetic field, they also found that the average domain wall velocity was highly sensitive to the domain rotation either side of the wall. The simple 1D approach was not sufficiently complex to describe the domain wall dynamics precisely.

The effect of actual wire width on domain wall velocity has also been studied by Lee et al. [237] who found in wider wires a second peak in velocity at high driving fields, followed by a fall and then steady rise with field. The effect of uniaxial anisotropy on domain wall propagation has been previously studied by Dean et al. [119]. They found that uniaxial anisotropies both parallel and orthogonal to the wire axis could result in marked changes in the behaviour before and immediately after the Walker breakdown. Uniaxial anisotropy which favoured magnetisation along the wire axis tended to reduce the Walker breakdown velocity. Uniaxial anisotropy favouring magnetisation transverse to the wire axis both increased the Walker breakdown velocity, and the breakdown field. This is interpreted in terms of changing the effective dimensions of the wire with axial anisotropy causing the wall to behave as if in a wider, thinner wire than for transverse anisotropy, even though the physical dimensions of the wires remain constant. Dean et al. did not however investigate the behaviour of domain walls at high driving magnetic fields. A consistent feature of the high-field regime, far beyond Walker breakdown seems to be a 'high-field kink', a second peak in average domain wall velocity,

that has been observed in wide wires [237], wires under transverse anisotropy [238], and out-of-plane magnetised GaMnAs and GaMnAsP wires [239]. A sketch of such a second peak in average domain wall velocity is shown in figure 5.14.

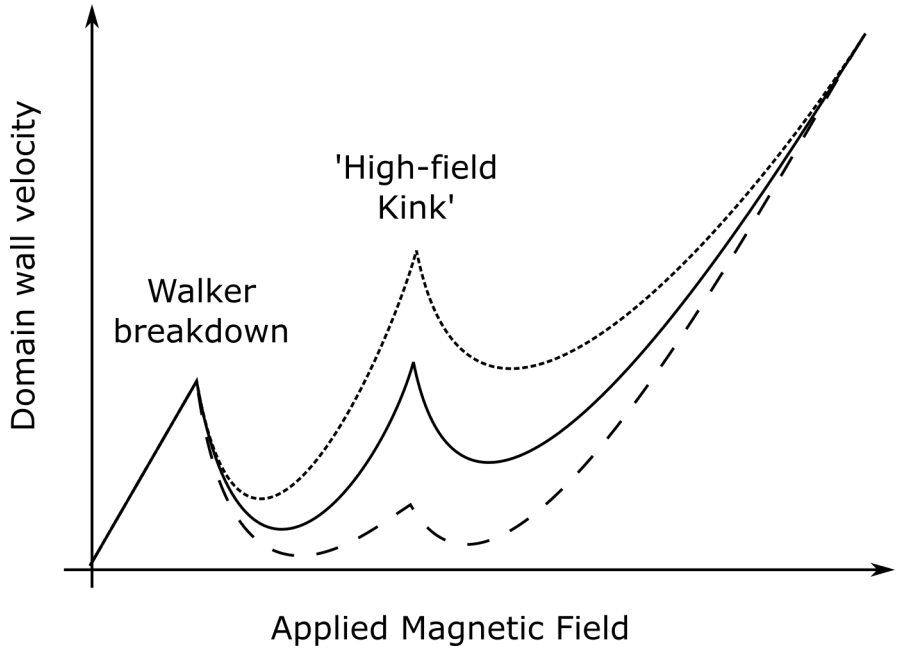

Figure 5.14: Sketch of the 'high-field kink' that has been observed in wide wires [237], wires under transverse anisotropy [238], and out-of-plane magnetised GaMnAs and GaMnAsP wires [239]. The second peak in high field may be comparable (solid line) to the Walker breakdown velocity, as in [239] and [238], or significantly smaller (wide dashed line) or larger (narrow dashed line), as in the case of [237]. Following the second peak, the average velocity returns to its asymptotically linear relation with applied magnetic field.

The exact origin of this second peak in average velocity has not yet been established, although there is evidence that suggests it may be due to flexing [239] or rotation [238] of the magnetisation around the domain wall. This section builds on these studies to explore the behaviour of domain walls under the influence of uniaxial anisotropies far beyond the Walker breakdown.

5.3.1 Simulation Details

The simulation parameters were as follows: a mesh of $4\,\text{nm} \times 4\,\text{nm} \times 10\,\text{nm}$ was used to create a two-dimensional array of three-dimensional spins, damping was $\alpha = 0.02$, saturation magnetisation was $M_S = 1378 \times 10^3\,\text{A/m}$ corresponding to $Fe_{81}Ga_{19}$, with an exchange stiffness was $A = 1.9 \times 10^{-11}\,\text{J/m}$. Wires of 48 nm and 100 nm width were studied both with and without a notch. The wires had an aspect ratio of 20, with tapers at both ends to suppress formation of domain walls.

To confirm that the wire widths studied favoured the formation of transverse walls, the total energies of different wire widths initialised with both transverse and vortex walls were compared. The difference in energies for the two wall types is shown in figure 5.15 which shows that the 48 nm wire studied strongly favours transverse walls, whereas the 100 nm wire is close to the point where vortex walls become more energetically favourable. Domain walls were initialised in the wires using an image file to coarsely define the domain wall configuration, which was then allowed to relax to equilibrium. The only anisotropy term included was a uniaxial anisotropy term with coefficient K_S. $K_S > 0$ anisotropy favoured magnetisation transverse to the wire axis while $K_S < 0$ favoured magnetisation pointing along the axis of the wire. In the context of this thesis this anisotropy can be thought of as that induced by the strain from a piezoelectric transducer.

To investigate depinning behaviour of the domain walls a notch was introduced to the initialisation image. The domain walls were brought up to the notch position with an applied field below the Walker breakdown field. The field was then increased until the domain wall depinned from the notch. For the 48 nm wide wire the notch depth was 25 % of the width of the wire and 15 % of the width of the 100 nm wire. A smaller notch depth was selected for the 100 nm wide wire to allow the wall to depin within a reasonable simulation time. This prevents direct comparison of the depinning behaviour of the domain walls in the wires.

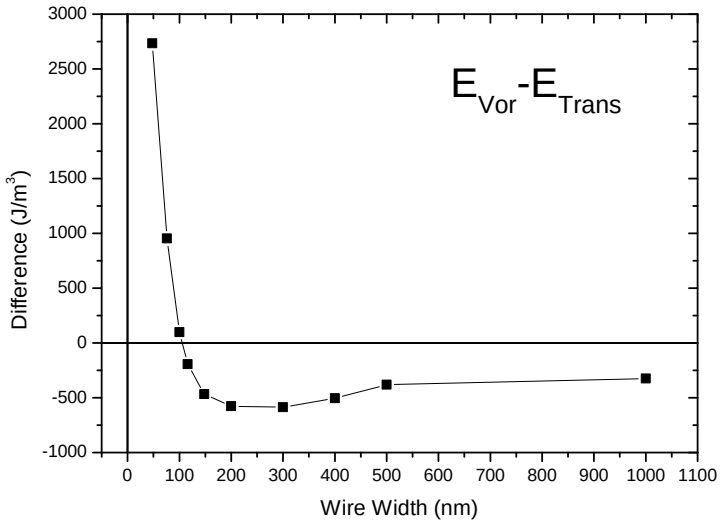

Figure 5.15: Comparison of total energies for vortex and transverse domain walls as a function of wire width. There is a transition between transverse and vortex domain walls at around 100 nm.

5.3.2 Domain Wall Velocities

The initialised domain walls were propagated along the wire by a magnetic field (simulated by a Zeeman term in the calculation). Figure 5.16 shows the average domain wall velocity for the 48 nm and 100 nm wire simulated, for both axial and transverse anisotropies, as a function of the applied field. The position of the domain wall was determined from the net magnetisation integrated over the wire. The domain wall position along the wire was taken to be the fraction of the wire with magnetisation aligned from left to right. The average velocity was taken from initial domain wall position to the end of the wire.

48 nm Wide Wire

The 48 nm wire is considered here first. In this case anisotropies of magnitude $10\,\mathrm{kJ/m^3}$ and $15\,\mathrm{kJ/m^3}$ were used to build up the average velocity curve in

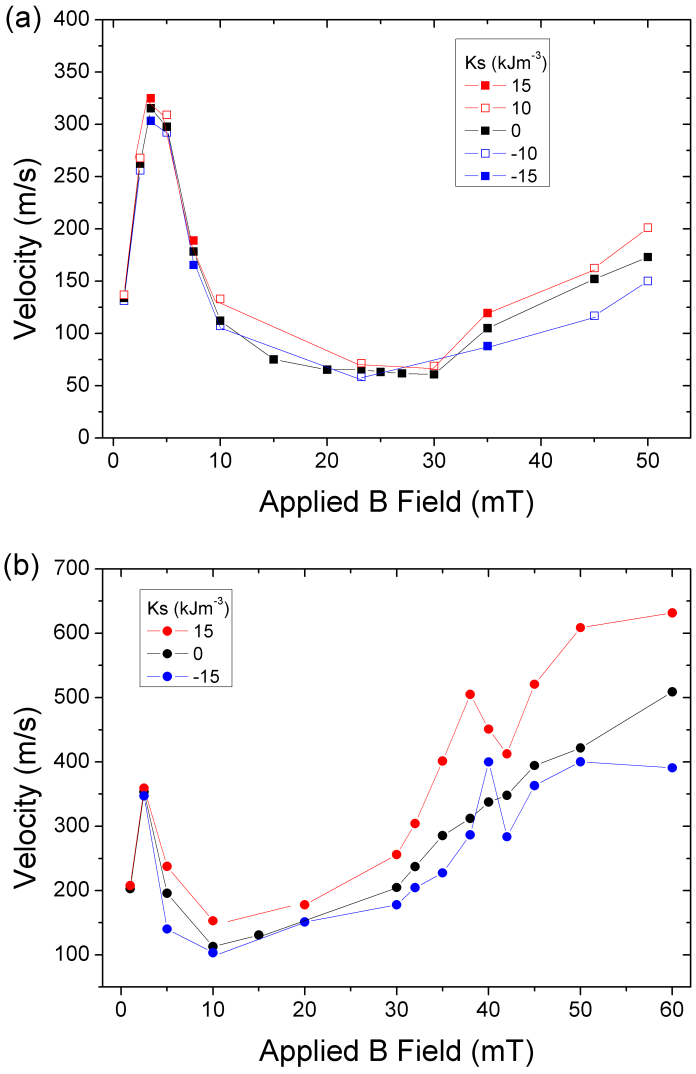

Figure 5.16: Average domain wall velocities for 48 nm (a) and 100 nm (b) for uniaxial anisotropy $K_s = \pm 15, \pm 10$, and $0\,\mathrm{kJ/m^3}$. $K_s > 0$ favours magnetisation transverse to the length of the wire whereas $K_s < 0$ favours magnetisation along the wire.

figure 5.16 (a). The average velocity as a function of field shows the steady increase in velocity up to the Walker breakdown field at which point the average velocity decreases as the domain wall enters the precessional motion regime. At higher fields the average velocity begins to recover back towards its pre-Walker breakdown level. The average velocity tends to be increased for $K_S > 0$, and decreased for $K_S < 0$. These changes are broadly in keeping with the understanding that a uniaxial anisotropy changes the effective width of the wire [119, 237]. Negative values of K_S correspond to anisotropy favouring magnetisation along the length of the wire. In shape anisotropy terms this could be achieved by a narrower wire. The opposite is true for positive values of K_S which favours magnetisation transverse to the wire axis.

It is possible to estimate the expected change in domain wall width associated with the uniaxial anisotropy by considering the fractional changes in domain wall width δ and anisotropy K. Differentiating the equation for domain wall width (equation (1.23)) yields:

$$\frac{d\delta}{\delta} = \frac{1}{2}\frac{dK}{K}. \tag{5.3}$$

where the sign of K has been reversed to be consistent with the definition of K used in the simulations. Starting with an approximate initial domain wall width δ equal to the width of the wire allows the initial shape-induced anisotropy K to be estimated using equation (1.23).

For the 48 nm wires, the initial domain wall width δ was taken to be 48 nm. Using equation (1.23) this width corresponds to an initial anisotropy of $78\,\mathrm{kJ/m^3}$. The fractional change in domain wall width determined from equation (5.3) was found to be ± 0.06 for $\pm 10\,\mathrm{kJ/m^3}$, and ± 0.1 for $\pm 15\,\mathrm{kJ/m^3}$. Since, from equation (5.2), domain wall velocity is linear in domain wall width, these are also the fractional changes in domain wall velocity associated with each uniaxial anisotropy, that is to say $\frac{d\delta}{\delta} = \frac{dv}{v}$. The fractional changes in velocity for the simulated data for the 48 nm wire are shown in figure 5.17 (a). The mean values of these data for $\pm 15\,\mathrm{kJ/m^3}$ and $\pm 10\,\mathrm{kJ/m^3}$ are given in table 5.3. It is clear from the data in figure 5.17 (a) that there is a dependence

of the fractional change in velocity on applied magnetic field. A table of the linear fitting parameters from fits to figure 5.17 (a) is shown in table 5.4 which shows that there is agreement between the two values of K_S studied for both positive and negative anisotropies. Why there should be a linear dependence on applied field is not immediately clear. Equations (5.2) (5.1) are linear in field and it may be that there is an additional mechanism involved in the fractional changes in simulated domain wall velocity, in addition to the changes in domain wall width on which the predicted changes in domain wall velocity were based. Investigating this linear dependence could be an interesting area of future work.

Table 5.3: Theoretically predicted and simulated relative velocities in the 48 nm wire for $\pm 15\,\mathrm{kJ/m^3}$ and $\pm 10\,\mathrm{kJ/m^3}$

$K_S(\mathrm{kJ/m^3})$	-15	15	-10	10
Theory	0.1	−0.1	0.06	−0.06
Simulated	0.09(4)	−0.08(3)	0.08(3)	−0.09(2)

Table 5.4: Fitting parameters to the relative changes in domain wall velocity as a function of applied magnetic field for 48 nm wires, as shown in figure 5.17(a)

K_S ($\mathrm{kJ/m^3}$)	Intercept	Slope (1/μT)
15	0.03(1)	3.2(4)
10	0.05(3)	2(1)
−10	−0.02(2)	−3.5(7)
−15	−0.03(1)	−3.6(5)

It is also possible to look at the instantaneous velocity determined from the relative magnetisation of the wire. The 10 mT case is considered first, which it can be seen from figure 5.16 is soon after the Walker breakdown. The instantaneous velocity curve for 0, $\pm 10\,\mathrm{kJ/m^3}$ shown in figure 5.18 (a) are similar to that reported previously [238] for domain wall motion soon after Walker breakdown. The change in behaviour at long times is due to the interactions of the domain wall with the end of the wire. The plots show an initial rise in velocity, followed after the breakdown by a marked reduction

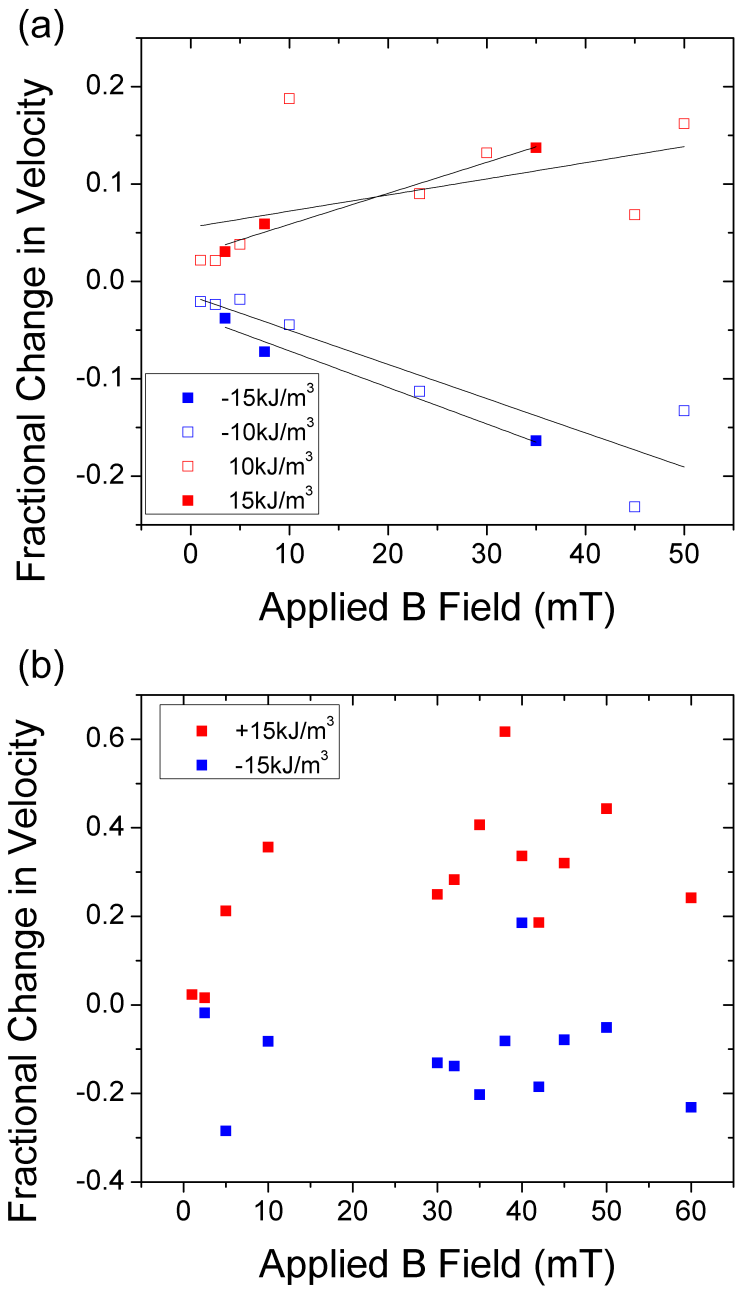

Figure 5.17: Fractional change in velocity as a function of applied field for different uniaxial anisotropy values. (a) 48 nm wires. Here, black lines are linear fits to the data. The fitting parameters for which are given in table 5.4. (b) 100 nm wires.

in velocity, then retrograde motion followed by a further Walker breakdown. The fast Fourier transform (FFT) of these velocity curves shown in figure 5.18 (b) reveals the frequencies of these different processes. There may be some slight changes in the peak at around 1.2 GHz as a function of anisotropy, but it is difficult to say for sure at this frequency resolution.

The instantaneous domain wall velocity under a 50 mT driving magnetic field in the 48 nm wire is shown in figure 5.19 (a). There is still a clear periodic component to the motion, but with additional higher frequency oscillations. The FFT shown in figure 5.19 (b) reveals peaks or clusters of peaks for oscillations at around 2, 3, and 6 GHz. There does seem to be a slight suppression of the amplitude of the peaks for 10 kJ/m^3 and enhancement at -10 kJ/m^3. The first of these peak groups may correspond to the oscillations also seen at a 10 mT driving field. Images of the domain wall propagation at 50 mT shown in figure 5.20 provide more insight into the origin of the higher frequency modes. In all three anisotropy cases the domain wall either side of the transverse component of the wall can be seen to flex as the wall moves forwards and backwards along the wire.

100 nm Wide Wire

The 100 nm wire also shows a rich range of behaviour in the range of fields and uniaxial anisotropies studied, as shown in figure 5.16. In particular there is a marked deviation from the zero uniaxial anisotropy condition at higher fields, with a second peak in average domain wall velocity, followed by a fall and return to the more gradual increase with applied field.

As for the 48 nm wires the expected change in domain wall width for the 100 nm wire was approximated using equation (5.3), with an initial domain wall width $\delta = 100$ nm, with a corresponding $K = 18.7$ kJ/m^3. For $K_s = 15$ kJ/m^3, the fractional change in domain wall width relative to the zero anisotropy case $\frac{d\delta}{\delta} = -0.4$. For $K_s = 15$ kJ/m^3, the fractional change in domain wall width $\frac{d\delta}{\delta} = 0.4$. This same analysis applied to the simulated

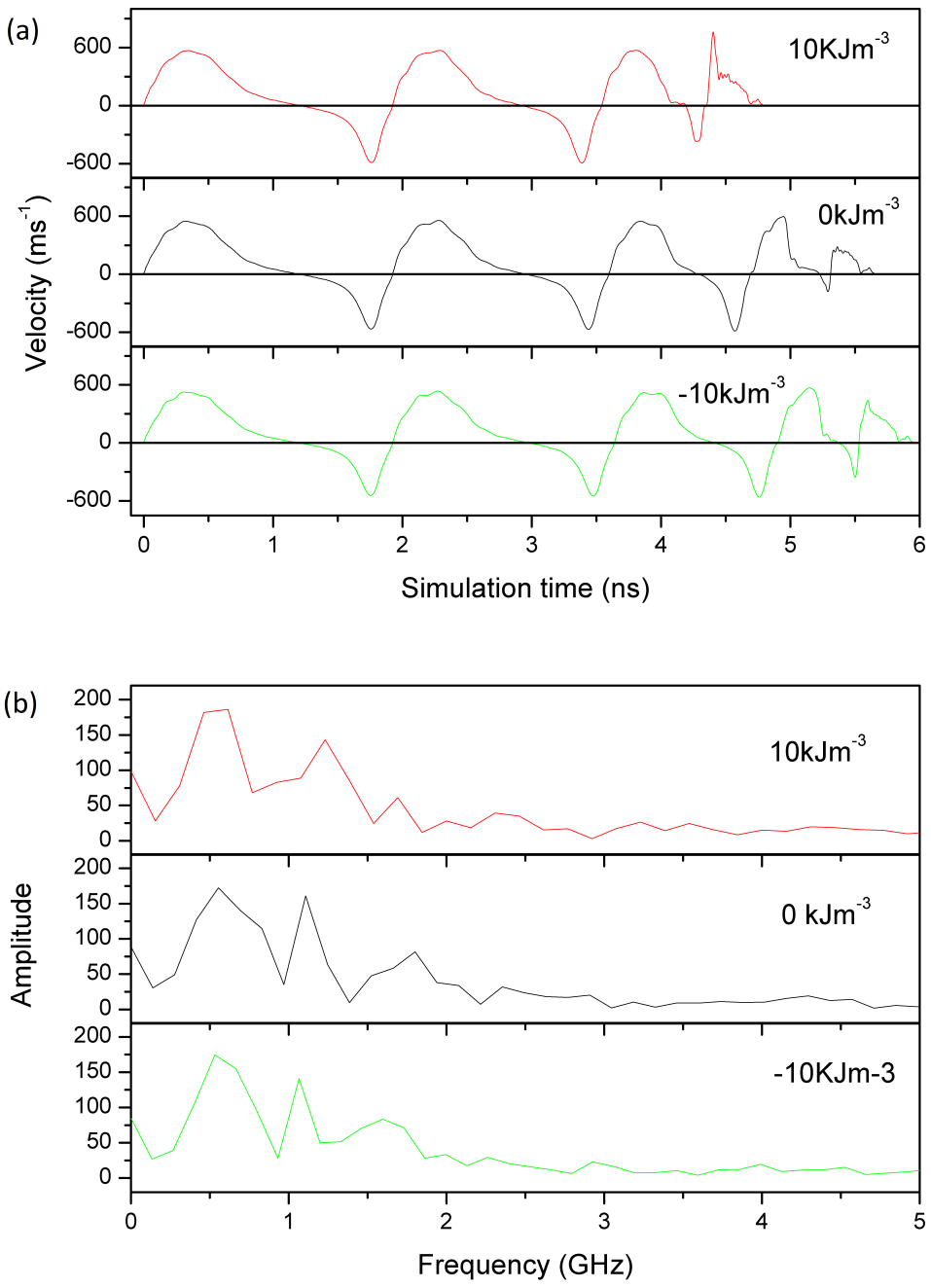

Figure 5.18: (a) Instantaneous domain wall velocity as a function of time in a 48 nm wide wire with a 10 mT applied magnetic field. (b) FFT of the instantaneous velocity.

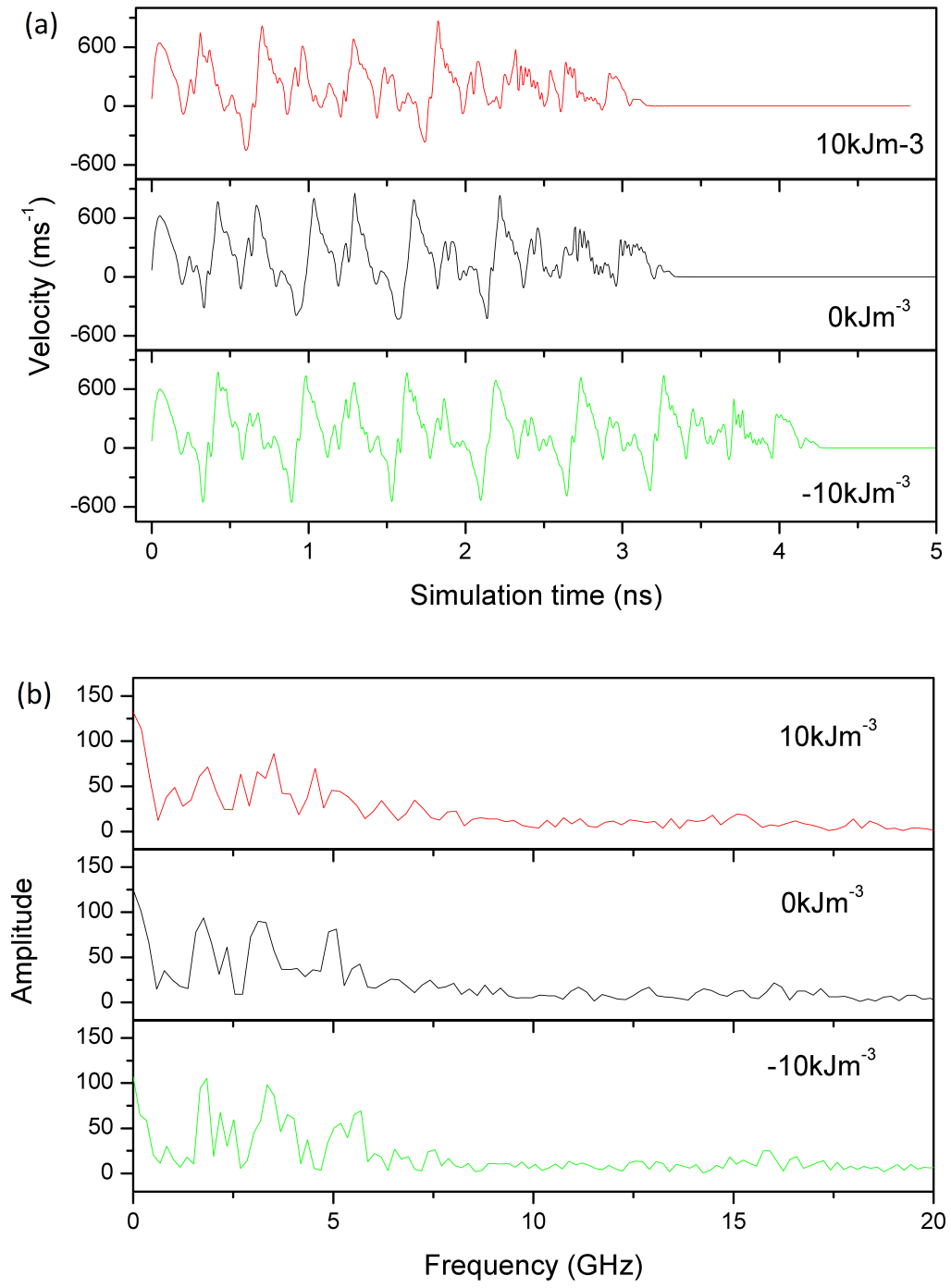

Figure 5.19: (b) Instantaneous domain wall velocity as a function of time in a 48 nm wire with a 10 mT applied magnetic field. (b) FFT of the instantaneous velocity.

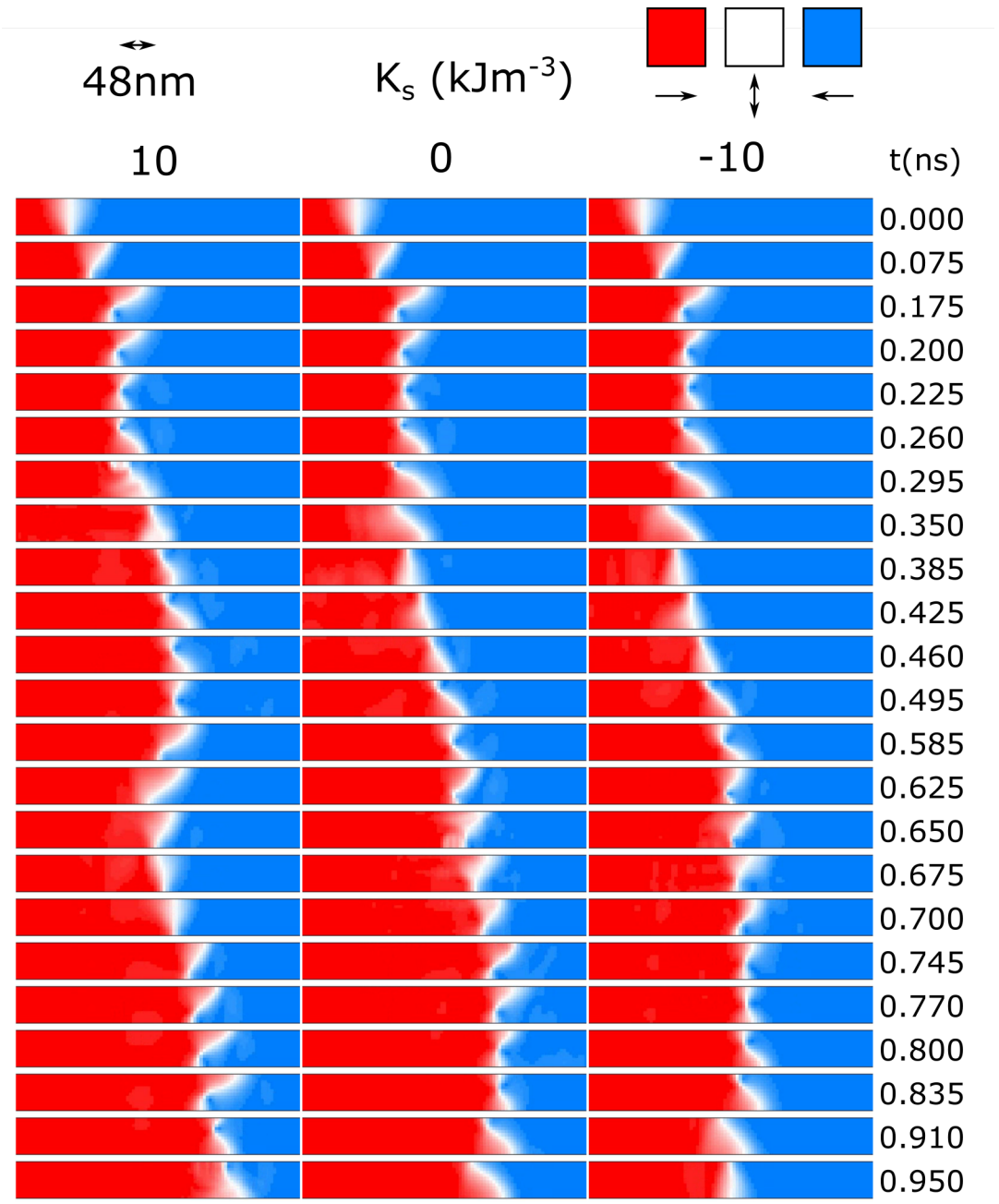

Figure 5.20: Examples of domain wall motion in the 48 nm wide wire with a driving field of 50 mT, for uniaxial anisotropy K_s. The magnetisation directions represented in the image are shown in the coloured boxes.

velocity data is shown in figure 5.17 (b), where the operation $(v_{K_s} - v_K)/v_K$ has been performed, where v_{K_s} is the velocity with the uniaxial anisotropy present, and v_K is the velocity with no uniaxial anisotropy present. Here the mean value of the relative velocity change is $\frac{dv}{v} = 0.28(5)$ for $K_S = 15\,\mathrm{kJ/m^3}$ which is within three standard errors of the predicted value. For $K_S = -15\,\mathrm{kJ/m^3}$ the average fractional velocity change is $\frac{dv}{v} = -0.11(4)$ which is significantly less than that predicted. The simulated and predicted average changes in velocity are summarised in table 5.5. The key assumption in the predicted value was the that the initial domain wall width was equal to the wire width. This approximation does yield values of fractional change in velocity that agree to within an order of magnitude of the average simulated values, but the approximation could be improved by examining in more detail the exact behaviour of the domain wall in the wire. Equations (5.1) and (5.2) are strictly valid below the turbulent regime, below around 30 mT in figure 5.17(b). Despite this the close agreement between the simulated and predicted values continues into the turbulent regime, as the change in velocity is relatively flat as a function of applied magnetic field.

Table 5.5: Theoretically predicted and simulated relative velocities in the 100 nm wire for $\pm 15\,\mathrm{kJ/m^3}$

$K_S(\mathrm{kJ/m^3})$	-15	15
Theory	-0.4	0.4
Simulated	$-0.11(4)$	0.28(5)

This study is particularly concerned with the behaviour of the domain wall at magnetic fields far beyond the Walker breakdown. First the intermediate field range is considered, in the precessional regime between approximately 5 and 30 mT. The instantaneous domain wall velocity for the 100 nm wire with a 10 mT driving magnetic field is shown in figure 5.21 (a). The curves for 0 and $-15\,\mathrm{kJ/m^3}$ resemble the form observed in the 48 nm wire, with the small addition of some higher frequency oscillations. The $15\,\mathrm{kJ/m^3}$ case shows markedly different behaviour, particularly following the Walker breakdown where there is a greater tendency for forward motion, along with relatively

strong higher frequency components. The FFTs of these velocity curves shown in figure 5.21 (b) reveal the frequencies of these oscillations. There are four peaks with frequencies below around 2.5 GHz which are likely to be due to the slower periodic behaviour also observed in the narrower wires. The peaks at around 2.6 and 5.2 GHz are strongest in the 15 kJ/m^3 case. The origin of this different behaviour is revealed by images of the domain wall motion shown in figure 5.22. For $K_s = 0$ and -15 kJ/m^3 an antivortex core forms on the bottom edge of the wire at $t = 0.250$ ns. The antivortex core moves across to the other side of the wire between $t = 0.480$ ns and $t = 1.525$ ns, where it annihilates at $t = 1.830$ ns. As in the case of the 48 nm wire the arms of the wall appear to flex as the wall moves, giving rise the the higher frequency components seen in the velocity curves. The behaviour of the domain wall for the 15 kJ/m^3 is markedly different as a vortex core nucleates on the top edge of the wire, and becomes a full vortex wall. This can happen because the anisotropy allows wider walls to be supported in the wire, therefore the vortex wall is more stable. The arms of this vortex wall also oscillate, giving rise to the different velocity behaviour and higher frequencies observed.

The average velocity profile (figure 5.16) reveals that in the presence of a positive uniaxial anisotropy, there is a second peak in velocity at around 38 mT. As before the instantaneous velocity of the domain wall was also examined, as shown in figure 5.23 (a). At such a high driving magnetic field, the velocity has lost its periodicity, and undergoes much more turbulent motion. The FFTs in figure 5.23 (b) indicate some periodicity at around 1 GHz. The velocity traces seem to show peaks in instantaneous velocity at around 1 ns for 15 kJ/m^3, 1.5 ns for 0 kJ/m^3 and 3.5 ns for -15 kJ/m^3. The origin of these peaks is revealed by images of the domain wall motion shown in figure 5.24. The peaks in instantaneous velocity coincide with the detachment of a transverse-like component of the domain wall, from an anti-vortex core. The transverse-like wall is able to proceed rapidly along the wire before being halted by a Walker breakdown event involving the nucleation of an anti-vortex core at the edge of the wire. Similar detachment has been observed previously in wide wires [244] and narrow wires under the influence

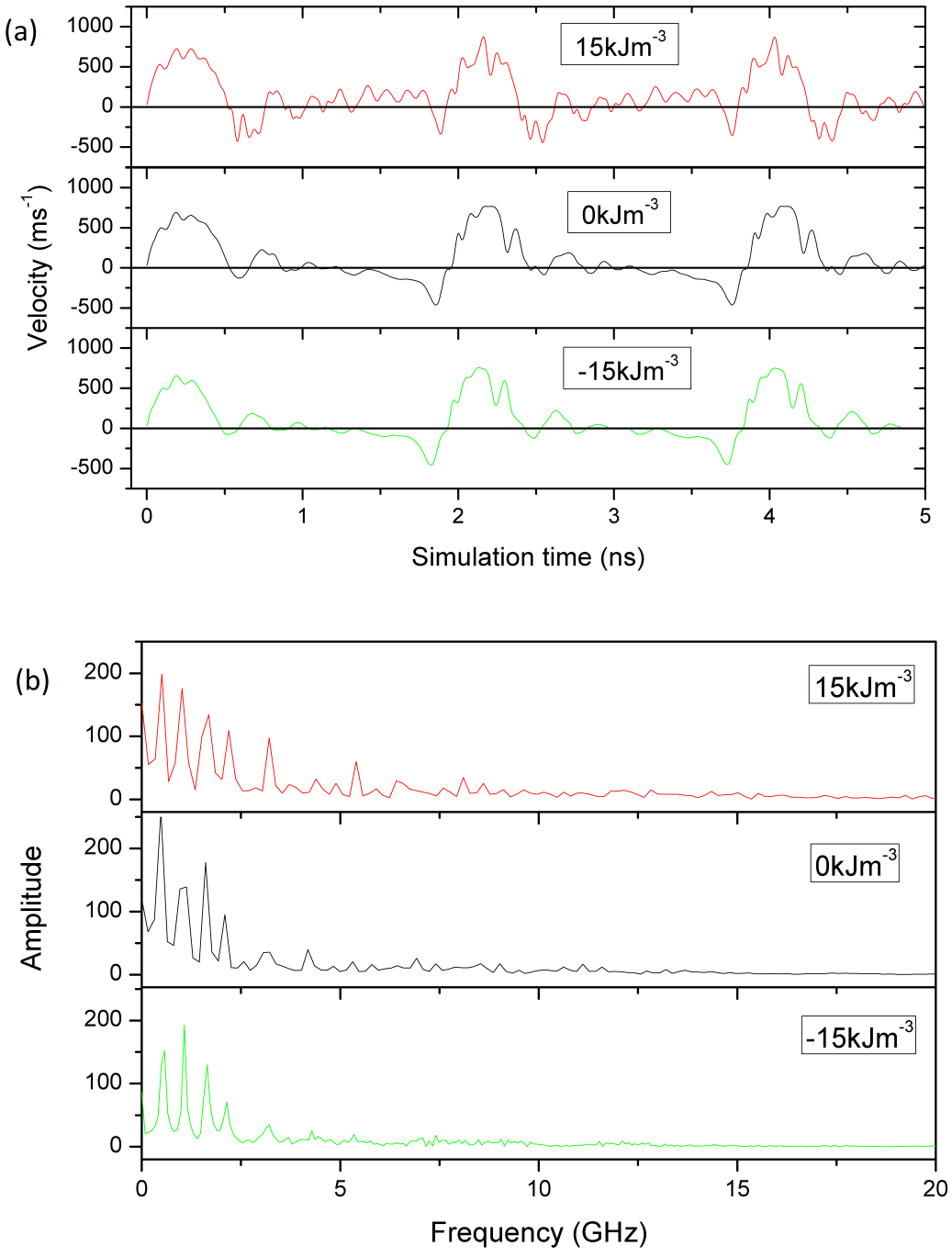

Figure 5.21: (a)Instantaneous domain wall velocity as a function of time in a 100 nm wire with a 10 mT applied magnetic field. (b) FFT of instantaneous velocity.

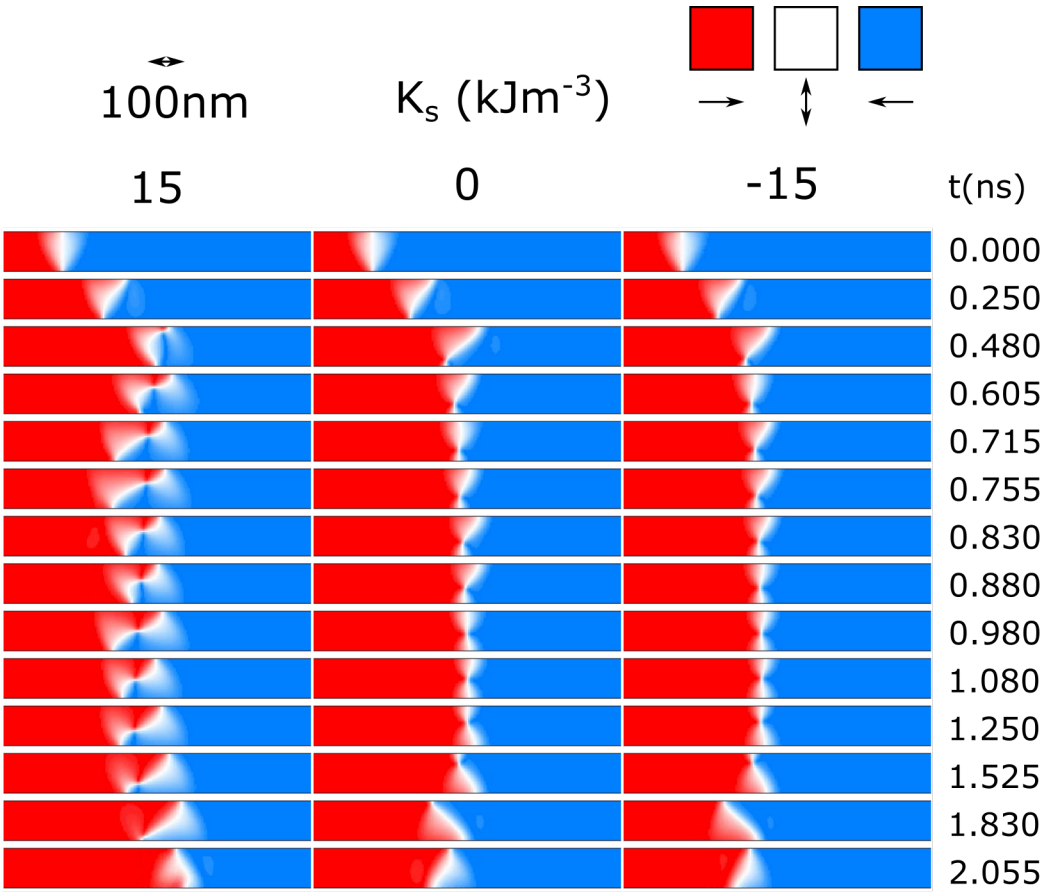

Figure 5.22: Examples of domain wall motion behaviour in 100 nm wire under a 10 mT driving field for uniaxial anisotropy K_s. The magnetisation directions represented in the image are shown in the coloured boxes.

of a transverse magnetic field [238, 245], in which case the transverse wall is sufficiently stabilised to breakaway from the anti-vortex core. In the data presented here the positive value of K_s seems to perform a similar role in stabilising the transverse-like wall, as the detachment happens at an earlier time step and the transverse component propagates along the wire at a higher velocity. This stabilising effect is reasonable as the $K_s > 0$ anisotropy favours magnetisation lying transverse to the wire axis, along which the transverse wall also lies. With zero and negative uniaxial anisotropy, the detachment takes place following a Walker breakdown event, with the anti-vortex core being pinned to the top, rather than the bottom edge of the wire in the zero uniaxial anisotropy case.

There is also a peak in average domain wall velocity at 40 mT for $K_s = -15\,\mathrm{kJ/m^3}$. Plots of the instantaneous velocity of the domain wall at this driving field are shown in figure 5.25(a). They reveal that there is again a peak in the velocity, this time close to 1 ns for all three anisotropies studied. There also seems to be a second peak between 2 and 3 ns. The second peak for $-15\,\mathrm{kJ/m^3}$ happens around 0.5 ns before the zero anisotropy case, and marginally before the $15\,\mathrm{kJ/m^3}$ case. These changes in peak velocities may be reflected in the FFTs in figure 5.25 which seem to show a slight increase in frequency in a peak at around 1 GHz, although it is difficult to resolve the lowest frequencies. These peaks in velocity coincide with particular domain wall behaviour shown in figure 5.26. For $15\,\mathrm{kJ/m^3}$ a first domain wall detachment at around 1 ns is followed by a return to an approximate vortex domain wall, and then a second detachment of the transverse-like wall component at about 2.2 ns. In both cases the anti-vortex core is pinned to the bottom of the wire. For $0\,\mathrm{kJ/m^3}$ the anti-vortex core is pinned during the detachment to the top edge of the wire. In the $-15\,\mathrm{kJ/m^3}$ there seems to be greater deformation of the domain wall prior to the full detachment of the transverse-like component. Why there should be a second peak in velocity at driving fields above the Walker breakdown field, and then only in the presence of a uniaxial anisotropy, are key questions raised by this work. The answers to these questions have previously proved elusive [237, 238, 239] and rather than provide

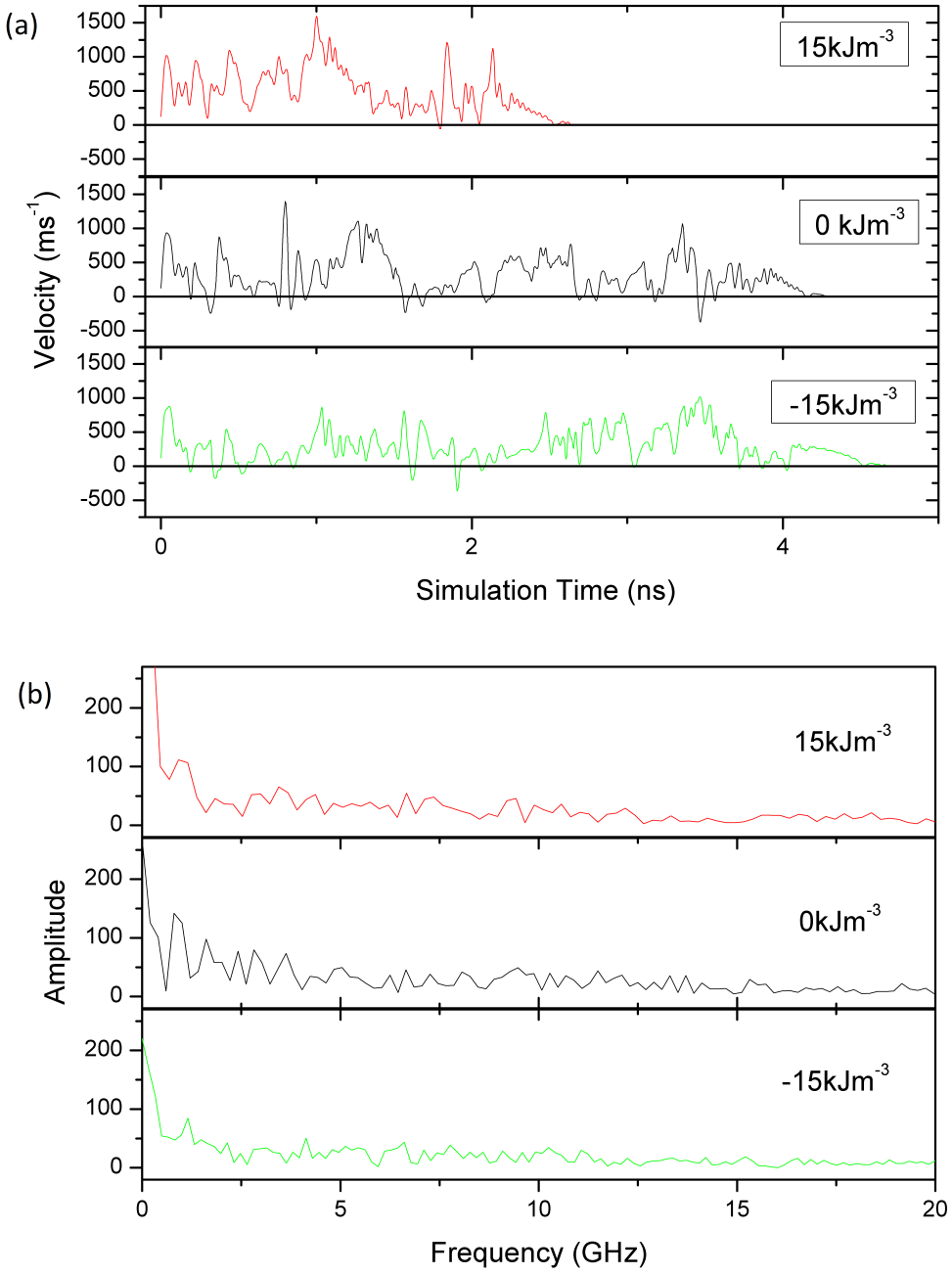

Figure 5.23: (a) Instantaneous domain wall velocity as a function of time in a 100 nm wire with a 38 mT applied magnetic field. (b) FFT of instantaneous velocity.

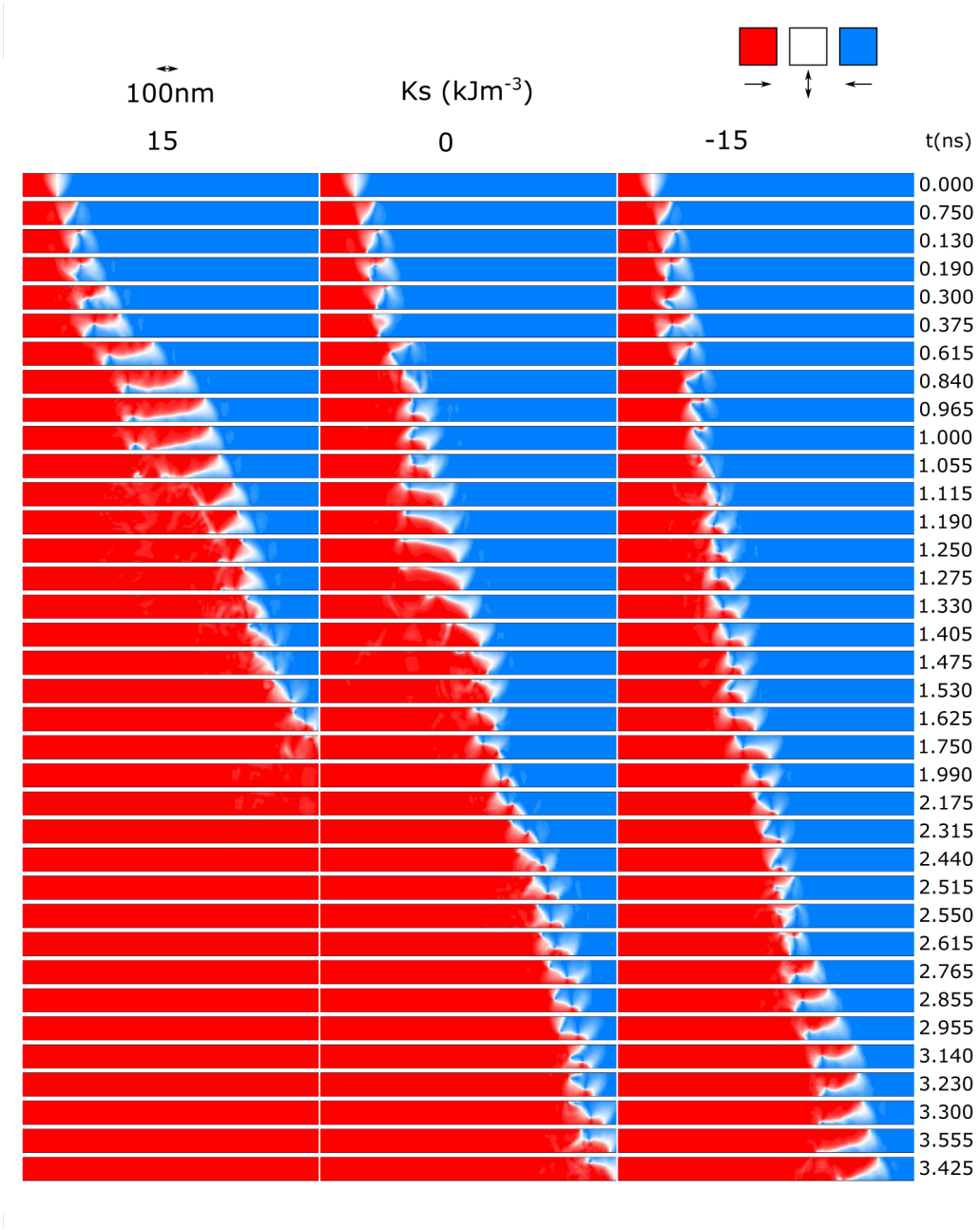

Figure 5.24: Examples of domain wall motion behaviour in 100 nm wire under a 38 mT driving field for uniaxial anisotropy K_s. The magnetisation directions represented in the image are shown in the coloured boxes.

an answer, this study provides another possible system where these questions could be investigated or exploited.

Finally the case for a 60 mT driving magnetic field in the 100 nm wire is examined. The instantaneous velocities at this magnetic field are shown in figure 5.27 (a). For 15 kJ/m^3 there seem to be four peaks, approximately every 0.5 ns. For 0 and -15 kJ/m^3 there is no apparent periodicity. The FFTs for each anisotropy, shown in figure 5.27 (b) do not seem to reveal a strong periodicity at the resolvable frequencies. Images of the domain wall motion (figure 5.28) do however reveal the occurrence of the domain wall detachment observed at lower magnetic fields. As for the lower driving magnetic fields the core seems to favour being pinned along the bottom edge of the wire for non-zero anisotropy, whereas for zero anisotropy the vortex core is pinned alternately to the bottom and top edges of the wire.

The turbulent nature of the domain wall motion at higher magnetic fields makes it difficult to fully explain the observations presented here. The general trend for positive uniaxial anisotropy values to increase domain wall velocities, and for negative values to decrease the velocity, is in keeping with the simple explanation that the effective width of the wire is being altered[119, 238]. Negative anisotropy values favour magnetisation along the length of the wire, effectively narrowing its width. Positive values of anisotropy in this study favour magnetisation orthogonal to the length of the wire, such that the domain wall width increases as if it were in a wider wire.

This study has not looked into the possible effect of domain rotation either side of the domain wall, which had a significant impact on the domain wall velocity in wires subjected to a transverse magnetic field [238]. The second peak in average velocity at high magnetic fields has previously been observed in (effectively) wide wires [237, 238], and may be attributable to the greater stability afforded to the domain wall under these conditions. The high-field kinks in out-of-plane magnetised GaMnAs and GaMnAsP were attributed to deformation of the domain wall, although no complete explanation was provided [239]. A significant factor in our observations of the 100 nm wire

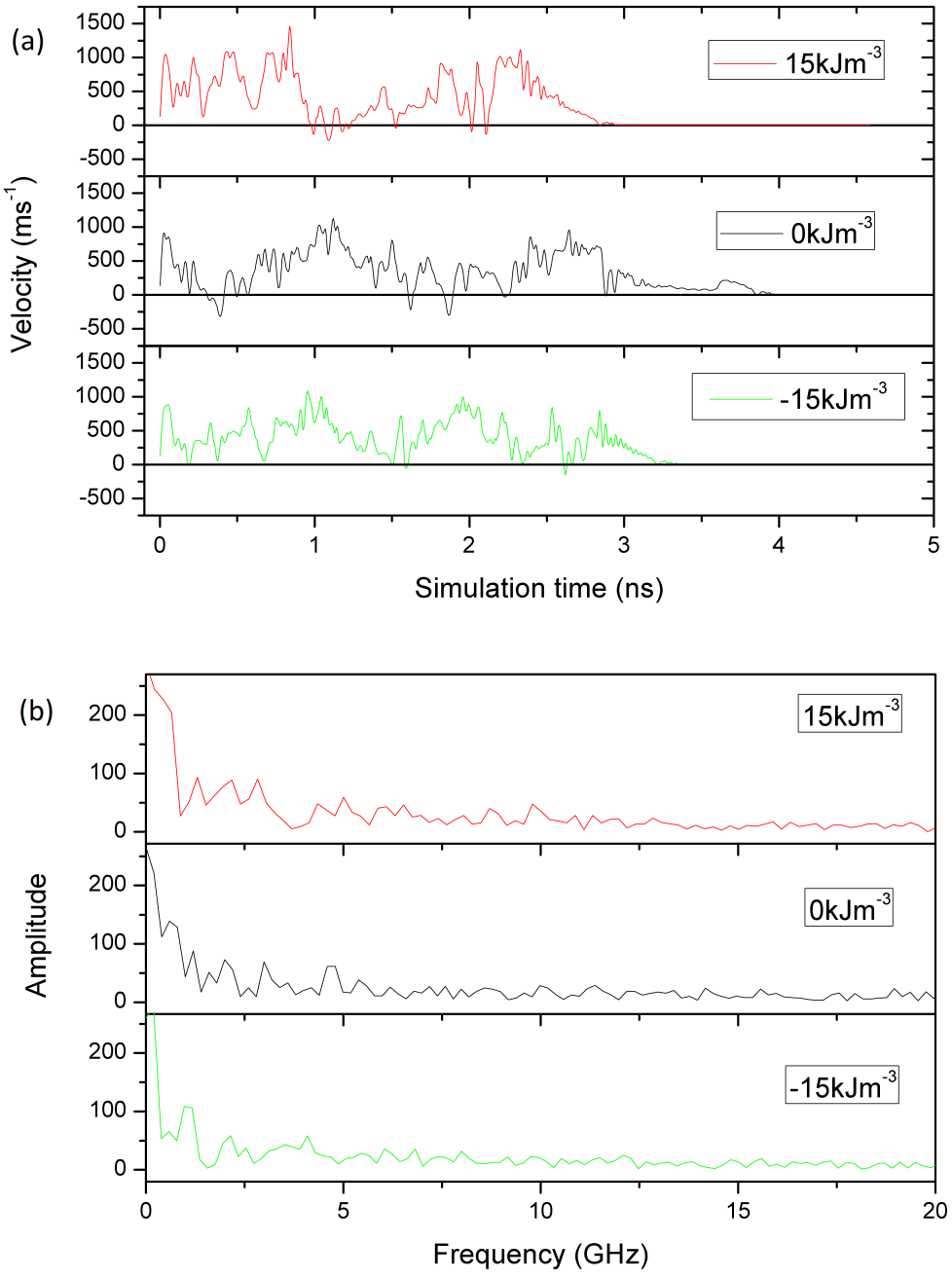

Figure 5.25: (a) Instantaneous domain wall velocity as a function of time in a 100 nm wire with a 40 mT applied magnetic field. (b) FFT of instantaneous velocity.

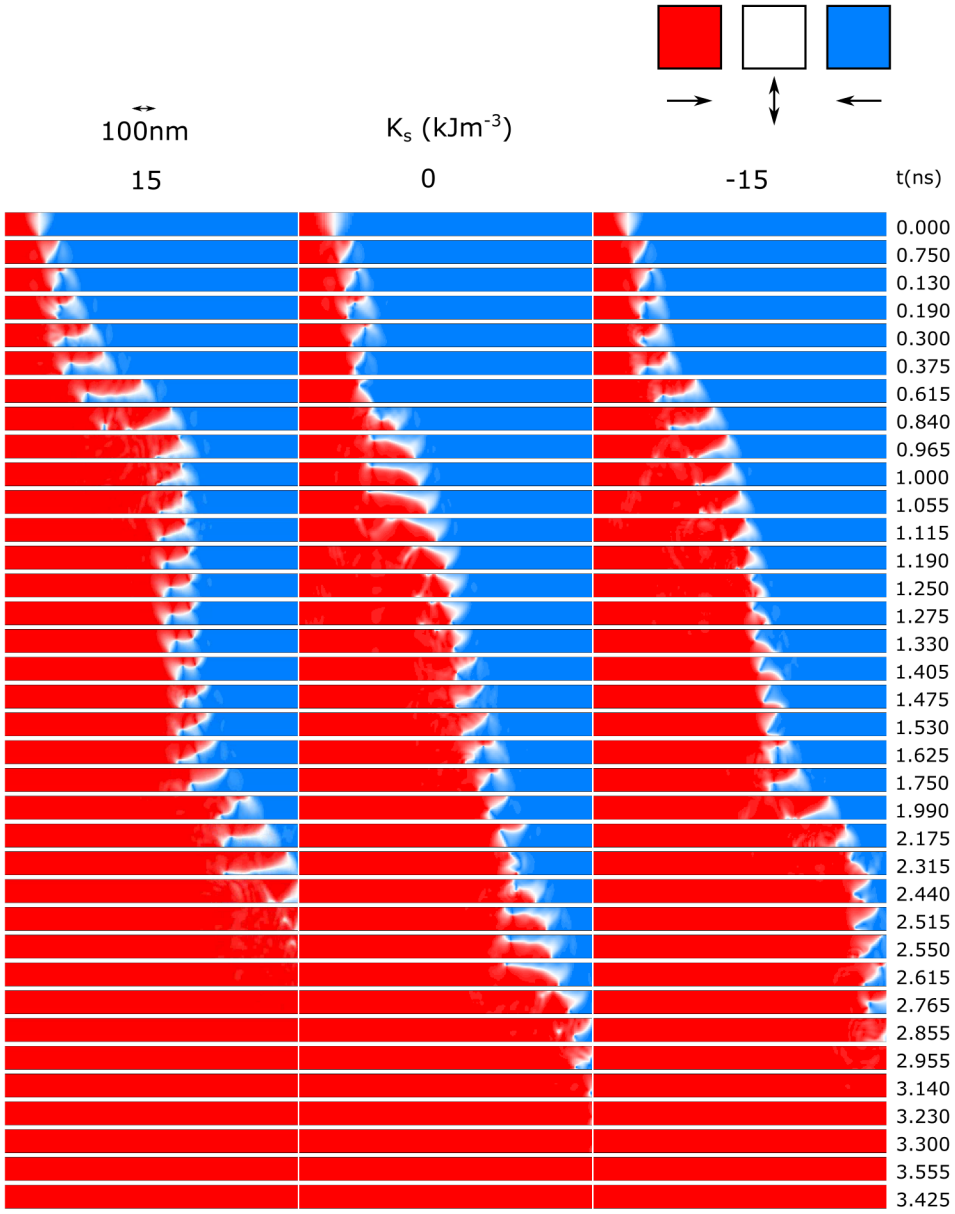

Figure 5.26: Examples of domain wall motion behaviour in 100 nm wire under a 40 mT driving field for uniaxial anisotropy K_s. The magnetisation directions represented in the image are shown in the coloured boxes.

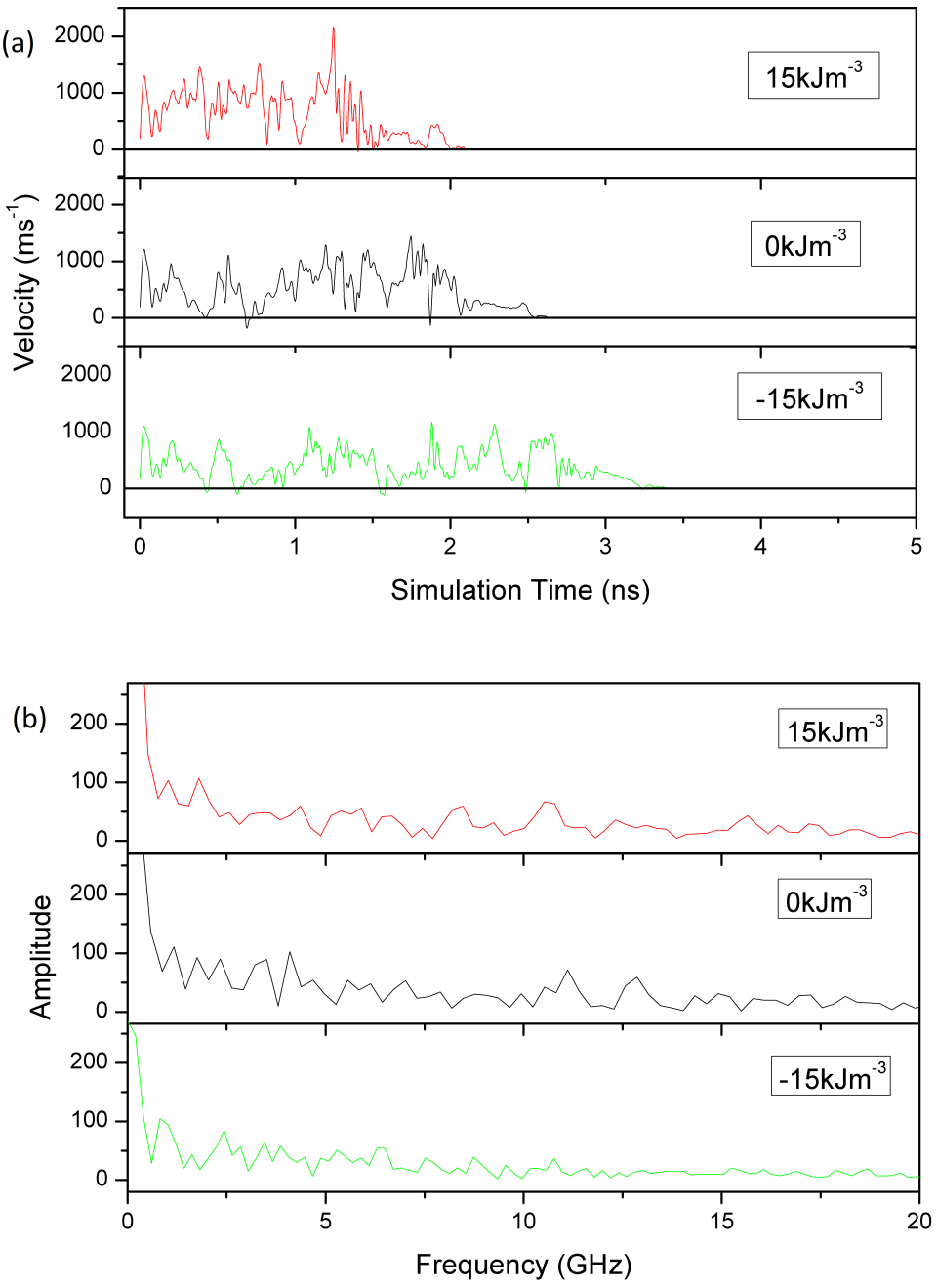

Figure 5.27: (a) Instantaneous domain wall velocity as a function of time in a 100 nm wire with a 60 mT applied magnetic field. (b) FFT of instantaneous velocity.

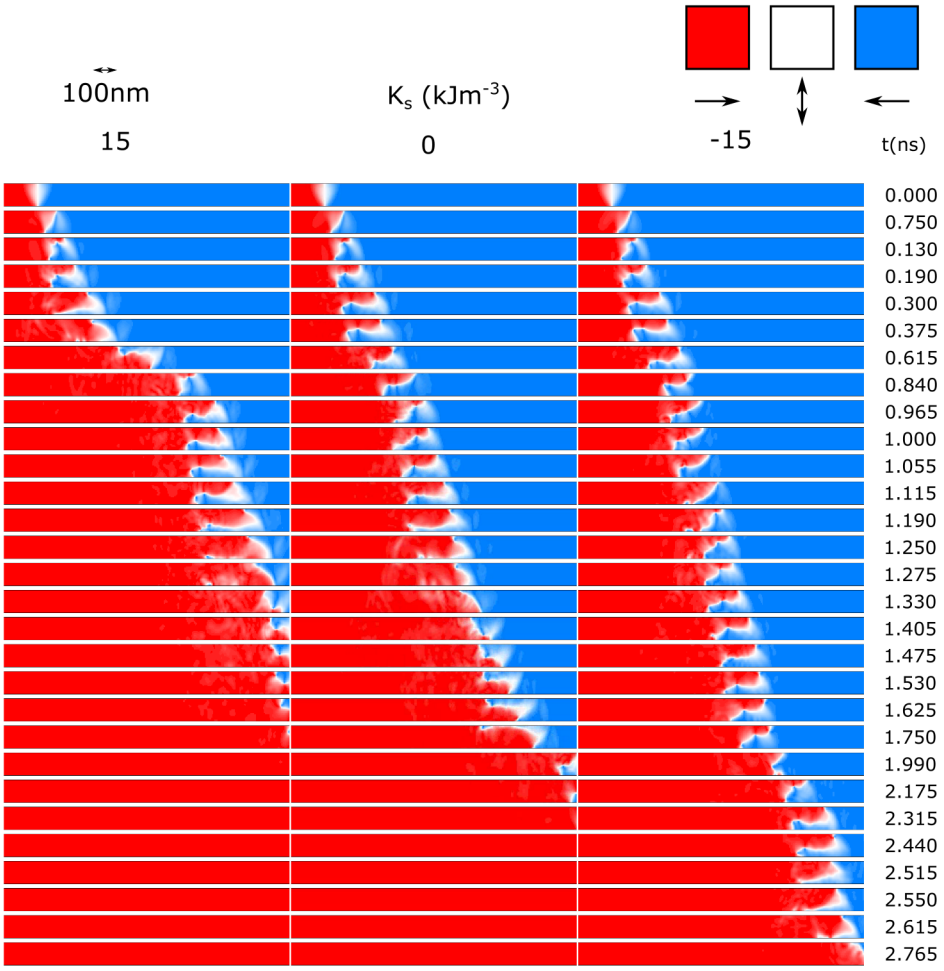

Figure 5.28: Examples of domain wall motion behaviour in 100 nm wire under a 60 mT driving field for uniaxial anisotropy K_s. The magnetisation directions represented in the image are shown in the coloured boxes.

is likely to be the proximity of this width to vortex domain walls being the favoured equilibrium state. This may well have made the behaviour of domain walls more susceptible to alteration by uniaxial anisotropy. The changes in instantaneous velocity at the higher driving magnetic fields are more difficult to explain and investigating further how exactly the uniaxial anisotropy affects the structure and motion of domain walls at these high fields will be an important area for future study.

5.3.3 Depinning Behaviour

This section builds on the investigation of domain wall velocities in wires 48 nm and 100 nm wide by exploring how the depinning behaviour of domain walls is affected by uniaxial anisotropy. In this case domain walls were propagated towards the notch at fields below the Walker breakdown field to minimise distortion of the domain wall before it reaches the notch. Differences in behaviour between the two wires are observed, although this study does not determine exactly the origin of the differences. The simulations presented reveal the range of behaviours one can expect to see when we study depinning behaviour as a function of uniaxial anisotropy. The depinning behaviour of domain walls is important for real device applications where pinning sites may be introduced deliberately or due to fabrication defects. Depinning is discussed further in section 1.2.5.1.

The depinning field was found by examining graphs of the magnetisation as a function of applied field, an example of which is shown in figure 5.29, where there is a rapid change in magnetisation as the domain wall depins, in this case the depinning field is about 38 mT. The depinning field as a function of anisotropy for the 48 nm and 100 nm wires is shown in figure 5.30. Also shown in these graphs are statistical fits to the data. A first order polynomial was fitted to the 48 nm width wire data in figure 5.30(a), with the depinning field $H_{\text{depin}} = 23.16(1)\,\text{mT} - 7.1(1) \times 10^{-5}\,\text{mT}/(\text{kJ}\,\text{m}^3)$. The 100 nm width wire data in figure 5.30 was fitted with a second order polynomial, the depinning field, $H_{\text{depin}} = 46.3(4)\,\text{mT} - 6.9(2) \times 10^{-4}\,\text{mT}/(\text{kJ}\,\text{m}^3) +$

$-1.9(2) \times 10^{-8}\,\mathrm{mT}/(\mathrm{kJ/m^3})^2$. It is clear that the anisotropy has a much greater influence on the depinning behaviour of the 100 nm wire than the 48 nm wire, the range of depinning fields being an order of magnitude larger in the wider wire over the range of anisotropies studied. This greater dependence on anisotropy is not unexpected as the narrower wire will have a larger shape anisotropy, meaning that the uniaxial anisotropy will have a relatively smaller effect. Also of interest is the difference in sign between the first order fitting coefficients, which may arise from a different depinning mechanism in each case.

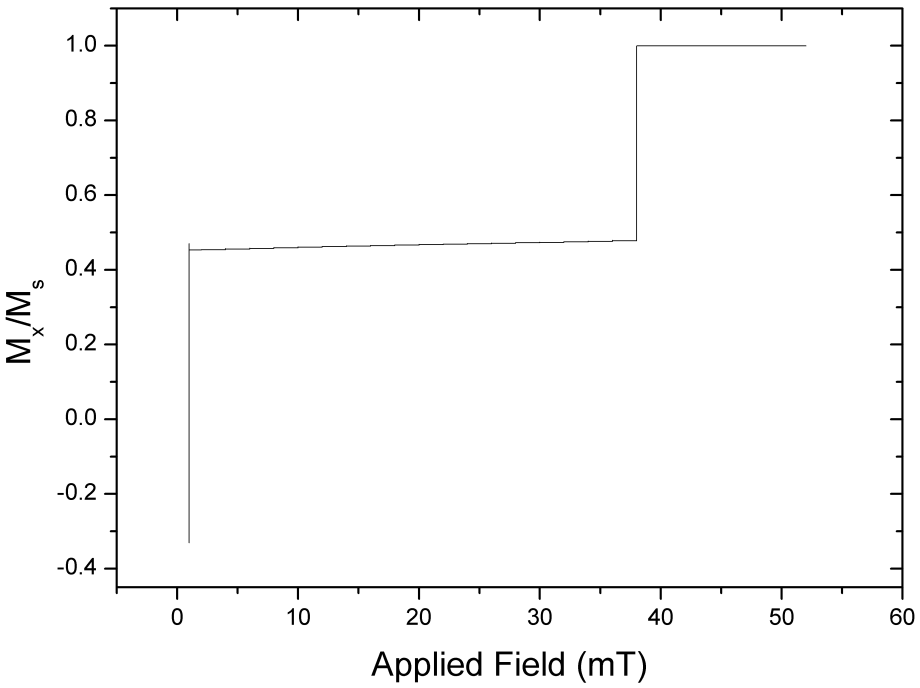

Figure 5.29: Example of graph of magnetisation as a function of applied field used to determine depinning field. The rapid change in magnetisation after depinning happens within one field step.

The images produced by the micromagnetic simulations were used to help further understand the depinning behaviour in these two wires. The 48 nm wire, shown in figure 5.31, is considered first. The domain wall approaches

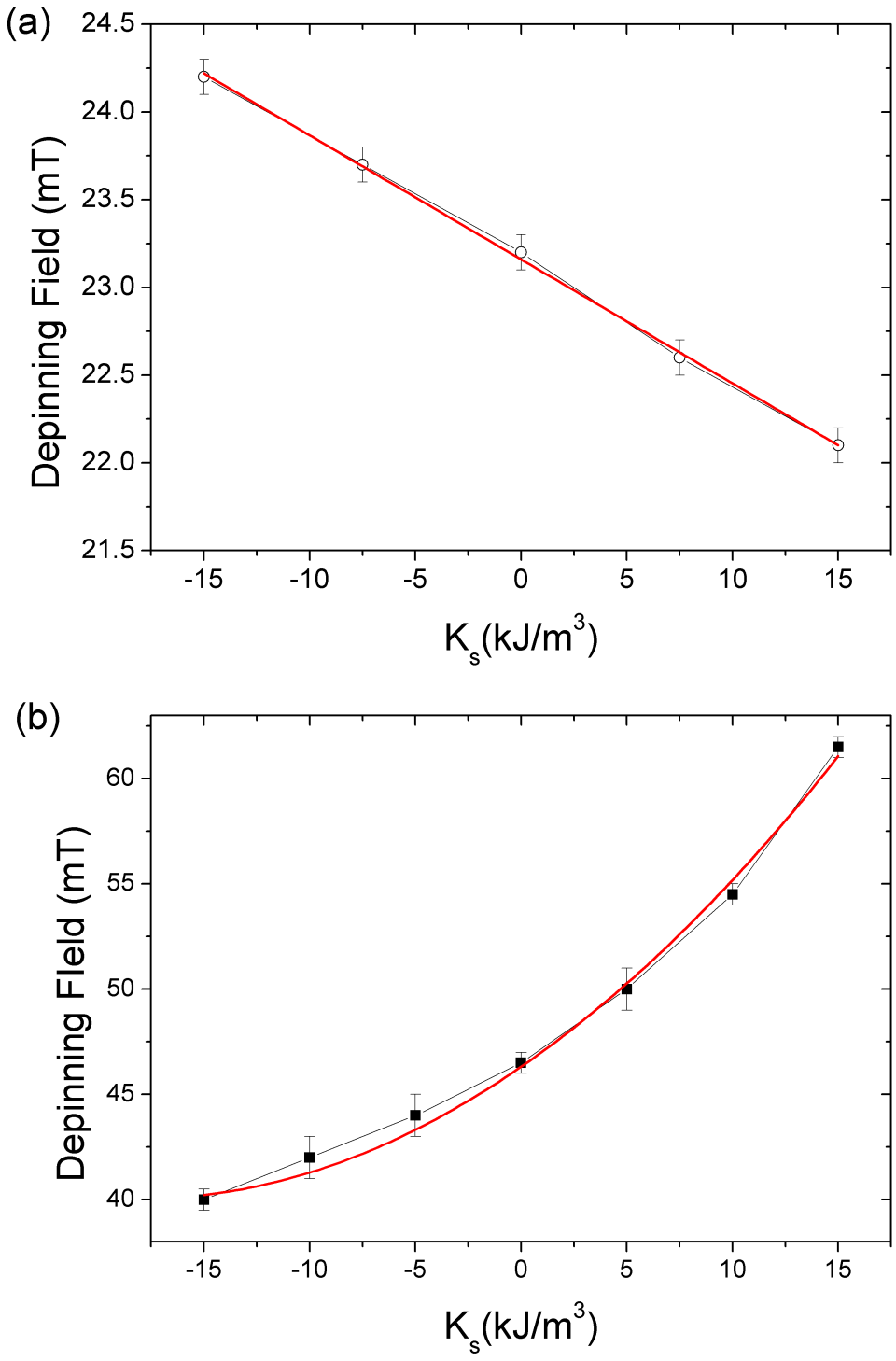

Figure 5.30: Simulated field required to depin domain walls in (a) 48 nm with linear fit and (b) 100 nm with second order polynomial fit as a function of uniaxial anisotropy (K_S). The error bars originate from the magnetic field step size used in each simulation.

the notch with field below the Walker breakdown field. As it reaches the notch the domain wall deforms before beginning to oscillate, before finally being pinned to the right hand side of the notch. As the field is increased the domain wall eventually depins from the notch whereupon the motion of the domain wall is in the precessional regime expected for such a driving field (close to 23 mT).

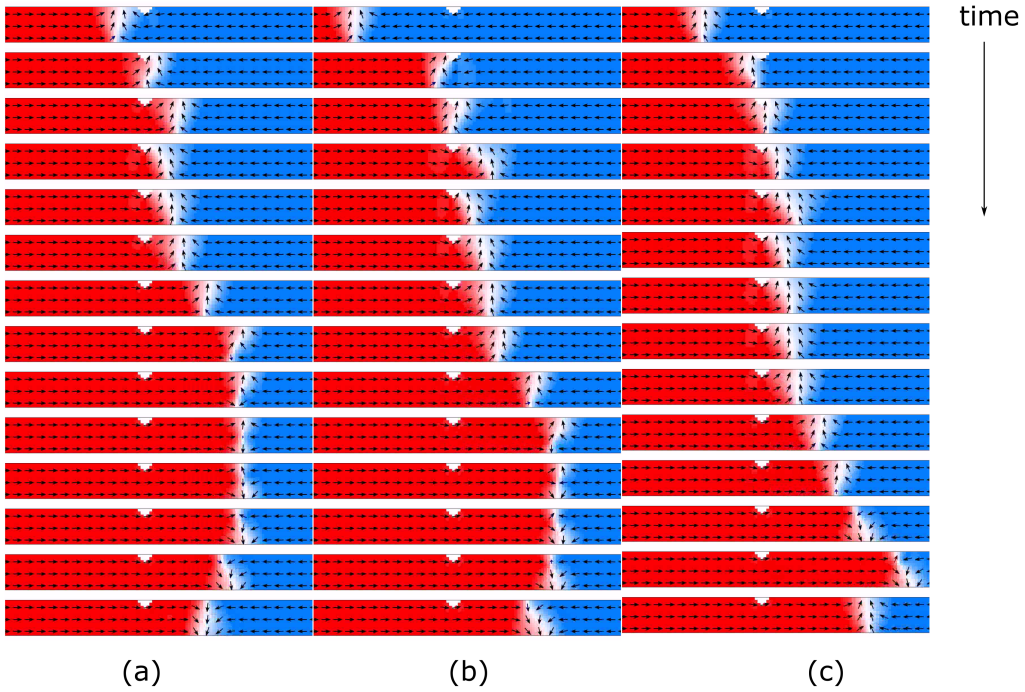

Figure 5.31: Examples of domain wall depinning in the 48 nm wire for uniaxial anisotropy $K_s = -10\,\mathrm{kJ/m^3}$ (a), $K_s = 0\,\mathrm{kJ/m^3}$ (b) and $K_s = 10\,\mathrm{kJ/m^3}$ (c). The depinning fields are 22.1 mT, 23.2 mT and 24.2 mT for $-10\,\mathrm{kJ/m^3}$, $0\,\mathrm{kJ/m^3}$ and $10\,\mathrm{kJ/m^3}$ respectively.

The behaviour of the domain wall in the 100 nm wire shows some differences to that observed in the 48 nm wire. Steps in the depinning of the domain wall in the 100 nm wire are shown in figure 5.32. As in the 48 nm wire the domain wall is brought up to the notch with a field below the Walker breakdown field. On reaching the notch the wall begins to flex whilst pinned, as in the 48 nm case. Unlike the 48 nm wire however, the domain wall oscillates on the left hand side of the notch, before settling into a position at the centre of the

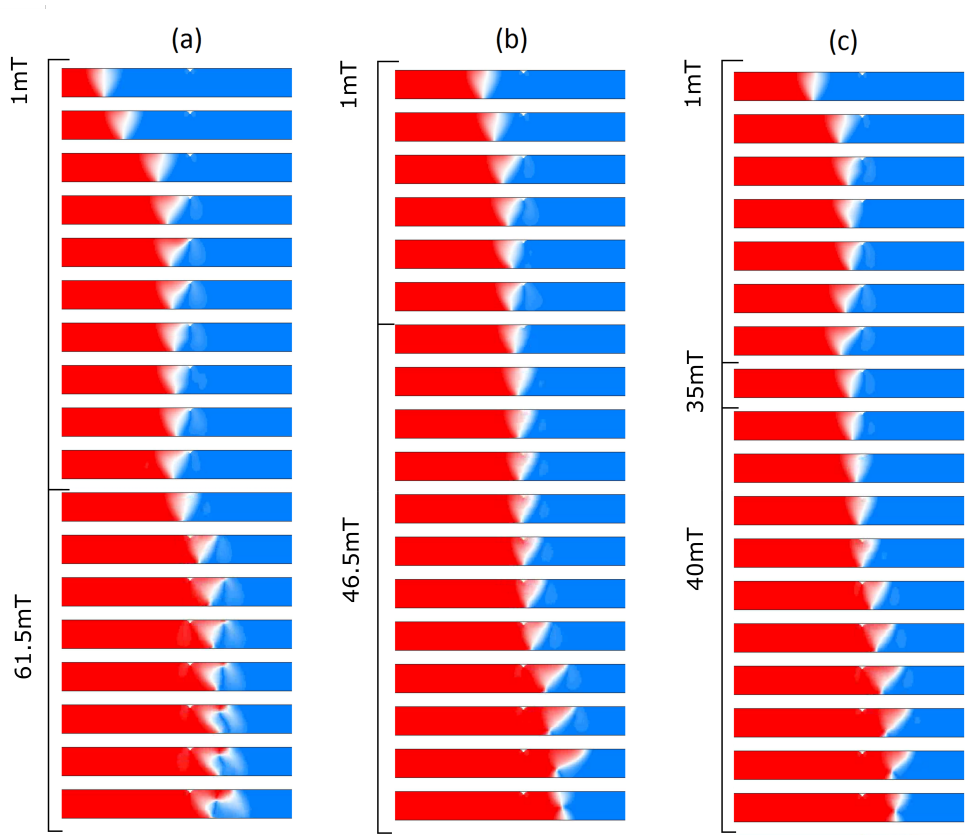

Figure 5.32: Examples of domain wall depinning in the 100 nm wire for uniaxial anisotropy $K_s = 15\,\mathrm{kJ/m^3}$ (a), $K_s = 0\,\mathrm{kJ/m^3}$ (b) and $K_s = -15\,\mathrm{kJ/m^3}$ (c). The domain walls approach the notch under a field of 2.5 mT.

notch. As the relative size of the notch in the wire is different in the two wire widths it is not possible to make a direct comparison between the behaviours in the two wire widths, but the observations may be used to guide further work into the effect of uniaxial anisotropy on depinning behaviour.

These results indicate that one can expect a large degree of control of domain walls with uniaxial anisotropy, and a broad range of behaviours with wire and notch dimensions. More work needs to be done to fully establish the reasons for the range of behaviour observed here. One possibility is that the domain wall is deformed by the uniaxial anisotropy as it travels along the wire, a phenomenon which has been reported elsewhere [118]. The depinning of a domain wall from a notch is dependent on its configuration as it approaches the notch [246], so any deformation could result in a change in depinning field. One way to check this would be to repeat the micromagnetic simulations using an initial magnetisation state of a domain wall already pinned at the notch. Only at this stage would the uniaxial anisotropy be introduced and the system allowed to evolve.

5.4 Conclusions

This chapter has begun to study the effect of uniaxial anisotropy on the behaviour of domain walls in micron and sub-micron wide wires. Focussed MOKE was used to demonstrate that in micron-sized Co wires, the depinning fields of two chiralities of vortex domain wall could be controlled by voltage-induced strain. This observed behaviour was supported by micromagnetic simulations. Experimentally, the depinning field of clockwise vortex walls was found to increase with uniaxial strain parallel to the bar axis, with a small positive gradient. The depinning field of the anticlockwise vortex domain walls had a stronger, negative dependence on the same anisotropy.

The micromagnetic simulations indicated that the clockwise domain wall was much more sensitive to variations in notch depth, and analysis of the output of the simulations revealed that two pinning regimes of the clockwise domain wall

were present, depending on the depth of the notch. The smaller notch depths of 500 nm and 625 nm allowed the vortex core to pass through the constriction following depinning of the wall. In the 675 nm deep notch, however, the vortex core was annihilated at the notch. These two depinning mechanisms resulted in significantly different dependencies of the depinning on the uniaxial anisotropy, with the 675 nm deep notch being much more strongly dependent than the smaller notches. Of the notch depths simulated, the 500 nm notch showed the greatest agreement with the experimentally obtained depinning fields for the clockwise and anticlockwise vortex domain walls.

Analysis of histograms of single shot, rather than averaged, MOKE hysteresis data indicated that there was a much greater range of depinning fields in the clockwise vortex domain walls than in the anticlockwise walls. It may be in the experiment, this greater sensitivity of the depinning of that domain wall chirality originated in variation in the micromagnetic configuration of the wall, such as vortex core position as it approached the notch. Further investigations are however required to establish exactly the origin of this experimentally observed variation in the depinning fields of clockwise domain walls. There was a large degree of variation in the behaviour of the two wires studied experimentally which may have been due to slight differences in the lithography or deposition of the two wires. Such variation in the effects observed between devices is likely to be problematic for device applications, so future studies must address the sensitivity of behaviour to such issues.

The changes in domain wall mobility observed in simulations of sub-micron wires showed that the mobility was increased for positive anisotropy constant K_S and reduced for negative K_S. The changes observed were broadly in keeping with the changes associated with a change in domain wall width resulting from the additional uniaxial anisotropy energy. In the 48 nm wide wire studied there was a linear dependence of fractional change in velocity on applied magnetic field, the origin of which may be an interesting area of future research. In future work it will also be important to more extensively study the two wire widths studied here. By extending the range of applied magnetic fields in the 48 nm wide wire it will be possible to see if this width also shows

the flattening off of the change in velocity with respect to field. Likewise it would be interesting to study the fractional change in domain wall velocity at lower fields in the 100 nm wide wire, so that a direct comparison between the behaviour in the two wire widths could be made. This could itself lead to a systematic study of the domain wall velocity behaviour observed here as a function wire width.

Previous studies of the effect of uniaxial anisotropy on domain wall motion did not investigate the regime for magnetic fields far beyond the Walker breakdown. This chapter demonstrated that for driving magnetic fields far beyond the Walker breakdown, domain walls under the influence of a uniaxial anisotropy show a second peak in average domain wall velocity, similar to that seen in wider wires, and those under the influence of a transverse magnetic field. An important next step for this work will be to better understand the mechanism for the changes in domain wall velocity under different uniaxial anisotropy conditions at high magnetic fields. One initial avenue for investigation could be the role of domain rotation either side of the domain wall.

Finally, this chapter also began to investigate how strain-induced uniaxial anisotropy affects the depinning of transverse walls from notches in wires of width 48 nm and 100 nm. A radically different dependence of depinning field on uniaxial anisotropy density for the wire widths was observed, with the 48 nm wire having a negative, linear dependence on uniaxial anisotropy transverse to the wire axis, while the 100 nm had a positive, parabolic dependence. These observations, although inconclusive, mark out a large area of parameter space to explore in the future.

Chapter 6

Conclusions

In this thesis a combination of magnetotransport, magnetic imaging techniques and micromagnetic simulations have been used to investigate the magnetostrictive properties of $Fe_{81}Ga_{19}$, and how the anisotropies and magnetic domain walls in metallic thin films can be manipulated by strain-induced uniaxial anisotropy. Devices across a range of length scales were studied, from 50 µm Hall bars in chapter 3, to sub-micron nanowires in chapter 5. Across these length scales the behaviour of the domains and domain walls, and their response to strain-induced uniaxial anisotropy has varied.

Chapter 3 began by presenting the characterisation of the basic structural and magnetic properties of the MBE-grown layer of $Fe_{81}Ga_{19}$ studied. XRD was used to find the out-of-plane lattice parameter in the compressed epitaxial layer, from which the fully relaxed lattice parameter was calculated. The XRD results presented also showed the good epitaxial and single-crystal growth of the $Fe_{81}Ga_{19}$ layer. SQUID magnetometry was used to determine the magnetocrystalline anisotropy constants of the $Fe_{81}Ga_{19}$ layer, which was found to have cubic magnetic anisotropy favouring the [100]/[010] directions and a weaker uniaxial component favouring the [110] direction. This resulted in a biaxial anisotropy with easy axes offset by 7° from the [100]/[010] directions. The AMR of $Fe_{81}Ga_{19}$ was studied at room temperature to provide a tool for determining the direction of magnetisation using magnetotransport.

Magnetotransport was further used to demonstrate the setting of two distinct magnetic easy axes using strain induced via a piezoelectric transducer. Simulations of magnetisation reversal based on the expression for the magnetic free energy were used to fit to the magnetotransport data in order to extract the magnetoelastic coupling constant. The value of $B_1 = 1.39(7) \times 10^7\,\mathrm{J/m^3}$ for this MBE-grown layer was comparable to that for single-crystal bulk material of $B_1 = 1.56 \times 10^7\,\mathrm{J/m^3}$ [123]. Chapter 3 also demonstrated that the measurement of the magnetotransport properties of hybrid ferromagnetic/piezoelectric devices provides a reliable method of determining the magnetostrictive properties of thin films clamped to substrates.

The highly magnetostrictive properties of the MBE-grown layer were exploited in chapter 3 to demonstrate switching of the magnetisation in the Hall bar between two easy axes in the absence of an externally applied magnetic field. Evidence from magnetotransport and MOKE microscopy data indicated that domain pinning processes are an important mechanism in the switching of magnetisation in the device studied. The fitting to magnetotransport-derived hysteresis loops did however seem to suggest that the domain wall depinning energy density is not strain-dependent within the resolution of the measurements. The demonstration in chapter 3 of voltage-controlled non-volatile switching of near-90° magnetisation direction is important for its potential applicability to technology. A device based on this could be used to create a memory that can be written with only an electric field. For the device to be of technological interest, however, the same, or similar effects must also be observed at more technologically relevant scales: certainly below 1 µm, and ideally below 100 nm. On these length scales the magnetisation reversal may occur by the motion of single domain walls, or an alternative single domain model may become relevant.

Chapter 4 studied devices with lateral dimensions an order magnitude smaller than those in chapter 3 and explored the control of anisotropies and magnetic domains in microfabricated $Fe_{81}Ga_{19}$ devices with sizes of order 10 µm and smaller. Chapter 4 highlights the importance of size and scaling on the future of devices based on magnetostrictive principles. The ability to control

the behaviour of magnetic domains was altered as different anisotropies were introduced to the system.

Chapter 4 first investigated an L-shaped bar with 8 µm and 15 µm wide sections, where the magnetic reversal characteristics as a function of voltage applied to a piezoelectric transducer were studied. By changing the voltage-induced strain it was possible to move between regimes where the magnetic domain configuration was determined mainly by the strain induced anisotropy or mainly by the shape anisotropy. By doing so the reversal mechanism was tuned between requiring the propagation of 90° domain walls, 180° domain walls and an intermediate flux closure pattern. Also in this bar it was demonstrated that the uniaxial anisotropy induced in the $Fe_{81}Ga_{19}$ layer could be used, in the absence of an externally applied magnetic field, to control the ordered flux-closing magnetic domain state found in the device. Another example of the control of an ordered domain configuration was investigated in micron-sized disks. XMCD-PEEM and micromagnetic calculations demonstrated the 'pinching' of the flux-closing domain configuration using strain-induced uniaxial anisotropy. The voltage-control of magnetisation in disks may have technological applications in microwave electronics, and this initial demonstration has laid the foundations for future work in this area.

The importance of the relaxation of growth strain in the magnetic domain configuration of a 1 µm wide $Fe_{81}Ga_{19}$ wire was also investigated in chapter 4. It was found that a distorted flux-closing domain pattern could be supported in the wire. Finite element structural calculations combined with micromagnetic calculations showed the important role of a growth-relaxation-induced uniaxial anisotropy, transverse to the long axis of the wire in stabilising the flux-closure state. This observation could be of use or a hindrance in the development magnetisation- and domain-wall-based technologies using $Fe_{81}Ga_{19}$. Further studies, for example of wires of varying width, or orientation would be needed to understand the quantitative discrepancies between the experimental and simulated results.

Chapter 5 continued the reduction in the length scale of devices studied to

investigate the effect of uniaxial anisotropy on the behaviour of individual domain walls in micron and sub-micron wide wires, two and three orders of magnitude smaller, respectively, than those devices initially studied in chapter 3. Focussed MOKE was used to demonstrate that in micron-sized Co wires, the depinning fields of two chiralities of vortex domain wall could be controlled by voltage-induced strain. This observed behaviour was supported by micromagnetic simulations. Experimentally, the depinning field of clockwise vortex walls was found to increase with uniaxial strain parallel to the bar axis, with a small positive gradient. The depinning field of the anticlockwise vortex domain walls had a stronger, negative dependence on the same anisotropy.

The micromagnetic simulations presented in chapter 5 indicated that the clockwise domain wall was much more sensitive to variations in notch depth, and analysis of the output of the simulations revealed that two pinning regimes of the clockwise domain wall were present, depending on the depth of the notch. The smaller notch depths of 500 nm and 625 nm allowed the vortex core to pass through the constriction following depinning of the wall. In the 675 nm deep notch, however, the vortex core was annihilated at the notch. These two depinning mechanisms resulted in significantly different dependencies of the depinning on the uniaxial anisotropy, with the 675 nm deep notch being much more strongly dependent than the smaller notches. Of the notch depths simulated, the 500 nm notch showed the greatest agreement with the experimentally obtained depinning fields for the clockwise and anticlockwise vortex domain walls.

Analysis of histograms of single shot, rather than averaged, MOKE hysteresis data indicated that there was a much greater range of depinning fields in the clockwise vortex domain walls than in the anticlockwise walls. It may that the sensitivity of the depinning of the domain wall chirality in the experiment originated in variation in the micromagnetic configuration of the wall, such as vortex core position as it approached the notch. Further investigations are however required to establish exactly the origin of this experimentally observed variation in the depinning fields of clockwise domain walls. There was a large degree of variation in the behaviour of the two wires studied experi-

mentally which may have been due to slight differences in the lithography or deposition of the two wires. Such variation in the effects observed between devices is likely to be problematic for device applications, so future studies must address the sensitivity of behaviour to such issues.

The changes in domain wall mobility observed in simulations of sub-micron wires in chapter 5 showed that the mobility was increased for positive anisotropy constant K_S and reduced for negative K_S. The changes observed were broadly in keeping with the changes associated with a change in domain wall width resulting from the additional uniaxial anisotropy energy. In the 48 nm wide wire studied there was a linear dependence on applied magnetic field of the fractional change in velocity due to the presence of uniaxial anisotropy, the origin of which may be an interesting area of future research. In future work it will also be important to investigate more extensively the two wire widths studied in this thesis. By extending the range of applied magnetic fields in the 48 nm wide wire it will be possible to investigate whether this width also shows the flattening off of the change in velocity with respect to field. Likewise it would be interesting to study the relative change in domain wall velocity at lower fields in the 100 nm wide wire, so that a direct comparison between the behaviour in the two wire widths can be made. This could itself lead to a systematic study of the domain wall velocity behaviour as a function wire width.

Previous studies of the effect of uniaxial anisotropy on domain wall motion did not investigate the regime for magnetic fields far beyond the Walker breakdown. Chapter 5 demonstrated that for driving magnetic fields far beyond the Walker breakdown, domain walls under the influence of a uniaxial anisotropy show a second peak in average domain wall velocity, similar to that seen in wider wires, and those under the influence of a transverse magnetic field. An important next step for this work will be to better understand the mechanism for the changes in domain wall velocity under different uniaxial anisotropy conditions at high magnetic fields. One initial avenue for investigation could be the role of domain rotation either side of the domain wall.

Finally, chapter 5 also began to investigate how strain-induced uniaxial anisotropy affects the depinning of transverse walls from notches in wires of width 48 nm and 100 nm. A radically different dependence of depinning field on uniaxial anisotropy density for the wire widths was observed, with the 48 nm wire having a negative, linear dependence on uniaxial anisotropy transverse to the wire axis, while the 100 nm had a positive, parabolic dependence. These observations, although inconclusive, mark out a large area of parameter space to explore in the future.

References

[1] W Thomson. On the Electro-Dynamic Qualities of Metals:–Effects of Magnetization on the Electric Conductivity of Nickel and of Iron. *Proceedings of the Royal Society of London*, 8:546–550, 1856. 1, 35

[2] Robert P. Hunt. A magnetoresistive readout transducer. *Magnetics, IEEE Transactions on*, 7(1):150–154, Mar 1971. 1

[3] Ching Tsang, Mao-Min Chen, and T. Yogi. Gigabit-density magnetic recording. *Proceedings of the IEEE*, 81(9):1344–1359, Sep 1993. 1

[4] Ching Tsang, Tsann Lin, S. MacDonald, M. Pinarbasi, N. Robertson, H. Santini, Mary Doerner, T. Reith, Lang Vo, T. Diola, and P. Arnett. 5 Gb/in^2 recording demonstration with conventional AMR dual element heads and thin film disks. *Magnetics, IEEE Transactions on*, 33(5):2866–2871, Sep 1997. 1

[5] M. N. Baibich, J. M. Broto, A. Fert, F. Nguyen Van Dau, F. Petroff, P. Etienne, G. Creuzet, A. Friederich, and J. Chazelas. Giant Magnetoresistance of (001) Fe/(001) Cr Magnetic Superlattices. *Phys. Rev. Lett.*, 61:2472–2475, Nov 1988. 3

[6] G. Binasch, P. Grünberg, F. Saurenbach, and W. Zinn. Enhanced magnetoresistance in layered magnetic structures with antiferromagnetic interlayer exchange. *Phys. Rev. B*, 39:4828–4830, Mar 1989. 3

[7] S. S. P. Parkin, Z. G. Li, and David J. Smith. Giant magnetoresistance in antiferromagnetic Co/Cu multilayers. *Applied Physics Letters*, 58(23):2710–2712, 1991. 3

[8] Stuart Parkin, Xin Jiang, Christian Kaiser, A. Panchula, K. Roche, and Mahesh Samant. Magnetically engineered spintronic sensors and memory. *Proceedings of the IEEE*, 91(5):661–680, May 2003. 3

[9] B. Dieny, V. S. Speriosu, S. Metin, S. S. P. Parkin, B. A. Gurney, P. Baumgart, and D. R. Wilhoit. Magnetotransport properties of magnetically soft spin-valve structures (invited). *Journal of Applied Physics*, 69(8):4774–4779, 1991. 3

[10] Ching Tsang, R.E. Fontana, Tsann Lin, D.E. Heim, Virgil S. Speriosu, B.A. Gurney, and M.L. Williams. Design, fabrication and testing of spin-valve read heads for high density recording. *Magnetics, IEEE Transactions on*, 30(6):3801–3806, Nov 1994. 3

[11] M. Julliere. Tunneling between ferromagnetic films. *Physics Letters A*, 54(3):225 – 226, 1975. 3, 4

[12] J Mathon. Theory of spin-dependent tunnelling in magnetic junctions. *Journal of Physics D: Applied Physics*, 35(19):2437, 2002. 4

[13] J. S. Moodera, Lisa R. Kinder, Terrilyn M. Wong, and R. Meservey. Large magnetoresistance at room temperature in ferromagnetic thin film tunnel junctions. *Phys. Rev. Lett.*, 74:3273–3276, Apr 1995. 4

[14] T. Miyazaki and N. Tezuka. Giant magnetic tunneling effect in Fe/Al2O3/Fe junction . *Journal of Magnetism and Magnetic Materials*, 139(3):L231 – L234, 1995. 4

[15] Stuart S. P. Parkin, Christian Kaiser, Alex Panchula, Philip M. Rice, Brian Hughes, Mahesh Samant, and See-Hun Yang. Giant tunnelling magnetoresistance at room temperature with MgO (100) tunnel barriers. *Nat Mater*, 3(12):862–867, December 2004. 4

[16] P P Freitas, R Ferreira, S Cardoso, and F Cardoso. Magnetoresistive sensors. *Journal of Physics: Condensed Matter*, 19(16):165221, 2007. 4

[17] Sining Mao, Yonghua Chen, Feng Liu, Xingfu Chen, Bin Xu, Puling Lu, M. Patwari, Haiwen Xi, Clif Chang, B. Miller, D. Menard, B. Pant, J. Loven, K. Duxstad, Shaoping Li, Zhengyong Zhang, A. Johnston, R. Lamberton, M. Gubbins, T. McLaughlin, J. Gadbois, Juren Ding, B. Cross, Song Xue, and P. Ryan. Commercial TMR heads for hard disk drives: characterization and extendibility at 300 Gb/in^2. *Magnetics, IEEE Transactions on*, 42(2):97–102, Feb 2006. 4

[18] M.H. Kryder and Chang Soo Kim. After hard drives – what comes next? *Magnetics, IEEE Transactions on*, 45(10):3406–3413, Oct 2009. 4

[19] D. Gogl and T. Schlösser. MRAM configuration, July 16 2002. US Patent 6,421,271. 4

[20] R.R. Katti, J.L. Tucker, and A. Kohli. Magnetoresistive random access memory (MRAM) package including a multilayer magnetic security structure, August 19 2014. US Patent 8,811,072. 4, 7

[21] ShiLei Zhang, JingYan Zhang, Alexander A. Baker, ShouGuo Wang, GuangHua Yu, and Thorsten Hesjedal. Three dimensional magnetic abacus memory. *Sci. Rep.*, 4:6109, August 2014. 4

[22] H. Cramman, David S. Eastwood, J.A. King, and D. Atkinson. Multi-level 3 bit-per-cell magnetic random access memory concepts and their associated control circuit architectures. *Nanotechnology, IEEE Transactions on*, 11(1):63–70, Jan 2012. 4

[23] T.M. Maffitt, J.K. DeBrosse, J.A. Gabric, E.T. Gow, M.C. Lamorey, J.S. Parenteau, D.R. Willmott, M.A. Wood, and W.J. Gallagher. Design considerations for MRAM. *IBM Journal of Research and Development*, 50(1):25–39, Jan 2006. 4

[24] J.M. Slaughter. Materials for magnetoresistive random access memory. *Annual Review of Materials Research*, 39(1):277–296, 2009. 4

[25] J.C. Slonczewski. Current-driven excitation of magnetic multilayers. *Journal of Magnetism and Magnetic Materials*, 159(12):L1 – L7, 1996. 6

[26] M. Tsoi, A. G. M. Jansen, J. Bass, W.-C. Chiang, M. Seck, V. Tsoi, and P. Wyder. Excitation of a magnetic multilayer by an electric current. *Phys. Rev. Lett.*, 80:4281–4284, May 1998. 6

[27] J. A. Katine, F. J. Albert, R. A. Buhrman, E. B. Myers, and D. C. Ralph. Current-driven magnetization reversal and spin-wave excitations in co /cu /co pillars. *Phys. Rev. Lett.*, 84:3149–3152, Apr 2000. 6

[28] Chun-Yeol You. Critical current density for spin transfer torque switching with composite free layer structure. *Current Applied Physics*, 10(3):952 – 956, 2010. 6

[29] J.M. Slaughter, N.D. Rizzo, J. Janesky, R. Whig, F.B. Mancoff, D. Houssameddine, J.J. Sun, S. Aggarwal, K. Nagel, S. Deshpande, S.M. Alam, T. Andre, and P. LoPresti. High density ST-MRAM technology (Invited). In *Electron Devices Meeting (IEDM), 2012 IEEE International*, pages 29.3.1–29.3.4, Dec 2012. 7

[30] Tai Min, Qiang Chen, R. Beach, G. Jan, Cheng Horng, W. Kula, T. Torng, R. Tong, T. Zhong, D. Tang, Pokang Wang, Mao min Chen, J.Z. Sun, J.K. DeBrosse, D.C. Worledge, T.M. Maffitt, and W.J. Gallagher. A study of write margin of spin torque transfer magnetic random access memory technology. *Magnetics, IEEE Transactions on*, 46(6):2322–2327, June 2010. 7

[31] Fanghui Ren, A. Jander, P. Dhagat, and C. Nordman. Radiation Tolerance of Magnetic Tunnel Junctions With MgO Tunnel Barriers. *Nuclear Science, IEEE Transactions on*, 59(6):3034–3038, Dec 2012. 7

[32] Stuart Parkin and See-Hun Yang. Memory on the racetrack. *Nat Nano*, 10(3):195–198, March 2015. 7, 8

[33] S. Chatterjee, Sayeef Salahuddin, Satish Kumar, and S. Mukhopadhyay. Impact of Self-Heating on Reliability of a Spin-Torque-Transfer RAM Cell. *Electron Devices, IEEE Transactions on*, 59(3):791–799, March 2012. 7

[34] W.J. Gallagher and S.S.P. Parkin. Development of the magnetic tunnel junction MRAM at IBM: From first junctions to a 16-Mb MRAM demonstrator chip. *IBM Journal of Research and Development*, 50(1):5–23, Jan 2006. 7, 118

[35] Stuart S. P. Parkin, Masamitsu Hayashi, and Luc Thomas. Magnetic domain-wall racetrack memory. *Science*, 320(5873):190–194, 2008. 7, 118

[36] Masamitsu Hayashi, Luc Thomas, Charles Rettner, Rai Moriya, Yaroslaw B. Bazaliy, and Stuart S. P. Parkin. Current driven domain wall velocities exceeding the spin angular momentum transfer rate in permalloy nanowires. *Phys. Rev. Lett.*, 98:037204, Jan 2007. 7

[37] See-Hun Yang, Kwang-Su Ryu, and Stuart Parkin. Domain-wall velocities of up to 750ms^{-1} driven by exchange-coupling torque in synthetic antiferromagnets. *Nat Nano*, 10(3):221–226, March 2015. 8

[38] A. Omari, K. and J. Hayward, T.˙ Chirality-based vortex domain-wall logic gates. *Phys. Rev. Applied*, 2:044001, Oct 2014. 8, 16

[39] Yoshinobu Nakatani, André Thiaville, and Jacques Miltat. Head-to-head domain walls in soft nano-strips: a refined phase diagram. *Journal of Magnetism and Magnetic Materials*, 290291, Part 1(0):750 – 753, 2005. Proceedings of the Joint European Magnetic Symposia (JEMS' 04). 8, 31, 169

[40] R.D. McMichael and M.J. Donahue. Head to head domain wall structures in thin magnetic strips. *Magnetics, IEEE Transactions on*, 33(5):4167–4169, Sep 1997. 8, 31

[41] D. McGrouther, S. McVitie, J. N. Chapman, and A. Gentils. Controlled domain wall injection into ferromagnetic nanowires from an optimized pad geometry. *Applied Physics Letters*, 91(2):022506, 2007. 8

[42] Andrew D. Kent and Daniel C. Worledge. A new spin on magnetic memories. *Nat Nano*, 10(3):187–191, March 2015. 10

[43] Chao Zhang, Guangyu Sun, Weiqi Zhang, Fan Mi, Hai Li, and Weisheng Zhao. Quantitative modeling of racetrack memory, a tradeoff among area, performance, and power. In *Design Automation Conference (ASP-DAC), 2015 20th Asia and South Pacific*, pages 100–105. IEEE, 2015. 10

[44] Jian-Gang (Jimmy) Zhu. New heights for hard disk drives. *Materials Today*, 6(78):22 – 31, 2003. 8

[45] M. Durlam, B. Craigo, M. DeHerrera, B.N. Engel, G. Grynkewich, B. Huang, J. Janesky, M. Martin, B. Martino, J. Salter, J.M. Slaughter, L. Wise, and S. Tehrani. Toggle mram: A highly-reliable non-volatile memory. In *VLSI Technology, Systems and Applications, 2007. VLSI-TSA 2007. International Symposium on*, pages 1–2, April 2007. 8

[46] A. Chavent, J. Alvarez-Herault, C. Portemont, C. Creuzet, J. Pereira, J. Vidal, K. Mackay, R.C. Sousa, I.L. Prejbeanu, and B. Dieny. Effects of the Heating Current Polarity on the Writing of Thermally Assisted Switching-MRAM. *Magnetics, IEEE Transactions on*, 50(11):1–4, Nov 2014. 10

[47] K. Hofmann, K. Knobloch, C. Peters, and R. Allinger. Comprehensive statistical investigation of STT-MRAM thermal stability. In *VLSI Technology (VLSI-Technology): Digest of Technical Papers, 2014 Symposium on*, pages 1–2, June 2014. 10

[48] Fumihiro Matsukura, Yoshinori Tokura, and Hideo Ohno. Control of magnetism by electric fields. *Nat Nano*, 10(3):209–220, March 2015. 10, 11

[49] P.M. Braganca, J.A. Katine, N.C. Emley, D. Mauri, J.R. Childress, Philip M. Rice, Eugene Delenia, Daniel C. Ralph, and R.A. Buhrman. A three-terminal approach to developing spin-torque written magnetic random access memory cells. *Nanotechnology, IEEE Transactions on*, 8(2):190–195, March 2009. 10

[50] N.N. Mojumder, S.K. Gupta, S.H. Choday, D.E. Nikonov, and K. Roy. A Three-Terminal Dual-Pillar STT-MRAM for High-Performance Robust Memory Applications. *Electron Devices, IEEE Transactions on*, 58(5):1508–1516, May 2011. 10

[51] S. Fukami, T. Suzuki, K. Nagahara, N. Ohshima, Y. Ozaki, S. Saito, R. Nebashi, N. Sakimura, H. Honjo, K. Mori, C. Igarashi, S. Miura, N. Ishiwata, and T. Sugibayashi. Low-current perpendicular domain wall motion cell for scalable high-speed MRAM. In *VLSI Technology, 2009 Symposium on*, pages 230–231, June 2009. 10

[52] Guillaume Prenat, Kotb Jabeur, Gregory Di Pendina, Olivier Boulle, and Gilles Gaudin. Beyond STT-MRAM, Spin Orbit Torque RAM SOT-MRAM for High Speed and High Reliability Applications. In Weisheng Zhao and Guillaume Prenat, editors, *Spintronics-based Computing*, pages 145–157. Springer International Publishing, 2015. 10

[53] Murat Cubukcu, Olivier Boulle, Marc Drouard, Kevin Garello, Can Onur Avci, Ioan Mihai Miron, Juergen Langer, Berthold Ocker, Pietro Gambardella, and Gilles Gaudin. Spin-orbit torque magnetization switching of a three-terminal perpendicular magnetic tunnel junction. *Applied Physics Letters*, 104(4):042406, 2014. 10, 11

[54] Yusung Kim, S.H. Choday, and K. Roy. DSH-MRAM: Differential Spin Hall MRAM for On-Chip Memories. *Electron Device Letters, IEEE*, 34(10):1259–1261, Oct 2013. 10

[55] H. Ohno, D. Chiba, F. Matsukura, T. Omiya, E. Abe, T. Dietl, Y. Ohno, and K. Ohtani. Electric-field control of ferromagnetism. *Nature*, 408(6815):944–946, December 2000. 12

[56] Maciej Sawicki, Daichi Chiba, Anna Korbecka, Yu Nishitani, Jacek A. Majewski, Fumihiro Matsukura, Tomasz Dietl, and Hideo Ohno. Experimental probing of the interplay between ferromagnetism and localization in (Ga, Mn)As. *Nat Phys*, 6(1):22–25, January 2010. 12

[57] H. Boukari, P. Kossacki, M. Bertolini, D. Ferrand, J. Cibert, S. Tatarenko, A. Wasiela, J. A. Gaj, and T. Dietl. Light and electric field control of ferromagnetism in magnetic quantum structures. *Phys. Rev. Lett.*, 88:207204, May 2002. 12

[58] Y. D. Park, A. T. Hanbicki, S. C. Erwin, C. S. Hellberg, J. M. Sullivan, J. E. Mattson, T. F. Ambrose, A. Wilson, G. Spanos, and B. T. Jonker. A Group-IV Ferromagnetic Semiconductor: Mn_xGe_{1-x}. *Science*, 295(5555):651–654, 2002. 12

[59] D. Chiba, M. Sawicki, Y. Nishitani, Y. Nakatani, F. Matsukura, and H. Ohno. Magnetization vector manipulation by electric fields. *Nature*, 455(7212):515–518, September 2008. 12

[60] D. Chiba, M. Yamanouchi, F. Matsukura, and H. Ohno. Electrical manipulation of magnetization reversal in a ferromagnetic semiconductor. *Science*, 301(5635):943–945, 2003. 12

[61] M. Wang, R. P. Campion, A. W. Rushforth, K. W. Edmonds, C. T. Foxon, and B. L. Gallagher. Achieving high Curie temperature in (Ga,Mn)As. *Applied Physics Letters*, 93(13):132103, 2008. 12

[62] Martin Weisheit, Sebastian Fhler, Alain Marty, Yves Souche, Christiane Poinsignon, and Dominique Givord. Electric field-induced modification of magnetism in thin-film ferromagnets. *Science*, 315(5810):349–351, 2007. 12

[63] T. Maruyama, Y. Shiota, T. Nozaki, K. Ohta, N. Toda, M. Mizuguchi, A. A. Tulapurkar, T. Shinjo, M. Shiraishi, S. Mizukami, Y. Ando, and Y. Suzuki. Large voltage-induced magnetic anisotropy change in a few atomic layers of iron. *Nat Nano*, 4(3):158–161, March 2009. 12

[64] M. Endo, S. Kanai, S. Ikeda, F. Matsukura, and H. Ohno. Electric-field effects on thickness dependent magnetic anisotropy of sputtered $MgO/Co_{40}Fe_{40}B_{20}/Ta$ structures. *Applied Physics Letters*, 96(21):212503, 2010. 12

[65] J. T. Heron, M. Trassin, K. Ashraf, M. Gajek, Q. He, S. Y. Yang, D. E. Nikonov, Y-H. Chu, S. Salahuddin, and R. Ramesh. Electric-field-induced magnetization reversal in a ferromagnet-multiferroic heterostructure. *Phys. Rev. Lett.*, 107:217202, Nov 2011. 12

[66] J. T. Heron, J. L. Bosse, Q. He, Y. Gao, M. Trassin, L. Ye, J. D. Clarkson, C. Wang, Jian Liu, S. Salahuddin, D. C. Ralph, D. G. Schlom, J. Iniguez, B. D. Huey, and R. Ramesh. Deterministic switching of ferromagnetism at room temperature using an electric field. *Nature*, 516(7531):370–373, December 2014. 12

[67] Masashi Tokunaga, Masaki Azuma, and Yuichi Shimakawa. High-Field Study of Strong Magnetoelectric Coupling in Single-Domain Crystals of $BiFeO_3$. *Journal of the Physical Society of Japan*, 79(6):064713, 2010. 12

[68] Carlos Antonio Fernandes Vaz and Urs Staub. Artificial multiferroic heterostructures. *J. Mater. Chem. C*, 1:6731–6742, 2013. 12, 14

[69] Li Shu, Zheng Li, Jing Ma, Ya Gao, Lin Gu, Yang Shen, Yuanhua Lin, and C. W. Nan. Thickness-dependent voltage-modulated magnetism in multiferroic heterostructures. *Applied Physics Letters*, 100(2):022405, 2012. 12

[70] Wei-Gang Wang, Mingen Li, Stephen Hageman, and C. L. Chien. Electric-field-assisted switching in magnetic tunnel junctions. *Nat Mater*, 11(1):64–68, 2012. 12

[71] H. Meng, R. Sbiaa, M. A. K. Akhtar, R. S. Liu, V. B. Naik, and C. C. Wang. Electric field effects in low resistance CoFeB-MgO magnetic tunnel junctions with perpendicular anisotropy. *Applied Physics Letters*, 100(12):122405, 2012. 12

[72] S. M. Wu, Shane A. Cybart, D. Yi, James M. Parker, R. Ramesh, and R. C. Dynes. Full electric control of exchange bias. *Phys. Rev. Lett.*, 110:067202, Feb 2013. 13

[73] V. Laukhin, V. Skumryev, X. Martí, D. Hrabovsky, F. Sánchez, M. V. García-Cuenca, C. Ferrater, M. Varela, U. Lüders, J. F. Bobo, and J. Fontcuberta. Electric-field control of exchange bias in multiferroic epitaxial heterostructures. *Phys. Rev. Lett.*, 97:227201, Nov 2006. 13

[74] V. Skumryev, V. Laukhin, I. Fina, X. Martí, F. Sánchez, M. Gospodinov, and J. Fontcuberta. Magnetization reversal by electric-field decoupling of magnetic and ferroelectric domain walls in multiferroic-based heterostructures. *Phys. Rev. Lett.*, 106:057206, Feb 2011. 13

[75] A.J. Schellekens, A. van den Brink, J.H. Franken, H.J.M. Swagten, and B. Koopmans. Electric-field control of domain wall motion in perpendicularly magnetized materials. *Nat Commun*, 3:847–, May 2012. 13

[76] D. Chiba, M. Kawaguchi, S. Fukami, N. Ishiwata, K. Shimamura, K. Kobayashi, and T. Ono. Electric-field control of magnetic domain-wall velocity in ultrathin cobalt with perpendicular magnetization. *Nat Commun*, 3:888–, June 2012. 13

[77] Uwe Bauer, Satoru Emori, and BeachGeoffrey S. D. Voltage-controlled domain wall traps in ferromagnetic nanowires. *Nat Nano*, 8(6):411–416, June 2013. 13

[78] Y. Tokura. Multiferroics – toward strong coupling between magnetization and polarization in a solid. *Journal of Magnetism and Magnetic Materials*, 310(2, Part 2):1145 – 1150, 2007. Proceedings of the 17th International Conference on Magnetism. 13

[79] K.F. Wang, J.-M. Liu, and Z.F. Ren. Multiferroicity: the coupling between magnetic and polarization orders. *Advances in Physics*, 58(4):321–448, 2009. 13

[80] Carlos A. F. Vaz, Jason Hoffman, Charles H. Ahn, and Ramamoorthy Ramesh. Magnetoelectric coupling effects in multiferroic complex oxide composite structures. *Advanced Materials*, 22(26-27):2900–2918, 2010. 13, 14

[81] T. Zhao, A. Scholl, F. Zavaliche, K. Lee, M. Barry, A. Doran, M. P. Cruz, Y. H. Chu, C. Ederer, N. A. Spaldin, R. R. Das, D. M. Kim, S. H. Baek, C. B. Eom, and R. Ramesh. Electrical control of antiferromagnetic domains in multiferroic $BiFeO_3$ films at room temperature. *Nat Mater*, 5(10):823–829, October 2006. 13

[82] Claude Ederer and Nicola A. Spaldin. Weak ferromagnetism and magnetoelectric coupling in bismuth ferrite. *Phys. Rev. B*, 71:060401, Feb 2005. 13

[83] Gustau Catalan and James F. Scott. Physics and applications of bismuth ferrite. *Advanced Materials*, 21(24):2463–2485, 2009. 13

[84] Shogo Imada, Takuya Kuraoka, Eisuke Tokumitsu, and Hiroshi Ishiwara. Ferroelectricity of $YMnO_3$ thin films on $Pt(111)/Al_2O_3$ (0001) and $Pt(111)/Y_2O_3$ (111)/Si(111) structures grown by molecular beam epitaxy. *Japanese Journal of Applied Physics*, 40(2R):666, 2001. 14

[85] Daisuke Ito, Norifumi Fujimura, Takeshi Yoshimura, and Taichiro Ito. Ferroelectric properties of $YMnO_3$ epitaxial films for ferroelectric-gate field-effect transistors. *Journal of Applied Physics*, 93(9):5563–5567, 2003. 14

[86] A. Posadas, J.-B. Yau, C. H. Ahn, J. Han, S. Gariglio, K. Johnston, K. M. Rabe, and J. B. Neaton. Epitaxial growth of multiferroic $YMnO_3$ on GaN. *Applied Physics Letters*, 87(17):171915, 2005. 14

[87] A. Posadas, J.-B. Yau, and C. H. Ahn. Epitaxial multiferroic hexagonal manganite thin films grown on ZnO. *Physica Status Solidi (b)*, 243(9):2085–2088, 2006. 14

[88] Koichi Kato and Shuichi Iida. Observation of ferroelectric hysteresis loop of Fe_3O_4 at 4.2 K. *Journal of the Physical Society of Japan*, 51(5):1335–1336, 1982. 14

[89] Yoshiko Miyamoto, Shozo Ishihara, Takahiro Hirano, Masayosi Takada, and Naruki Suzuki. Ferroelectricity of magnetite (Fe_3O_4) observed by means of magnetoelectric effect. *Solid State Communications*, 89(1):51 – 54, 1994. 14

[90] C. Medrano, M. Schlenker, J. Baruchel, J. Espeso, and Y. Miyamoto. Domains in the low-temperature phase of magnetite from synchrotron-radiation x-ray topographs. *Phys. Rev. B*, 59:1185–1195, Jan 1999. 14

[91] Kuntal Roy, Supriyo Bandyopadhyay, and Jayasimha Atulasimha. Hybrid spintronics and straintronics: A magnetic technology for ultra low energy computing and signal processing. *Applied Physics Letters*, 99(6):063108, 2011. 14

[92] Ce-Wen Nan, M. I. Bichurin, Shuxiang Dong, D. Viehland, and G. Srinivasan. Multiferroic magnetoelectric composites: Historical perspective, status, and future directions. *Journal of Applied Physics*, 103(3):031101, 2008. 14

[93] G. Srinivasan. Magnetoelectric composites. *Annual Review of Materials Research*, 40(1):153–178, 2010. 14

[94] Yao Wang, Jiamian Hu, Yuanhua Lin, and Ce-Wen Nan. Multiferroic magnetoelectric composite nanostructures. *NPG Asia Mater*, 2:61–68, April 2010. 14

[95] Rahul C. Kambale, Dae-Yong Jeong, and Jungho Ryu. Current status of magnetoelectric composite thin/thick films. *Advances in Condensed Matter Physics*, 2012:15, 2012. 14

[96] M Weiler, A Brandlmaier, S Geprgs, M Althammer, M Opel, C Bihler, H Huebl, M S Brandt, R Gross, and S T B Goennenwein. Voltage controlled inversion of magnetic anisotropy in a ferromagnetic thin film at room temperature. *New Journal of Physics*, 11(1):013021, 2009. 14

[97] Joshua L. Hockel, Alexandre Bur, Tao Wu, Kyle P. Wetzlar, and Gregory P. Carman. Electric field induced magnetization rotation in patterned Ni ring $[Pb(Mg_{1/3}Nb_{2/3})O_3]_{(1-0.32)} - [PbTiO_3]_{0.32}$ heterostructures. *Applied Physics Letters*, 100(2):022401, 2012. 14

[98] Sang-Koog Kim, Jeong-Won Lee, Sung-Chul Shin, Han Wook Song, Chang Ho Lee, and Kwangsoo No. Voltage control of a magnetization easy axis in piezoelectric/ferromagnetic hybrid films. *Journal of Magnetism and Magnetic Materials*, 267(1):127 – 132, 2003. 14

[99] Jeong-Won Lee, Sung-Chul Shin, and Sang-Koog Kim. Spin engineering of copd alloy films via the inverse piezoelectric effect. *Applied Physics Letters*, 82(15):2458–2460, 2003. 14

[100] C. A. F. Vaz, J. Hoffman, A.-B. Posadas, and C. H. Ahn. Magnetic anisotropy modulation of magnetite in $Fe_3O_4/BaTiO_3(100)$ epitaxial structures. *Applied Physics Letters*, 94(2):022504, 2009. 14

[101] Stephan Geprägs, Matthias Opel, Sebastian T. B. Goennenwein, and Rudolf Gross. Giant magnetoelastic effects in $BaTiO_3$-based extrinsic multiferroic hybrids. *Phys. Rev. B*, 86:134432, Oct 2012. 14

[102] Stephan Geprägs, Dan Mannix, Matthias Opel, Sebastian T. B. Goennenwein, and Rudolf Gross. Converse magnetoelectric effects in $Fe_3O_4/BaTiO_3$ multiferroic hybrids. *Phys. Rev. B*, 88:054412, Aug 2013. 14

[103] Guodong Zhu, Kin L. Wong, Jing Zhao, Pedram Khalili Amiri, Jian Zhu, Ilya Krivorotov, and Kang L. Wang. Quantitative analysis of electric field induced change in anisotropy field in $Co_{60}Fe_{20}B_{20}/(011)$ $x Pb(Mg_{1/3}Nb_{2/3})O_3-(1-x)PbTiO_3$ ($x \approx 0.68$) heterostructures. *Applied Physics Letters*, 101(20):202404, 2012. 14

[104] Ming Liu, Jason Hoffman, Jing Wang, Jinxing Zhang, Brittany Nelson-Cheeseman, and Anand Bhattacharya. Non-volatile ferroelastic switching of the verwey transition and resistivity of epitaxial Fe_3O_4/PMN-PT (011). *Scientific Reports*, 3:1876, May 2013. 14

[105] A. W. Rushforth, E. De Ranieri, J. Zemen, J. Wunderlich, K. W. Edmonds, C. S. King, E. Ahmad, R. P. Campion, C. T. Foxon, B. L. Gallagher, K. Výborný, J. Kučera, and T. Jungwirth. Voltage control of magnetocrystalline anisotropy in ferromagnetic-semiconductor-piezoelectric hybrid structures. *Phys. Rev. B*, 78:085314, Aug 2008. 14, 58, 125

[106] M. Overby, A. Chernyshov, L. P. Rokhinson, X. Liu, and J. K. Furdyna. Gamnas-based hybrid multiferroic memory device. *Applied Physics Letters*, 92(19):192501, 2008. 15

[107] V. Uhlíř, M. Urbanek, L. Hladik, J. Spousta, M-Y. Im, P. Fischer, N. Eibagi, J. J. Kan, E. E. Fullerton, and T. Sikola. Dynamic switching of the spin circulation in tapered magnetic nanodisks. *Nat Nano*, 8(5):341–346, May 2013. 15

[108] V. S. Pribiag, I. N. Krivorotov, G. D. Fuchs, P. M. Braganca, O. Ozatay, J. C. Sankey, D. C. Ralph, and R. A. Buhrman. Magnetic vortex oscillator driven by d.c. spin-polarized current. *Nat Phys*, 3(7):498–503, July 2007. 15

[109] S. I. Kiselev, J. C. Sankey, I. N. Krivorotov, N. C. Emley, R. J. Schoelkopf, R. A. Buhrman, and D. C. Ralph. Microwave oscillations of a nanomagnet driven by a spin-polarized current. *Nature*, 425(6956):380–383, September 2003. 15

[110] J. Wunderlich, A. C. Irvine, J. Zemen, V. Holý, A. W. Rushforth, E. De Ranieri, U. Rana, K. Výborný, Jairo Sinova, C. T. Foxon, R. P. Campion, D. A. Williams, B. L. Gallagher, and T. Jungwirth. Local control of magnetocrystalline anisotropy in (Ga,Mn)As microdevices:

Demonstration in current-induced switching. *Phys. Rev. B*, 76:054424, Aug 2007. 15

[111] J. Wenisch, C. Gould, L. Ebel, J. Storz, K. Pappert, M. J. Schmidt, C. Kumpf, G. Schmidt, K. Brunner, and L. W. Molenkamp. Control of magnetic anisotropy in (Ga, Mn)As by lithography-induced strain relaxation. *Phys. Rev. Lett.*, 99:077201, Aug 2007. 15

[112] C. S. King, J. Zemen, K. Olejník, L. Horák, J. A. Haigh, V. Novák, A. Irvine, J. Kučera, V. Holý, R. P. Campion, B. L. Gallagher, and T. Jungwirth. Strain control of magnetic anisotropy in (Ga,Mn)As microbars. *Phys. Rev. B*, 83:115312, Mar 2011. 15

[113] F. Hoffmann, G. Woltersdorf, W. Wegscheider, A. Einwanger, D. Weiss, and C. H. Back. Mapping the magnetic anisotropy in (Ga,Mn)As nanostructures. *Phys. Rev. B*, 80:054417, Aug 2009. 15

[114] Aakash Pushp, Timothy Phung, Charles Rettner, Brian P. Hughes, See-Hun Yang, Luc Thomas, and Stuart S. P. Parkin. Domain wall trajectory determined by its fractional topological edge defects. *Nat Phys*, 9(8):505–511, August 2013. 16

[115] L. K. Bogart, D. Atkinson, K. O'Shea, D. McGrouther, and S. McVitie. Dependence of domain wall pinning potential landscapes on domain wall chirality and pinning site geometry in planar nanowires. *Phys. Rev. B*, 79:054414, Feb 2009. 16, 34, 35, 151

[116] S Goolaup, S C Low, M Chandra Sekhar, and W S Lew. Dependence of pinning on domain wall spin structure and notch geometry. *Journal of Physics: Conference Series*, 266(1):012079, 2011. 16

[117] Na Lei, Thibaut Devolder, Guillaume Agnus, Pascal Aubert, Laurent Daniel, Joo-Von Kim, Weisheng Zhao, Theodossis Trypiniotis, Russell P. Cowburn, Claude Chappert, Dafiné Ravelosona, and Philippe Lecoeur. Strain-controlled magnetic domain wall propagation in hybrid piezoelectric/ferromagnetic structures. *Nat Commun*, 4:1378–, January 2013. 16

[118] M T Bryan, S Bance, J Dean, T Schrefl, and D A Allwood. Transverse and vortex domain wall structure in magnetic nanowires with uniaxial in-plane anisotropy. *Journal of Physics: Condensed Matter*, 24(2):024205, 2012. 16, 199

[119] J.S. Dean, M.T. Bryan, D.A. Allwood, Simon Bance, M.A. Bashir, Gino Hrkac, Alexander Goncharov, and T. Schrefl. Tailoring domain-wall dynamics with uniaxial anisotropy in nanowires. *Magnetics, IEEE Transactions on*, 45(10):4067–4069, Oct 2009. 16, 170, 175, 189

[120] M. T. Bryan, J. Dean, and D. A. Allwood. Dynamics of stress-induced domain wall motion. *Phys. Rev. B*, 85:144411, Apr 2012. 16, 169, 170

[121] A.G. Olabi and A. Grunwald. Design and application of magnetostrictive materials. *Materials & Design*, 29(2):469 – 483, 2008. 16

[122] Saleem H. Ali. Social and environmental impact of the rare earth industries. *Resources*, 3(1):123, 2014. 17

[123] A. E. Clark, K. B. Hathaway, M. Wun-Fogle, J. B. Restorff, T. A. Lograsso, V. M. Keppens, G. Petculescu, and R. A. Taylor. Extraordinary magnetoelasticity and lattice softening in bcc Fe-Ga alloys. *Journal of Applied Physics*, 93(10):8621–8623, 2003. 17, 25, 44, 47, 102, 106, 143, 203

[124] A.E. Clark, M. Wun-Fogle, J.B. Restorff, T.A. Lograsso, and James R. Cullen. Effect of quenching on the magnetostriction on Fe_{1-x}/Ga_x ($0.13 > x > 0.21$). *Magnetics, IEEE Transactions on*, 37(4):2678–2680, 2001. 17, 44

[125] O. M. J. van 't Erve, C. H. Li, G. Kioseoglou, A. T. Hanbicki, M. Osofsky, S.-F. Cheng, and B. T. Jonker. Epitaxial growth and electrical spin injection from $Fe_{(1-x)}Ga_x$ (001) films on AlGaAs/GaAs (001) heterostructures. *Applied Physics Letters*, 91(12):122515, 2007. 17

[126] Damon A. Resnick, A. McClure, C. M. Kuster, P. Rugheimer, and Y. U. Idzerda. Field dependent magnetic anisotropy of $Ga_{0.2}Fe_{0.8}$ thin films. *Journal of Applied Physics*, 109(7):07A938, 2011. 17

[127] B.D. Cullity. *Introduction to Magnetic Materials*. Addison-Wesley Publishing Company, 1972. 18, 23, 47

[128] J. Stöhr and H.C. Siegmann. *Magnetism: From Fundamentals to Nanoscale Dynamics*. Springer Series in Solid-State Sciences. Springer Berlin Heidelberg, 2006. 18, 20

[129] S.L. Murov, I. Carmichael, and G.L. Hug. *Handbook of Photochemistry, Second Edition*. Taylor & Francis, 1993. 19

[130] C H Marrows. Spin-polarised currents and magnetic domain walls. *Advances In Physics*, 54:585–713, 2005. 19, 48

[131] R.C. O'Handley. *Modern Magnetic Materials: Principles and Applications*. A Wiley-Interscience publication. Wiley, 1999. 20, 21, 22, 23, 29

[132] K Y Wang, K W Edmonds, R P Campion, L X Zhao, C T Foxon, and B L Gallagher. Anisotropic magnetoresistance and magnetic anisotropy in high-quality (Ga,Mn)As films. *Phys. Rev. B*, 72(8):85201, August 2005. 23

[133] S. Chikazumi and C.D. Graham. *Physics of Ferromagnetism*. International Series of Monographs on Physics. Clarendon Press, 1997. 24, 25

[134] M. Shayegan, K. Karrai, Y. P. Shkolnikov, K. Vakili, E. P. De Poortere, and S. Manus. Low-temperature, in situ tunable, uniaxial stress measurements in semiconductors using a piezoelectric actuator. *Applied Physics Letters*, 83(25):5235–5237, 2003. 25, 64

[135] A. Brandlmaier, S. Geprägs, M. Weiler, A. Boger, M. Opel, H. Huebl, C. Bihler, M. S. Brandt, B. Botters, D. Grundler, R. Gross, and S. T. B.

Goennenwein. *In situ* manipulation of magnetic anisotropy in magnetite thin films. *Phys. Rev. B*, 77:104445, Mar 2008. 25

[136] D Sander. The correlation between mechanical stress and magnetic anisotropy in ultrathin films. *Reports on Progress in Physics*, 62(5):809, 1999. 25

[137] S. Blundell. *Magnetism in Condensed Matter*. Oxford Master Series in Condensed Matter Physics 4. OUP Oxford, 2001. 27

[138] Amikam Aharoni. Micromagnetics: past, present and future. *Physica B: Condensed Matter*, 306(14):1 – 9, 2001. Proceedings of the Third International Symposium on Hysteresis an d Micromagnetics Modeling. 27

[139] J. A. Osborn. Demagnetizing factors of the general ellipsoid. *Phys. Rev.*, 67:351–357, Jun 1945. 27

[140] M Kläui. Head-to-head domain walls in magneticnanostructures. *Journal of Physics: Condensed Matter*, 20(31):313001, 2008. 31, 34, 35

[141] M. Kläui, C.A.F. Vaz, A. Lapicki, T. Suzuki, Z. Cui, and J.A.C. Bland. Domain wall pinning in ferromagnetic structures fabricated by focused ion beam. *Microelectronic Engineering*, 7374:785 – 789, 2004. Micro and Nano Engineering 2003. 31, 34, 35

[142] M. Laufenberg, D. Backes, W. Buhrer, D. Bedau, M. Klaui, U. Rdiger, C. A. F. Vaz, J. A. C. Bland, L. J. Heyderman, F. Nolting, S. Cherifi, A. Locatelli, R. Belkhou, S. Heun, and E. Bauer. Observation of thermally activated domain wall transformations. *Applied Physics Letters*, 88(5):052507, 2006. 31

[143] Backes, D. and Schieback, C. and Kläui, M. and Junginger, F. and Ehrke, H. and Nielaba, P. and Rdiger, U. and Heyderman, L. J. and Chen, C. S. and Kasama, T. and Dunin-Borkowski, R. E. and Vaz, C. A. F. and Bland, J. A. C. Transverse domain walls in nanoconstrictions. *Applied Physics Letters*, 91(11):112502, 2007. 31

[144] N. L. Schryer and L. R. Walker. The motion of 180 degree domain walls in uniform dc magnetic fields. *Journal of Applied Physics*, 45(12):5406–5421, 1974. 31

[145] A. Hubert and R. Schäfer. *Magnetic Domains: The Analysis of Magnetic Microstructures*. Springer, 1998. 31, 33, 38, 40, 125

[146] Andrew Kunz and Sarah C. Reiff. Enhancing domain wall speed in nanowires with transverse magnetic fields. *Journal of Applied Physics*, 103(7):07D903, 2008. 31, 33

[147] Geoffrey SD Beach, Corneliu Nistor, Carl Knutson, Maxim Tsoi, and James L Erskine. Dynamics of field-driven domain-wall propagation in ferromagnetic nanowires. *Nature materials*, 4(10):741–744, 2005. 31, 33, 169

[148] A. Thiaville, J.M. Garciá, and J. Miltat. Domain wall dynamics in nanowires. *Journal of Magnetism and Magnetic Materials*, 242245, Part 2(0):1061 – 1063, 2002. 33

[149] Jusang Yang, Corneliu Nistor, G. S. D. Beach, and J. L. Erskine. Magnetic domain-wall velocity oscillations in permalloy nanowires. *Phys. Rev. B*, 77:014413, Jan 2008. 33

[150] Jacques Ferre, Peter J. Metaxas, Alexandra Mougin, Jean-Pierre Jamet, Jon Gorchon, and Vincent Jeudy. Universal magnetic domain wall dynamics in the presence of weak disorder. *Comptes Rendus Physique*, 14(8):651 – 666, 2013. Disordered systems / Systemes desordonnes. 33

[151] M. Kläui, H. Ehrke, U. Rdiger, T. Kasama, R. E. Dunin-Borkowski, D. Backes, L. J. Heyderman, C. A. F. Vaz, J. A. C. Bland, G. Faini, E. Cambril, and W. Wernsdorfer. Direct observation of domain-wall pinning at nanoscale constrictions. *Applied Physics Letters*, 87(10):102509, 2005. 34

[152] M. Kläui, C. A. F. Vaz, J. Rothman, J. A. C. Bland, W. Wernsdorfer, G. Faini, and E. Cambril. Domain wall pinning in narrow ferromagnetic

ring structures probed by magnetoresistance measurements. *Phys. Rev. Lett.*, 90:097202, Mar 2003. 34, 35

[153] Dorothee Petit, Ana-Vanessa Jausovec, Dan Read, and Russell P. Cowburn. Domain wall pinning and potential landscapes created by constrictions and protrusions in ferromagnetic nanowires. *Journal of Applied Physics*, 103(11):114307, 2008. 34, 35

[154] D. Bedau, M. Kläui, S. Krzyk, U. Rüdiger, G. Faini, and L. Vila. Detection of current-induced resonance of geometrically confined domain walls. *Phys. Rev. Lett.*, 99:146601, Oct 2007. 35

[155] Xiaobin Zhu, P. Grtter, V. Metlushko, and B. Ilic. Control of domain patterns in square shaped nickel rings. *Journal of Applied Physics*, 93(10):7059–7061, 2003. 35

[156] A. Libal, M. Grimsditch, V. Metlushko, P. Vavassori, and B. Janko. Control of magnetic vortex chirality in square ring micromagnets. *Journal of Applied Physics*, 98(8):083904, 2005. 35

[157] C. Brownlie, S. McVitie, J. N. Chapman, and C. D. W. Wilkinson. Lorentz microscopy studies of domain wall trap structures. *Journal of Applied Physics*, 100(3):033902, 2006. 35

[158] Luc Thomas, Charles Rettner, Masamitsu Hayashi, Mahesh G. Samant, Stuart S. P. Parkin, Andrew Doran, and Andreas Scholl. Observation of injection and pinning of domain walls in magnetic nanowires using photoemission electron microscopy. *Applied Physics Letters*, 87(26):262501, 2005. 35

[159] D. Atkinson, D. S. Eastwood, and L. K. Bogart. Controlling domain wall pinning in planar nanowires by selecting domain wall type and its application in a memory concept. *Applied Physics Letters*, 92(2):022510, 2008. 35

[160] L. W. McKeehan. Electrical resistance of nickel and permalloy wires as affected by longitudinal magnetization and tension. *Phys. Rev.*, 36:948–977, Sep 1930. 35

[161] J Smit. Magnetoresistance of ferromagnetic metals and alloys at low temperatures. *Physica*, 17(6):612 – 627, 1951. 35

[162] I A Campbell, A Fert, and O Jaoul. The spontaneous resistivity anisotropy in Ni-based alloys. *Journal of Physics C: Solid State Physics*, 3(1S):S95, 1970. 35, 36

[163] T McGuire and R Potter. Anisotropic magnetoresistance in ferromagnetic 3d alloys. *IEEE Transactions on Magnetics*, 11(4):1018–1038, 1975. 35, 36, 37, 38

[164] A. P. Malozemoff. Anisotropic magnetoresistance of amorphous and concentrated polycrystalline iron alloys. *Phys. Rev. B*, 32:6080–6083, Nov 1985. 36

[165] R. P. van Gorkom, J. Caro, T. M. Klapwijk, and S. Radelaar. Temperature and angular dependence of the anisotropic magnetoresistance in epitaxial Fe films. *Phys. Rev. B*, 63:134432, Mar 2001. 36, 37

[166] W. Doring. Die abhangigkeit des widerstandes von nickelkristallen von der richtung der spontanen magnetisierung. *Annalen der Physik*, 424(3):259–276, 1938. 37

[167] Yasuo Gondo and Zenya Funatogawa. On the temperature dependency of magneto-resistance effect of iron single crystal. *Journal of the Physical Society of Japan*, 7(1):41–43, 1952. 38

[168] D C Price and G Williams. Two current conduction in ferromagnetic transition metal alloys: Sn in Fe, Co and Ni. *Journal of Physics F: Metal Physics*, 3(4):810, 1973. 38

[169] T. R. McGuire. Magnetoresistance anisotropy in ferromagnetic Ni-Co alloys at low temperatures. *AIP Conference Proceedings*, 24(1):435–436, 1975. 38

[170] Michael Faraday. Experimental researches in electricity. nineteenth series. *Philosophical Transactions of the Royal Society of London*, 136:1–20, 1846. 38

[171] P. Weinberger. John kerr and his effects found in 1877 and 1878. *Philosophical Magazine Letters*, 88(12):897–907, 2008. 38

[172] J.C. Maxwell. *A Treatise on Electricity and Magnetism*. Number v. 2 in A Treatise on Electricity and Magnetism. Clarendon Press, 1873. 38

[173] W. Voigt. Magnetooptic. In L. Graetz, editor, *Handbuch der Eletrizität und des Magnetismus*. A. Barth, Leipzig, 1920. 38

[174] Z. Q. Qiu and S. D. Bader. Surface magneto-optic kerr effect. *Review of Scientific Instruments*, 71(3):1243–1255, 2000. 38, 39

[175] H. R. Hulme. The faraday effect in ferromagnetics. *Proceedings of the Royal Society of London A: Mathematical, Physical and Engineering Sciences*, 135(826):237–257, 1932. 40

[176] Petros N. Argyres. Theory of the faraday and kerr effects in ferromagnetics. *Phys. Rev.*, 97:334–345, Jan 1955. 40

[177] J. Stohr and S. Anders. X-ray spectro-microscopy of complex materials and surfaces. *IBM Journal of Research and Development*, 44(4):535–551, 2000. 41

[178] Stefania Pizzini, Jan Vogel, Marlio Bonfim, and Alain Fontaine. Time-resolved x-ray magnetic circular dichroism–a selective probe of magnetization dynamics on nanosecond timescales. *Spin Dynamics in Confined Magnetic Structures II*, 87:157–187, 2003. 41

[179] A. E. Clark, B. F. DeSavage, and R. Bozorth. Anomalous thermal expansion and magnetostriction of single-crystal dysprosium. *Phys. Rev.*, 138:A216–A224, Apr 1965. 44

[180] Jayasimha Atulasimha and Alison B Flatau. A review of magnetostrictive iron-gallium alloys. *Smart Materials and Structures*, 20(4):043001, 2011. 44

[181] A.E. Clark, R. Abbundi, and W. Gillmor. Magnetization and magnetic anisotropy of $TbFe_2$, $DyFe_2$, $Tb_{0.27}Dy_{0.73}Fe_2$ and $TmFe_2$. *Magnetics, IEEE Transactions on*, 14(5):542–544, Sep 1978. 44

[182] Yan V. Yang, Yongxin Y. Huang, and Yongmei M. Jin. Effects of magnetocrystalline anisotropy constant K2 on magnetization and magnetostriction of Terfenol-D. *Applied Physics Letters*, 98(1):012503, 2011. 44

[183] A.E. Clark, M. Wun-Fogle, J.B. Restorff, T.A. Lograsso, and J.R. Cullen. Effect of quenching on the magnetostriction on Fe_{1-x}/Ga_x ($0.13 > x > 0.21$). *IEEE Transactions on Magnetics*, 37(4):2678–2680, July 2001. 44

[184] Jason R. Hattrick-Simpers, Dwight Hunter, Corneliu M. Craciunescu, Kyu Sung Jang, Makoto Murakami, James Cullen, Manfred Wuttig, Ichiro Takeuchi, Samuel E. Lofland, Leonid Benderksy, Noble Woo, Robert Bruce Van Dover, Toshiya Takahashi, and Yasubumi Furuya. Combinatorial investigation of magnetostriction in Fe-Ga and Fe-Ga-Al. *Applied Physics Letters*, 93(10):102507, 2008. 45

[185] A. E. Clark, J. B. Restorff, M. Wun-Fogle, K. B. Hathaway, T. A. Lograsso, M. Huang, and E. Summers. Magnetostriction of ternary Fe-Ga-X (X=C,V,Cr,Mn,Co,Rh) alloys. *Journal of Applied Physics*, 101(9):09C507, 2007. 45

[186] D. Viehland, J. F. Li, T. A. Lograsso, A. Ross, and Manfred Wuttig. Structural studies of $Fe_{0.81}Ga_{0.19}$ by reciprocal space mapping. *Applied Physics Letters*, 81(17):3185–3187, 2002. 45

[187] O Ikeda, R Kainuma, I Ohnuma, K Fukamichi, and K Ishida. Phase equilibria and stability of ordered b.c.c. phases in the Fe-rich portion

of the FeGa system . *Journal of Alloys and Compounds*, 347(12):198 – 205, 2002. 45

[188] H. Cao, P. M. Gehring, C. P. Devreugd, J. A. Rodriguez-Rivera, J. Li, and D. Viehland. Role of nanoscale precipitates on the enhanced magnetostriction of heat-treated galfenol ($Fe_{1-x}Ga_x$) alloys. *Phys. Rev. Lett.*, 102:127201, Mar 2009. 45

[189] M. Laver, C. Mudivarthi, J. R. Cullen, A. B. Flatau, W.-C. Chen, S. M. Watson, and M. Wuttig. Magnetostriction and magnetic heterogeneities in iron-gallium. *Phys. Rev. Lett.*, 105:027202, Jul 2010. 45

[190] M. P. Ruffoni, S. Pascarelli, R. Grössinger, R. Sato Turtelli, C. Bormio-Nunes, and R. F. Pettifer. Direct measurement of intrinsic atomic scale magnetostriction. *Phys. Rev. Lett.*, 101:147202, Oct 2008. 45

[191] G. Petculescu, K. B. Hathaway, T. A. Lograsso, M. Wun-Fogle, and A. E. Clark. Magnetic field dependence of galfenol elastic properties. *Journal of Applied Physics*, 97(10):10M315, 2005. 46

[192] Manfred Wuttig, Liyang Dai, and James Cullen. Elasticity and magnetoelasticity of Fe-Ga solid solutions. *Applied Physics Letters*, 80(7):1135, 2002. 46

[193] J. Crangle and G. M. Goodman. The magnetization of pure iron and nickel. *Proceedings of the Royal Society of London A: Mathematical, Physical and Engineering Sciences*, 321(1547):477–491, 1971. 47, 87

[194] HPR Frederikse. *Elastic constants of single crystals*, volume 12. section, 2008. 47

[195] Richard M. Bozorth. *Ferromagnetism*. Wiley-IEEE Press, 8 1978. 47

[196] Yaroslav Tserkovnyak, Arne Brataas, Gerrit E. W. Bauer, and Bertrand I. Halperin. Nonlocal magnetization dynamics in ferromagnetic heterostructures. *Rev. Mod. Phys.*, 77:1375–1421, Dec 2005. 48

[197] M. C. Hickey and J. S. Moodera. Origin of intrinsic gilbert damping. *Phys. Rev. Lett.*, 102:137601, Mar 2009. 48

[198] C. Scheck, L. Cheng, I. Barsukov, Z. Frait, and W. E. Bailey. Low relaxation rate in epitaxial vanadium-doped ultrathin iron films. *Phys. Rev. Lett.*, 98:117601, Mar 2007. 48, 87

[199] J Walowski, M Djordjevic Kaufmann, B Lenk, C Hamann, J McCord, and M Munzenberg. Intrinsic and non-local Gilbert damping in polycrystalline nickel studied by Ti:sapphire laser fs spectroscopy. *Journal of Physics D: Applied Physics*, 41(16):164016, 2008. 48, 87

[200] G.S. Abo, Yang-Ki Hong, Jihoon Park, Jaejin Lee, Woncheol Lee, and Byoung-Chul Choi. Definition of magnetic exchange length. *Magnetics, IEEE Transactions on*, 49(8):4937–4939, Aug 2013. 48

[201] A. T. Hindmarch, **Parkes, D. E.**, and A. W. Rushforth. Fabrication of metallic magnetic nanostructures by argon ion milling using a reversed-polarity planar magnetron ion source. *Vacuum*, 86(10):1600 – 1604, 2012. 53

[202] R. Williams. *Modern GaAs processing methods*. Artech House Antennas And Propagation Library. Artech House, 1990. 54

[203] Imam H. Kazi, P.M. Wild, T.N. Moore, and M. Sayer. The electromechanical behavior of nichrome (80/20 wt.) film . *Thin Solid Films*, 433(12):337 – 343, 2003. Proceedings from the 12th International Conference on Thin Films. 62

[204] G. C. Kuczynski. Effect of elastic strain on the electrical resistance of metals. *Phys. Rev.*, 94:61–64, Apr 1954. 62

[205] A.A. Barlian, Woo-Tae Park, J.R. Mallon, A.J. Rastegar, and B.L. Pruitt. Review: Semiconductor piezoresistance for microsystems. *Proceedings of the IEEE*, 97(3):513–552, March 2009. 62

[206] M.A. Angadi and R. Whiting. Longitudinal and transverse strain sensitivity of nichrome films. *Materials Science and Engineering: B*, 7(12):L1 – L4, 1990. 62

[207] Rainer Heintzmann and Gabriella Ficz. Breaking the resolution limit in light microscopy. *Briefings in Functional Genomics & Proteomics*, 5(4):289–301, 2006. 68

[208] S. S. Dhesi, S. A. Cavill, A. Potenza, H. Marchetto, R. A. Mott, P. Steadman, A. Peach, E. L. Shepherd, X. Ren, U. H. Wagner, and R. Reininger. The nanoscience beamline (i06) at diamond light source. *AIP Conference Proceedings*, 1234(1):311–314, 2010. 73

[209] J. Lenz and Alan S. Edelstein. Magnetic sensors and their applications. *Sensors Journal, IEEE*, 6(3):631–649, 2006. 74

[210] K.-Y. Wang, M. Sawicki, K. W. Edmonds, R. P. Campion, S. Maat, C. T. Foxon, B. L. Gallagher, and T. Dietl. Spin reorientation transition in single-domain (Ga, Mn)As. *Phys. Rev. Lett.*, 95:217204, Nov 2005. 76

[211] B.D. Cullity. *Elements of X-ray Diffraction*. Addison-Wesley series in metallurgy and materials. Addison-Wesley Publishing Company, 1978. 79, 80, 81

[212] A. Stierle, P. Bdeker, and H. Zabel. Epitaxial oxide formation on cr(110) films. *Surface Science*, 327(12):9 – 16, 1995. 81

[213] Miho Yasaka. X-ray thin-film measurement techniques v. x-ray reflectivity measurement. *The Rigaku Journal*, 26(2):1 – 9, 2010. 82

[214] T.C. Huang, R. Gilles, and G. Will. Thin-film thickness and density determination from x-ray reflectivity data using a conventional power diffractometer. *Thin Solid Films*, 230(2):99 – 101, 1993. 83

[215] Josef Fidler and Thomas Schrefl. Micromagnetic modelling - the current state of the art. *Journal of Physics D: Applied Physics*, 33(15):R135, 2000. 83, 85

[216] J. Fidler, R.W. Chantrell, T. Schrefl, and M.A. Wongsam. Micromagnetics: Basic principles. In Editors in Chief: K. H. Jrgen Buschow, Robert W. Cahn, Merton C. Flemings, Bernard Ilschner (print), Edward J. Kramer, Subhash Mahajan, , and Patrick Veyssire (updates), editors, *Encyclopedia of Materials: Science and Technology (Second Edition)*, pages 5642 – 5650. Elsevier, Oxford, second edition edition, 2001. 83, 85

[217] Jacques E. Miltat and Michael J. Donahue. *Numerical Micromagnetics: Finite Difference Methods*. John Wiley & Sons, Ltd, 2007. 85

[218] M. J. Donahue and D. G. Porter. OOMMF user's guide, version 1.0. Technical Report NISTIR 6376, National Institute of Standards and Technology, Gaithersburg, MD, 1999. 85, 86

[219] M.J. Donahue and D.G. Porter. Exchange energy formulations for 3d micromagnetics. *Physica B: Condensed Matter*, 343(14):177 – 183, 2004. Proceedings of the Fourth Intional Conference on Hysteresis and Micromagnetic Modeling. 85

[220] Andrew J. Newell, Wyn Williams, and David J. Dunlop. A generalization of the demagnetizing tensor for nonuniform magnetization. *Journal of Geophysical Research: Solid Earth*, 98(B6):9551–9555, 1993. 86

[221] Amikam Aharoni. Demagnetizing factors for rectangular ferromagnetic prisms. *Journal of Applied Physics*, 83(6):3432–3434, 1998. 86

[222] M.J. Donahue and R.D. McMichael. Exchange energy representations in computational micromagnetics. *Physica B: Condensed Matter*, 233(4):272 – 278, 1997. Hysteresis Modeling and Micromagnetism. 86, 87

[223] **Parkes, D.E.** and P. Wadley and M. Wang and A.T. Hindmarch and R.P. Campion and K.W. Edmonds and A.W. Rushforth and L.R. Shelford and Van Der Laan, G. and S.A. Cavill and V. Holý. Magnetostrictive thin films for microwave spintronics. *Scientific Reports*, 3, 2013. 87, 134

[224] T. A. Ostler, R. Cuadrado, R. W. Chantrell, A. W. Rushforth, and S. A. Cavill. Strain induced vortex core switching in planar magnetostrictive nanostructures. *Phys. Rev. Lett.*, 115:067202, Aug 2015. 87

[225] T. Devolder, P.-H. Ducrot, J.-P. Adam, I. Barisic, N. Vernier, Joo-Von Kim, B. Ockert, and D. Ravelosona. Damping of $Co_xFe_{80-x}B_{20}$ ultrathin films with perpendicular magnetic anisotropy. *Applied Physics Letters*, 102(2):022407, 2013. 87

[226] Erol Girt, W. Huttema, O. N. Mryasov, E. Montoya, B. Kardasz, C. Eyrich, B. Heinrich, A. Yu. Dobin, and O. Karis. A method for measuring exchange stiffness in ferromagnetic films. *Journal of Applied Physics*, 109(7):–, 2011. 87

[227] Somnath Bhattacharyya, J. R. Jinschek, A. Khachaturyan, H. Cao, J. F. Li, and D. Viehland. Nanodispersed DO_3-phase nanostructures observed in magnetostrictive Fe-19%Ga Galfenol alloys. *Phys. Rev. B*, 77:104107, Mar 2008. 89

[228] Holly Marie Schurter. Experimental investigation of the mechanical properties and auxetic behavior of iron-gallium alloys. Master's thesis, University of Maryland, 2009. 90

[229] Heng Gong, Wei Yang, Maithri Rao, D.E. Laughlin, and D.N. Lambeth. Epitaxial growth of quad-crystal Co-alloy magnetic recording media. *Magnetics, IEEE Transactions on*, 35(5):2676–2678, Sept 1999. 90

[230] S F Xu, H P Zhang, W Q Wang, S H Guo, W Zhu, Y H Zhang, X L Wang, D L Zhao, J L Chen, and G H Wu. Magnetostriction and electrical resistivity of Mn doped $Fe_{81}Ga_{19}$ alloys. *Journal of Physics D: Applied Physics*, 41(1):015002, 2008. 94

[231] G. Wastlbauer and J. A. C. Bland. Structural and magnetic properties of ultrathin epitaxial Fe films on GaAs(001) and related semiconductor substrates. *Advances in Physics*, 54(2):137–219, April 2005. 97

[232] H. Iwai. Roadmap for 22nm and beyond (invited paper). *Microelectronic Engineering*, 86(79):1520 – 1528, 2009. 118

[233] D. A. Allwood, G. Xiong, C. C. Faulkner, D. Atkinson, D. Petit, and R. P. Cowburn. Magnetic domain-wall logic. *Science*, 309(5741):1688–1692, 2005. 118

[234] Nobuyuki Otsu. A threshold selection method from gray-level histograms. *Automatica*, 11(285-296):23–27, 1975. 128, 143

[235] Mehmet Sezgin and Bulent Sankur. Survey over image thresholding techniques and quantitative performance evaluation. *Journal of Electronic Imaging*, 13(1):146–168, 2004. 128, 143

[236] **Parkes, D. E.**, R. Beardsley, S. Bowe, I. Isakov, P. A. Warburton, K. W. Edmonds, R. P. Campion, B. L. Gallagher, A. W. Rushforth, and S. A. Cavill. Voltage controlled modification of flux closure domains in planar magnetic structures for microwave applications. *Applied Physics Letters*, 105(6):062405, 2014. 133, 135

[237] Jun-Young Lee, Ki-Suk Lee, Sangkook Choi, Konstantin Y. Guslienko, and Sang-Koog Kim. Dynamic transformations of the internal structure of a moving domain wall in magnetic nanostripes. *Phys. Rev. B*, 76:184408, Nov 2007. 148, 170, 171, 175, 186, 189

[238] Matthew T. Bryan, Thomas Schrefl, Del Atkinson, and Dan A. Allwood. Magnetic domain wall propagation in nanowires under transverse magnetic fields. *Journal of Applied Physics*, 103(7):073906, 2008. 148, 169, 171, 176, 186, 189

[239] L. Thevenard, C. Gourdon, S. Haghgoo, J-P. Adam, H. J. von Bardeleben, A. Lemaître, W. Schoch, and A. Thiaville. Domain wall propagation in ferromagnetic semiconductors: Beyond the one-dimensional model. *Phys. Rev. B*, 83:245211, Jun 2011. 148, 171, 186, 189

[240] Thomas Schrefl, Josef Fidler, K.J. Kirk, and J.N. Chapman. Domain structures and switching mechanisms in patterned magnetic elements. *Journal of Magnetism and Magnetic Materials*, 175(12):193 – 204, 1997. Proceedings of the First Toyota Workshop on Magnetism and Magnetic Materials for High Density Information Storage. 149

[241] Masamitsu Hayashi, Luc Thomas, Charles Rettner, Rai Moriya, Xin Jiang, and Stuart S. P. Parkin. Dependence of current and field driven depinning of domain walls on their structure and chirality in permalloy nanowires. *Phys. Rev. Lett.*, 97:207205, Nov 2006. 151

[242] Maximilian Albert, Matteo Franchin, Thomas Fischbacher, Guido Meier, and Hans Fangohr. Domain wall motion in perpendicular anisotropy nanowires with edge roughness. *Journal of Physics: Condensed Matter*, 24(2):024219, 2012. 169

[243] A.P. Guimarães. *Principles of Nanomagnetism*. NanoScience and Technology. Springer Berlin Heidelberg, 2009. 169

[244] C. Zinoni, A. Vanhaverbeke, P. Eib, G. Salis, and R. Allenspach. Beyond the compact magnetic domain wall. *Phys. Rev. Lett.*, 107:207204, Nov 2011. 183

[245] S. Glathe, M. Zeisberger, U. Hübner, R. Mattheis, and D. V. Berkov. Splitting of a moving transverse domain wall in a magnetic nanostripe in a transverse field. *Phys. Rev. B*, 81:020412, Jan 2010. 186

[246] Sheng-Huang Huang and Chih-Huang Lai. Domain-wall depinning by controlling its configuration at notch. *Applied Physics Letters*, 95(3):032505, 2009. 199